SANDIA REPORT

SAND2005-3226
Unlimited Release
Printed May 2005

Condition Monitoring Through Advanced Sensor and Computational Technology Final Report (January 2002 to May 2005)

Vincent K. Luk and Jung-Taek Kim

Prepared by
Sandia National Laboratories
Albuquerque, New Mexico 87185 and Livermore, California 94550

Sandia is a multiprogram laboratory operated by Sandia Corporation,
a Lockheed Martin Company, for the United States Department of Energy's
National Nuclear Security Administration under Contract DE-AC04-94AL85000.

Sandia National Laboratories

Issued by Sandia National Laboratories, operated for the United States Department of Energy by Sandia Corporation.

Available to DOE and DOE contractors from
U.S. Department of Energy
Office of Scientific and Technical Information
P.O. Box 62
Oak Ridge, TN 37831

Telephone: (865)576-8401
Facsimile: (865)576-5728
E-Mail: reports@adonis.osti.gov
Online ordering: http://www.osti.gov/bridge

Available to the public from
U.S. Department of Commerce
National Technical Information Service
5285 Port Royal Rd
Springfield, VA 22161

Telephone: (800)553-6847
Facsimile: (703)605-6900
E-Mail: orders@ntis.fedworld.gov
Online order: http://www.ntis.gov/help/ordermethods.asp?loc=7-4-0#online

SAND2005-3226
Unlimited Release
Printed May 2005

US Department of Energy

International Nuclear Energy Research Initiative (I-NERI)

Condition Monitoring Through Advanced Sensor and Computational Technology Final Report

(January 2002 to May 2005)

Project Number: 2002-021-K

Vincent K. Luk
Penetrator and Technology Department
Sandia National Laboratories
PO Box 5800, MS 1160
Albuquerque, NM 87185, USA

Jung-Taek Kim
Instrumentation and Control/Human Factors Division
Korea Atomic Energy Research Institute (KAERI)
PO Box 105, Yusong
Daejon, 305-600, Korea

The project was funded by the International Nuclear Energy Research Initiative (I-NERI) Program at the Office of Nuclear Energy, Science, and Technology (NE), United States Department of Energy.
Work Authorization No.: AF/3503/4AL/08

Abstract

The overall goal of this joint research project was to develop and demonstrate advanced sensors and computational technology for continuous monitoring of the condition of components, structures, and systems in advanced and next-generation nuclear power plants (NPPs). This project included investigating and adapting several advanced sensor technologies from Korean and US national laboratory research communities, some of which were developed and applied in non-nuclear industries. The project team investigated and developed sophisticated signal processing, noise reduction, and pattern recognition techniques and algorithms.

The researchers installed sensors and conducted condition monitoring tests on two test loops, a check valve (an active component) and a piping elbow (a passive component), to demonstrate the feasibility of using advanced sensors and computational technology to achieve the project goal. Acoustic emission (AE) devices, optical fiber sensors, accelerometers, and ultrasonic transducers (UTs) were used to detect mechanical vibratory response of check valve and piping elbow in normal and degraded configurations. Chemical sensors were also installed to monitor the water chemistry in the piping elbow test loop. Analysis results of processed sensor data indicate that it is feasible to differentiate between the normal and degraded (with selected degradation mechanisms) configurations of these two components from the acquired sensor signals, but it is questionable that these methods can reliably identify the level and type of degradation. Additional research and development efforts are needed to refine the differentiation techniques and to reduce the level of uncertainties.

Acknowledgements

The International Nuclear Energy Research Initiative (I-NERI) project on condition monitoring through advanced sensor and computational technology took more than three years of hard work and concerted effort from many researchers in the United States and Korea to bring it to a successful completion. The Project Team deeply appreciates their support and cooperation.

The Project Team acknowledges the leadership and vision from Dennis L. Berry, Director of Nuclear and Risk Technologies at Sandia National Laboratories (SNL), who made the initial contact with the senior management at Korea Atomic Energy Research Institute (KAERI) to facilitate the realization of this international joint project. The project team is also indebted to Suibel M. H. Schuppner, the I-NERI Program Manager, Kenneth Osborne, the DOE Project Manager, and Dennis K. Kreid, the Executive Agent, for their guidance and coordination of this joint project.

This project is very fortunate to be supported by a large group of dedicated researchers in the United States and Korea. Vincent Luk (SNL) and Jung-Taek Kim (KAERI) would like to acknowledge the contribution from the entire project team including the following members:

Korea:	KAERI: Jung-Soo Kim, Won Man Pak, Seung-Hwan Seong, Seop Hur, and Cheol Kwon Lee
	Seoul National University: Il Soon Hwang, Na Young Lee, and graduate students
	Pusan National University: Joon-Hyun Lee, Min-Rae Lee, and graduate students
	Chungnam National University: Joon Lyou, Sang Jeong Lee, and graduate students
United States:	SNL: David Craft, Greg Homicz, Jason Petti, Benjamin Spencer, Laura Swiler, Stephen Webb, and Jonathan Weiss.
	Applied Research Laboratory: Mitchell Lebold and Jeff Bracken.

Special thanks are extended to Barbara Meloche for compiling the database on the performance of steam generator tubes in the Unites States and Janise Baldo-Pulaski for providing technical editing of this final project report.

Contents

Figures

Tables

Executive summary

Research objective

The overall goal of this joint research project was to develop and demonstrate advanced sensors and computational technology for continuous monitoring of the condition of components, structures, and systems in advanced and next-generation NPPs. This project included investigating and adapting several advanced sensor technologies from Korean and US national laboratory research communities. To fulfill the project goal, the project chose to conduct condition monitoring tests on check valves and piping elbows using several advanced sensors such as optical fiber sensors, acoustic emission (AE) devices, ultrasonic transducers (UTs), accelerometers, and chemical sensors. The project team investigated and developed sophisticated signal processing, noise reduction, and pattern recognition techniques and algorithms to differentiate various degradation stages of these two components.

Research progress

The research project team conducted two condition monitoring test series to demonstrate the feasibility of using advanced sensors to detect and acquire the dynamic response of subject components and sophisticated computational techniques to process sensor data. The first test series focused on conducting condition monitoring of a selected check valve as an active component. The second test series involved investigating and developing a condition monitoring system for a secondary piping elbow in a non-safety-related environment as a passive component.

KAERI check valve test loop

There are many check valves in use in NPPs; therefore, the integrity of their performance is of genuine concern in plant safety and operational efficiency. This project conducted a series of condition monitoring tests of check valves to provide an effective maintenance and surveillance method to safeguard their functioning and operation. The KAERI researchers tested a check valve in the normal as well as degraded configurations to simulate various identified failure modes, including disc wear and foreign object interference. In this test loop, ultrasonic transducers, AE sensors, accelerometers, and an ultrasonic flow meter were used to obtain sensor signals of the check valve at various flow conditions. Sensor data from each predetermined configuration and flow condition were processed to establish recognizable patterns of check valve response. A schematic diagram of the check valve test loop is shown in Figure E-1. The actual installation of the check valve test loop and the placement of sensors are shown in Figure E-2.

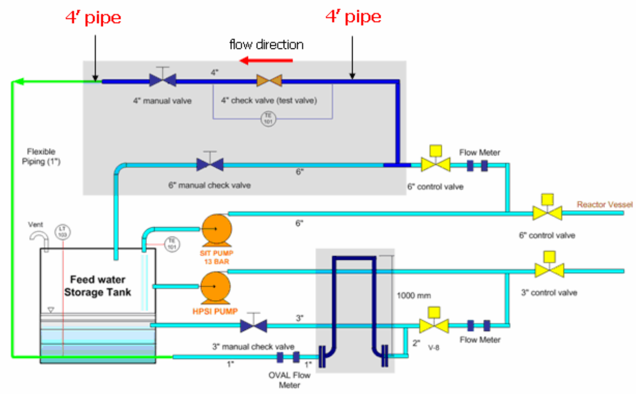

Figure E-1 **Schematic diagram of the KAERI check valve test loop**

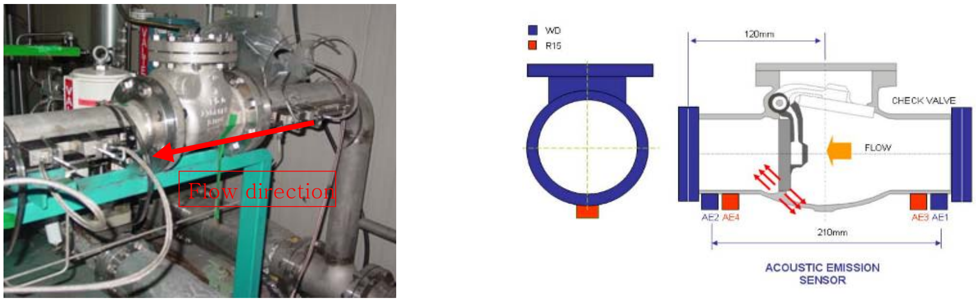

(a) Actual installation

(b) Placement of sensors

Figure E-2 Actual installation and sensor placement of the KAERI check valve test loop

ARL check valve test loop

Separate condition monitoring tests with the ARL check valve test loop, as shown in Figure E-3, were performed to mirror the test matrix at KAERI, including the same check valve design having normal and degraded configurations with disc wear and foreign object interference. These separate ARL tests were conducted to obtain independent data of check valves to help demonstrate the repeatability of test results at KAERI and ARL. Experiments were conducted over a sweep in pressure range (1 to 10 bars), including static pressure.

Figure E-3 Check valve test loop at ARL

Signal processing analyses for the check valve test data

Sensor signal processing analyses using various techniques were performed with all acquired data from the condition monitoring tests at KAERI and ARL. Vibration patterns of the check valve were obtained in its normal configuration as well as in the degraded states with disc wear and foreign objects. Figure E-4 shows the spectral analysis results of AE signals from the KAERI check valve test loop. The processed results indicate that the AE sensor data provide a clear differentiation between the normal and the fault conditions and a resolution for different levels of disc wear simulated in the condition monitoring tests.

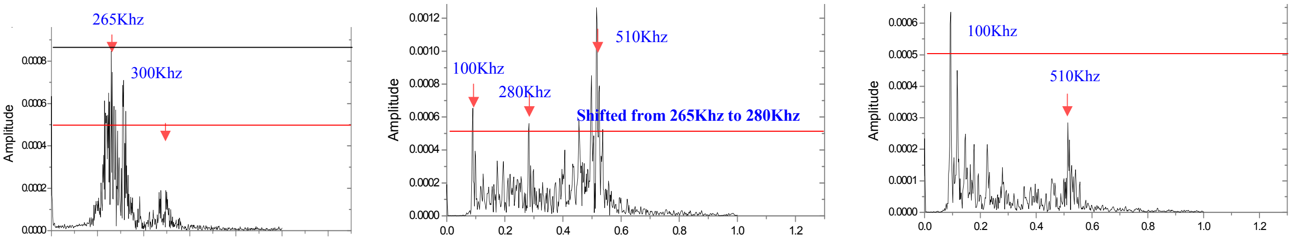

(a) Normal configuration

(b) Degraded state with disc wear

(c) Degraded state with foreign object

Figure E-4 Spectral analysis results of AE signals

Eigen pseudo spectral techniques (EPST), which apply eigendecomposition methods to produce a pseudo spectrum, were investigated to process sensor data. A particular spectral technique, the Multiple Signal

Classification (MUSIC), was selected to process the check valve sensor data due to its use of the noise subspace and its uniform weighting of that subspace to determine the signal spectrum. The MUSIC technique, which does not involve a noise filtering process, provides a very useful procedure to detect faults as shown in Figures E-5 and E-6 for KAERI and ARL data, respectively. Figure E-5 shows the MUSIC pseudo spectra of AE signals for normal configuration and various levels of degradation at a pressure of 9 bar while Figure E-6 shows those for accelerometer signals of a degraded check valve of 3 mm at various pressures.

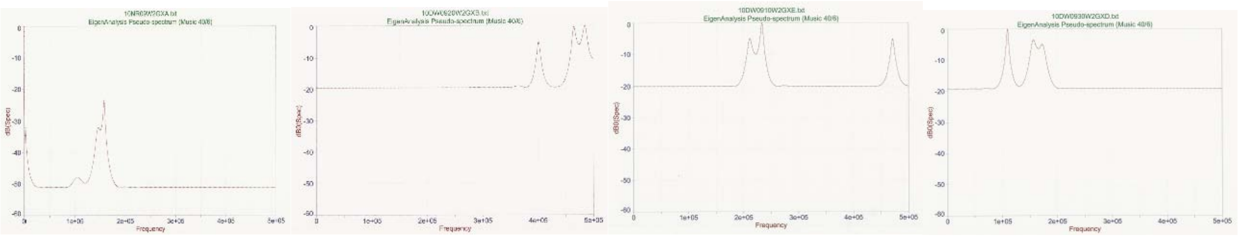

(a) Normal **(b) 1 mm disc wear** **(c) 2 mm disc wear** **(d) 3 mm disc wear**

Figure E-5 MUSIC pseudo spectrum of KAERI data at 9 bars

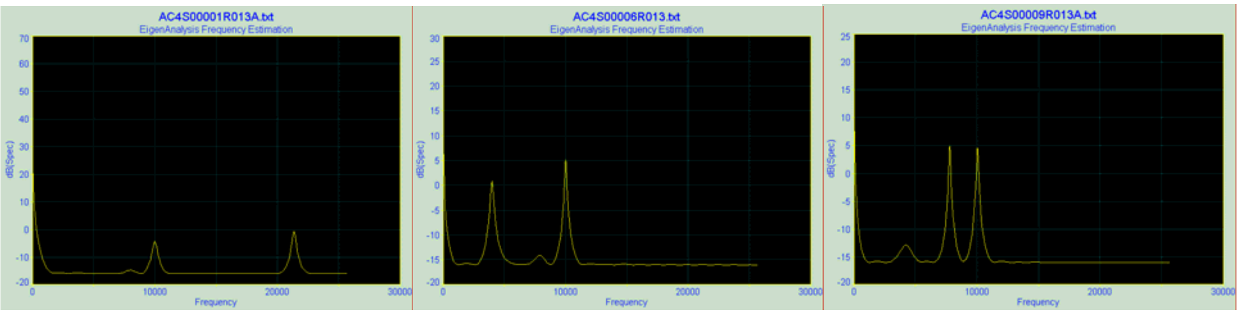

(a) 1 bar **(b) 2 bar** **(c) 3 bar**

Figure E-6 MUSIC pseudo spectrum of ARL data for disc wear of 3 mm

Accelerometer data were also collected from the ARL check valve tests for both the pump (primary noise source) and choke valve (secondary noise source) to allow applying cross correlation and coherence functions in analyzing these data. Figures E-7 and E-8 show the incoherent spectra for different cases of disc wear and foreign objects at a pressure of 9 bar. The plotted results indicate that the multiple coherence method provides one of the possible data processing procedures to differentiate check valve response of normal and faulty conditions, and may be able to characterize different types of fault.

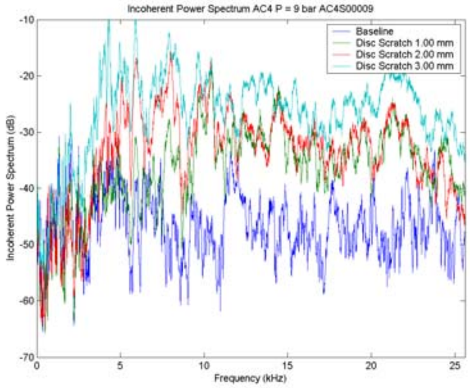

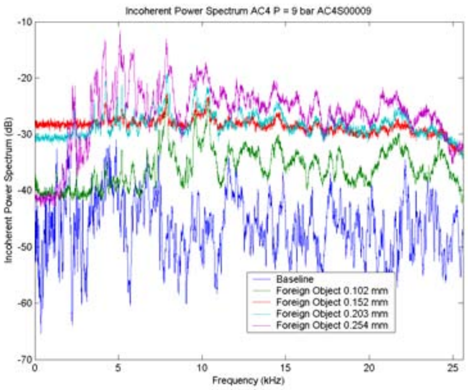

Figure E-7 Incoherent spectra for disc wear **Figure E-8 Incoherent spectra for foreign object**

Application of Artificial Neural Network (ANN)

A trained neural network was developed and applied to examine the sensor data from the check valve tests. The neural network results obtained from disc wear and foreign object failure modes indicate that the neural network algorithm can distinguish between the normal and degraded configurations, it can also differentiate between disc wear and foreign object failure modes, and it is very difficult to estimate the level of degradation.

Finite element analyses of check valve

Several attempts were made to develop and analyze finite element models (FEMs) of the check valve to evaluate the flow-induced vibration response of its various parts in degraded states. Analysts performed simulations with the disc positioned at various angles to the flow direction to study the effect of turbulent flow on the vibration response of the disc. Modal analyses of disc were also performed to investigate its vibration modal shape. Analysis results indicate that the analysts in this project team could only get limited information on the flow-structure interaction response of the check valve, and additional research and development efforts are needed to advance the analysis techniques in this area.

Flow-accelerated corrosion (FAC) test loop at SNU

This test series addressed the degradation of piping systems subjected to corrosion or erosion (or both) attacks in a hostile environment of high temperature, high pressure, and undesirable water chemistry. The flow-accelerated corrosion (FAC) test loop was installed at SNU to investigate this degradation mechanism by conducting condition monitoring tests of a secondary piping elbow in a non-safety related environment as a passive component. The test effort involved investigating the degradation behavior of the piping elbow in an accelerated corrosion/erosion environment, monitored by an Au Electrode-Non PTFE (AUEN) sensor (gold-coated electrode with metal-ceramic brazing seal). Multiple sensors were used to monitor the dynamic response of the piping elbow in the normal and degraded (thinned) configurations in this test loop, including an advanced optical fiber displacement sensor, a micro accelerometer, and a capacitance displacement sensor. A schematic diagram of the piping elbow test loop and its installation are shown in Figure E-9.

(a) Schematic diagram

(b) Actual installation

Figure E-9 Piping elbow test loop

A research effort was undertaken in this project to perform computational fluid dynamics (CFD) analyses of the piping elbow to investigate the flow characteristics, which is important for estimating the corrosion/erosion expected to occur. There are various state-of-the-art computational methods, such as direct numerical simulation (DNS) and large eddy simulation (LES), to calculate the transient turbulent fluctuations. However, these computational techniques are not practical for dynamic flows of engineering interests due to high computational costs. Instead, a turbulent model using the FLUENT code was developed in this project to examine the steady state solution of a turbulent flow inside a piping elbow. Figure E-10 shows the analysis results from this model in terms of regions of high shear stresses and kinetic energy for assessing potential areas vulnerable to the corrosion/erosion attack.

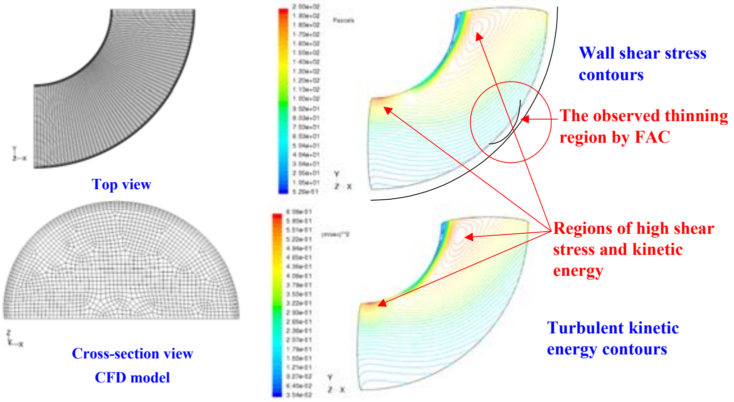

Figure E-10 CFD analyses of piping elbow

SNU researchers investigated to determine the dependence of FAC rate on the water environment including its temperature, flow velocity, ECP, and pH. The ECP and pH electrodes performed well in the FAC test to acquire key ECP and pH data to be monitored and maintained throughout the test. Figure E-11 shows the responses from these electrodes during the chemical tests. Figure E-12 shows the frequency responses from accelerometers due to flow-induced vibration during the tests. The fast Fourier transform (FFT) results of accelerometer data, as shown in E-13 and E-14, indicate that the vibration mode of the piping elbow changes as its thickness reduces with the progress of the FAC tests, but these changes are small indicating that the local pipe thinning is less than expected.

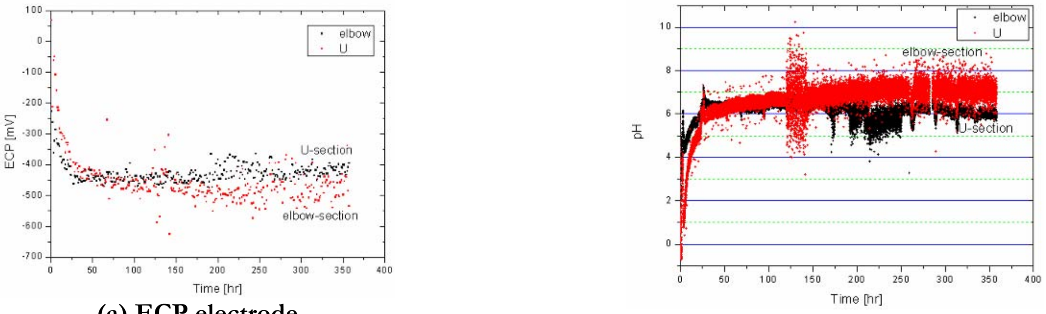

(a) ECP electrode

(b) pH electrode

Figure E-11 Monitored ECP and pH data during the chemical tests

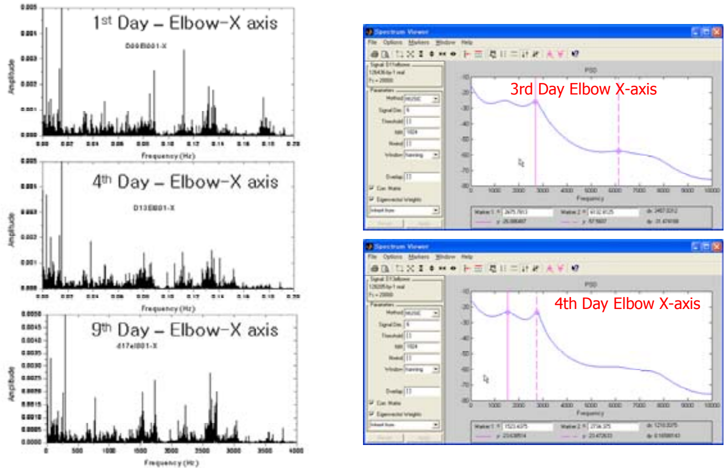

Frequency Analysis (FFT)

Frequency Analysis (MUSIC)

Figure E-12 Frequency responses from accelerometers due to flow-induced vibration

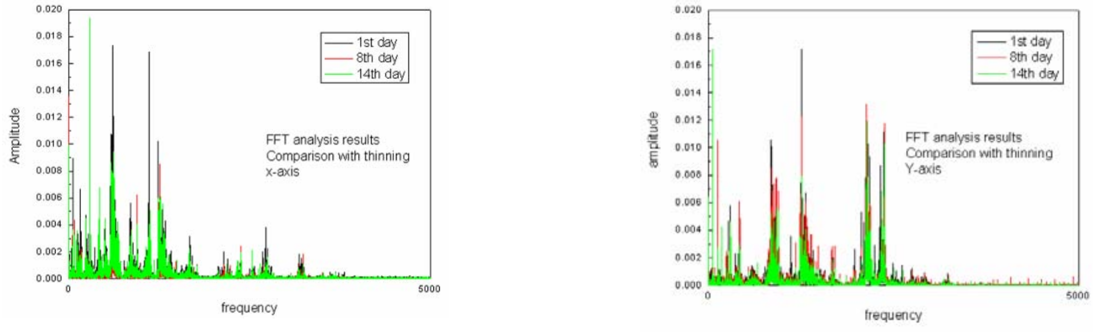

Figure E-13 FFT analysis results of top portion of U-tube

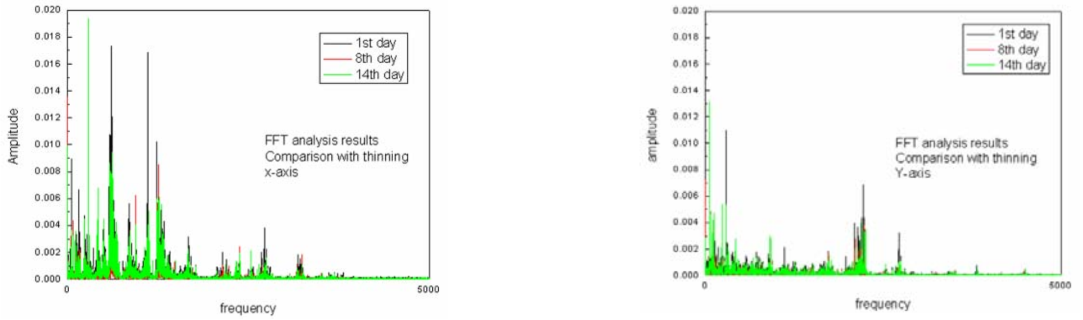

Figure E-14 FFT analysis results of straight portion of U-tube

Conclusion

In summary, the research team focused on accomplishing the project goal of developing and demonstrating continuous condition monitoring techniques by conducting tests on two selected check valve and piping elbow test loops to demonstrate the feasibility of using vibratory characteristics of these structural components to monitor their health status. In both test loops, advanced sensors were used to acquire vibration signals to be analyzed and evaluated with sophisticated data processing technologies that are specific for every sensor. In all condition monitoring tests, the predetermined configuration of the test component, either normal or degraded (associated with an identified degradation mechanism), were included in test matrix to establish pattern recognition that correlates component response patterns to different selected degradation modes.

For the check valve test loop, analysis results of processed sensor data indicate that it is feasible to differentiate between the normal and degraded (with disc wear and foreign object) configurations, but it is questionable that these techniques can reliably identify the level and type of degradation. Condition monitoring tests of check valves were conducted with separate test loops at KAERI and ARL to help demonstrate the repeatability of test results. For the piping elbow test loop, different vibratory response of the U-tube was observed with various stages of local thinning of piping thickness caused by the corrosion/erosion process in the FAC tests. However, since the test data indicate only small changes in the vibration mode of the piping elbow due to lower than expected local pipe thinning, a clear-cut conclusion to use mechanical vibration as a passive monitoring technique to assess local thinning of pipes cannot be reached.

Nomenclature

AC	accelerometer, alternating current
ACC	accelerometer
ADC	analog-to-digital converter
AE	acoustic emission
ARL	Applied Research Laboratory
ASME	American Society of Mechanical Engineers
AP	Access Point
AUEN	Au Electrode-Non PTFE
BEM	boundary element model
BIBO	Bounded Input/Bounded Output
BOP	balance of plant
BPF	blade pass frequency
BPSK	binary phase shift keying
BSS	Basic Service Set
CANDU	Canadian deuterium uranium (a reactor)
COFDM	Coded Orthogonal Frequency Division Multiplexing
CFD	computational fluid dynamics
DAS	data acquisition system
DFS	Dynamic Frequency Selection
DNS	Direct Numerical Simulation
DS-CDMA	Direct Sequence Code Division Multiple Access
DSP	digital signal processing
DSSS	direct-sequence spread-spectrum technology
DVI	Direct Vessel Injection
DWT	discrete wavelet transform
EAC	environmentally assisted cracking
ECP	electrochemical corrosion potential
ED	energy distribution
EPST	eigen pseudo spectral techniques
EREP	external reference electrode-PTFE
ESS	Extended Service Set
ETSI	European Telecommunication Standards Institute
FAC	flow-accelerated corrosion
FEM	finite element method, finite element model
FFT	fast Fourier transform
FIR	Finite Impulse Response
FOM	figure of merit

GUI	graphic user interface
HDTB	Hydraulic Diagnostic Test Bed
HE	Hurst exponent
HTUT	high-temperature ultrasonic transducer
IE	Inspection and Enforcement
IEEE	Institute of Electrical and Electronics Engineers
IIR	Infinite Impulse Response
I-NERI	International Nuclear Energy Research Initiative
INPO	Institute of Nuclear Power Operation
IP	Internet Protocol
KAERI	Korea Atomic Energy Research Institute
LAN	local area network
LER	licensee event report
LES	Large-Eddy Simulation
LPG	long-period fiber grating
MAC	media access control
MSR	moisture separator and reheater
MUSIC	Multiple Signal Classification
NFD	no fault detected
NPP	nuclear power plant
NRC	Nuclear Regulatory Commission
NUREG	A number issued for an NRC document
ODSCC/IGA	outer-diameter stress corrosion cracking and intergranular attack
OFDM	Orthogonal Frequency Division Multiplexing
OM	Operating & Maintenance
PAC	Physical Acoustics Corporation
PDE	partial-differential equation
PHY	Physical (layer)
PSD	power spectral density
PSU	Pennsylvania State University
PWR	pressurized-water reactor
PWSCC	primary-water stress corrosion cracking
QoS	Quality of Service
R15	resonance
RMS	root mean square
RNG	ReNormalization Group
R/S	rescaled range
SCC	stress corrosion cracking
SNR	signal-to-noise ratio

STFT	short-time Fourier transform
TFR	time frequency representation
TKIP	Temporary Key Integrity Protocol
UT	ultrasonic transducer
VSWR	Voltage Standing Wave Ratio
WBS	Work Breakdown Structure
WD	wide band
WEP	Wired Equivalent Privacy
WT	wavelet transform
WVD	Wigner-Ville distribution, Wavelet-Vaguelette deconvolution

1. Introduction

This final report is a compilation of material that Sandia National Laboratories (SNL) and Korea Atomic Energy Research Institute (KAERI) have gathered from all the I-NERI team members: Applied Research Laboratory (ARL) at Pennsylvania State University (PSU), Seoul National University (SNU), Pusan National University (PNU), and Chungnam National University (CNU).

The overall goal of this joint research project was to develop and demonstrate advanced sensors and computational technology for continuous monitoring of the condition of components, structures, and systems in advanced and next-generation nuclear power plants (NPPs). This project included investigating and adapting several advanced sensor technologies from Korean and US National Laboratory research communities, some of which were developed and applied in non-nuclear industries. The project team investigated and developed sophisticated signal processing, noise reduction, and pattern recognition techniques and algorithms, as well as evaluated encryption and data authentication techniques for the wireless transmission of sensor data.

1.1 Roles and responsibilities

Figure 1-1 shows a project organization chart that illustrates the breakdown of project tasks. This research project was actively engaged in conducting two condition monitoring test series that involved a check valve and a piping elbow. The first series focused on conducting condition monitoring of a selected check valve as an active component using a modified test loop at KAERI. The test series involved the check valve in the normal as well as degraded configurations to simulate various identified failure modes. Ultrasonic transducer (UT), acoustic emission (AE), accelerometer, and ultrasonic flow meter were used in this test loop to obtain sensor signals of the check valve at various flow conditions. The KAERI staff members were responsible for designing and installing the test loop, conducting the test series, and analyzing test data with support from PNU and CNU. The PNU staff members were tasked with analyzing the data on the check valve tests. The SNL and CNU analysts principally worked on sensor signal processing. The SNL staff members performed the finite element analyses.

The primary role of ARL was to provide support to SNL in the areas of signal analysis, data fusion, pattern recognition, and wireless system integration for component health monitoring. In this role, ARL designed and installed a separate check valve test loop and conducted suites of condition monitoring tests of this loop to collect independent data to identify and develop advanced signal processing techniques for diagnostic/prognostic methods.

The second series focused on conducting condition monitoring of a selected elbow and U-section of piping systems as a passive components using a FAC test loop at Seoul national University (SNU). The test series involved pipes in the normal as well as degraded configurations to simulate various identified failure modes, uniform thinning, non-uniform thinning and chemical thinning. A group of selected sensors, such as AUEN and EREP as chemical sensors, accelerometer, optical displacement sensor, capacitance sensor, and ultrasonic device as mechanical sensors, and ultrasonic flow meter, were used in this test loop to obtain sensor signals of the FAC thinning phenomena at various test conditions. KAERI staff members were responsible for manufacturing the test loop, and analyzing test data of vibration by FAC thinning with support from SNU and CNU. SNU staff members were tasked with conducting the test series and analyzing the testing data on FAC chemical tests. KAERI, SNU and CNU analysts principally worked on sensor signal processing, and SNL staff performed the finite element analyses.

Since there are multiple organizations in US and Korea participating in this joint research project, a protected project website was installed at SNL to facilitate communication and exchange of test data, evaluation and analysis results, and diagnostic/prognostic methods. This project website proved to be extremely valuable to project team members in transmitting huge volumes of test data and analysis results in real time.

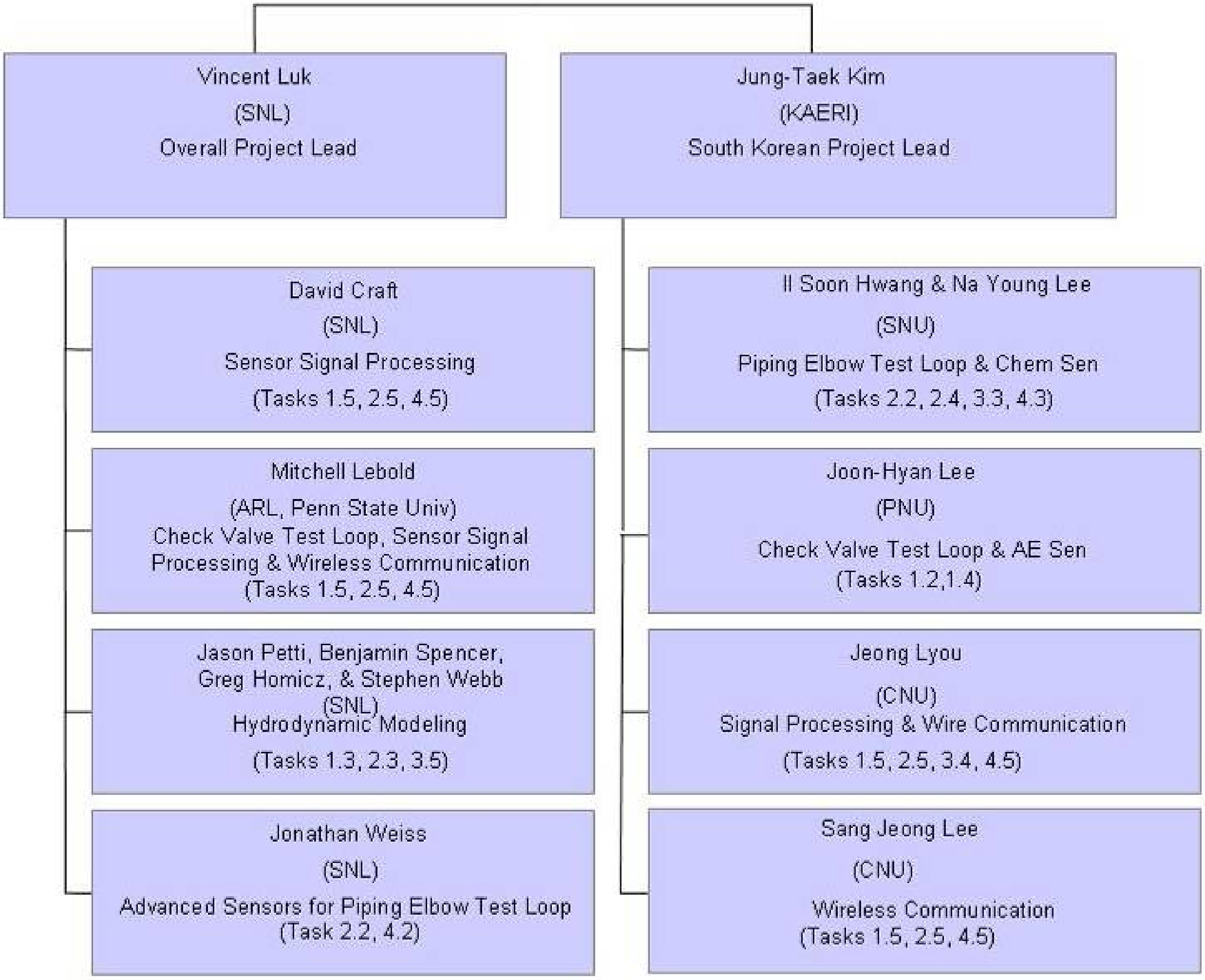

Figure 1-1 **Project organization chart.** *Note: The task descriptions are included in the Contents and Table 6-1.*

2. TASK 0: project management and coordination

Task lead: SNL and KAERI

This task manages and coordinates project activities between US and Korean team members. The project team identified and planned to conduct two condition monitoring test series of a selected check valve and a piping elbow to demonstrate the applicability of condition monitoring techniques in evaluating their health status. In each condition monitoring test, sequential project activities included design and installation of test loop, selection of advanced sensors, conduct of test, simulation with finite element and hydrodynamic models, sensor signal processing, and evaluation and documentation of results. The planned activities are described in detail in the Work Breakdown Structure (WBS) in Figure 2-1.

This international joint project presented an array of challenges besides executing the technical details of the planned tasks. The main challenges lied in the cultural and organizational differences in the US and Korean institutions in executing the planned tasks. Additional challenges were associated with language barrier and vast separation between institutions. The project team members used meetings and electronic communications via project website, e-mails, and telephone communications to confront and resolve these challenges. One of the most effective channels to promote communication among project team members was to hold meetings to discuss technical details and to resolve potential differences.

A project website was developed and maintained at SNL to facilitate communication among project members and storage of project documents and test data files. This secure project website provides a forum for project members to share reports, memos, test plans, test data, and analysis results.

ID	WBS	Task Name	Duration	Start	Finish
1	**0**	**Project Management & Coordination**	**891 days**	**Tue 1/1/02**	**Tue 5/31/05**
2	0.1	Project Planning & Coordination	784 days	Tue 1/1/02	Fri 12/31/04
3	**0.2**	**Quarterly Progress Reporting**	**803 days**	**Fri 3/1/02**	**Tue 3/29/05**
17	**0.3**	**Annual Report Preparation**	**652 days**	**Mon 12/2/02**	**Tue 5/31/05**
21	**1**	**Condition Monitoring of Check Valves**	**729 days**	**Fri 3/1/02**	**Wed 12/15/04**
22	1.1	Performance/failure/inspection data on check valves in Korea and US	63 days	Wed 3/6/02	Fri 5/31/02
23	1.2	Sensor & communications options for data acquisitioin for condition monitoring of check valves	152 days	Fri 3/1/02	Mon 9/30/02
24	1.3	Finite element analyses of selected check valve design to investigate its dynamic response characteristics and to select optimal sensor locations	338 days	Wed 5/15/02	Fri 8/29/03
25	1.4	Tests with the KAERI DVI test loop and ARL test bed to obtain condition monitoring data on check valves using selected sensors	588 days	Mon 4/1/02	Wed 6/30/04
26	1.5	Signal data processing analyses for noise filtering and pattern recognition	479 days	Mon 12/2/02	Thu 9/30/04
27	1.6	Demostrate integrated system analyses on check valves for recommending mitigation and correction options	189 days	Fri 3/26/04	Wed 12/15/04
28	**2**	**Condition Monitoring of a Secondary Piping Elbow in a Non-Safety Related Environment**	**729 days**	**Fri 3/1/02**	**Wed 12/15/04**
29	2.1	Performance/failure/inspection data on passive components in an accelerated erosion cracking environment in Korea and US	175 days	Fri 3/1/02	Thu 10/31/02
30	2.2	Sensors & communications options for test loop to obtain condition monitoring data on piping elbows	325 days	Mon 3/4/02	Fri 5/30/03
31	2.3	Finite element analyses of the piping elbow to investigate its dynamic response characteristics and to select optimal sensor locations	436 days	Wed 5/1/02	Wed 12/31/03
32	2.4	Tests with test loop at KAERI to obtain condition monitoring data on piping elbow using selected sensors	543 days	Thu 8/1/02	Mon 8/30/04
33	2.5.1	Manufacture and install selected sensors and data acquisition systems to test loop of piping elbow	282 days	Thu 8/1/02	Fri 8/29/03
34	2.5.2	Signal data processing analyses for noise filtering and pattern recognition	316 days	Wed 10/1/03	Wed 12/15/04
35	2.6	Demostrate integrated system analyses on piping elbow for recommending mitigation and correction options	188 days	Mon 3/29/04	Wed 12/15/04
36	**3**	**Condition Monitoring of an Assembly of Tubesheet and Tube Bundle in Steam Generator**	**488 days**	**Mon 2/3/03**	**Wed 12/15/04**
37	3.1	Performance/failure/ inspection data on steam generator assembly	85 days	Mon 2/3/03	Fri 5/30/03
38	3.2	Scenario to demonstrate condition monitoring for steam generator assembly	174 days	Tue 4/1/03	Fri 11/28/03
39	3.3	Design options for a steam generator assembly test loop	141 days	Mon 6/2/03	Mon 12/15/03
40	3.4	Sensor and communication options for test loop to obtain condition monitoring data on steam generator tube assembly	174 days	Fri 8/1/03	Wed 3/31/04
41	3.5	Fluid and finite element analyses of steam generator assembly to investigate dynamic response characteristics	359 days	Fri 8/1/03	Wed 12/15/04
42	**4**	**Technical Task Reports & Deliverables**	**891 days**	**Tue 1/1/02**	**Tue 5/31/05**
43	4.1	Condition Monitoring Technologies Report	837 days	Mon 3/18/02	Tue 5/31/05
44	4.2	Advanced Sensor Technologies Report	847 days	Mon 3/4/02	Tue 5/31/05
45	4.3	Erosion/Corrosion Monitoring Data	891 days	Tue 1/1/02	Tue 5/31/05
46	4.4	Baseline Software Using Operational and Lab Data	307 days	Mon 3/29/04	Tue 5/31/05
47	4.5	Signal Processing & Smart Communication Technologies Report	432 days	Mon 10/6/03	Tue 5/31/05
48	4.6	Final Technical Project Report on methods and results of prototype demonstrations	247 days	Mon 6/21/04	Tue 5/31/05

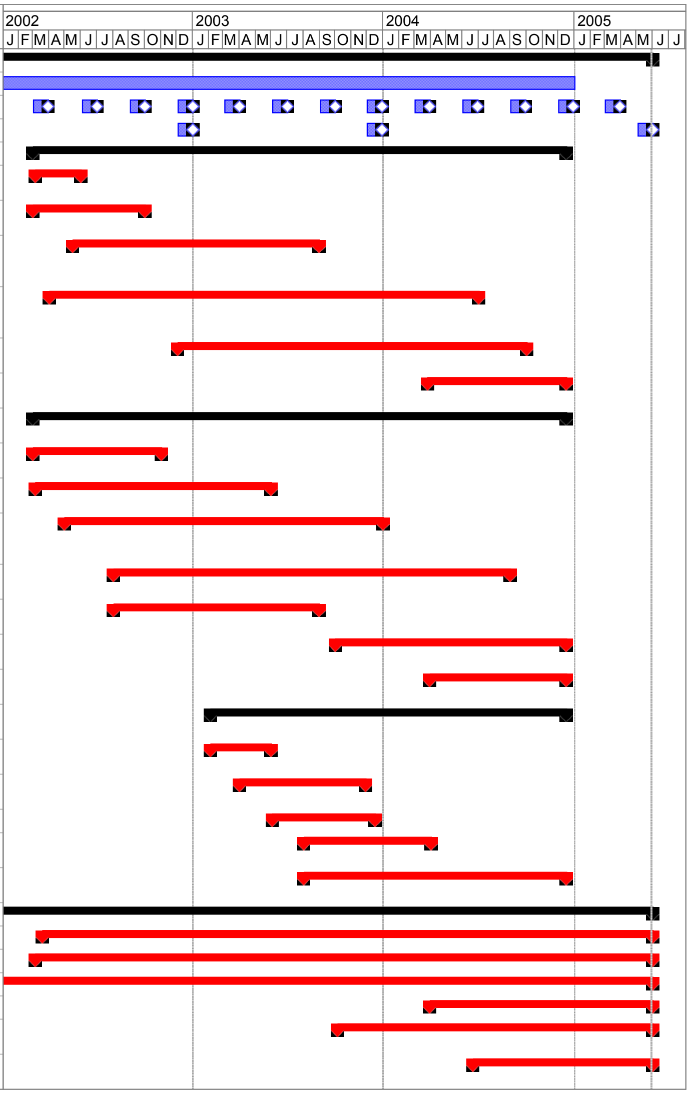

Figure 2-1 Work Breakdown Structure (WBS)

3. TASK 1: condition monitoring of check valves (active components)

This task focuses on investigating and developing a condition monitoring test loop of a selected check valve as an active component. The tasks include collecting and reviewing existing performance, failure, and inspection data on check valves in the US and Korea, investigating and identifying advanced sensors and communication options, developing and performing finite element and hydrodynamic analyses of the check valve model, developing and conducting tests to acquire condition monitoring data, processing signal data, and performing integrated system analyses.

3.1 Task 1.1: performance, failure, and inspection data on check valves in Korea and the US

Performed by KAERI, CNU, and SNL

There are many check valves in use in NPPs; therefore, the integrity of their performance is of genuine concern in plant safety and operational efficiency. This project included a series of condition monitoring tests of check valves to provide an effective maintenance and surveillance method to safeguard the functioning and operation of check valves. SNL and KAERI performed a survey on the performance, failure, and inspection data on check valves in the US and collected 46 licensee event reports (LERs) and 1 notification letter from 19 different plants. These reports cover a span of 10 years from 1990 to 2000. KAERI also performed a survey on the performance, failure, and inspection data on check valves in Korea from March 1993 to January 2001. Although the collected information was limited by source database and time span, the basic characteristics of relative percentages of performance and failure is not expected to change much with additional data. A database was organized using the Microsoft® Access™ program to categorize the collected reports.

There were four main categories of design for check valves in use in NPPs: tilting disc, lift, conventional swing, and Y swing check valves. This project included condition monitoring tests of 4 in. conventional swing check valves. Survey results indicate that surveillance leak tests and troubleshooting systems were used to discover check valve failures at ~0.44 occurrences/plant every year. The check valve failure modes were dominated by reverse leakage (about 53%) followed by failure to close and failure to open, as shown in Figure 3-1. The failure mechanisms of check valves can be categorized into a list of causes as demonstrated in Figure 3-2, which identifies disc/seat wear, hinge/bushing wear, foreign object interference, and improper assembly as the four major failure mechanisms. The disc/seat and hinge/bushing were the moving elements inside the check valve housing. The erosion or corrosion processes due to turbulent flow conditions inside the housing may cause their wear and degradation. Poor workmanship and questionable quality control and inspection procedures in fabrication may be the main causes of foreign object interference and improper assembly revealed in the survey results.

Investigators artificially introduced these four major failure mechanisms inside the check valves and investigated their influence in the condition monitoring tests. The details of license issues and failure analysis for the passive and active components are discussed in Appendix A, Section I.

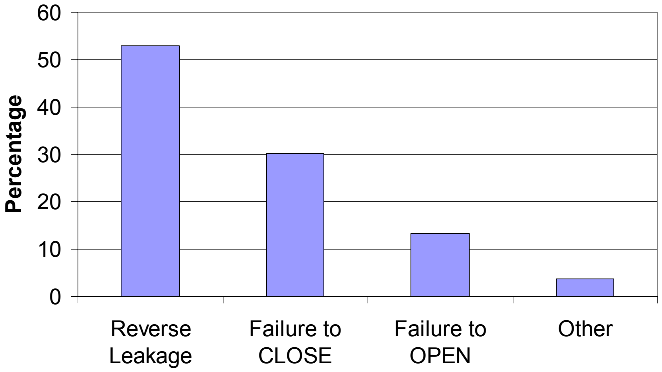

Figure 3-1 Check valve failure modes

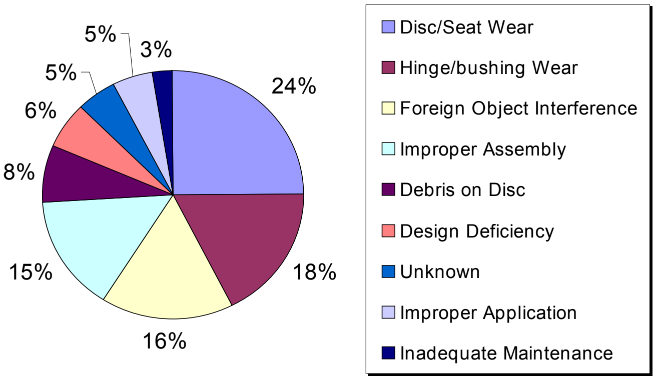

Figure 3-2 Failure mechanisms of check valves

3.1.1 The failure mode analysis of check valves in the US

Check valves are used extensively in nuclear power safety systems and balance-of-plant (BOP) systems. Sizes of check valves vary depending on service requirements, and range from 0.5 to 28 in. in nominal pipe diameter. The four most commonly used types are swing, horizontal lift, vertical lift, and ball check valves. Table 3-1, which summarizes the usage of check valves in typical pressurized-water reactor (PWR) NPPs, indicates number of valves, size ranges, and types used in various systems.

Table 3-1 Summary of check valve application in NPPs

System	Number of check valves	Valve size range (in.)
Auxiliary feedwater	4 to 23	4 to 8
Containment spray	4 to 14	6 to 14
High-pressure cooling injection	12 to 28	2.5 to 4
Low-pressure cooling injection/residual heat removal	5 to 14	8 to 10
BOP	200 to 400	2 to 60

The failures of these check valves have resulted in significant maintenance efforts, water hammer, over-pressurization of low-pressure systems, and damage to flow system components. These failures have largely been attributed to severe degradation of internal parts (for example, hinge pin, hinge arms, discs, and disc nut pins) resulting from instability (flutter) of check valve discs under normal plant operating conditions. For example, a post-service examination performed on a 10 in. swing check valve from a local installation following its failure to close in service revealed extreme wear in the hinge mechanism that caused the disc to hang up on the valve body before seating occurred.

Although service conditions were not known, the wear appears to have been caused by disc instability (oscillation) during service. In addition, check valve instability may be a result of misapplication (using oversized valves) and may be exacerbated by low-flow conditions or upstream flow disturbance (or both). At present, an inspection requirement for NPPs has been inadequate for timely detection and trending of such degradation because neither the flutter nor the resulting wear can be detected before failure. From the licensing perspective, the Licensing Authority has a continuing strong interest in resolving the check valve failure problem. Table 3-2 includes the titles of selected Nuclear Regulatory Commission (NRC) Inspection and Enforcement (IE) Notices and Bulletins during 1980 to 1990. These notices and bulletins were indicative of the types of check valve problems that have occurred during this period and the continued interest that NRC has in identifying and solving these problems.

In particular, IE Information Notice 86-01 describes an event that occurred at San Onofre, Unit 1, on November 21, 1985. The most significant aspect of the event was the failure of safety-related feedwater system check valves (three main feedwater regulator check valves and two feedwater pump discharge check valves). The failure of these valves was the primary cause of a severe water hammer event that extensively damaged a portion of the feedwater system. A similar failure caused by a check valve occurred at Kori, Unit 3, in 1985. From a licensing standpoint and a failure example, if early detection of the failure was available, it could have been prevented, thus controlling the system damage. It is therefore necessary to develop reliable condition monitoring for check valves.

Table 3-2 Titles of selected NRC IE Bulletins

Number	Title
90-03	Malfunction of Borg-Warner Bolted Bonnet Check Valve Caused by Failure of the Swing Arm
89-02	Malfunction of Borg-Warner Pressure Seal Bonnet Check Valve Caused by Vertical Misalignment of Disc
88-05	Broken Retaining Block Studs on Anchor Darling Check Valve
88-70	Check Valve In-Service Testing Program
86-06	Failure of Check and Stop Check Valve Subjected to Low-Flow Conditions
86-01	Failure of Main Feedwater Check Valves Causes Loss of Feedwater System Integrity and Water Hammer Damage
84-12	Failure of Soft Seat Valve Seals
84-06	Steam Binding of Auxiliary Feedwater Pumps
83-54	Common Mode Failure of Main Steam Isolation Nonreturn Check Valve
83-06	Nonidentical Replacement Parts
82-35	Failure of Three Check Valves on High-Pressure Injection to Pass Flow
82-26	Reactor Core Isolation Cooling and High-Pressure Coolant Injection Turbine Exhaust Check Valve Failure
82-20	Check Valve Problems
81-35	Check Valve Failures
81-30	Velan Swing Check Valves
80-41	Failure of Swing Check Valve in the Decay Heat Removal System at Davis-Besse Unit No. 1
89-02	Stress Corrosion Cracking of High-Hardness Type 410 Stainless Steel Internal Preloaded Bolting in Anchor Darling Model S350W Swing Check Valves or Valves of Similar Design
85-01	Steam Binding of Auxiliary Feedwater Pumps
83-03	Check Valve Failures in Raw Water Cooling Systems of Diesel Generator
80-01	Operability of Automatic Depressurization System (ADS) Valve Pneumatic Supply

3.1.2 The failure mode analysis of check valve in Korea

Figure 3-3 shows check valve failure during March 1993 to January 2001. In this figure, gasket/disc and leakage cause more than 70% of failure occurrences. This database was compared to the data in NUREG-CR 4302, *Aging and Service Wear of Check Valve Used in Engineered Safety-Feature Systems of Nuclear Power Plants*. In Table 3-3, the right chart shows the failure mode and detection method used in NUREG-4302, and the left chart shows the Korean data. The right chart shows the failures in percentages and the left chart shows failures in number. If the percentages were converted to numbers, the Korean data compares closely to the NUREG data.

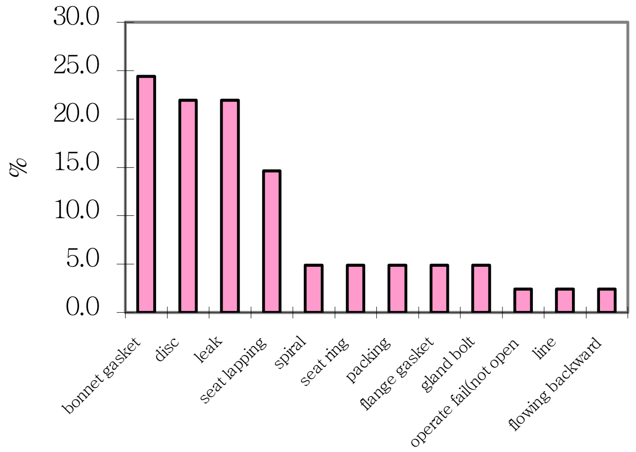

Figure 3-3 **Check valve failure modes during March 1993 to January 2001 in Korea**

Table 3-3 **Comparison of check valve failure modes from NUREG 4302 (left) and Korean data (right)**

Failure mode	#
Seat leakage	17
External leakage	6
Failed to open	1
Failed to close	0
Damaged interals	0

Method of detection	#
Inspection	9
disassemble	4
Prevention maintenance	2

Failure mode	%
Seat leakage	70
External leakage	16
Failed to open	8
Failed to close	2
Damaged interals	4

Method of detection	%
In-service and surveillance test	67
Incidental observation	4
Routine observation	14
Operational abnormality	11
Maintenance	2
Special inspection	2

Table 3-4 describes the details of check valve failure modes. Note that the leakage failure caused by the seating surface occurred more frequently than failure due to the gasket. In Table 3-4, the right chart is the NUREG data as reported in LERs and the left chart is Korean data. However, from a maintenance standpoint, component change is the choice of action in Korea but repair is the choice for the NUREG data.

Table 3-4 Comparison of detailed failure modes of Korean check valves to NUREG 4302

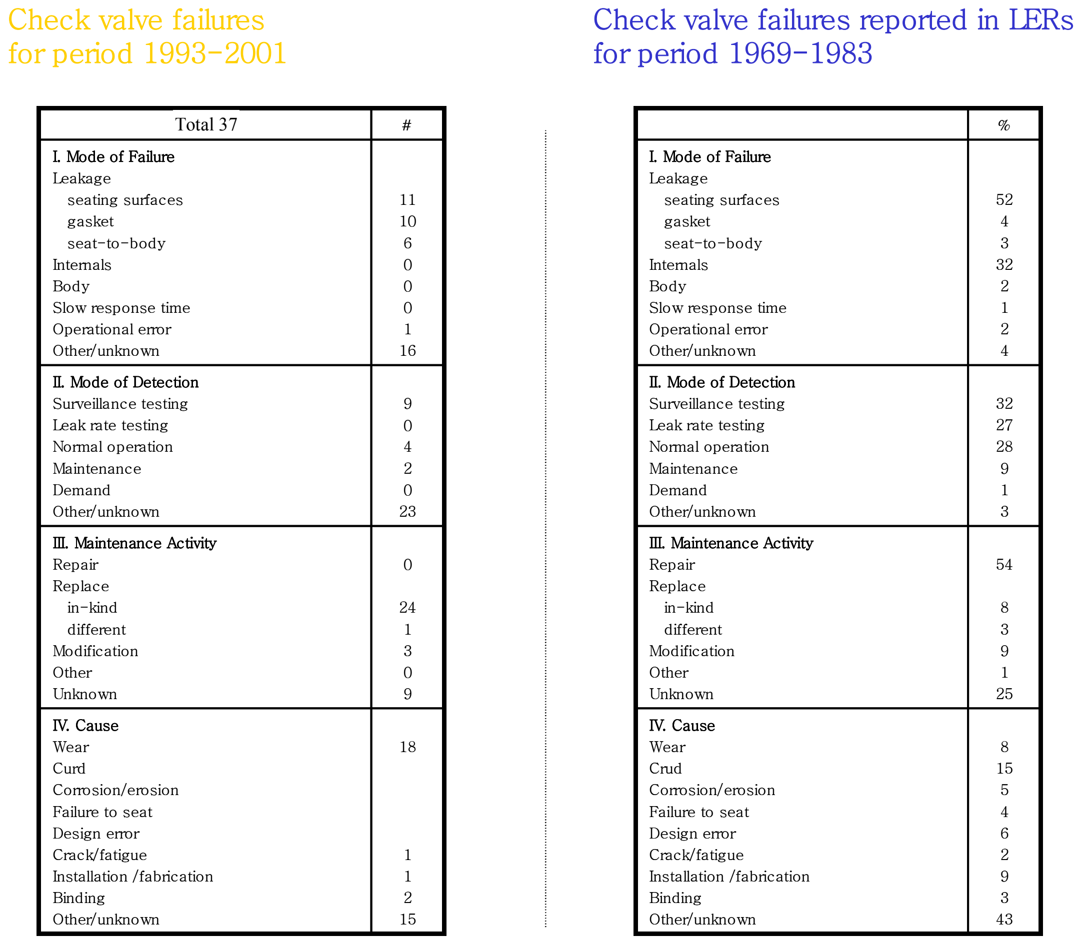

Check valve failures
for period 1993-2001

Total 37	#
I. Mode of Failure	
Leakage	
seating surfaces	11
gasket	10
seat-to-body	6
Internals	0
Body	0
Slow response time	0
Operational error	1
Other/unknown	16
II. Mode of Detection	
Surveillance testing	9
Leak rate testing	0
Normal operation	4
Maintenance	2
Demand	0
Other/unknown	23
III. Maintenance Activity	
Repair	0
Replace	
in-kind	24
different	1
Modification	3
Other	0
Unknown	9
IV. Cause	
Wear	18
Curd	
Corrosion/erosion	
Failure to seat	
Design error	
Crack/fatigue	1
Installation /fabrication	1
Binding	2
Other/unknown	15

Check valve failures reported in LERs
for period 1969-1983

	%
I. Mode of Failure	
Leakage	
seating surfaces	52
gasket	4
seat-to-body	3
Internals	32
Body	2
Slow response time	1
Operational error	2
Other/unknown	4
II. Mode of Detection	
Surveillance testing	32
Leak rate testing	27
Normal operation	28
Maintenance	9
Demand	1
Other/unknown	3
III. Maintenance Activity	
Repair	54
Replace	
in-kind	8
different	3
Modification	9
Other	1
Unknown	25
IV. Cause	
Wear	8
Crud	15
Corrosion/erosion	5
Failure to seat	4
Design error	6
Crack/fatigue	2
Installation /fabrication	9
Binding	3
Other/unknown	43

3.2 Task 1.2: sensor and communication options for data acquisition for condition monitoring of check valves

Performed by KAERI/PNU

3.2.1 Sensor options

Condition monitoring method for check valves

Figure 3-4 shows the swing-type check valve selected for the condition monitoring test loop.

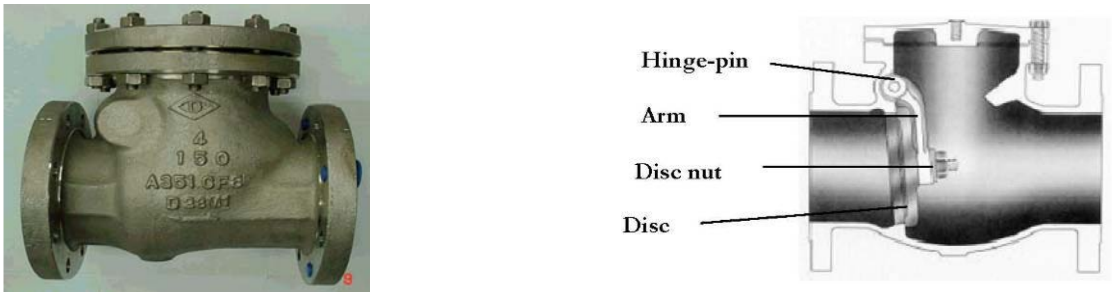

(a) Check valve **(b) Cross-sectional view**

Figure 3-4 Swing-type check valve

There were many possible failure mechanisms caused by system flow oscillations or system piping vibrations that can lead to check valve component wear and failure. The most common types of physical damage in check valves were discs separated from the hinge pin; broken stud pin; loose disc nut; partially open disc; disc caught on inside of the seat ring; cracked disc; or worn hinge pin, bent hinge pin, disc, or hinge arm. Most of these faults cause vibratory noises that were detectable by monitoring AE from the valve body. Abnormal movement of discs can be detected by ultrasonic measurements or through motion (usually acceleration) sensors attached to the valve body. In addition, leakage caused by these faults in the reverse flow condition can be measured conveniently by using the ultrasonic flow meter.

Four types of sensors–AE, ultrasonic, accelerometer, and ultrasonic flow meter–were used in the check valve test loop. The specifications of input characteristics and output signal on data acquisition systems (DASs) as well as a discussion on the application of each of these sensors follow.

3.2.1.1 AE monitoring

Acoustic emission signals are detected by sensors (such as piezoelectric-type accelerometers or microphones) that respond to pressure waves over a wide range of frequencies. Analyses of AE signals obtained from check valves can be used to monitor check valve disc position, movement, and mechanical condition as well as internal flow or leakage through the valve. Various methods of obtaining and analyzing data were available. These include filtering, fast Fourier transform (FFT), and as pattern recognition techniques.

In this project, AE monitoring was used to detect check valve disc movement and to evaluate valve degradation such as disc/seat and hinge pin wear. The specifications of input characteristics and output signal on DASs for the AE sensors were as follows:

- Physical Acoustics Corporation® (PAC): Resonance (R15)
- Frequency range: 50 to 200 kHz, central frequency: 150 kHz
- PAC: Wide band (WD)
- Frequency range: 100 to 1000 kHz, central frequency: 650 kHz, 100 to 1200 kHz blade pass frequency (BPF).

3.2.1.2 Ultrasonic monitoring

Ultrasonic measurement involves introducing high-frequency sound waves into a part and analyzing the characteristics of the reflected signal. Typically, one or two ultrasonic transducers were used to provide both transmission and receiving capabilities. The ultrasonic signal is injected from outside the valve at the transmitting transducer and passes through the valve body, where it is reflected by an internal part (such as a disc or hinge arm) back toward the receiving transducer.

The ultrasonic technique is usually used to produce a time waveform display from which disc position and movement may be easily determined and can be used to detect a missing or stuck disc.

The specifications of input characteristics and output signal on DASs for ultrasonic sensors were as follows:

Input frequency range for the ultrasonic device:

- 2 MHz angle beam transducer, 0.25 in. element diameter (Techsonic®, USA)
- 5 MHz angle beam transducer, 0.25 in. element diameter (Techsonic, USA)
- 20°, 30°, 45°, 60°, and 70° wedges (Techsonic, USA)

Frequency of ultrasonic data to be stored by the DAS: Oscilloscope (LeCroy® 9310A, Dual 400 MHz).

3.2.1.3 Accelerometer monitoring

Accelerometers were used to detect vibration signals from pressure waves over a low-frequency range (<100 kHz) and were usually attached to the valve body. The specifications of input and output signals on DASs for the accelerometers were as follows:

- Wilcoxon® Research: Model 736 (Serial Number, SN 11173)
- Frequency range: 5 Hz to 24.5 kHz, central frequency: 52 kHz, sensitivity: 98 mV/g
- Wilcoxon Research: Model 736 (SN 11174)
- Frequency range: 5 Hz to 24 kHz, central frequency: 52 kHz, sensitivity: 100 mV/g.

3.2.1.4 Ultrasonic flow meter

The Controlotron® ultrasonic flow meter can perform reliably at high temperatures (>250°F) to attenuate signals. This transducer provides both internal and external coupling for ultrasonic energy to be transmitted to and from the transducer. Therefore, this device can be used non-intrusively to detect leakage failure of check valve by a direct flow measurement. Figure 3-5 shows a schematic diagram for condition monitoring of the check valve. AE sensors with different frequency ranges were used to detect leak signals as shown in Table 3-5.

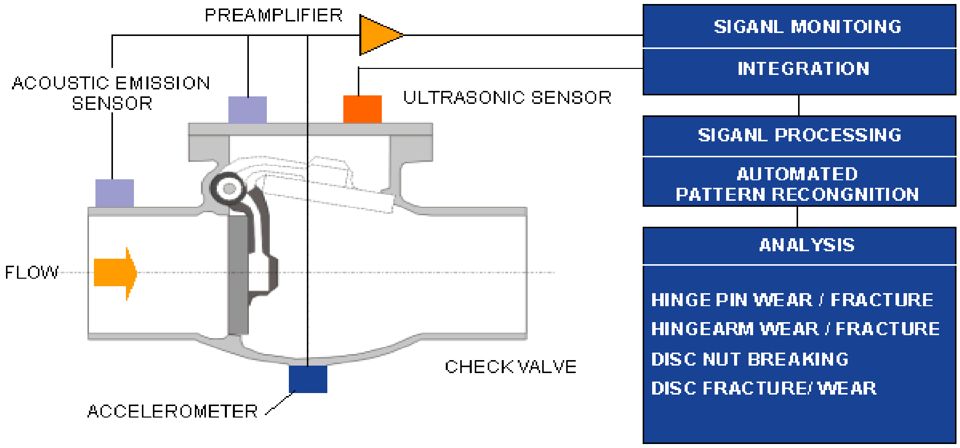

Figure 3-5 Schematic diagram for condition monitoring of the check valve

Table 3-5 Frequency range of AE sensor and preamplifier

Type	Frequency Range	Center Frequency	Filter (BPF)
WD	100 to 1000 kHz	650 kHz	100 to 1000 kHz
R15	50 to 200 kHz	150 kHz	100 to 300 kHz

The details of sensor characteristics are discussed in Appendix A, Section II.

3.2.2 Communication options

Different communication options (both wired and wireless) to transmit sensor signals from DASs to data processing and storage units were investigated.

3.2.2.1 Prototype using wired communication (KAERI/CNU)

Prototype using wired communication hardware overview

Figure 3-6 shows the prototype configuration using wired communication.

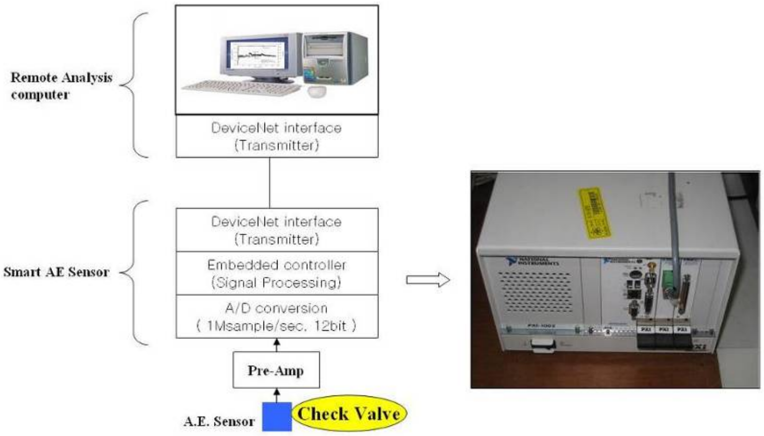

Figure 3-6 A configuration of prototype using wired communication

Development of prototype using wire communication

The master program. The master program took charge of the input/output communication as a DeviceNet™ master with a single slave device. Figure 3-7 shows the Lab View™ display, which set the input value and displayed the output of block diagram for this task. This display comprised graphs and charts displaying the actual data. The DeviceNet communication setup and input data can be adjusted using switches, input windows, and buttons on the front panel.

The structural elements of display were as follows:

- DeviceNet setting
- Neural Net input parameter
- Neural Net output
- Error

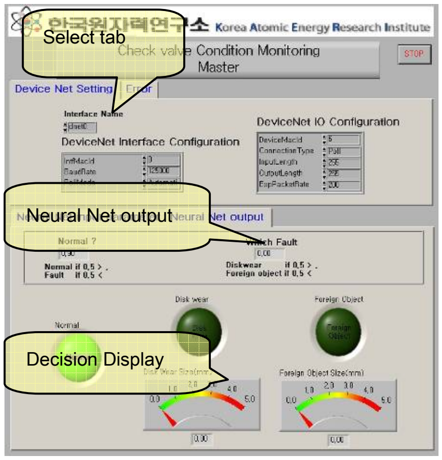

Interface Name: dnet0

DeviceNet Interface Configuration
IntfMacId: 0
BaudRate: 125000

DeviceNet IO Configuration
DeviceMacId: 5
ConnectionType: Poll
InputLength: 256
OutputLength: 256
ExpPacketRate: 200

Normal ?: 0,90
Normal if 0,5 > .
Fault if 0,5 <

Which Fault: 0,00
Diskwear if 0,5 > .
Foreign object if 0,5 <

0,00
0,00

Figure 3-7 The display of master program of prototype

Figure 3-8 is a block diagram of the master program. The block diagram is the program source of LabView. The block diagram components include terminals, nodes, and wires. The flow of data was executed through the wire.

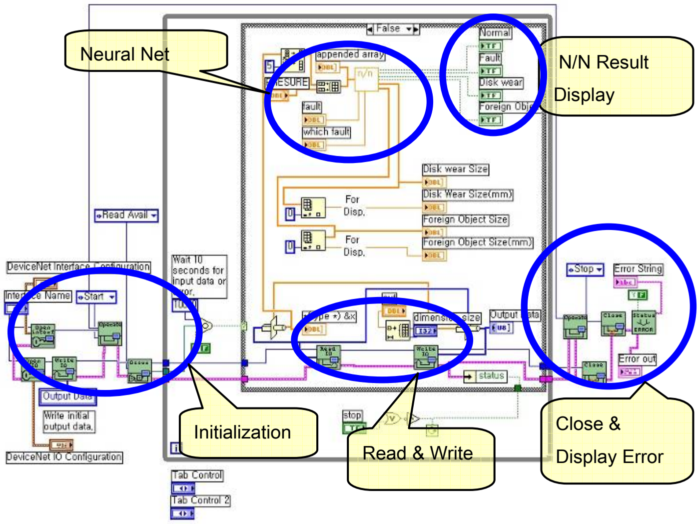

Figure 3-8 The block diagram of master program of prototype

Slave program. The slave program performed the data acquisition from the sensor, displayed the acquisition data and the value of extracted parameters and filtering (Butterworth filter), and sent the extracted parameters to a master through a wired network. The block diagram flows likes this:

- DeviceNet communication
- Data acquisition
- FFT
- Parameter extraction
- Display error

Figure 3-9 shows the display of the slave program before and after input data filtering. The right side of the figure displays the results of the FFT; the amount of low-frequency noise was lower compared to the original data. Figure 3-10 shows the slave program block diagram; the image on the right shows the FFT.

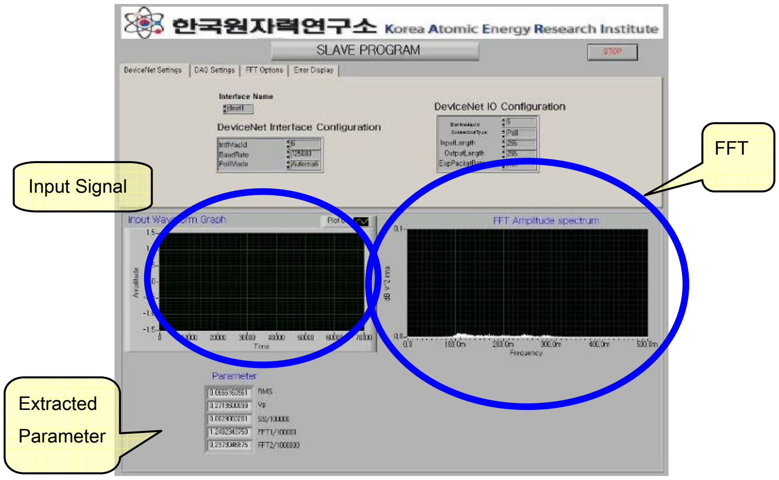

Figure 3-9 Slave program display before and after input data filtering

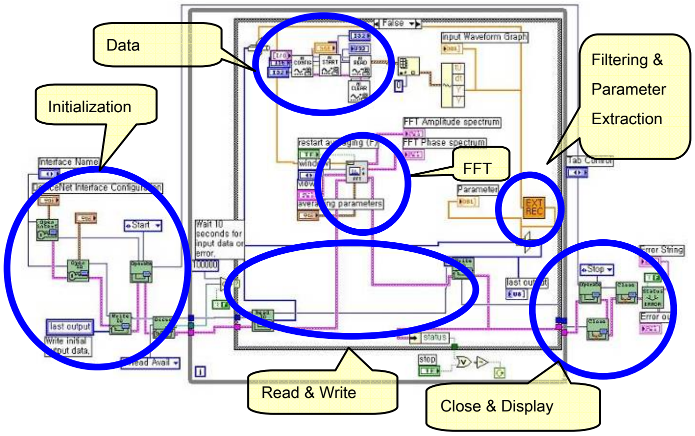

Figure 3-10 Slave program block diagram

Demonstration of prototype using the experimental data

A demonstration program was executed using the experimental data files. A graphic user interface (GUI) of the demonstration program is similar to a slave program except for the file path tab, which is used when the experimental data file was opened. Figures Figure 3-11 and Figure 3-12 show the display of the demonstration prototype and the block diagram of the demonstration program, respectively.

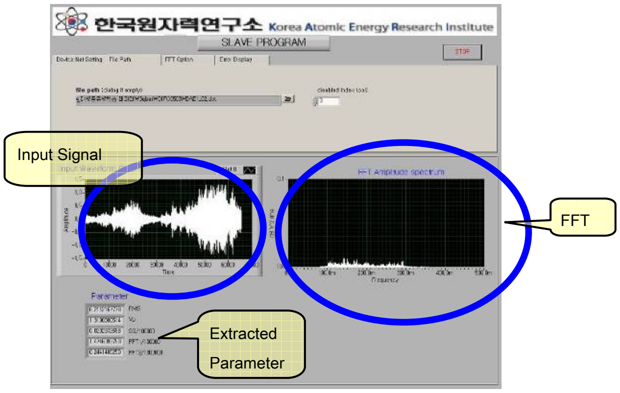

Figure 3-11 A display of the demonstration prototype

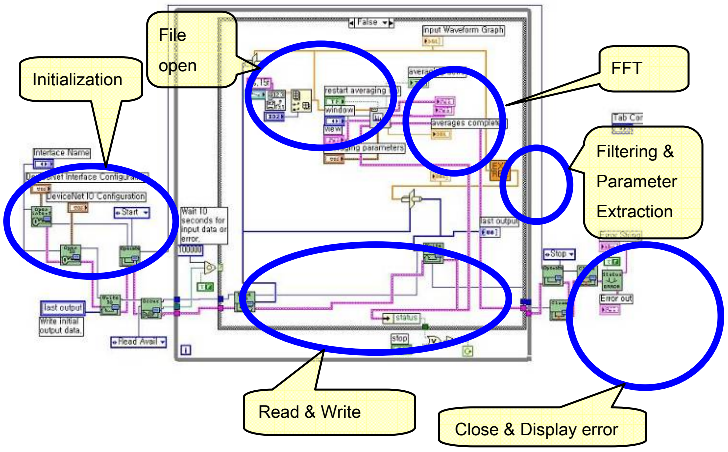

Figure 3-12 Demonstration program block diagram

3.2.2.2 Prototype using wireless communication (KAERI/CNU)

Configuration of prototype of the wireless communication part

The implementation of a wireless system required short-distance, low-power wireless technology, which was included for high-level security. Accordingly, it was needed to develop the embedded Linux™ and wireless local area network (LAN) technology.

The system was implemented on the embedded Linux. The acquired data from sensors were processed at the digital signal processing (DSP) unit. Through the RS-232 connection, the data were transmitted to the smart transmitter and the DSP transferred the data to the monitoring system through a wireless LAN. The monitoring system was implemented using the LabView. The overall schematic of the developed system is shown in Figure 3-13.

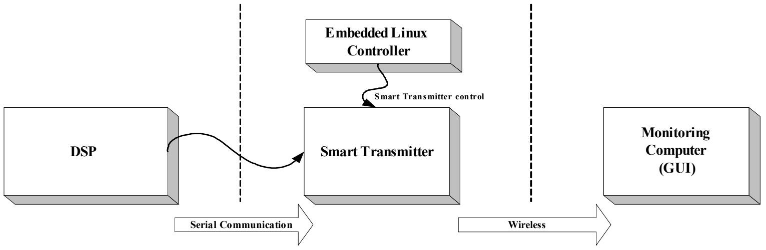

Figure 3-13 The overall schematic of the developed system

Development of prototype using wireless communication

Wireless LAN communication programs, such as the Linux Socket and the Windows Socket, were developed in Linux and Windows for a smart transmitter and GUI, respectively. At the evaluation stage, the designed communication program was tested using wired connection between a Linux-based computer and a Windows-based computer. The wireless LAN (802.11b) connection between the smart transmitter and the monitoring system implemented for this project is shown in Figure 3-14 (see Table 3-6 for specifications).

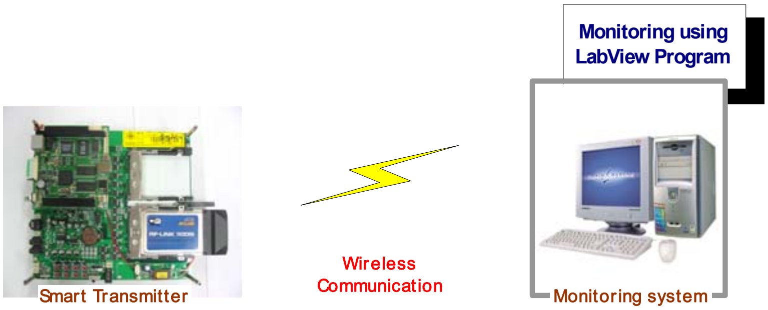

Figure 3-14 Wireless communication between smart transmitter and monitoring system

Table 3-6 Wireless LAN specification

Protocol	802.11b
Transmission type	direct-sequence spread-spectrum (DSSS)
Maximum transmission rate	11 Mbps
Bandwidth	22 MHz
Frequency	2.4 GHz
Transmission range	100 m

Smart transmitter

The smart transmitter was implemented with the serial emulation program based on Minicom™, a serial emulation program, was used to develop the smart transmitter. The smart transmitter board is shown in Figure 3-15. The Linux socket program is designed for RS-232 communication.

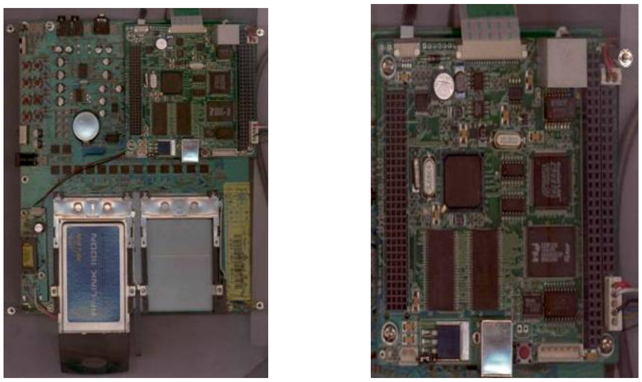

Figure 3-15 Smart transmitter board

Transmission of designed data structure

Maximum peak voltage, root mean square (RMS), FFT1, FFT2, and signal strength values and the DSP data parceled into 1 B (8 b) packets was transmitted to the smart transmitter through the RS-232 cable and port. The gap of transmission time was ~0.5 s. The data structure transmitted to the smart transmitter through the RS-232 port is shown in Figure 3-16.

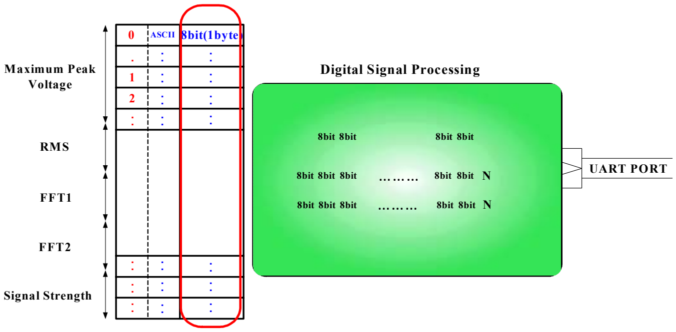

Figure 3-16 Data structure in DSP

The smart transmitter data structure used to assign a file descriptor to the received data and transmit the data via wireless LAN is shown in Figure 3-17.

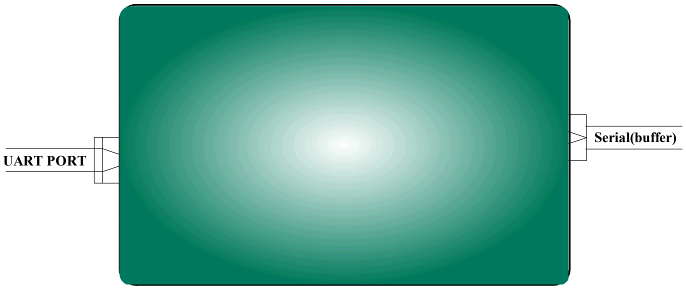

Figure 3-17 Smart transmitter data structure

The transmitted data were received by the monitoring system Windows socket program, which converts it into a socket descriptor as shown in Figure 3-18. The socket descriptor was reinterpreted by socket descriptor client, which loads a buffer with reinterpreted data. The received data were analyzed for condition monitoring using an advanced sensor and computational technology.

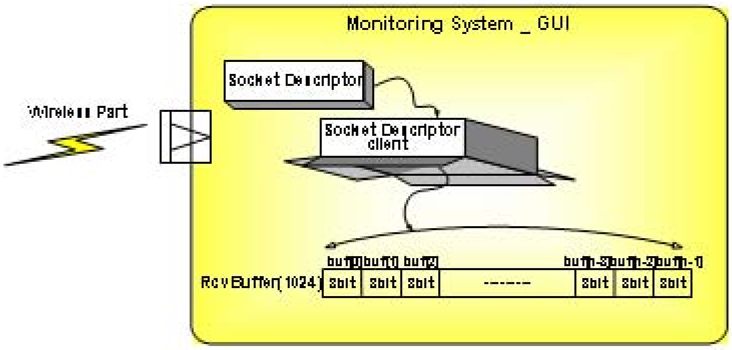

Figure 3-18 Program structure in monitoring system

The master program (GUI)

The Windows socket program saves the data transmitted from the smart transmitter as data files, which are used to analyze the condition of the check valve. The LabView-based GUI (see Figure 3-19.) can identify the abnormal symptoms with the saved file analysis. The flow was as follows:

- Monitoring system setting
- Neural Net input parameter
- Neural Net output
- Error
- File path

Figure 3-19 GUI for wireless communication of prototype

The slave program

The slave program performed the data acquisition from the sensor, displayed the acquisition data and the value of extracted parameter, and sent the extracted parameters to a master (the GUI) through wireless network as shown in Figure 3-20. The configuration of block diagram includes the following:

- Smart transmitter communication
- Data acquisition
- FFT
- Parameter extraction
- Display error

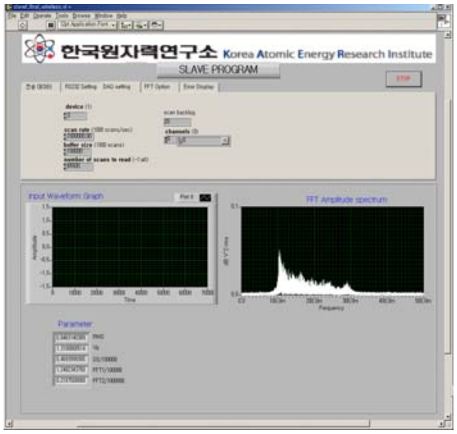

Figure 3-20 The slave program using LabView

Data transmission and smart sensor techniques via wired and wireless communication provided by KAERI and CNU are discussed in Appendix A, Section III.

3.2.2.3 Smart sensor techniques using wired and wireless communication (ARL)

Traditional wired technologies have several drawbacks when deployed in existing NPP facilities. Wiring is expensive, heavy, vulnerable, and adds an additional layer of complexity to the design of a plant. If wiring is damaged, the lines of communication are literally cut, and still-operating machinery on the other side is inaccessible or possibly rendered useless. The wiring is the nervous system of a plant; therefore, an unforeseen, well-placed failure can effectively paralyze an entire platform by severing communication among critical systems.

An obvious remedy to this weakness is provided by the growing field of wireless communication, which involves sending an electromagnetic wave of encoded data. The communication is near instantaneous and eliminates the need for wiring. On the other hand, electromagnetic waves cannot travel through metal (the primary component of many structures) and have limits on distance and data rate. Thick concrete walls similar to those used in NPPs also hinder communications; however, there are simple devices called “repeaters” that could be used to overcome these barriers. Clearly, the benefits and drawbacks of wireless communication must be weighed carefully before it can be relied upon.

To complicate the matter, device level wireless communications involve many variables affecting its suitability for a given purpose. For instance, the frequency band at which the transmissions propagate has a significant impact on such factors as range, data rate, and potential interference. Additionally, the way a technology utilizes its frequency band affects interference handling, power consumption, security, and multiple signal path (multipath) tolerance. Various data modulation schemes can also increase the effective bit rate. There are many different encryption algorithms, authentication mechanisms, and other measures used to secure wireless transmissions. Indeed, nearly every facet of wireless communication has more than one way to approach it and the system features were highly dependent on the design requirements.

Because of the myriad of variations available to a developer, many wireless communication standards have been created. Standardizing the technology enables interoperability and encourages competition among manufacturers. To end users, standards result in lower costs, better technologies, less dependence on individual manufacturers, and increased growth for the industry. Several promising standards are still in the process of ratification by the Institute of Electrical and Electronics Engineers (IEEE) standards committee, and most other standards were quickly maturing. The key to finding a wireless solution is figuring out which standard is best suited for a specific application. The wireless technologies provided by ARL are discussed in Appendix B.

3.3 Task 1.3: FEAs of selected check valve designs to investigate dynamic response and to select optimal sensor locations

Performed by SNL and KAERI/PNU

3.3.1 Finite element method (FEM) data analysis

Finite element models (FEMs) of the check valve were developed to investigate the response of different internal parts of the check valve with various flow conditions and degradations. This information provides guidance in selecting the optimal sensor positions.

ANSYS®'s commercially available software package FLOTRAN™ was used to develop the finite element models. Simulations were performed for disc angle varying from 0° to 90° in increments of 15°. The numerical model was validated by simulating turbulent flow at high Reynolds numbers in check valve leaks for inlet boundary layer flows. FLOTRAN was used to model the turbulent flows (Re > 4000). The numerical values of the predicted Reynolds number were compared to experimental values available for turbulent flows.

The distributions of flow velocity for inlet and outlet boundary layer flows in a check valve are plotted in Figure 3-21, respectively, as a function of disc angle for high Reynolds number turbulent flow. As shown in this figure, for the case of the disc angle of 15°, 30°, 45°, flow velocity was maximum in lower part of check valve. They increase with decreasing disc angle. However, as the disc angle increasing, flow separation occurs, which is associated with Reynolds number.

Figure 3-22 shows the pressure drop with disc angle of 15°, 30°, 45°, and 90°. As shown in this figure, the same phenomena were observed for the disc angle; that is, it was confirmed that pressure becomes maximum from the disc's lower parts. Although there is a reasonable agreement between the predicted and experimental results, in general, the predictions were lower. For the experimental verification for turbulent flow in check valve leaks, leak tests were performed with a specially designed check valve at modified Direct Vessel Injection (DVI) test loop. Figure 3-23 shows a photographic series for the check valve leak test setup. Turbulent leakage flow was observed through head and acrylic piping to confirm its occurrence in check valve leaks.

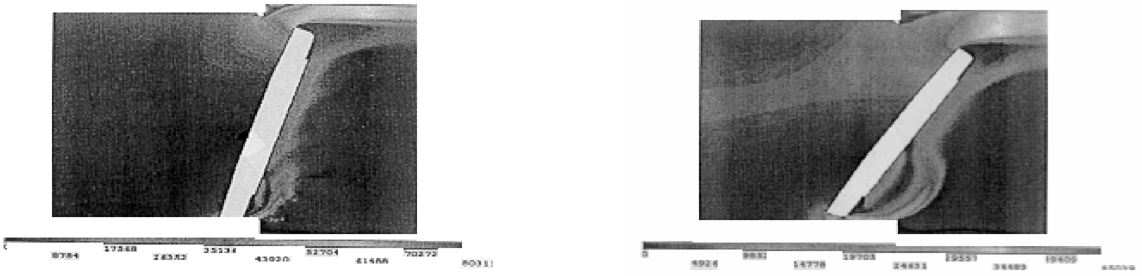

(a) Disc angle = 15° **(b) Disc angle = 30°**

(c) Disc angle = 45° **(d) Disc angle = 90°**

Figure 3-21 The flow velocity for varying disc angle

(a) Disc angle = 15° (b) Disc angle = 30°

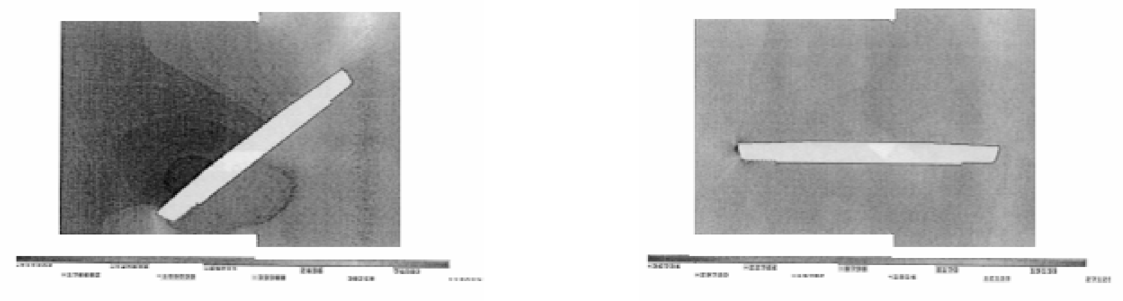

(c) Disc angle = 45° (d) Disc angle = 90°

Figure 3-22 The pressure drop for varying disc angle

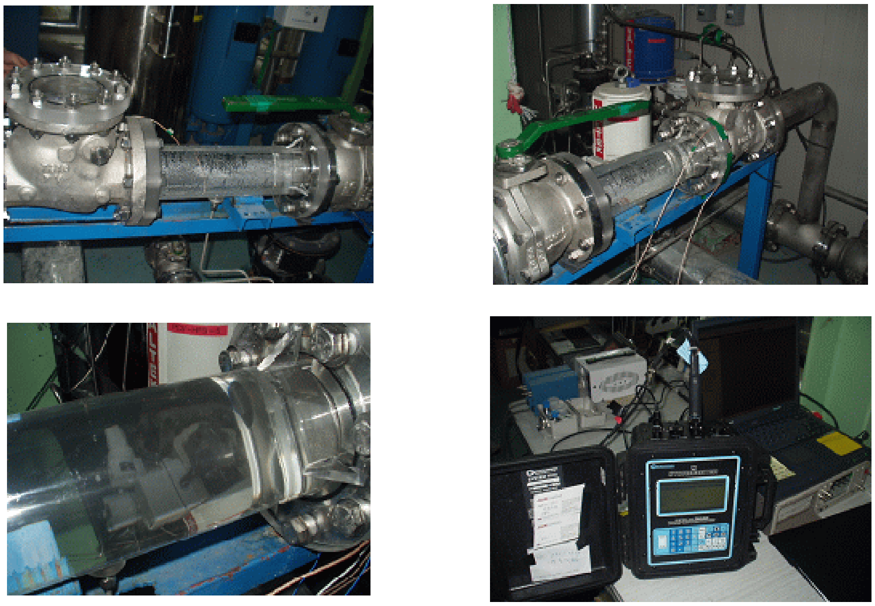

Figure 3-23 Photograph of experimental setup

The flow behavior inside a check valve with a faulty internal part can be modeled or simulated with one of the following techniques:

- Computational fluid dynamics (CFD) model with turbulence
- Fluid-structure interaction
- Structural FEM with acoustic fluid

3.3.2 CFD model with turbulence

The primary purpose of turbulence modeling in CFD calculations is to model the effects of turbulence on the mean flow:

$u(\vec{x},t)=\overline{u}(\vec{x})+u'(x,t)$ (mean flow + turbulent fluctuation)

Empirically based models solve additional differential equations, typically for the turbulence kinetic energy per unit mass and the dissipation rate per unit mass. From these calculations, the turbulent viscosity is computed and used in the mean flow equations. Unfortunately, such models cannot predict the turbulent fluctuations.

In the Direct Numerical Simulation (DNS) method, the full, unsteady, Navier-Stokes equations are solved for the fluctuating flow quantities. No empirical approximations are made and all spatial and temporal scales of the turbulence are resolved. This simulation method requires extremely fine-grid resolution and very short time steps. As a result, it can be done only for very simple geometries and low Reynolds number flows.

A compromise between turbulence modeling and DNS, the Large-Eddy Simulation (LES), employs a filtered set of equations that simulate only the largest turbulent eddies in the flow. The effect of smaller eddies are modeled empirically as before. This reduces the computational effort somewhat, but is still very expensive in terms of time and storage requirements. For these reasons, both DNS and LES were regarded as in their infancy and are still areas of active research. They were not considered practical for typical engineering calculations.

3.3.2.1 Fluid-structure interaction

In modeling the coupled behavior of fluid-structure interaction, there are two methods to pass boundary condition information between structure and fluid domains:

- One-way coupling: Fluid → Structure can be done with separate codes
- Full two-way coupling: Fluid ←→ Structure can be done by overlapping grids or by regenerating the fluid grid when the structure moves.

Structural FEM with acoustic fluid

In FEM, structure and fluid components can be modeled with finite elements. In particular, acoustic elements are used to represent fluid by specifying density and wave speed. This simulation technique can model acoustic waves and inertia effects (with added mass), but fails to model fluid flow and viscosity.

Check valve in reverse flow condition

In this flow condition, leakage flow dominates and there were negligible fluid-structure interaction effects. The check valve may experience vibrations turbulence, cavitation, and the general noise in piping system. Steady-state turbulent flow analysis can be used to study the flow behavior, but it does not give unsteady flow that induces vibration. It is impractical to use LES for this application. The modeling effort for this project was limited to a simplified steady-state axisymmetric CFD model of the valve and generating three-dimensional (3D) solid models of a check valve and its interior components as shown in Figure 3-24.

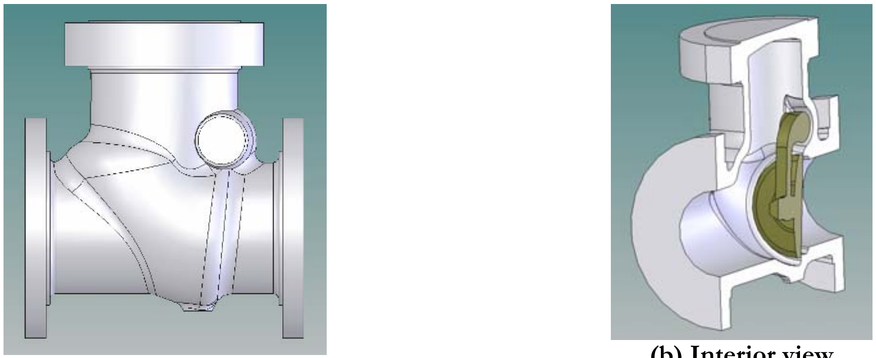

(a) Exterior view

(b) Interior view

Figure 3-24 3D solid models of check valve

3.4 Task 1.4: tests with the KAERI DVI test loop and ARL test bed to obtain condition monitoring data on check valves using selected sensors

Performed by KAERI, PNU, PSU, and SNL

3.4.1 KAERI test loop

The purpose of this task was to identify and recommend methods of inspection, surveillance, and monitoring that would provide timely detection of valve degradation and service wear so that maintenance or replacement could be performed before loss of safety functions. This task used AE, UT, and accelerometer in the check valve test loop. A schematic diagram and an actual installation of the check valve test loop were shown in Figure 3-25. Separate condition monitoring tests of this test loop in a normal configuration and manually degraded states with disc wear and foreign object were performed July 3, 7, and 8, September 25 to 27, 2003, and March and April 2004.

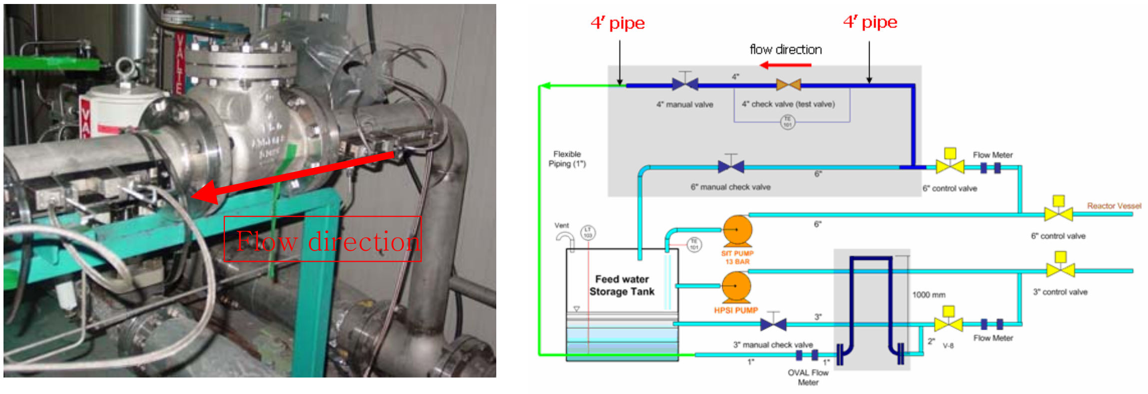

(a) An actual installation

(b) A schematic diagram

Figure 3-25 Check valve test loop

3.4.1.1 Leak test configuration

In this task, the following check valve operational conditions were used to detect disc movement and to evaluate valve degradation with disc/seat and hinge pin wear:

- Valve with new disc and artificial disc scratch: 1 mm, 2 mm, and 3 mm depth half-circle
- Valve with new disc and artificial leakage: 0.5 mm, 1.0 mm, 1.2 mm, 1.5 mm, 2.0 mm, 2.4 mm foreign object interfered between body and disc
- Valve with new and artificially hinge pin wear: 3 mm, 6 mm, and 9 mm depth hinge pin cutting
- Valve with improper assembly: separating disc from disc arm by loosened disc pin

- Loop operation condition (steady state, transient operation 0, 3, 6, 9 bar).

3.4.1.2 Modification of DVI test loop

At KAERI the check valve test loop, a modified DVI test loop, was modified to resolve some observed problems in the test loop caused by the severe limitation of leakage flow in 1 in. pipe connecting to the 4 in. main pipe. The leakage flow rate in the foreign object failure tests could not be increased above 300 liter/min, because the 1 in. pipe for leakage line was very small. Figure 3-26 shows the schematic diagram and picture of the modified test loop with increased leakage flow. An acrylic cover for the check valve and a 4 in. acrylic pipe were used to observe the leakage flow behavior.

These tests were performed using water as the process fluid. Check valves were initially tested in a "good" condition and subsequently with one or more simulated degradations and operational failures. Several flow conditions were also used. At the end of March 2004, two sets of condition monitoring tests were performed with the modified test loop for abnormal configurations with foreign object interference of 0.5 mm, 1.0 mm, 1.2 mm, 1.5 mm, 2.0 mm and 2.4 mm welding rod and with disc wear sizes of 1 mm, 2 mm, and 3 mm depth. Figure 3-27 shows an example of artificial disc wear.

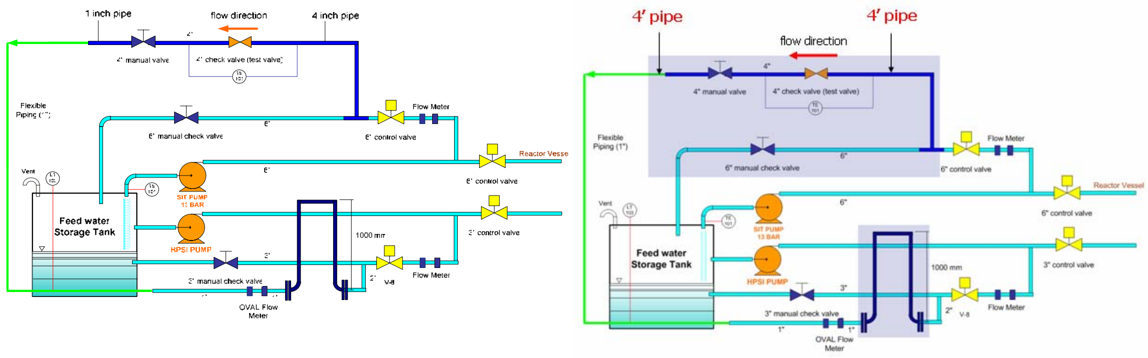

(a) original DVI test loop (b) modified DVI test loop

Figure 3-26 Schematic diagram of DVI test loop

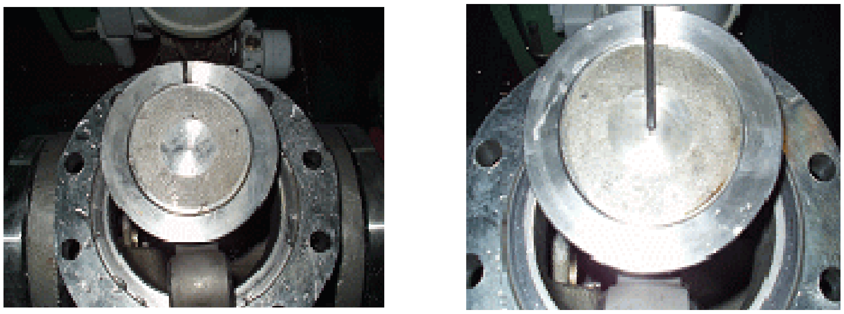

(a) 1.0 mm (b) 3.0 mm

Figure 3-27 Example of artificial disc wears of check valve

3.4.1.3 Experimental setup

A schematic diagram of the sensor installation is shown in Figure 3-28. The AE signals detected from the sensors were amplified by a preamplifier, which had a fixed gain of 40 dB. After passing through a band-pass filter of 300 to 400 kHz to remove the electrical and mechanical background noise, the signals were amplified by the main amplifier (40 dB). The AE parameters, such as RMS, energy, and frequency of AE signals, were analyzed in the AE system (MISTRAS 2001™). In addition, a digital oscilloscope (LeCroy 9310A) was used to analyze the AE signal waveform. AE data of the WD sensor was recorded at a 2 MHz sample/s rate, and AE data of the R15 sensor was recorded at a 1 MHz sample/s rate. The details of experimental setup of the check valve test loop are discussed in Appendix A, Section IV.

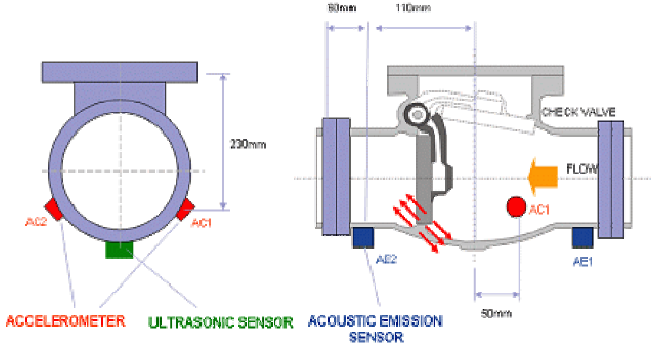

Figure 3-28 Typical attached position of sensors

3.4.2 ARL test bed

3.4.2.1 Description of Hydraulic Diagnostic Test Bed (HDTB)

The Hydraulic Diagnostic Test Bed (HDTB) was assembled at the ARL facility as a check valve test bed. Figure 3-29 shows a piping schematic of the test loop and Figure 3-30 shows pictures of the completed test loop. Initial tests were planned to mirror those of I-NERI partners and include normal, leak (foreign object), and disc wear tests. The investigators originally proposed to conduct these tests at a minimum of zero, 3, 6, and 9 bar for foreign objects 0.30 mm, 0.41 mm, 0.64 mm and 0.89 mm and disc wear faults of 1 mm, 2 mm, and 3 mm. The test plan was later modified as shown in Table 3-7. In addition to static pressure tests, a transient pressure experiment was also conducted.

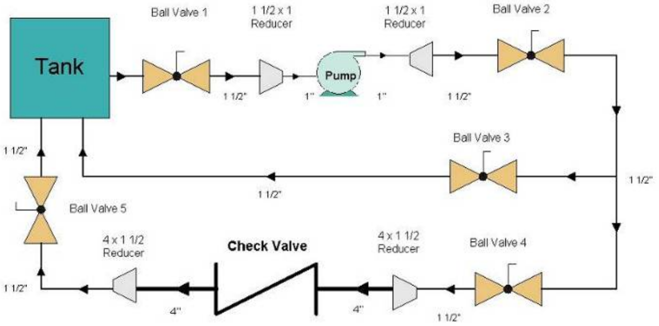

Figure 3-29 HDTB piping schematic

Figure 3-30 ARL check valve test bed

Table 3-7 Updated ARL valve test matrix

	Pressure (bar)									
Valve Condition	1	2	3	4	5	6	7	8	9	10
Normal										
Disc wear 1.0 mm										
Disc wear 2.0 mm										
Disc wear 3.0 mm										
Foreign Object 0.102 mm										
Foreign Object 0.152 mm										
Foreign Object 0.203 mm										
Foreign Object 0.254 mm										

The valve selected for testing was from FNW® Valves, class 150, 316SS swing check valve (see specifications in Figure 3-31).

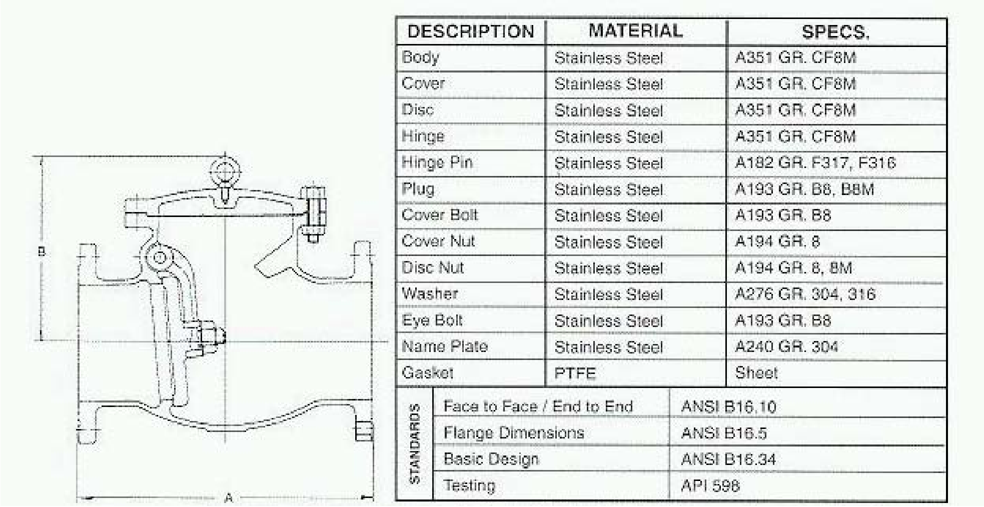

DESCRIPTION	MATERIAL	SPECS.
Body	Stainless Steel	A351 GR. CF8M
Cover	Stainless Steel	A351 GR. CF8M
Disc	Stainless Steel	A351 GR. CF8M
Hinge	Stainless Steel	A351 GR. CF8M
Hinge Pin	Stainless Steel	A182 GR. F317, F316
Plug	Stainless Steel	A193 GR. B8, B8M
Cover Bolt	Stainless Steel	A193 GR. B8
Cover Nut	Stainless Steel	A194 GR. 8
Disc Nut	Stainless Steel	A194 GR. 8, 8M
Washer	Stainless Steel	A276 GR. 304, 316
Eye Bolt	Stainless Steel	A193 GR. B8
Name Plate	Stainless Steel	A240 GR. 304
Gasket	PTFE	Sheet

STANDARDS	Face to Face / End to End	ANSI B16.10
	Flange Dimensions	ANSI B16.5
	Basic Design	ANSI B16.34
	Testing	API 598

Figure 3-31 FNW check valve specifications

Several valve components were fabricated for use during testing. A LEXAN® top cover was machined to allow visual inspection of the valve disc, as shown in Figure 3-32 (a). Five additional discs were machined and used for seeded fault tests. The original disc from the valve is shown in the lower right corner of Figure 3-32 (b). The difference in appearance is due to the fact the original disc was cast and not machined on the top surface of the disc.

Figure 3-32 LEXAN top cover (a) and check valve discs (b).

DAS

A C-sized, VXI rack-mount DAS with an IEEE-1394 FireWire™ interface was used for recording high-bandwidth data from the HDTB. The rack-mounted system was capable of housing thirteen different types of VXI boards. The selected system contained one Agilent® E1433 digitizer module, which provided 8 channels of 196,000 samples/s at 16 bits of resolution and an Agilent E1432 digitizer module, which provided 16 channels of 51,200 samples/s at a 16 b resolution. The E1433 and E1432 provide transducer signal conditioning, anti-alias protection, digitization, and measurement computation in a single module. The onboard digital signal processor and 32 MB of RAM maximize total system performance and simplify system integration. The analog input range of each channel was 10 V peak to peak and different external breakout boxes allowed quick configuration of different types of channel input.

The E1433 and E1432 used analog-to-digital converters (ADCs) for each channel to provide simultaneous sampling across all inputs. Simultaneous sampling guarantees accurate channel-to-channel comparisons in the time and frequency domains, and is required for phase analysis and order re-sampling analysis. The E1433 and E1432 used sigma-delta ADCs with 64X over-sampling, which allows for low-order analog anti-alias filters and permits all filtering and sample-rate conversions to be performed digitally, hence providing stable and drift-free filtering. Sampling rate conversion, digital filters, range, coupling, and many other features were controlled through a custom software package. A VXI system has the advantage of triggering all the DAS boards installed in the mainframe (and across multiple mainframes) at once to provide simultaneous sampling across all boards.

ARL HDTB shakedown

The tested performance of the pump and components yielded the several results. Pressure capability of the pump was at or above expected levels (tested to ~200 psi) to meet the pressure level of 9 bar (130.5 psi), which were the test conditions at KAERI. However, the flow rate was ~1 L/s lower than expected. Table 3-8 lists the location and sensor type for each sensor attached to the test bed. Note that accelerometers located at the pump were mounted in a tri-axial configuration at the outlet.

Table 3-8 HDTB sensor configuration, session 1

	Sensor ID	Model	SN	Manufacturer	Cal. Factor (Units)		Bias (V)	Component	Description
1	VAB	CV 3-1000	NA	LEM USA	100	V/mv	NA	Motor	Voltage T1-T2
2	VBC	CV 3-1000	NA	LEM USA	100	V/mv	NA	Motor	Voltage T2-T3
3	VCA	CV 3-1000	NA	LEM USA	100	V/mv	NA	Motor	Voltage T3-T1
4	IOA	LA 100P	NA	LEM USA	4.0056	A/V	NA	Motor	Current T1
5	IOB	LA 100P	NA	LEM USA	3.9628	A/V	NA	Motor	Current T2
6	IOC	LA 100P	NA	LEM USA	3.9968	A/V	NA	Motor	Current T3
7	P01	102A02	21211	PCB Piezo	209.8196	psi/V	10.7	Pump	Inlet Fluid Pressure -pump
8	P02	102A02	21212	PCB Piezo	210.6594	psi/V	10.8	Pump	Outlet Fluid Pressure- pump
9	AC1	353B16	67207	PCB Piezo	10.0000	g/V	8.7	Pump	Accelereation x', pump
10	AC2	353B16	67213	PCB Piezo	10.0301	g/V	8.6	Choke Valve	Accelereation y' pump
11	AC3	353B16	67214	PCB Piezo	9.7276	g/V	8.7	Pump	Accelereation z', pump
12	P03	102A02	21213	PCB Piezo	223.6636	psi/V	10.7	Ch Valve	Inlet Fluid Pressure -ch valve
13	P04	102A02	21237	PCB Piezo	173.9130	psi/V	10.9	Ch Valve	Outlet Fluid Pressure- ch valve
14	AC4	353B16	59352	PCB Piezo	9.4340	g/V	8.6	Ch Valve	Accel check valve - bottom
15	AC5	353B16	59354	PCB Piezo	9.4340	g/V	8.7	Ch Valve	Accel ch valve -body
16	AC6	353B16	66053	PCB Piezo	9.9010	g/V	8.7	Ch Valve	Accel ch valve -hinge

DAS noise floor

The Agilent VXI data collection system was installed and configured at the HDTB with the check valve positioned in the reverse flow direction. The researchers spent some time verifying signals and reducing the system noise floor. Figure 3-33 (a) shows the original spectral content of the noise floor for the accelerometer signals (pump off condition). Figure 3-33 (b) shows the results after taking measures to reduce ground loops and power line noise issues. Data for these plots was acquired at the accelerometer mounted at the base of the check valve (AC4). The noise floor for AC4 was typical of most of the accelerometers. The small amplitude energy content remaining in the 15 to 20 kHz band was present in the electrical power line of the building. The nominal floor of -76 dB, shown in Figure 3-33, was sufficient for testing the check valve.

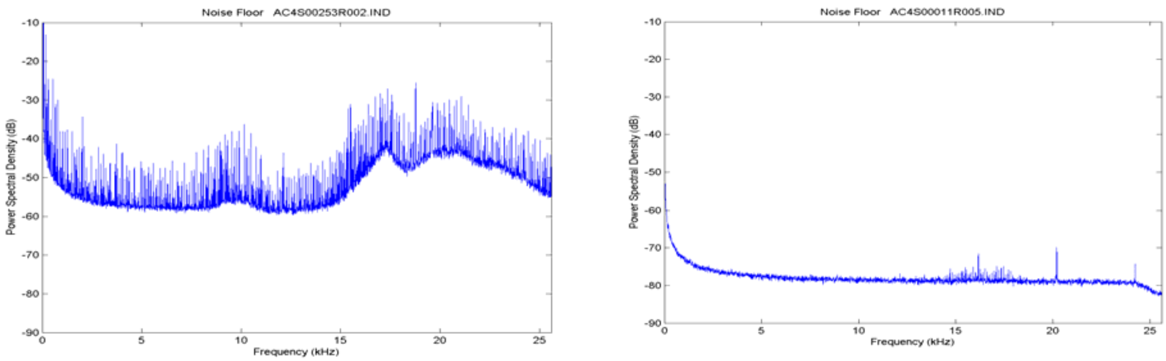

(a)

(b)

Figure 3-33 Typical initial noise floor (a) and final noise floor for AC4 (b)

The measures used to reduce the noise floor were unique to each experimental configuration. Ground loops and input line noise were the most frequently encountered problems. DAS, amplifiers, and signal conditioners that employ a common bus ground will experience more difficulties than those where each channel is isolated. The measures required to reduce the noise floor for the ARL HDTB system included the following:

- Tying all case grounds of the test equipment to the check valve
- Separating the ground circuit of pump motor from the circuit used to power the test equipment
- Electrically isolating all sensors from the pump case, piping and valve
- Reducing the gain of the accelerometers.

Reverse flow shakedown

A waterfall plot of the power spectral density (PSD) for baseline data is shown in Figure 3-34. Qualitatively, the spectrum exhibits some consistency across pressures, except at 1 bar. It was noted during this test that the throttle valve, which is used to regulate pressure at the check valve, introduced high amplitude flow noise into the system. For this reason, a transient test was conducted with the test section initially pressurized to 10 bar but the pump (and flow through the throttle valve) turned off.

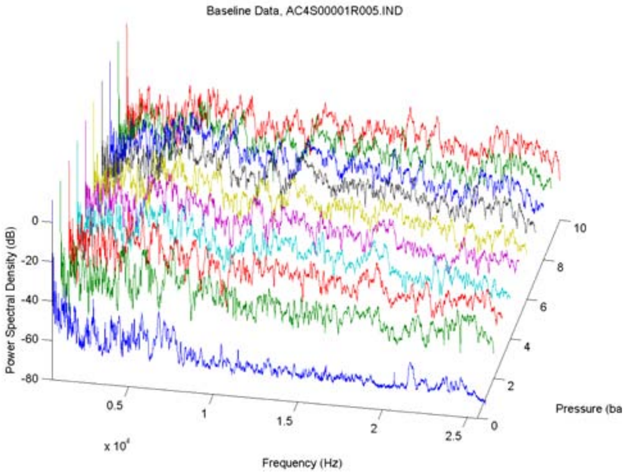

Figure 3-34 Baseline PSD for AC4

3.4.2.2 Modeling of check valve disc

One of the technical difficulties with check valve condition monitoring is the lack of deterministic signals. Aside from the BPF of the pump's impeller, there is no deterministic energy source for the valve. One possible noise or vibration source is from the turbulent flow of fluid as it leaks past the disc. A slightly different but related source may arise from fluid structure interaction exciting vibrations of the valve disc. The theory was that if the fluid structure interaction were to excite a disc mode(s) and the discs' fluid-coupled natural frequencies could be detected experimentally, the signal near these frequencies could be correlated to a change in boundary conditions (such as the disc not seated properly) or change in geometry (such as wear or damage to the disc). It would then be possible to not only detect a leak but also characterize the nature of the fault. Investigation of the theory required an estimate the fluid coupled natural frequencies of the disc. An FEM and a boundary element model (BEM) were constructed to estimate the fluid coupled natural frequencies of the disc. I-DEAS software was utilized to create a solid model and perform the uncoupled modal analysis. Sysnoise™ direct BEM analysis was then employed to estimate the fluid coupled natural frequencies.

I-DEAS FEM

An FEM of the disc was generated using I-DEAS based on measurements of an actual disc, which was cast from 316 stainless steel (ASTM A351 CF8M) and machined on the shaft and seating surfaces. Dimensions of the disc were plate radius = 56.8 mm, average plate thickness = 13.4 mm, maximum height at shaft = 61.5 mm. Material properties were defined as

Young's modulus: E = 250 GPa

Shear modulus: G = 179.856 GPa

Poisson's ratio: υ = 0.305

Density: ϱ = 8000 kg/m3

Side and top views of the disc model are shown in Figure 3-35 (a) and (b), respectively.

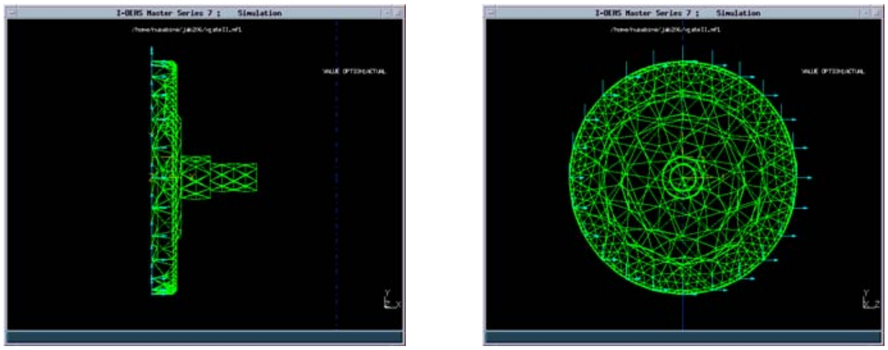

(a) Side view **(b) Top vie**

Figure 3-35 Views of I-DEAS disc mesh

Two representative mode shapes are shown in Figure 3-36. There were degenerate modes present in the model because the disc was symmetric. Table 3-9 shows the relationship between mode shapes and computed modal frequencies.

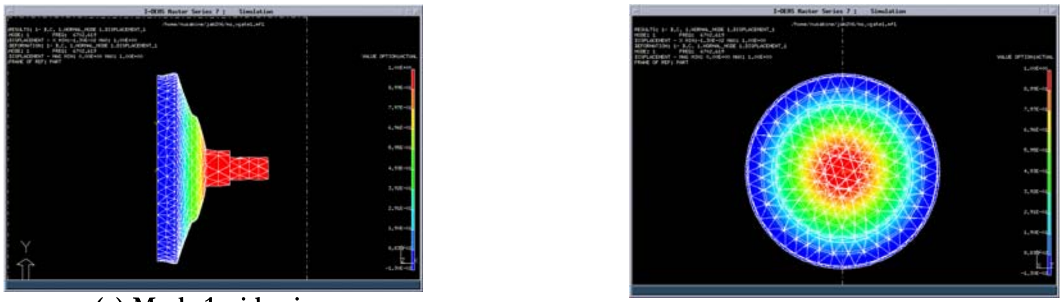

(a) Mode 1, side view

(b) Mode 1, bottom view

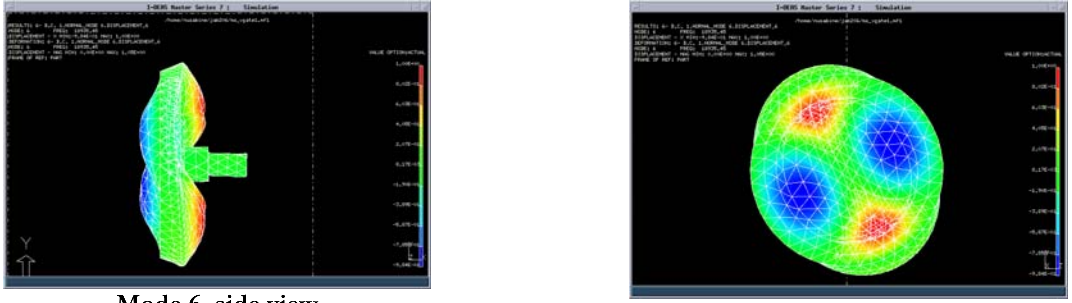

Mode 6, side view

Mode 6, bottom view

Figure 3-36 Two representative mode shapes

Table 3-9 Natural frequencies of the valve disc

Real mode #	FE mode #	Frequency (Hz)
1	1	6702.6
2	2,3	8010.2
3	4,5	11501
4	6,7	18939
5	8,9	19766
6	10	19839

Sysnoise BEM

To estimate the effect of fluid loading on the natural frequencies of the disc, additional analysis was undertaken using LMS® Sysnoise™ software. A coupled FEM/BEM model was created to allow the modal analysis to include the effects of fluid loading. The importance of Sysnoise modeling is shown in Table 3-10, which shows a marked reduction in frequency for three of the modes. The fluid loaded natural frequencies in Table 3-10 were compared to experimental data. If the fluid structure interaction is exciting a mode of the disc, it may be possible to detect an increase in energy about the fluid loaded modal frequency.

Table 3-10 Effects of fluid loading on the valve disc

Real mode #	FE mode #	Natural freq (Hz)	Fluid loaded (Hz)	Reduction (%)
1	1	6702.6	6068.4	9.46
2	2,3	8010.2	7114.8	11.2
3	4,5	11501	9661.5	16.0
4	6,7	18939	15739	16.9
5	8,9	19766	18993	3.90

6	10	19839	19455	1.94

3.4.2.3 Data analysis–ARL session 1

Baseline data was collected with the check valve in the reverse flow direction. The original disc was replaced with one of the spares manufactured at ARL. The LEXAN access cover was substituted for the original stainless steel cover. The foreign object fault was simulated by placing a wire of known diameter between the disc and valve seat. The disc wear fault was simulated by milling a “V” notch on the disc as shown in Figure 3-37. Width at the base of the notch is designated as the nominal size (for example, a = 1.00 mm).

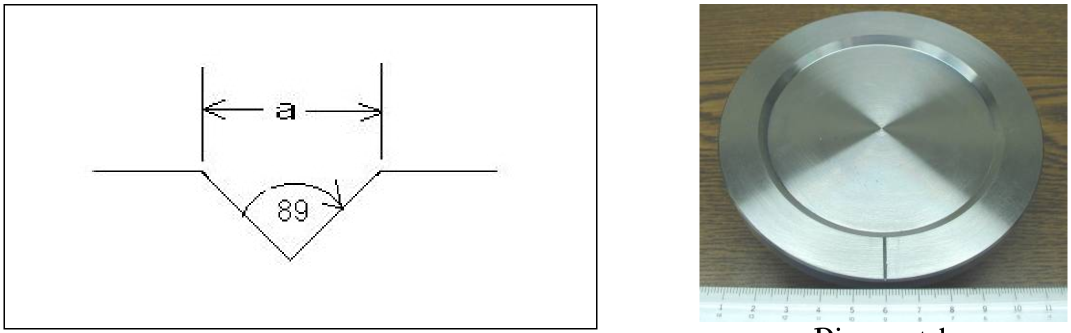

Simulated disc wear **Disc scratch**

Figure 3-37 Geometry of simulated disc wear and disc scratch

Test runs have been completed for baseline, foreign object of 0.30 mm and 0.41 mm, disc wear of 1.0 mm, and transient disc wear of 1.0 mm at pressures of 1 to 10 bar (at 1 bar increments). Sensor locations are shown in Figure 3-38. Signal levels for the check valve accelerometers were low amplitude, with AC4 generally showing the best response. Time series for AC4, AC5, and AC6 baseline at 6 bar pressure are shown in Figure 3-39.

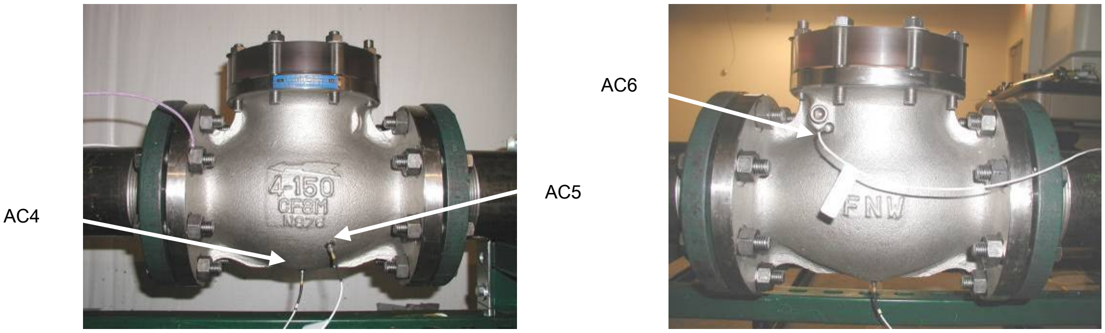

Figure 3-38 Accelerometer AC4, AC5, (left) and AC6 (right) locations

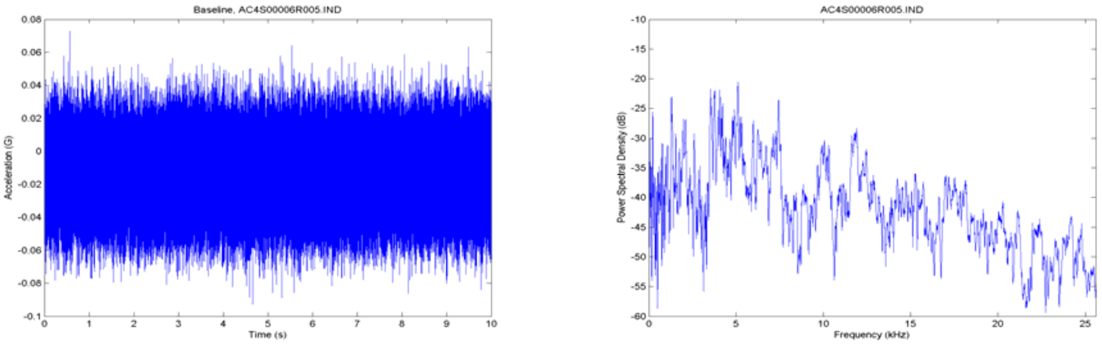

Baseline AC4 time series **Baseline AC4 PSD**

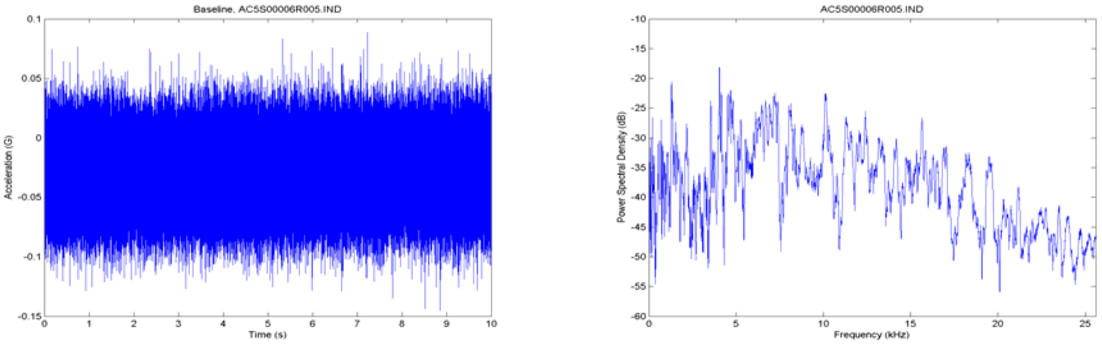

Baseline AC5 time series **Baseline AC5 PSD**

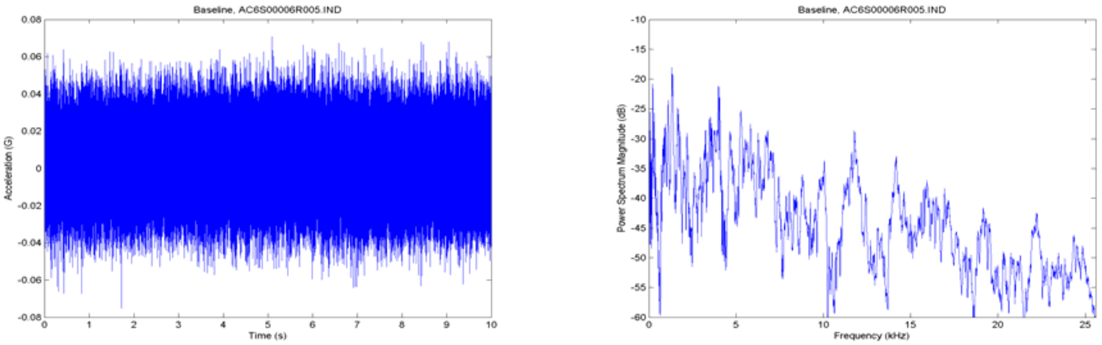

Baseline AC6 time series **Baseline AC6 PSD**

Figure 3-39 Baseline time series and PSDs

Table 3-11 Test condition reference table, session 1

Run number	Valve condition	Comment
R005	Baseline data	Steady state
R006	Foreign object 0.30 mm	Steady state
R007	Foreign object 0.41 mm	Steady state
R008	Disc Scratch 1.00 mm	Steady state
R001	Disc Scratch 1.00 mm	Transient response

Steady-state testing

Data was collected at a sampling frequency of 51.2 kHz over a 10 s time window resulting in a record length of 512000. Sample frequency response of the valve, from AC4, is shown in Figure 3-40 at 3, 6, and 9 bar. The PSD was computed using a FFT length of 8192 records, a corresponding Hanning window N = 8192, and 50% overlap. The resulting frequency resolution was 6.25 Hz. The vertical black lines on the graphs correspond to the fluid loaded natural frequencies of the valve disc.

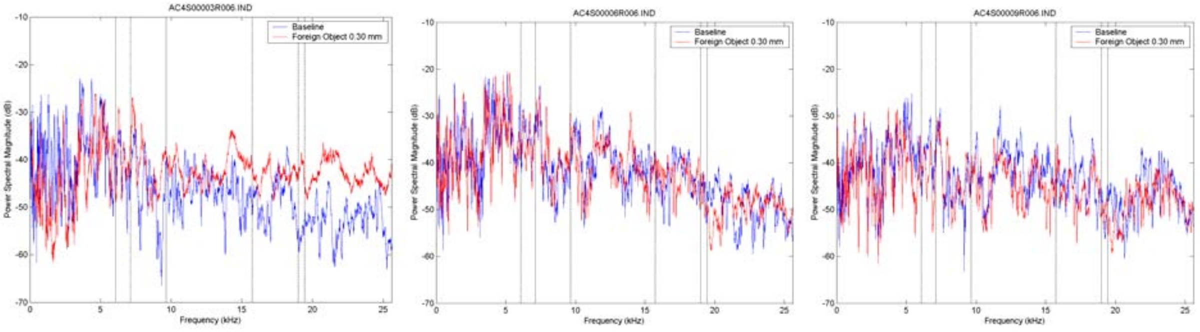

(a) pressure 3 bar **(b) pressure 6 bar** **(c) pressure 9 bar**

Figure 3-40 Foreign object 0.30 mm

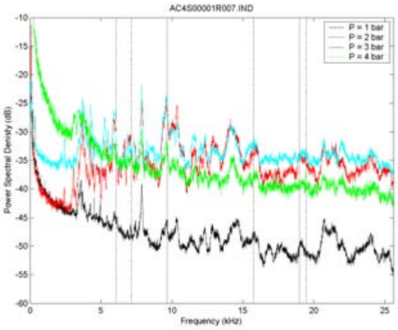

Figure 3-41 Foreign object 0.41 mm pressure series

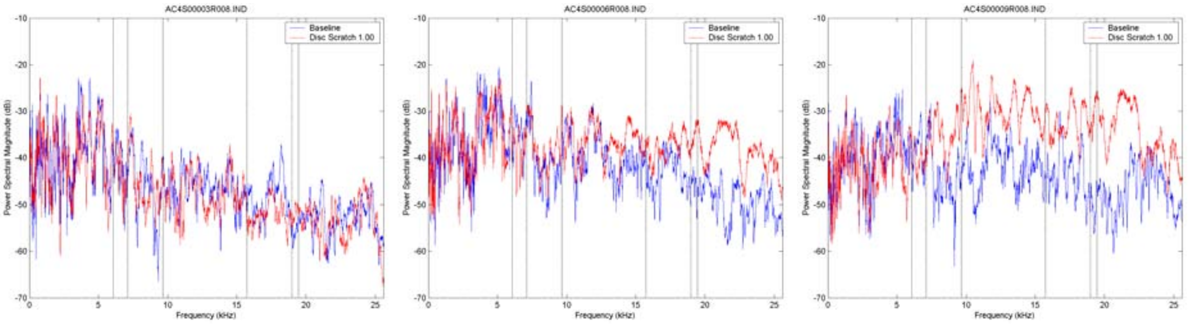

(a) pressure 3 bar **(b) pressure 6 bar** **(c) pressure 9 bar**

Figure 3-42 Disc wear 1.0 mm

Discussion of steady-state results

The foreign object 0.30 mm tests (Figure 3-40 (a) to (c)) show some separation from the baseline at 3 bar, with several peaks in the energy spectrum. The separation was less evident as pressure increased to 6 and 9 bar. This trend may be due to two effects of the test loop. First, at pressures above 1 bar, the throttle valve used to regulate pressure introduces a large amount of noise into the loop. Second, the wire used to simulate the fault was compressed and deformed due to the force exerted by the pressure on the valve disc. As pressure increased and the wire deformed, the foreign object size decreased and the valve/disc geometry approached the baseline condition. The method of simulating foreign objects was modified in test Session 2.

The foreign object with 0.41 mm wire showed little deformation from the test and should be a better representation of the fault. However, it was found that the pump flow rate was not sufficient to supply full pressure for this leak size. In spite of this, the foreign object 0.41 mm data (Figure 3-41) exhibit very encouraging characteristics. Frequency content above 5 kHz was relatively stable and showed strong correlation to the estimated fluid loaded frequencies of the disc. There were also well-defined peaks at 7.85 kHz and 14.2 kHz, which were not evident in the baseline.

The disc wear with 1.00 mm fault (Figure 3-42) appears to increase energy in the upper half of the frequency range with amplitude increasing proportionate to pressure. Note the broad peak from 20 to 22.5 kHz. There appears to be some correlation to the third and sixth modal disc frequencies.

Effects of air entrapment

An additional effect on signal levels involving air entrapment was noted during testing involved air entrapment. Air entrapment was observed below the service cover (that is, the LEXAN top cover) following a changeover between fault types. It was noted that the amplitude of accelerometer signals dropped significantly if the valve body was not completely flooded. It is believed the air cavity above the valve disc acts as a weak spring in series with the water; therefore, the impedance at the interface serves as a pressure-release boundary. Several qualitative snapshots were taken to investigate the effect. It was concluded that the valve body should be completely free of air to ensure an accurate measurement of the valve response.

Transient testing

Transient testing was performed on the disc wear with 1.00 mm fault. This was accomplished by pressurizing the loop to 10 bar then closing an isolation valve and cutting power to the pump. The data snapshot was started ~1 s before isolation of the test section. Snapshot 4 was selected as a representative sample. Note from Figure 3-43, the pump was off by t= 0.5 s, and the valve response (due to the disc wear leak, Figure 3-44) extends to t~3 s. The PSD shown in Figure 3-45 were calculated by discarding the data from t<0.5 s. This analysis should give a better understanding of valve response by isolating it from other sources (pump and isolation valve). There were residual effects due to the light damping present within the system, but direct excitation was removed.

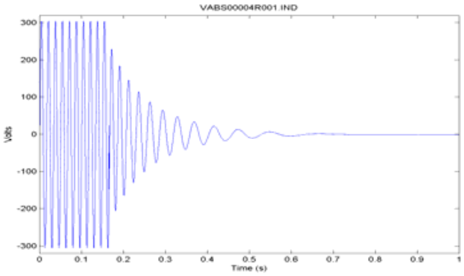

Figure 3-43 **Transient pump voltage**

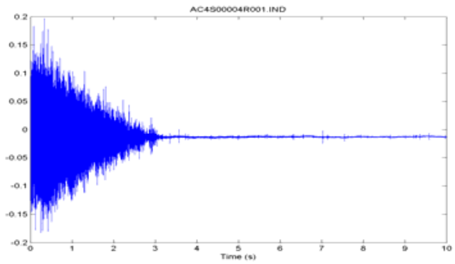

Figure 3-44 **Transient time series, AC4**

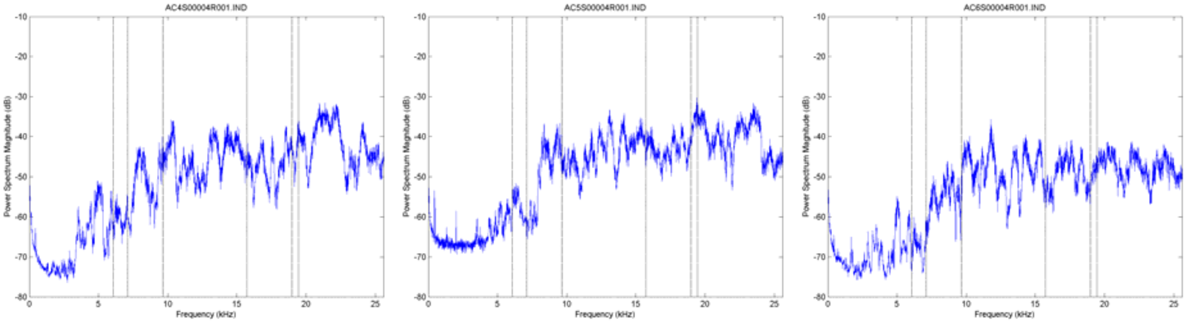

(a) AC4 (b) AC5 (c) AC6

Figure 3-45 Transient disc wear 1.00 mm, 10 bar starting pressure

Discussion of transient testing

Transient data on disc wear with 1.00 mm fault for the three accelerometers highlights three issues noted in the steady-state data: AC4 exhibits the highest amplitude signal, energy is heavily weighted to the upper half of the spectrum, and most of the energy below 5 kHz is due to the pump/motor (see Figure 3-45). For AC4, the energy in the 20-22.5 kHz band appears to be strongly related to valve noise. The transient testing was used mainly to qualitatively verify that there were detectable signals from the leak. Additional transient tests were not pursued since there is a low probability of utilizing this technique in the field.

3.4.2.4 Data analysis–ARL Session 2

Additional testing was performed on the check valve during May 2004. The following changes to the test setup were implemented: AC2 was moved from the pump to the throttle valve and ½ in. wide shim stock was used to simulate foreign objects (Figure 3-46). The shims and disc were inspected following testing and no permanent deformation of the shims or damage to the disc was noted. The disc wear and foreign object faults were positioned at 6 o'clock relative to the axis of the test section. The sensor configuration is shown in Table 3-12 and test runs were listed in Table 3-13. Session 2 data represents the first complete set of data available for comparative analysis.

Figure 3-46 Shim stock used for foreign object simulation

Table 3-12 HDTB sensor configuration, session 2

	Sensor ID	Model	SN	Manufacturer	Cal. Factor (Units)		Bias (V)	Component	Description
1	VAB	CV 3-1000	NA	LEM USA	100	V/mv	NA	Motor	Voltage T1-T2
2	VBC	CV 3-1000	NA	LEM USA	100	V/mv	NA	Motor	Voltage T2-T3
3	VCA	CV 3-1000	NA	LEM USA	100	V/mv	NA	Motor	Voltage T3-T1
4	IOA	LA 100P	NA	LEM USA	4.0056	A/V	NA	Motor	Current T1
5	IOB	LA 100P	NA	LEM USA	3.9628	A/V	NA	Motor	Current T2
6	IOC	LA 100P	NA	LEM USA	3.9968	A/V	NA	Motor	Current T3
7	P01	102A02	21211	PCB Piezo	209.8196	psi/V	10.7	Pump	Inlet Fluid Pressure -pump
8	P02	102A02	21212	PCB Piezo	210.6594	psi/V	10.8	Pump	Outlet Fluid Pressure- pump
9	AC1	353B16	67207	PCB Piezo	10.0000	g/V	8.7	Pump	Accelereation x', pump
10	AC2	353B16	67213	PCB Piezo	10.0301	g/V	8.6	Choke Valve	Accelereation choke valve
11	AC3	353B16	67214	PCB Piezo	9.7276	g/V	8.7	Pump	Accelereation z', pump
12	P03	102A02	21213	PCB Piezo	223.6636	psi/V	10.7	Ch Valve	Inlet Fluid Pressure -ch valve
13	P04	102A02	21237	PCB Piezo	173.9130	psi/V	10.9	Ch Valve	Outlet Fluid Pressure- ch valve
14	AC4	353B16	59352	PCB Piezo	9.4340	g/V	8.6	Ch Valve	Accel check valve - bottom
15	AC5	353B16	59354	PCB Piezo	9.4340	g/V	8.7	Ch Valve	Accel ch valve -body
16	AC6	353B16	66053	PCB Piezo	9.9010	g/V	8.7	Ch Valve	Accel ch valve -hinge

Table 3-13 Test condition reference table, session 2

Run Number	Valve Condition	Disc #	Comment
R010	Baseline Data Disc 01	Disc 01	Steady state
R011	Foreign object 0.102 mm	Disc 01	Steady state
R012	Foreign object 0.154 mm	Disc 01	Steady state
R013	Foreign object 0.203 mm	Disc 01	Steady state
R014	Foreign object 0.254 mm	Disc 01	Steady state
R015	Foreign object 0.305 mm	Disc 01	Steady state
R100	Baseline Data Disc 02	Disc 02	Steady state
R101	Disc wear 1.00 mm	Disc 02	Steady state
R102	Disc wear 2.00 mm	Disc 02	Steady state
R103	Disc wear 3.00 mm	Disc 02	Steady state

Discussion of results

Data was analyzed in the time domain to find figures of merit (FOMs) that may be used to characterize fault type and size. The statistical FOMs computed from the data were RMS, skewness, kurtosis, and crest factor. Referencing Figure 3-47 and Figure 3-48, three characteristics of the data were apparent from the figures. First, the RMS value increases with pressure and fault size. Above pressures of 6 bar, there is enough difference in RMS values that this FOM could be used as an indicator of fault size for a disc wear fault, *if the static pressure is known.* However, knowledge of the static pressure at the valve may be difficult to determine without introducing a pressure tap into the system. Second, the values of kurtosis and crest factor for pressure ≤ 2 bar were very different from higher-pressure values. The reason for this difference may be related to the noise from the throttle valve. Third, there is no clear pattern or separation to distinguish a disc wear fault from the baseline condition using kurtosis, skewness, or crest factor.

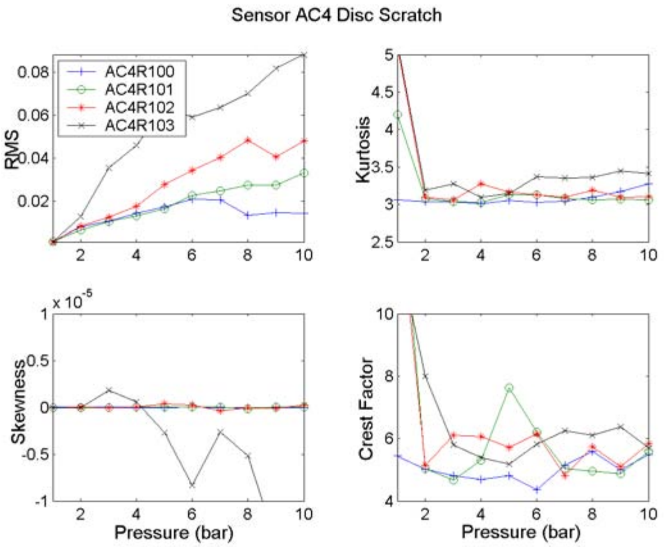

Figure 3-47 Time domain FOMs, sensor AC4

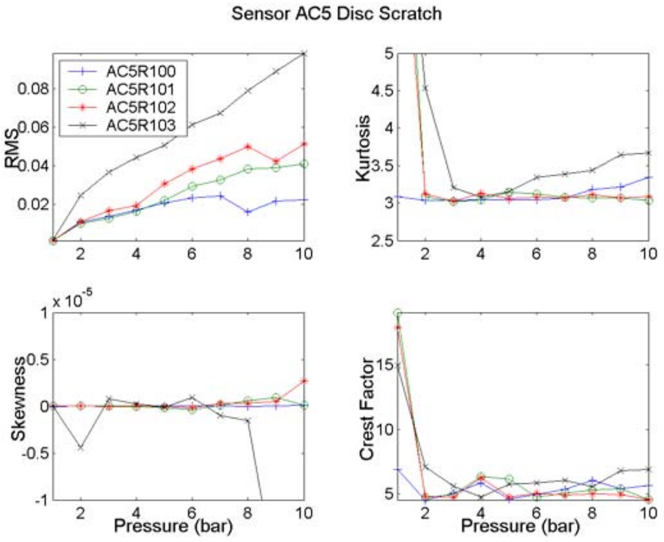

Figure 3-48 Time domain FOMs, sensor AC5

Analysis in the frequency domain seemed to hold more promise of success. The primary reason for moving AC2 to the throttle valve was to gather data near the throttle valve. As noted earlier, the flow noise from the throttle valve was higher in amplitude between 3 and 9 bar. Collecting data from both the pump (primary noise source) and throttle valve (secondary noise source) enables the use of cross-correlation and coherence functions. Other noise sources were obviously present, but the pump and throttle valve were likely the two most significant sources of noise and vibration energy in the system. Employing a multiple input/multiple output model, the multiple coherence function can be used to remove effects directly correlated to the pump and throttle valve from the check valve accelerometer signals. Figure 3-49 shows a comparison of the raw spectrum and the incoherent spectrum for AC5. In this example, the coherence was high for the baseline signal but low for the fault signal. In effect, the baseline was reduced so there is a greater difference than the standard power spectrum. The multiple coherence method was employed as part of the investigative process [5]. Data was collected at a sampling frequency of 51.2 kHz over a 10 s time window resulting in a record length of 512000 samples. The incoherent power spectrum was computed (using the multiple coherence method to remove direct linear excitation of the pump and throttle valve) with an FFT length of 8192 records, a corresponding Hanning window N = 8192, and 50% overlap. The resulting frequency resolution was 6.25 Hz.

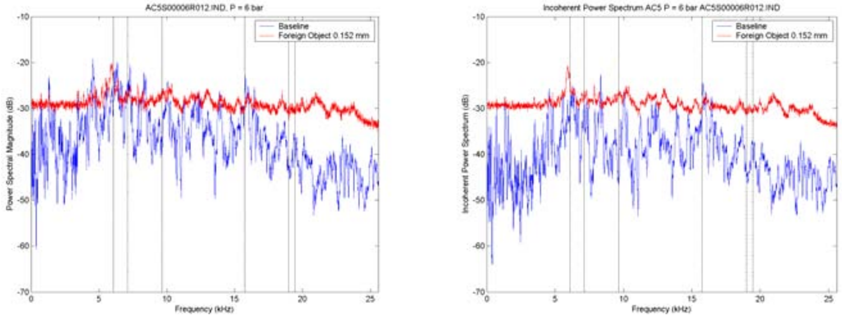

Figure 3-49 PSD (left) and incoherent power spectrum (right). *FO 0.152 mm, pressure 6 bar***.**

Figure 3-50 shows the various disc wear fault sizes at a pressure of 6 bar. Clearly, the difference in the signals compared to the baseline will enable a high degree of confidence in detecting a disc wear fault. In addition, significant differences in the fault signals should allow for some degree of characterization of fault size.

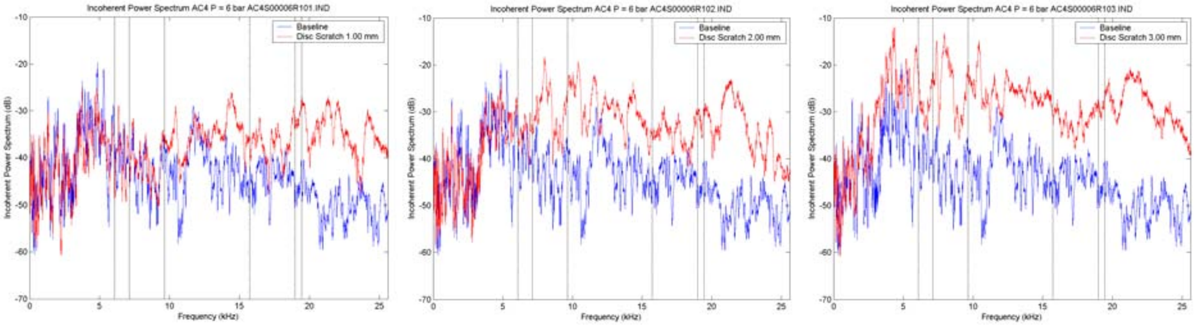

(a) Disc wear 1.00 mm **(b) Disc wear 2.00 mm** **(c) Disc wear 3.00 mm**

Figure 3-50 pressure 6 bar

Figure 3-51 shows the foreign object fault size series at a pressure of 6 bar. There were several notable characteristics notable concerning the foreign object data. The low pressure or small fault spectrums were similar to the disc wear data. The spectrum was characterized by rich frequency content with mean amplitude slightly above the baseline. However, for midrange pressures, a broadband source of energy is evident as seen in Figure 3-51. The energy level was nearly constant across the tested range with peaks only 6 dB above the mean level.

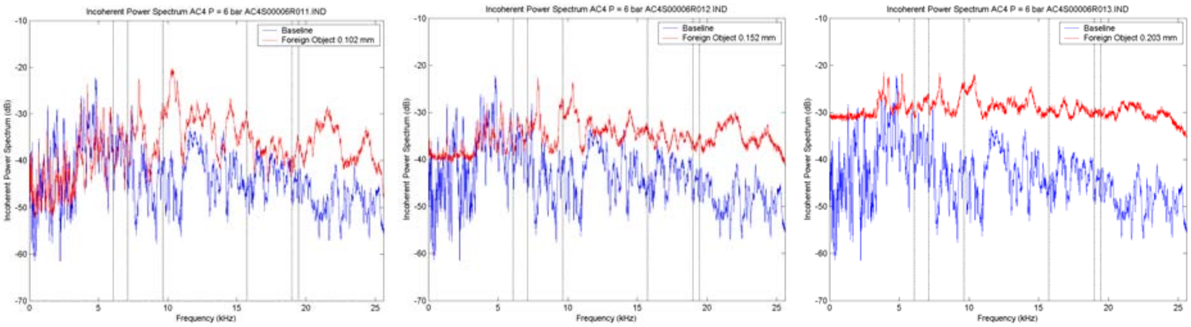

(a) Foreign object 0.102 mm (b) Foreign object 0.152 mm (c) Foreign object 0.203 mm

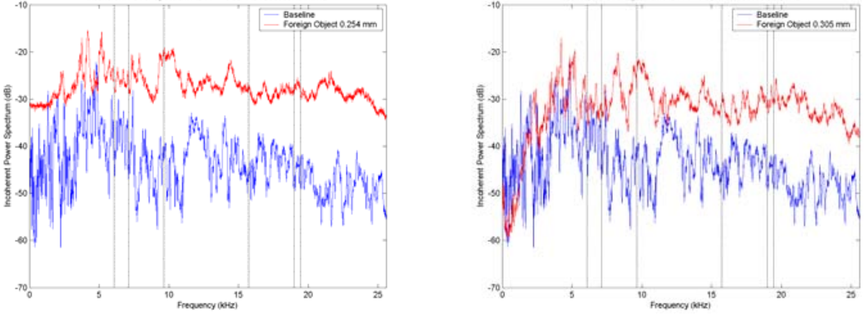

(d) Foreign object 0.254 mm (e) Foreign object 0.305 mm

Figure 3-51 Pressure 6 bar

3.4.2.5 Data analysis–ARL Session 3

Additional testing was performed on the check valve during June 2004. The seeded fault tests from Session 2 were repeated to obtain a complete set of pressures. In addition to the VXI test system (channels 1 to 16), a PAC μDiSP AE system was also employed. The model 1220C voltage amplifier with 40 dB gain, 100 kHz high pass filter, was used to couple the sensors to the PAC μDiSP. The sensor configuration is shown in Table 3-14 and test runs were listed in Figure 3-15. Location of the AE sensors is shown in Figure 3-52.

Table 3-14 HDTB sensor configuration, session 3

	Sensor ID	Model	SN	Manufacturer	Cal. Factor (Units)		Bias (V)	Component	Description
1	VAB	CV 3-1000	NA	LEM USA	100	V/mv	NA	Motor	Voltage T1-T2
2	VBC	CV 3-1000	NA	LEM USA	100	V/mv	NA	Motor	Voltage T2-T3
3	VCA	CV 3-1000	NA	LEM USA	100	V/mv	NA	Motor	Voltage T3-T1
4	IOA	LA 100P	NA	LEM USA	4.0056	A/V	NA	Motor	Current T1
5	IOB	LA 100P	NA	LEM USA	3.9628	A/V	NA	Motor	Current T2
6	IOC	LA 100P	NA	LEM USA	3.9968	A/V	NA	Motor	Current T3
7	P01	102A02	21211	PCB Piezo	209.8196	psi/V	10.7	Pump	Inlet Fluid Pressure -pump
8	P02	102A02	21212	PCB Piezo	210.6594	psi/V	10.8	Pump	Outlet Fluid Pressure- pump
9	AC1	353B16	67207	PCB Piezo	10.0000	g/V	8.7	Pump	Accelereation x', pump
10	AC2	353B16	67213	PCB Piezo	10.0301	g/V	8.6	Choke Valve	Accelereation choke valve
11	AC3	353B16	67214	PCB Piezo	9.7276	g/V	8.7	Pump	Accelereation z', pump
12	P03	102A02	21213	PCB Piezo	223.6636	psi/V	10.7	Ch Valve	Inlet Fluid Pressure -ch valve
13	P04	102A02	21237	PCB Piezo	173.9130	psi/V	10.9	Ch Valve	Outlet Fluid Pressure- ch valve
14	AC4	353B16	59352	PCB Piezo	9.4340	g/V	8.6	Ch Valve	Accel check valve - bottom
15	AC5	353B16	59354	PCB Piezo	9.4340	g/V	8.7	Ch Valve	Accel ch valve -body
16	AC6	353B16	66053	PCB Piezo	9.9010	g/V	8.7	Ch Valve	Accel ch valve -hinge
PAC1	AE1	Micro15	NA	PAC				Ch Valve	Valve - hinge
PAC2	AE2	Micro15	NA	PAC				Ch Valve	Valve - bottom
PAC3	AE3	Micro15	NA	PAC				Ch Valve	Valve - Flange
PAC4	AE4	Micro15	NA	PAC				Pipe	Pipe

Table 3-15 Test condition reference table, session 3

Run Number	Valve Condition	Disc #	Comment
R211	Foreign object 0.102 mm	Disc 01	Steady state
R212	Foreign object 0.154 mm	Disc 01	Steady state
R213	Foreign object 0.203 mm	Disc 01	Steady state
R214	Foreign object 0.254 mm	Disc 01	Steady state
R201	Disc wear 1.00 mm	Disc 03	Steady state
R202	Disc wear 2.00 mm	Disc 03	Steady state
R203	Disc wear 3.00 mm	Disc 03	Steady state

Figure 3-52 AE sensor location

Discussion of results

Data from the VXI system was collected matching the settings in Session 2 (sampling frequency of 51.2 kHz over a 10 s time window). Repeatability from Session 2 to Session 3 was qualitatively assessed for various faults and pressures. There was slight variability across sessions in most of the data, but agreement was generally quite good. A representative sample is shown in Figure 3-53.

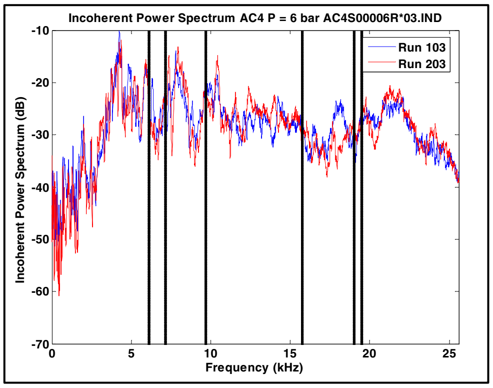

Figure 3-53 Disc wear 3.00 mm, 6 bar

Acoustic emission data were collected using a sample rate of 10 MHz. The PAC DAS is capable of high sample rates up to 20 MHz. Although the sampling rate is impressive, the proprietary software was found to be very limiting for steady-state analysis. Collection of continuous time series raw data is only possible when using the "waveform" capture option (a sample of a waveform is shown in Figure 3-54). The software allows a very limited time record to be recorded, determined by a total record length setting. Due to the high sample rate and short record length, the resolution in the frequency domain is not sufficient for further analysis.

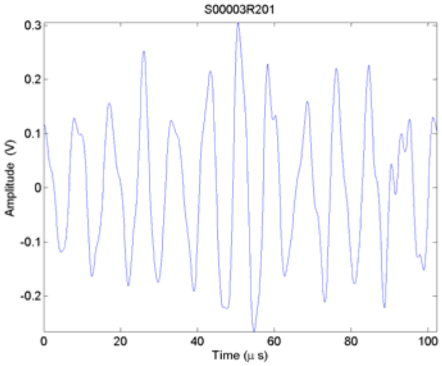

Figure 3-54 AE data, disc wear 1.00 mm, 3 bar pressure

3.4.2.6 Fault detection

Following analysis of ARL accelerometer data, a strategy for fault detection was devised. As noted in previous sections, the frequency domain seemed to hold the most promise for success. The fault detection method was focused ton addressing the following issues:

- Identify the least expensive, yet reliable, method to discern a fault from a normal condition
- Investigate the repeatability of the method in discerning fault size
- Investigate the robustness of the method to perform absolute detection versus relative comparisons.

Visual comparison of the various signals versus baseline readings clearly show that detection of a fault versus normal configuration is achievable. Yet, comparison to a baseline is probably the most complex or very expensive method, and by design, cannot accomplish the last task. Due to cost and safety concerns, methods that are independent of pressure would be desirable. As noted previously, the RMS value is proportional to pressure, so a normalization factor would need to be used if the amplitude (either RMS or PSD amplitude) was incorporated in the method. In weighing all these factors, it appeared that a frequency only based method might achieve the objective. To that end, the following method was devised:

1. Compute the (averaged) PSD from the raw time signal
2. Digitally select a number of "peaks" from the PSD to act as markers that characterize the spectrum.
3. Process the PSD markers with a decision making algorithm that determines
   A. If a fault exists
   B. If it exists, characterize the fault type and size.

To accomplish step 1, the raw data was processed with the parameters shown in Table 3-16. The data were high-pass filtered with a 2^{nd} order Chebyshev filter with 3 kHz cutoff. The multiple coherence function was not used in this analysis.

Table 3-16 Welsh's method parameters for the PSD estimate

Parameter	Size (number of samples)	Comment
N(FFT)	4096	Length of FFT
Fs	51,200	Sampling frequency
Hanning	4096	Envelope window
Overlap	2048 (50%)	Amount of window overlap

Step 2 involves the digital selection of peaks, or local maxima, from the PSD. There were numerous algorithms, both shareware and commercial, available for this task. The chosen version selects a local maximum from a selectable frequency range. This function was nested inside a “while” loop that indexed the sensitivity parameter until it retuned a specified number of maxima from the PSD. A subtle, but very useful characteristic of this algorithm is that it *does not* use a global amplitude threshold. Instead, it searches for a single local maximum within a local frequency band determined from the sensitivity parameter. That is important in this case because the differences in PSD were often in the low amplitude/high frequency part of the spectrum. Figure 3-55 shows the baseline linearly scaled PSD for pressures 3-10 bar with the selected maxima noted as black circles. The loop was set to return 25 maxima points for each PSD. The linear scaling accentuates the maxima for visual comparison.

Step 3 of the process required a decision-making algorithm based on the location of the maxima from the PSD. Session 2 data were used for development and Session 3 data were reserved for testing the fault detection method. The algorithm uses only the frequency of maxima markers, not the full PSD or amplitude of the maxima. Although amplitude is implicit in the process, the actual value is not used. In an analog domain, it is analogous to using band-pass filters and detecting if a signal is present in the passband. Selection of 25 maxima points from each PSD resulted in three to seven common “bands” across the pressure series for each fault type. The bandwidths were empirically derived by reviewing the pressure series for each fault type and accelerometer. Figure 3-56 shows the selection bands (in yellow) for disc wear 2.00 mm, sensor AC4.

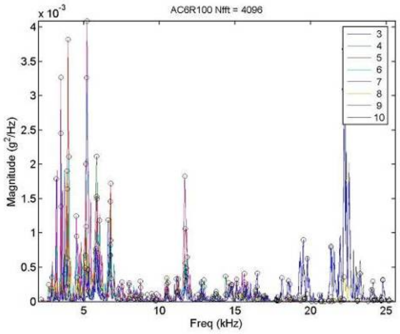

Figure 3-55 AC6, baseline, PSD and selected maxima, pressure 3 to 10 bar

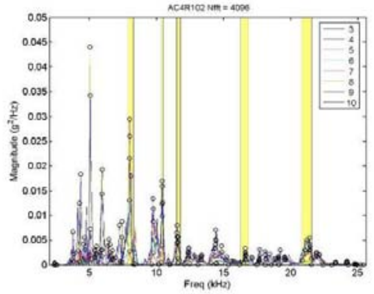

Figure 3-56 AC4, disc wear 2.00 mm, session 2 data

The detection of a fault and characterization of fault size was poor at low pressures (<3 bar). This result was expected because there was very little difference in the PSD from the baseline for low pressure/small fault conditions. Detection levels with a single sensor were also poor, at least with the settings used to process the data. Increasing the length of the PSD and the number of maxima may help increase the detection rate, but at the cost of less averaging. Fusing data from all three accelerometers dramatically increased the detection rate. Results for Session 2 data are shown in Table 3-17. The success rate for P≥4 bar was 95%. Note that for run R010, there were no faults detected (NFDs) at baseline.

Table 3-17 Fault detection results, session 2 data

Run#	R010	R011	R012	R013	R101	R102	R103
Actual fault	**Baseline**	**FO 0.102**	**FO 0.152**	**FO 0.203**	**DS 1.00**	**DS 2.00**	**DS 3.00**
1	NFD	NFD	NFD	NFD	NFD	NFD	NFD
2	NFD	NFD	NFD	NFD	NFD	NFD	NFD
3	NFD	NFD	FO 0.152	FO 0.203	NFD	NFD	NFD
4	NFD	FO 0.102	FO 0.152	FO 0.203	NFD	DS 2.00	DS 3.00
5	NFD	FO 0.102	FO 0.152	FO 0.203	DS 1.00	DS 2.00	DS 3.00
6	NFD	FO 0.102	FO 0.152	FO 0.203	DS 1.00	DS 2.00	DS 3.00
7	NFD	FO 0.102	FO 0.152	FO 0.203	DS 1.00	DS 2.00	DS 3.00
8	NFD	FO 0.152	FO 0.152	FO 0.203	DS 1.00	DS 2.00	DS 3.00
9	NFD	FO 0.102	FO 0.152	FO 0.203	DS 1.00	DS 2.00	DS 3.00
10	NFD	FO 0.102	FO 0.152	FO 0.203	DS 1.00	DS 2.00	DS 3.00

After the Session 2 data established the bandwidth settings, the fault detection algorithm was then tested on Session 3 data. The results are shown in Table 3-18. The success rate for P≥4 bar was 97%.

Table 3-18 Fault detection results, session 3 data

Run #	R100	R211	R212	R213	R201	R202	R203
Actual fault	**Baseline**	**FO 0.102**	**FO 0.152**	**FO 0.203**	**DS 1.00**	**DS 2.00**	**DS 3.00**
1	NFD	NFD	NFD	NFD	NFD	NFD	NFD
2	NFD	NFD	NFD	NFD	NFD	FO 0.102	NFD
3	NFD	NFD	NFD	FO 0.203	NFD	DS 2.00	DS 3.00
4	NFD	FO 0.102	FO 0.152	FO 0.203	DS 1.00	DS 2.00	DS 3.00
5	NFD	FO 0.102	FO 0.152	FO 0.203	DS 1.00	DS 2.00	DS 3.00
6	NFD	FO 0.102	FO 0.152	FO 0.203	DS 1.00	DS 2.00	DS 3.00
7	NFD	FO 0.102	FO 0.152	FO 0.203	DS 1.00	DS 2.00	DS 3.00
8	NFD	FO 0.102	FO 0.203	FO 0.203	DS 1.00	DS 2.00	DS 3.00
9	NFD	FO 0.102	FO 0.152	FO 0.203	DS 1.00	DS 2.00	DS 3.00
10	NFD	FO 0.102	FO 0.152	FO 0.203	DS 1.00	DS 2.00	DS 3.00

3.4.3 Check valve data analysis

This section describes the results of data analyses from KAERI, SNU, CNU, PNU, and PSU conducted at SNL using a particular subset of data collected at various times from the test loops. The purpose of the analysis process was to determine the suitability of the signals (and thus the suitability of the sensors themselves) to provide means for in situ fault condition determination, subject to proper computational signal processing. The planned course of the analysis included first determination of the presence of clear signals corresponding to the fault conditions, and subsequently determination of the ability of these signals/sensors to convey information regarding changes of the degree of the particular fault condition, and further to determine the ability of the signals or sensors to differentiate between various failure modes. Two additional analytical goals included the following:

- Determination (or at least the suggestion) of a physical link between the signal feature(s) used to make these determinations and failure mode associated with those feature(s)

- Assessment of the possibility of achieving a detection method for failed valves, type of failure, and failure degree that is independent of any historical knowledge of signals associated with the particular valve or its local operating condition during previous (possibly non-faulty) operation.

Signals clearly differentiating the normal condition from the disc wear fault condition and differentiating the normal condition from the foreign object fault condition were obtained. Changes in the degree of the disc wear failure mode, evaluated at a constant operating pressure, could be resolved. Results for other types of failure were not obtained due to operating limitations. A signal analysis methodology initially developed during analysis of the September 2003 data and used to successfully distinguish the disc wear fault condition from the normal valve condition within that dataset, was subsequently applied (without adjustment) to those data resulting from later collections in March and April 2004. This methodology again successfully distinguished the presence of both disc wear and foreign object faults, despite slight differences in piping and operating conditions. Sub-optimal data acquisition features particular to the March and April data collections preclude any determination of the ability of these signals/sensors to differentiate between the disc wear and the foreign object failure modes. This same un-adjusted signal analysis methodology was applied to some of the May 2004 data, which occurred at an alternate test site having a different valve, pumps, piping, sensors, and operating conditions. These differences in operating conditions between the September 2003 data and the May 2004 data confounded one of the two complementary signal-processing techniques; however, the presence of a fault condition could be identified. These results demonstrate that although the methodology may be robust relative to slightly changing conditions, it does not perform flawlessly when applied without modification across strongly differing operating conditions and differing sensors.

It seems very likely that signals suitable for in situ condition monitoring that lead to effective preventative maintenance and thus to both enhanced safety and reduced cost can be achieved using AE sensors. The suitability of other sensor types, ability to differentiate between differing failure modes using these sensors, and possibility of achieving identification of fault conditions without developing information from data resulting from prior proper operation remains to be determined.

Eight valuable results follow from SNL's and KAERI's check valve monitoring data analysis:

- Problem Decomposition. Separating the data analysis problem into components
- Sensor Comparison. Evaluating the relative performance of multiple sensor types
- Analysis Technique Evaluation. Evaluating the performance of multiple signal analysis techniques
- Possible Check Valve Monitoring Process. Identifying an analysis process that could be used in future testing
- Hypothetical Phenomenological Model. Describing a hypothetical physical model of conditions contributing to the data
- Monitoring Without Prior Knowledge. Understanding issues that influence the possibility of developing means for accurately assessing in situ check valve condition without prior assessment of that particular valve during "known good" operation
- Status of Analytical Techniques. Describing the status of various analytical techniques based upon observation of modeled valve faults evaluated within multiple test beds
- Future Work. Suggesting subsequent activities.

3.4.3.1 Data

Multiple degrees-of-fault of check valve were tested at KAERI, which involved the substitution of multiple modified clappers for each of the conditions. Details of the data descriptors used for the 168 unique test instances particular to the September test are in [i]. The May data collection occurred at PSU; the component under test was a swing-type clapper check valve operated in a normal condition and subsequently with the incorporation of a hardware-modeled failure mode. This two test bed sequence allowed both the evaluation of the (nominally) same valve (in just slightly modified operating environment) and the evaluation of a different valve (of the same fundamental configuration) in a separate and dissimilar operating environment.

A test "instance" comprises a unique combination of sensor type, sensor location, time and time interval, system pressure, failure mode being modeled, and fault degree. During the September 2003 data collection, 168 test instances were recorded. A complete list of these test instances is included in [1]. Three operating conditions: normal, disc wear failure, and foreign object failure were tested. Three operating pressures were tested, including 3 bar, 6 bar, and 9 bar. Three different degrees of each failure mode were tested, the dimensions characterized the degrees, and in each case, a larger number "dimension" corresponds to a greater degree of fault. Different sampling rates were used during these tests in a sensor-dependent fashion. Table 3-19 describes the sensor suite for this data collection and the physical location of those sensors is described in [ii].

Table 3-19 Sensor designations

Sensor Type	Designators	
Accelerometer	A1	A2
WD AE	W1	W2
Narrow band AE	R1	R2
Flow meter	F1	F2

The modeled failure modes for the September 2003, and March and April 2004 data collections were the same. Different selection criteria were used to determine the subset of the September data to be used in the initial analysis. One criterion was an estimation of the likely strongest signal; this was judged to result from the disc wear condition because the pressures were known to be the same for each failure mode and the hole size was judged to be smaller for disc wear in contrast with the foreign object failure mode. Another criterion was the perceived ease of developing a quantitative understanding of those phenomena responsible for the signal; the disc wear failure mode allows easier evaluation of the size of the check valve leakage path, which was expected to influence the features of the signal. Finally, data quality influenced the selection of sensors selected for inclusion in this initial analysis.

Individual datasets associated with a particular test instance were not used in their entirety because the datasets were too long to be handled conveniently by those signal analysis tools useful for preliminary analysis. The full datasets were useful because they allow evaluation of several portions of data that were more widely separated in time. Initially, four or five data portions, each of 4 s length, were generated for every test instance evaluated. In some analytical processes, the complete 4 s portion was used, but in other analytical processes, only the first 65000 data points were used from each 4 s portion. In either of those cases, data spanning several seconds of each test instance was evaluated. Subsequent to the initial analysis of the September data, the data interval used was selected to facilitate the implementation of those particular techniques. In these subsequent cases, five adjacent data intervals of 0.10 s length were extracted from the beginning of the data files.

In the September data collection, all test instances incorporating the wideband AE sensor W2 and both the normal condition and the disc wear failure mode were analyzed using the full range of test conditions. The March and April data collections were more widely sampled than was the September collection. The operating pressures of 3 bar, 6 bar, and 9 bar used during the September collection were favored during analysis of the March and April datasets. The test instances incorporating both the W1 and W2 wideband AE sensors and both the R1 and R2 narrowband emission sensors were analyzed for the normal condition and for disc wear and foreign object failure modes. Sixty-one test instances incorporating AE sensors during the March and April data collections were evaluated.

3.4.3.2 Analysis and results

Common data characteristics

The data from the September 2003 data collection were evaluated for general characteristic features and content, because knowledge of the both the signal and the noise contents is useful for selecting analysis techniques and interpreting the results. Some general observations regarding both the quality and the characteristics of these data should be made. Some observations raise questions about the quality of those datasets used within this analysis process. First, PSDs derived from a variety of Fourier transform based methods show both high levels of signal energy very near to the Nyquist frequency (cutoff frequency) and show no clear evidence of the presence of any anti-aliasing filtration intended to reduce signal energy below that cutoff.

The data quality concerns influenced the selection of those analytical techniques used to derive characterization features from the data and the subjective weighting of the results. One consideration guiding the selection of analytical techniques was the desire to develop information that would retain validity despite the data corruption.

In general, the check valve fault related signal characteristics include atonality and the lack of harmonic content. Considering the data intervals provided and those data intervals likely to be relevant to check valve condition monitoring, the data do not seem to exhibit strict stationarity [iii]. In addition, the datasets generally include additive background noise, which may contribute greatly to the lack of stationarity. The stationarity of these signals was not explicitly tested; such testing does not seem warranted when considering that the future source of the real signals of interest will be within an NPP, which is expected to include more noise sources than those present in the more closely controlled test-loop environment. Data generated in any type of noisy physical plant environment wherein the noise contribution to the signal can reasonably be expected to change at every moment should not be expected to exhibit stationarity. Although the stationarity of the data was not explicitly tested, the signal power level of several of the datasets used within this analysis was evaluated, and the results suggest that the assumption of stationarity should be avoided. Figure 3-57 presents the result of 4 million contiguous signal power measurements where each power measurement represents the average power within a 12 ms (overlapping) window. The signal power varies between a low of approximately 0.32 and a high of approximately 0.52. Figure 3-58 shows the same type of signal power estimate over the shorter interval of 1 s. If this power fluctuation were considered in isolation, it may seem irrelevant because the statistical properties of signal power may itself be unimportant. Combined with the reasonable assumption that power fluctuations may be an indicator of fluctuations of frequency ratio, these measurements assume greater significance. Such fluctuations of frequency ratio are described here.

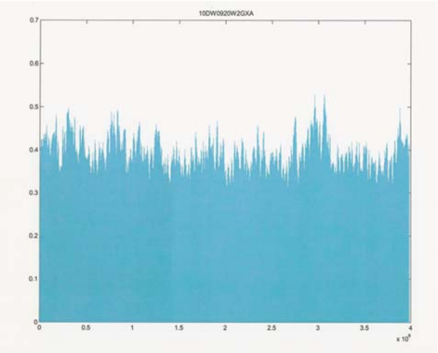

Figure 3-57 Signal power variation shown for an interval of 4 s. *The Y axis represents signal power in (AU), the X axis is shown having units of microseconds. This data results from a check valve with a disc wear of 2 mm at a test pressure of 9 bar.*

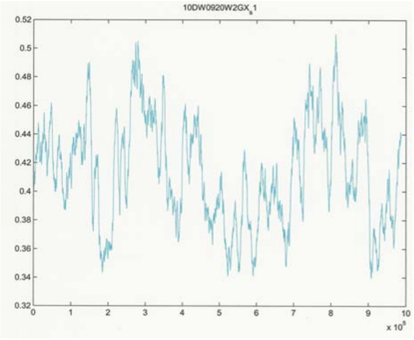

Figure 3-58 Signal power variation over an interval of 1 s. *These data were taken from the same test instance as the data used in Figure 3-57. The Y axis represents signal power in (AU), the X axis is shown having units of microseconds.*

The histogram in Figure 3-59 depicts a multi-modal distribution of signal power measurements typical of the September data collection. Pulsating additive noise having either multiple states or being generated by multiple means could be the source of these signal power fluctuations.

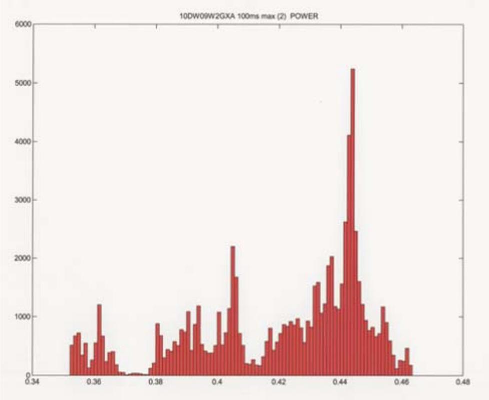

Figure 3-59 Histogram of signal power measurements showing a multi-modal distribution of the signal power levels. *These power measurements were taken from the same test instance as those data shown in Figure 3-57. The X axis is given in arbitrary units of signal power; the Y axis shows the number of occurrences.*

It is important to develop an understanding of the contribution of any additive noise combined with the fault signal to guide the selection of those data-derived features used to characterize the condition of the NPP component being monitored. Thus, it becomes important to understand whether these signal power variations represent changes of the actual physical mechanism producing the desired signal, or alternatively, if these fluctuations represent changes in the state of one or more noise generators creating additive noise.

Changes in the degree of the actual physical mechanism causing the desired signal may be likely to cause a smaller variation in the PSD of the signal than would additive noise. To investigate the influence of additive noise, the temporal power fluctuations of frequency-filtered data were evaluated for various frequency bands. Figure 3-60 shows the unfiltered signal power fluctuation over a 100 ms interval, and Figure 3-61, Figure 3-62, and Figure 3-63 show the power below 100 kHz, below 200 kHz, and above 470 kHz respectively, for the identical 10 ms interval. The dissimilarity of the curve shapes clearly indicates the presence of a dynamic PSD of the signal, of roughly 20% of the in-band energy.

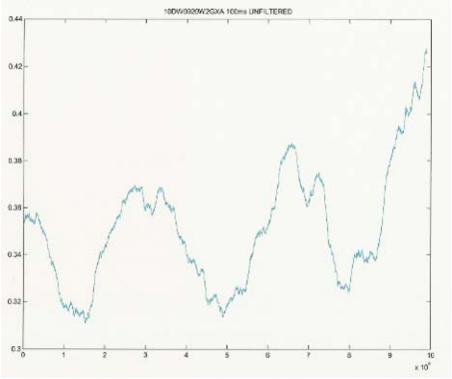

Figure 3-60 Signal power fluctuation of unfiltered signal for a 100 ms interval of data taken from the test instance of Figure 3-57. *The Y axis represents signal power in (AU), the X axis is shown having units of microseconds.*

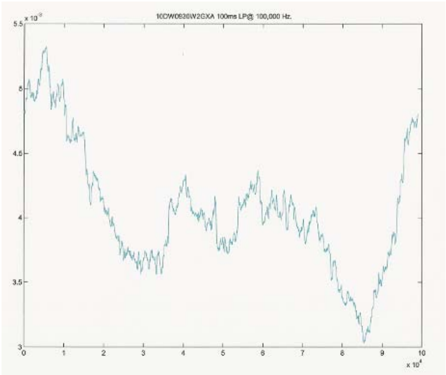

Figure 3-61 Signal power fluctuations of 100 kHz low-pass filtered data from the interval identical with the interval of Figure 3-60. *The Y axis represents signal power in (AU), the X axis is shown having units of microseconds. In this low frequency region, which is below the low frequency cutoff of the band-pass filter, the signal power is 100 times smaller than it is for those signals within the sensor band pass.*

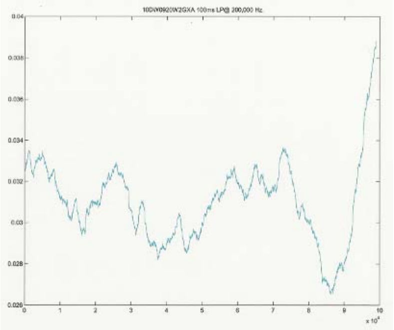

Figure 3-62 Signal power fluctuations of 200 kHz low-pass filtered data from the interval identical with the interval of Figure 3-60. *The Y axis represents signal power in (AU), the X axis is shown having units of microseconds.*

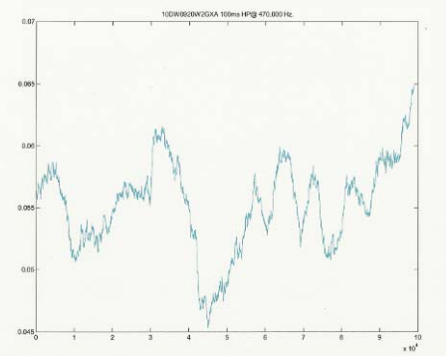

Figure 3-63 Signal power fluctuation of 470 kHz high-pass filtered data of the interval identical with the interval of Figure 3-60. *The Y axis represents signal power in (AU), the X axis is shown having units of microseconds.*

Evidence suggesting the presence of pulsating additive noise can also be seen in signal power estimates derived from other test instances. The signal power fluctuation occurring during a 100 ms interval during the 9 bar testing of simulated disc wear is shown in Figure 3-64. In this case, the power was estimated in a slightly different fashion, using a window width only 10% of the previous window width. This change has the effect of enhancing the detectability of any short-duration pulses present in the signal. Figure 3-64 clearly suggests the presence of quasi-periodic pulses of signal energy. The leakage flow of the test clapper-type check valve under reverse pressure cannot introduce a physical mechanism expected to create near-equal energy impulses (having a period of about 15 ms). Note that the pulse period is similar to the common power transmission frequencies (50 to 60 Hz) and that NPPs can be expected to include devices having operations that are synchronized to the power line frequency.

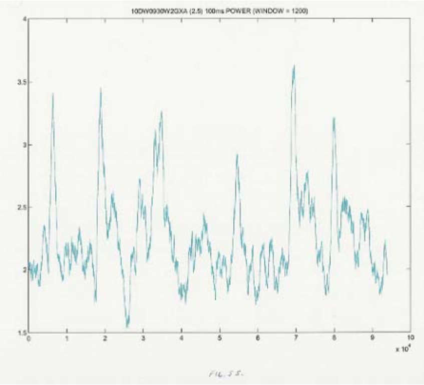

Figure 3-64 Quasi-periodic signal power fluctuations observed during the 9 bar testing of disc wear. *The signal power estimates each represents a 1.2 ms average, in contrast to the previous signal power estimates. The presence of these pulses suggests that the data includes some contribution from an additive noise source.*

The presence of check valve faults does create useable signal, which can partially mask the presence of underlying additive noise. Some of the test matrix involves the use of a normal, non-faulty check valve, and portions of the data collected during these test instances were evaluated for the presence of additive noise. Since fault conditions were not present and thus did not contribute any noise-masking signals of their own, additive noise was more easily identified. Figure 3-65 shows the presence of pulsed, periodic signals from two clearly differentiable pulse sources. Each source has a frequency of ~100 Hz, but both their pulse amplitudes and shapes were distinctly different. These different pulse trains appear to be asynchronous. Observe how the first pulse involves the combination of one of each of the pulse types as does the sixth pulse–the progressive "advancement" of the lower amplitude pulses is also clear during the interval between pulses one and six. This asynchronicity is a strong indication that two noise generators were involved.

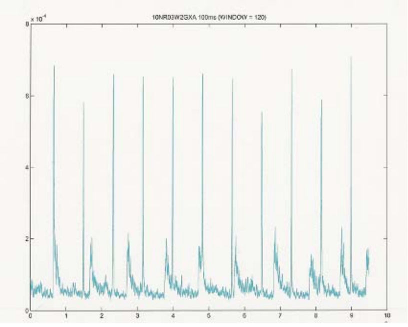

Figure 3-65 Signal power fluctuation showing two pulsed additive noise sources

Noise pulses can be clearly discerned in the time series data plotted directly if both the test instance and the timescale were selected appropriately. A test instance having both low pressure and low levels of desired signal works well, coupled with a timescale offering strong contrast between the narrow pulse duration and the approximately 10 ms pulse period. Figure 3-66 depicts a sub-second interval of time series data clearly showing additive noise pulses.

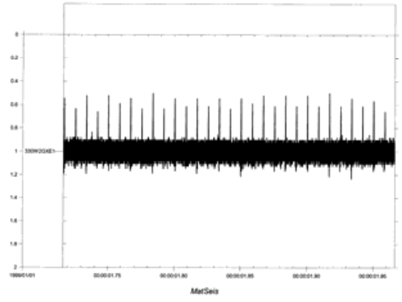

Figure 3-66 Unprocessed time series data scaled in time to clearly show additive noise pulses. *These data were collected with 1 mm disc wear at a pressure of 3 bar.*

Steady tonal noise is also present. Figure 3-67 shows a spectrogram of a 4 s interval of data created during the same test instance used for Figure 3-65. The W type sensor used in this test instance is specified to include a band-pass filter with a low frequency cutoff of 100 kHz. The spectrogram of Figure 3-67 depicts only the frequency range from 5 Hz to 1000 Hz, which is well below the 100 kHz cut-off frequency of the band-pass filter. This means that if these tonal noises were actually detected by the W sensor, the band-pass filter would have strongly attenuated them. This suggests that in this case, these tonal noise signals must be strong enough to remain easily detected after such attenuation.

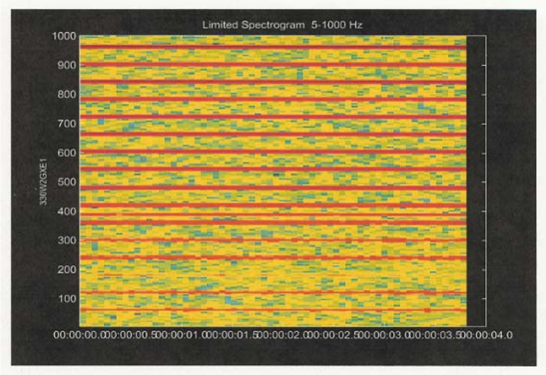

Figure 3-67 Spectrogram showing tonal noise. *The horizontal and vertical axes represent time and frequency, increasing upward, respectively.*

Throughout the following discussion of the analysis process, the datasets were assumed to include data that was a composite of both desired data and noise, with the noise generator(s) being all of those capable of being detected under the prevailing test condition. *No* noise-reduction steps were applied to these datasets.

3.4.3.3 Scope of analysis

The purpose of the previously described analysis was to identify constraints that may manifest from general characteristics that could impose upon analysis efforts to address specific questions relating to the in situ monitoring of NPP components:

- Are clear signals generated by fault conditions?
- Are the signals sufficient to convey information about changing conditions or degrees of the fault? If so, which signal features were best suited for this evaluation?
- Are the signals sufficient to convey information supporting reliable identification of which particular fault condition is occurring? If so, which signal features were best suited for this evaluation?
- Which “in-plant” factors have significant impact upon the signal component or the noise component of the data?
- What knowledge can be gained regarding the possibility of developing methods of performing classification of the failure mode independent of prior knowledge of those signals generated by the particular component/sensor being evaluated?
- Can those physical processes associated with particular fault conditions be linked to those signal features selected to address the previous questions?

3.4.3.4 Component failure evaluation

In the early stage of this condition monitoring assessment, the analysis process was primarily a search for signal features coupled with an evaluation of the relative merits of discovered features. One key measure of merit was contrast, which means that the signal feature present during the fault condition strongly differs from that during the non-fault condition. Various data transformations were applied in the search for features, and the resulting contrast differs. The information gained from the initial standard transformations guided the selection of those additional transformations explored.

Figure 3-68 shows time series data generated for the 9 mm disc wear at a test pressure of 9 bar, during the September data collection. There are 24 s of data were displayed in this figure. At this scale, it is impossible to discern details of the underlying waveform; however, the long-term envelope shape is also a relevant signal feature. The envelope shape does not indicate the occurrence of large-scale changes in the signal level during the 24 s interval. It also does not indicate baseline drift nor long-term (multiple-second) trends. No strong, intermittent noise sources were evident. These signal characteristics were typical of all W-type sensor data assessed during this analysis.

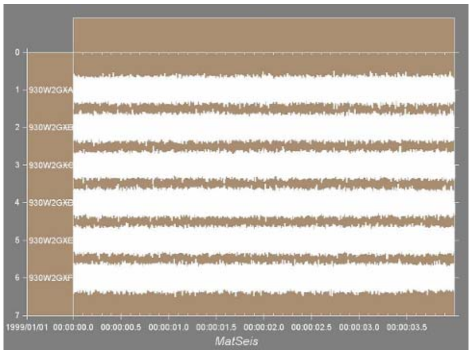

Figure 3-68 Time series data of 6 contiguous data intervals, each of 4 s length

PSD estimates based upon Fourier transformation were developed for several data segments including several test instances. The interaction between several parameters of FFT PSDs and these data were evaluated to approach an optimal application of this technique. In due course, a 200 Hz frequency bin size was selected, coupled with a Hanning window and 50% overlap. FFT PSDs incorporating multi-taper techniques to better control spectral leakage were not an effective improvement.

Figure 3-69 and Figure 3-70 show PSDs of 2 contiguous 500 ms data intervals; it can be seen from comparison that the gross humps and dips in signal level versus frequency contain clear information, but the level of grass riding upon these gross features obscures that information to be obtained from more narrow peaks and dips. As can be observed when contrasting Figure 3-71 with either

Figure 3-69 or Figure 3-70, FFT PSDs clearly differentiate between the disc wear type fault operating condition and the normal operating condition. Both the signal level and the frequency content of the signals strongly indicate the presence of the fault condition; this is an indication that signals sufficient for some degree of in situ condition monitoring of components may be achieved.

Further FFT PSD evaluations of data generated during test instances incorporating different pressures and different degrees of disc wear were performed. In general, the degree of FFT PSD difference occurring between test instances of the same fault condition but differing degrees of fault was judged sub-optimal. Although close inspection of FFT PSDs from, for example, low-pressure testing of both the 1 mm and 2 mm of disc wear yields some differentiating signal features, the differences were not strong enough to provide contrast sufficient to unmistakably characterize the fault degree without further signal processing. Figure 3-72 depicts the FFT PSD of the test instance of 9 bar pressure and 2 mm of disc wear. Comparing Figure 3-72 with

Figure 3-69 and Figure 3-70, the similarities were easy to spot. The band-pass filter cutoff frequency is clear; the humps at frequencies below 100 kHz were similar; both the peak just below 100 kHz and the slope from that peak to the dip at 150 kHz were similar; the humps at 220 kHz, 300 kHz, and 470 kHz were also similar. Several other similarities can also be noted from cursory examination. Differences can also be observed; Figure 3-72 includes a double peak within the range of 450 to 500 kHz whereas the lesser degree of disc wear generates only a single peak in this region. The level of grass in that region between 300 and 400 kHz has roughly doubled; and near 150 kHz, a discernable hump is added.

Although a trained operator *may* be able to judge between component conditions using such FFT PSDs, given the degree of differences, the degree of similarities and the degree of noise, a reliable computer-based algorithm for evaluation of such FFT PSDs is likely to be difficult to create. The key result is that although both the levels and the frequency content of signals varies strongly between the normal condition and the fault conditions, those differences created by differing failure modes and fault degrees were far smaller. These smaller differences were also likely to be masked by changes to the noise component of the signal introduced by other sources within the plant. Using Fourier techniques to detect the presence of a fault is likely to be effective. However, using this technique to classify the fault type and to determine the degree of fault is likely to be frustrating. One possible solution to this problem would be to apply further signal processing methods, such as filtering the data using a variety of filters, before performing the FFT PSD upon each filtered version of the data. Three or more filters may be required to significantly heighten the contrast between FFT PSDs, allowing improved differentiation between these two degrees of fault.

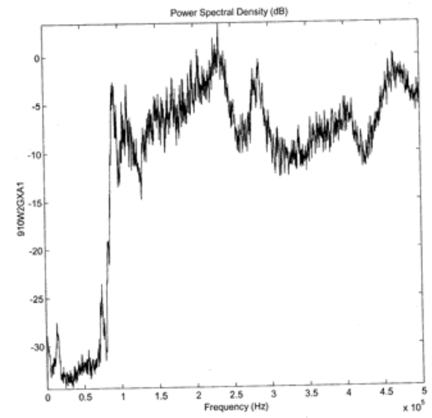

Figure 3-69 **FFT-based PSD estimate of a 500 ms interval of 9 bar, smallest degree disc wear (1 mm)**

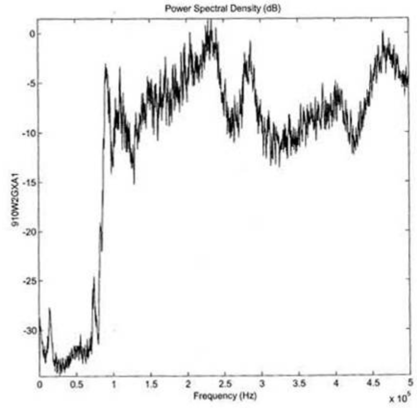

Figure 3-70 **FFT-based PSD estimate of a 500 ms interval of 9 bar, with 1 mm of disc wear.** *This data interval immediately follows the data interval evaluated in the estimate shown in Figure 3-69. Although the larger features of the PSD curve were retained from one interval to the next, the smaller spike-like grass features were dissimilar.*

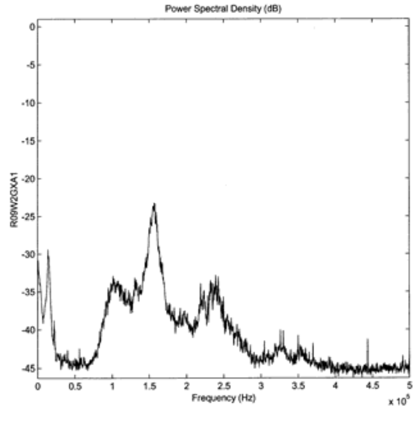

Figure 3-71 **FFT-based PSD estimate of a 500 ms interval of 9 bar, normal operation of a check valve**

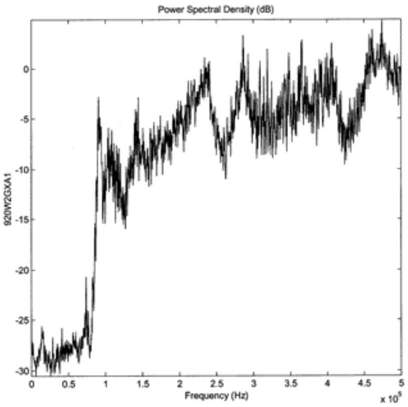

Figure 3-72 FFT-based PSD of 2 mm of disc wear. *The difficulties associated with using an FFT-based PSD to discriminate between degrees of valve fault become evident by considering that Figure 3-69 and Figure 3-70 need comparison and the result is that they represent the same condition, and Figure 3-70 and Figure 3-72 need comparison and the result is that they represent different conditions.*

Although Fourier-based PSDs can be used to detect the presence of a fault condition, such techniques may not be necessary for simply detecting the presence of a fault. Data generated during the September data collection using the W-type sensor show strong variation in signal level when a fault is present. Perhaps a fault can be adequately detected simply from a determination that the signal has become stronger. Figure 3-73 shows the influence of the degree of the modeled fault condition (corresponding to the width of a slit machined into the clapper) upon the signal level. Each RMS level estimate was developed from a data segment having 4 million data points. It is interesting to note the very good linear fit possible if those points corresponding to the 2 mm slit width were deleted. Although signal level evaluation may make an important contribution to future systems performing condition monitoring, this metric is unlikely to be sufficient for classifying among different types of fault conditions.

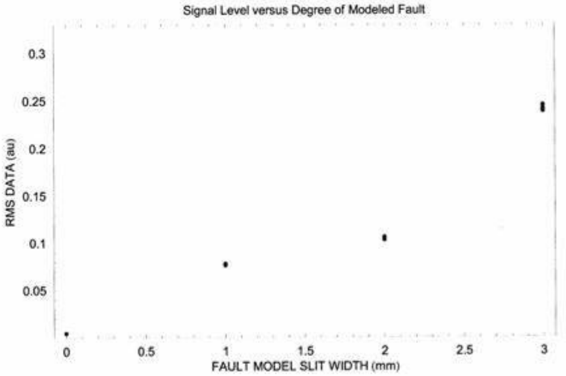

Figure 3-73 Signal level versus degree of fault. *The RMS value of the signal level was determined for four or more 4 s data intervals during each of the fault conditions shown here. Generally, within this test range, the signal level increases with the leakage flow.*

3.4.3.5 Rescaled range (R/S) analysis

Rescaled range (R/S) analysis lacks the underlying expectation of an harmonic energy content common to Fourier techniques, and may be a more theoretically sound technique for evaluating check valve faults because no physical mechanism capable of producing significant harmonic energy has been associated with these check valve faults. R/S analysis was originally developed to characterize changes in the flow of the Nile River [iv], and has been used to evaluate the "whiteness" of suspected white Gaussian noise, and to determine fractal dimension. A description of R/S analysis is in [v]. The Hurst exponent (HE) is a numeric characterization of the persistence or anti-persistence data, and R/S analysis is one method used to determine its value [vi].

The model of the disc wear fault involves milling a slit into an otherwise fully functional check valve clapper. During these tests, the fluid pressure causes a flow from the high-pressure region of the piping through the opening of the fault and into the low- pressure portion of the piping. The entrance area and volume of the fault were far less than either the area or the volume of the pressurized piping. Transitions from a large volume flow into a smaller volume flow were known to generate turbulence; such flow transitions seem to be required by the nature of both the disc wear fault and the foreign object fault. Although turbulence measurements have not been performed in association with these data collections (such measurements were also difficult to accomplish), it is reasonable to expect turbulence to be generated by these fault conditions.

Although flow transitions from a large volume into a small volume are known to generate turbulence, the reverse transitions, those from a small flow volume into a larger flow volume are known to produce cavitation bubbles [vii]. Bubbles produced in this way were likely to be transient. Possibly, both a turbulence-generated signal component and a cavitation generated signal component were present in the composite signal.

Figure 3-74 and Figure 3-75 show R/S curves developed from R/S analysis of data resulting from normal valve operation, and of data resulting from faulty valve operation during the September data collection. The slope of the curve reflects the value of the HE.

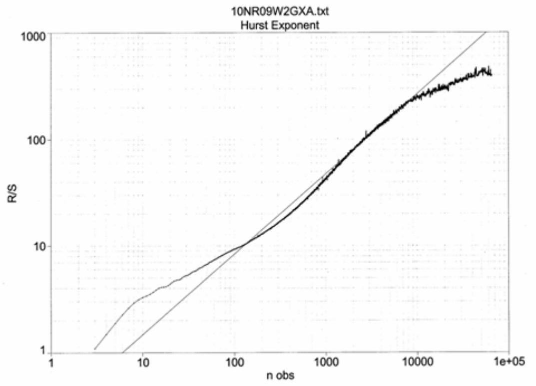

Figure 3-74 R/S analysis plot derived from data with normal operation

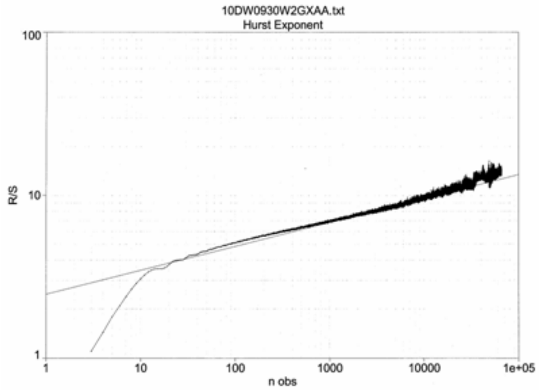

Figure 3-75 R/S analysis plot of 3 mm disc wear measured at 9 bar

R/S analysis was performed for many data instances of normal operation, of disc wear fault operation, and of foreign object fault operation. The R/S results from nominally similar conditions occurring during the September data collection and later during the March data collection were compared; similar results were obtained in each case.

R/S evaluation of the data developed by normally operating valves for a range of operating pressures is shown in Figure 3-76. Only the wideband AE sensor results were shown because the reduced bandwidth of the narrowband AE sensors [2] fails to respond to the high frequency signals developed by turbulence, therefore generating skewed results. Increases in the operating pressure produce corresponding increases in the flow rate. In many operating regimes, increased flow would generate a corresponding increase in turbulence; more turbulence would result in more turbulent signal, increasing the ratio of turbulent signal to background noise. Such an increasing ratio would reduce the HE value, leading to an inverse relationship between pressure and HE value, as shown in Figure 3-76.

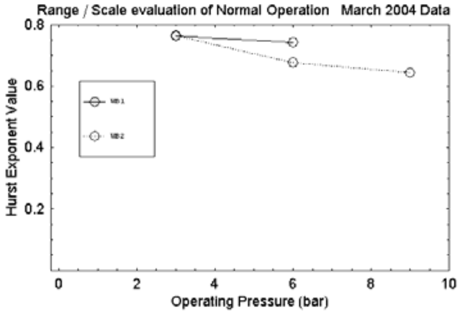

Figure 3-76 Piece-wise linear interpolation of HE value versus operating pressure for the normal valve condition. *Each of the five points represents the median value of a set of five measurements of equal data interval at the particular operating condition or test instance.*

R/S analysis of wideband AE sensors reveals an inverse relationship between the degree of disc wear fault and HE value, as shown in Figure 3-77 and Figure 3-78. This is consistent with a model wherein leakage flow through a worn disc wear becomes both more turbulent and generates more cavitation bubbles than does the normal flow. The pressure increase from 3 bar to 9 bar also causes an added decrease in HE value. This would be consistent with increased flow inducing added turbulence noise. It is interesting to note that HE values below approximately 0.15 do not occur within the 9 bar data evaluation, so the slope of the 9 bar curve within the interval from 1 mm to 3 mm disc wear differs from the slope of the corresponding part of the 3 bar curve. This characteristic remains anomalous.

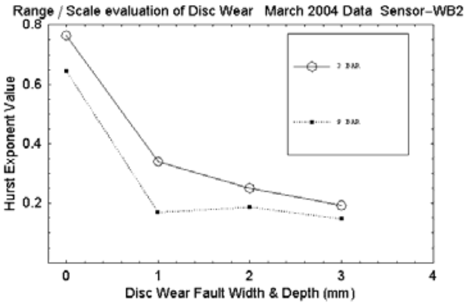

Figure 3-77 Piece-wise linear interpolation of HE value versus fault degree for the disc wear fault condition, with operating pressure as a parameter. *Each of the eight points represents the median value of a set of five measurements of equal data interval at the particular operating condition or test instance.*

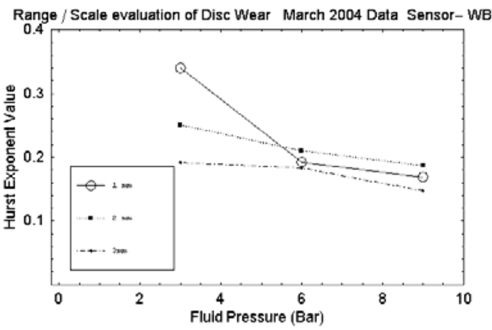

Figure 3-78 Piece-wise linear interpolation of HE value versus operating pressure for the disc wear fault condition, with fault degree as a parameter. *Each of the nine points represents the median value of a set of five measurements of equal data interval at the particular operating condition or test instance.*

R/S analysis of the foreign object fault data generated during the March and April data collections is not reported. In the majority of cases, sub-optimal matching of the signal level and the input level of the DAS corrupted the data. Although some datasets were not corrupt, it was not possible to determine HE values over the full range of pressures, or over the full range of fault degrees. The test instances of low pressure and small fault degree did generate usable data, and these data for the foreign object fault do follow the pattern described previously for the disc wear fault because the HE values for the fault condition were far lower than the HE values for the normal operating condition.

R/S analysis has been applied to some of those datasets generated at PSU in May. The test apparatus in PSU differs from that used in Korea as the configuration, pump equipment, piping size, the valve size, the sensor types, and the hardware models of fault conditions were different. R/S analysis of data for normally operating valves shows a decrease of HE value with increasing pressure. Further, the HE values for the largest degree of disc wear fault also decrease with increasing pressure, and were very similar to the HE values for normal operation, making the HE value a poor indicator of a valve fault within the PSU test bed. Figure 3-79 shows an R/S result from the May tests; comparison with Figure 3-74 and Figure 3-75 indicates the dissimilarity between results obtained from differing test beds.

Several possible factors could explain the difference between the R/S results at PSU and KAERI. First, the sensor used for the PSU data collection is an accelerometer having a much-reduced bandwidth in comparison to the AE sensors used for the KAERI data collections. *None* of the signal detected by the wideband AE sensors would be detected by those accelerometers used during the PSU test. In addition, the majority of in-plant noise sources should be expected to generate noise energy within the bandwidth of the accelerometer, but the turbulence and cavitation generated signals developed by the fault condition and sensed by the wideband AE sensor occur largely beyond the sensitivity range of the PSU accelerometer. The ratio of noise energy to fault induced signal energy is expected to be greater for sensors having the bandwidth used at PSU, thus it is reasonable for higher HE values to be obtained, reflecting the presence of the predominantly persistent noise energy. In addition, some data from the PSU test also contain long-term trends. Figure 3-80 shows a time series envelope from the PSU test in May. This time series clearly shows near-sub-Hertz oscillatory behavior. Several ½ s monotonic trends in this short data interval were apparent; such trends were a classic example of persistence in datasets. The presence of these long-term trends in data level would significantly increase the HE value.

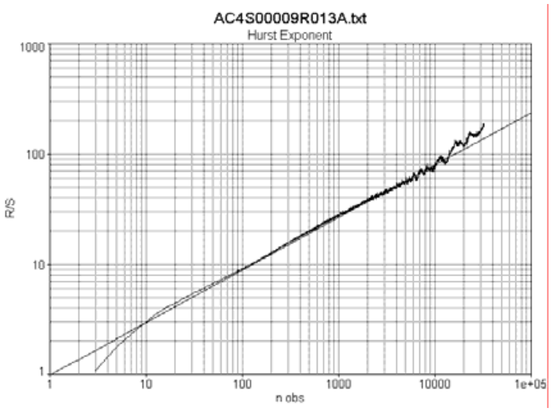

Figure 3-79 R/S analysis plot of the largest degree of disc scratch measured at a test pressure of 9 bar within the PSU test bed

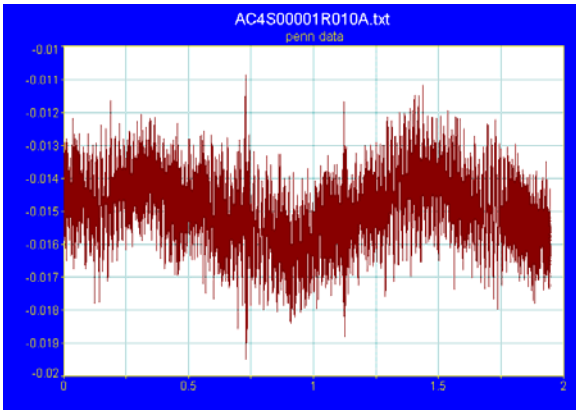

Figure 3-80 Time series representation of a data interval during low pressure (1 bar) normal operation at PSU. *Note the presence of long term (sub-Hertz) trends in the data.*

3.4.3.6 Eigen pseudo-spectral analysis

No analytical techniques described previously were expected to create information sufficient for reliable differentiation of fault degree and for easy automated determination of the fault degree. This situation prompts the investigation of additional analytical tools capable of producing information from more subtle variations within the data. Whereas multiple check valve failure modes produce a similar physical result (a leak) and some manifestation of this physical condition is being monitored, it is reasonable to expect some difficulties in differentiating between failure modes. It can also be assumed that the slight differentiating characteristics of these similar failure modes may produce a slight variation in the frequency content of the signal. Figure 3-70 and Figure 3-72 show that the variation of frequency content between those signals generated by an incremental degree of disc wear were indeed slight, compared to the total energy content of the signal. For the purpose of classification, the slight variation of frequency content contrasting the fault degree can be the desired signal and the large balance of the energy content within the data can be considered the noise; therefore, analytical techniques less influenced by signal-to-noise ratio (SNR) were possibly promising for use in fault classification.

Many current techniques apply Eigen decomposition methods to create a pseudo-spectrum; such Eigen pseudo spectral techniques (EPST) can be less influenced by SNR [viii]. EPST have two additional desirable characteristics: a response to the degree of variance of a signal regardless of the degree of harmonic content within the signal, and a response to low power components of the signal. EPST separate the eigenspace of the covariance matrix of the signal into orthogonal subspaces–a signal subspace and a noise subspace. Standard techniques were available for identifying the optimal separation point between these subspaces [ix].

Because the problem presented by in situ condition monitoring of check valves is different, standard techniques were not used to establish the separation point between the signal and noise subspaces during this analysis process. Instead, the magnitude of the eigenvectors of a trial signal (normal valve at 9 bar) were evaluated by inspection; 40 eigenvectors were judged to be a useful compromise between frequency resolution and computational demand, and both 6 and 13 eigenvectors were initially selected to define the size of the signal subspace. Subsequently, 6 signal eigenvectors were judged to be more optimal than 13, because the desired contrast was achieved using 6 and the spectral repeatability using 6 eigenvectors exceeded the repeatability when using 13 because the noise subspace is represented uniformly as one level. This procedure of using 40 eigenvectors and assigning 6 of them as the signal subspace was followed throughout the evaluation of the September 2003, and the March, April, and May 2004 data.

The particular EPST selected for use was Multiple Signal Classification (MUSIC) [x] due to its use of the noise subspace, and its uniform weighting of this subspace to determine the signal spectrum. The performance was better than expected. The MUSIC algorithm was applied over one hundred times to multiple disc wear test instances with a common test pressure of 9 bar from the September data collection. The data intervals evaluated were uniformly 64 ms long. Several (4 to 6) different intervals were evaluated for each of the four test conditions (normal operation, and disc wears of 1 mm, 2 mm, and 3 mm depth), and these different intervals were separated in time by 4 s. In this way, the combined evaluation sampled 16 to 24 s of data for each test condition. The repeatability of the MUSIC results was promising. Figure 3-80 (a) to (d) depicts typical pseudo-spectral results for the four test conditions. One scale is common to these four figures. The results shown in the figures were typical of 4 of 4, 5 of 5, 3 of 4, and 4 of 6 trials, respectively. The degree of repeatability exceeded expectation. Subsequently, this technique was applied to disc wear data from the March and April data collections and similar repeatability resulted. The effectiveness of MUSIC for identifying changes of the degree of foreign object faults could not be assessed because of the corrupted condition of most of the foreign object data files.

The variation of the pseudo spectra resulting from the differing degrees of disc wear is very encouraging. The spectral levels of Figure 3-81 (a) to (d) can easily be differentiated either by eye or by algorithm. The pseudo-spectra shown in these figures represent four differing degrees of the same valve fault condition. Comparing

Figure 3-69, Figure 3-70, and Figure 3-72 with Figure 3-81 (a) to (d) demonstrates that a greater degree of contrast has been achieved through use of the MUSIC algorithm.

The disc wear MUSIC results from the September test were compared to those from the April test. As previously mentioned, the April test was *not* a duplication of the September test because the apparatus was modified. However, both the operating pressures and valve fault conditions were nominally equivalent, therefore this comparison could be considered similar to the comparison of two similar valves located in two dissimilar situations within the same power generation facility. This comparison yielded two important results:

- The capability of MUSIC to respond to changes in fault degree was remarkably good in both test instances, and the repeatability of MUSIC when tested against different data intervals representative of the same valve fault condition at different times was very high for both the September and April datasets.
- The spectra were remarkably different, indicating that MUSIC may be a useful tool for tracking changes of the severity of a faulty valve, but particular observations may be only useful locally and not be applicable to every similar valve.

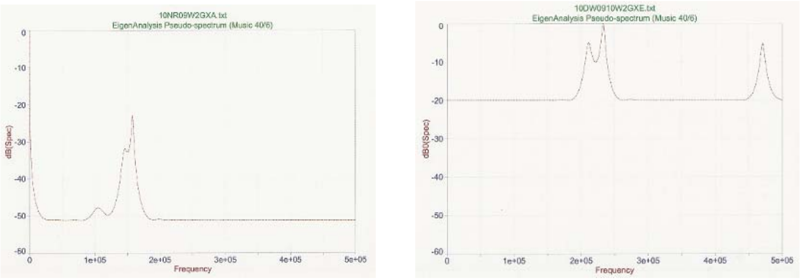

(a) Normal configuration (b) Disc wear of 1 mm

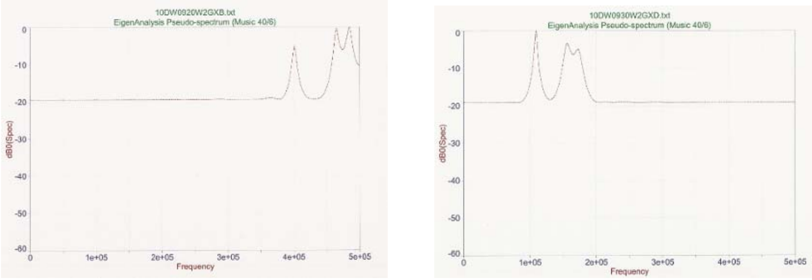

(c) Disc wear of 2 mm (d) Disc wear of 3 mm

Figure 3-81 MUSIC pseudo spectrum of check valve at 9 bar pressure

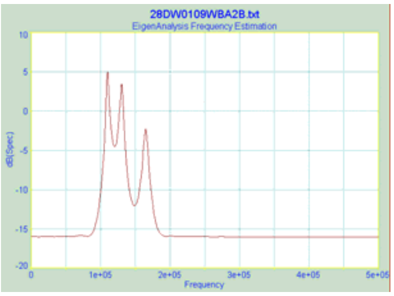

Figure 3-82 MUSIC pseudo spectrum of the smallest degree of disc wear during operation at 9 bar pressure, during the April 2004 data collection

Data generated by a disc wear fault condition was also collected using accelerometers at PSU in May. Since the frequency ranges sensed by accelerometers and AE device do not significantly overlap, the resulting MUSIC pseudo-spectra will also differ. Clear differences between the normal operating condition and the fault condition were observed. Figure 3-83 (a) to (c) show the MUSIC results for 3 mm disc wear at three operating pressures; the degree of contrast from the May test is similar to those observed in KAERI tests. This suggests that MUSIC may be applicable to valve condition monitoring.

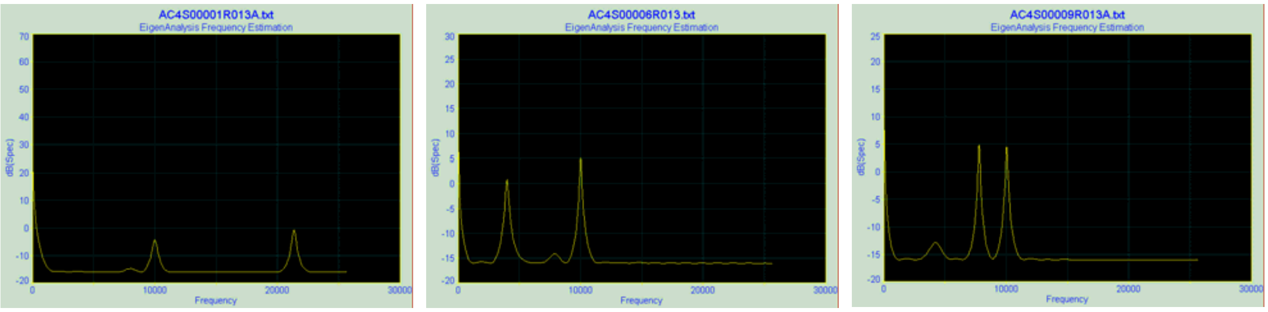

(a) 1 bar pressure (b) 6 bar pressure (c) 9 bar pressure

Figure 3-83 MUSIC pseudo spectrum of disc wear of 3 mm during the May 2004 data collection at PSU

3.4.4 Conclusion

The key finding is that there were useful signals and their implementation must be developed successively. A physical model of the signal sources, combined with an increased understanding of the range of probable noise sources, will aid such development. Condition prognosis, which is processed through use of intelligently fused, multiple outcomes of dissimilar analysis techniques, will find widespread application.

Clear signals from faulty check valves were found and changes of the degree of fault were detected. The ability to differentiate between differing types of failure may be realizable.

Eight valuable results follow from the data analysis:

Problem Decomposition. The in situ check valve condition monitoring problem can be addressed in six areas including:

- The presence of a valve fault is expected to be detectable using two different types of sensors (accelerometer, AE), combined with one of several analysis techniques.
- The stability of fault is expected to be detectable using accelerometers and AE, combined with several analysis techniques. A fusion of results from multiple analysis techniques is anticipated to provide information superior to the information derived from any single technique. Historical data is required for this detection.
- Identification of the degree of any valve fault remains questionable.
- The ability to identify the nature of a particular valve fault type remains uncertain.
- The ability to identify the leakage flow through a particular valve fault remains uncertain.
- The identification of any necessity to acquire historical performance data on check valve
- The ability to identify the presence of a particular valve fault without any historical performance data may be limited to those cases of faults causing a “medium size” leakage flow. Although very small faults were not evaluated in this project, it is reasonable to assume that faults causing leakage rates below some local threshold value will remain undetectable. Beyond simple fault detection, all the other condition monitoring issues separately listed previously were expected to benefit from the availability of historical performance data.

Sensor Comparison. The data from three sensor types were evaluated with some degree of detail. The wideband AE sensors seem to be capable of yielding the most information, and these sensors may most closely match the sensing requirements of underlying physical phenomena. The narrow band accelerometers seem to have a bandwidth and a resonance that inhibits their capability to contribute information. Although the wideband AE sensors and the accelerometers were never deployed together, evaluation of their separately observed performances leads to the expectation that accelerometers lack the bandwidth needed to reliably respond to the high-frequency signals generated by valve faults. If so, accelerometers would produce an unfavorable SNR in comparison with wideband AE sensors.

Analysis Technique Evaluation. Six analytical techniques resulted in a degree of useful information when applied to the check valve fault data. These are average signal level, Fourier spectra, time-dependent signal power, signal power histogram, range-scale analysis, and Eigen decomposition pseudo-spectra. The average signal level may be very useful for fault detection, but is not, by itself, expected to contribute strongly to determining either the leakage flow or identifying the nature of the fault. Fourier spectra are likewise useful for determining the presence of a fault condition; however, this technique seems sub-optimal for generating the other desired information: change detection, leakage flow, fault type, and fault degree. Time-dependent signal power is a useful technique for learning about the noise contribution to the data and may be useful for identifying constraints that should be applied in particular in-plant situations where strong, discontinuous noise sources occur.

Since the signal power histogram has the same value as time-dependent signal power evaluation, the histogram is also a useful technique for this purpose.

Range-scale analysis is a level-independent technique capable of producing results characterized by a single, slope-related, numeric value to represent the general character of the underlying PSD of the data. When coupled with the appropriate sensor, this analysis technique can differentiate the presence of a valve fault from the presence of previously unobserved noise. Eigen decomposition pseudo-spectra, as exemplified by the particular MUSIC algorithm used herein is expected to contribute to change detection and possibly, when combined with other analytical results, to identifying fault degree and fault type.

Possible Check Valve Monitoring Process. The analysis of check valve data described herein resulted in identifying a possible initial check valve monitoring procedure. This procedure involves installing a wide-band AE sensor near the test valve's flapper and either an AE sensor or other sensor (such as an accelerometer) capable of responding to a relative flow rate in an upstream location. Signal level, HE, and MUSIC data collected from periodic monitoring of the flapper sensor signal would be referenced to the relative flow rate determined by the upstream sensor. A signal level increase matched to a coincident decrease in HE (both relative to previous results at a comparable flow rate) indicates the presence of a valve fault.

Effective determination of the check valve fault condition can be enhanced by the intelligent fusion of the three separate analysis results. The MUSIC analysis provides sensitivity to changes in fault degree and to other changes of condition, such as operating pressure. The signal power analysis provides sensitivity to the presence of a leak. However, the signal power analysis based on a single sensor is unlikely to distinguish between an increase in the size of the leakage pathway and an increase in operating pressure. R/S analysis adds a degree of discrimination between increases of in situ noise and the occurrence of a faulty valve. The intelligent fusion of separate analysis results can provide a useful initial monitoring capability.

Hypothetical Phenomenological Model. The condition monitoring data comprises two components–signal and noise. The signal is that component of the data that only occurs when there is a valve fault condition and the noise is that component of the data that occurs when there is not. Valve faults introduce leakage flow; the physical dimensions of the leakage flow path influence the degree of turbulence and cavitation of the leakage flow. These conditions of turbulence and/or of cavitation determine the characteristics of the signal, which were non-tonal, somewhat broadband, and of generally higher frequency than the frequency of the majority of the noise.

When no fault or leak is present and the signal level is zero, only noise remains. In this case, the "signal" power of the data is actually the noise power and can be considered the baseline for all future signal power evaluations. A relatively higher value HE value is determined by the characteristics of the noise. The MUSIC result will represent the pseudo-spectra of the noise, and the frequency of tonal noises, the frequency response of the sensor, and the relative strengths of those various tonal noises will influence this result. When a fault occurs, leakage flow develops; fluid properties, pressure, and geometry of the leakage path influence the character of the leakage signals and these leakage signals combine with the preexisting noise. Leakage conditions above a threshold value would generate detectable changes. A wide range of leakage conditions (including those conditions evaluated during this work) would generate easily detectable signals.

Monitoring Without Prior Knowledge. Condition monitoring of clapper-type check valves without any requirement to obtain data from the particular in situ valve before failure would be highly desirable because obtaining and archiving such data is costly. Analytical results to date suggest such monitoring without prior knowledge may be applicable to a *limited range* of valve fault conditions if the fault detection process provides a detection outcome based upon the fusion of the results of multiple analytical techniques.

Status of Analytical Techniques. The description of the present status of various analytical techniques is based upon observation of modeled valve faults evaluated within multiple test beds. If the modeled valve faults fail to accurately represent actual valve faults, or if the test bed conditions fail to accurately represent in-plant conditions (or both), the performance of these analytical techniques may deviate from the anticipated performance.

Future Work. The results of the check valve condition monitoring data analysis effort suggest two future activities: validation of the hypothetical model and extension of the investigative dataset. Careful data collection should be used to validate the hypothetical model using data from both wideband AE sensors and co-located accelerometers affixed to a clapper-type check valve placed in an experimental test bed. The experimental process could be extended and enhanced by additional analysis of that same dataset to provide a record of the level, HE, MUSIC results for each of the various operating conditions and fault conditions, and sensor types.

The second future activity is the creation and subsequent analysis of a far larger dataset using multiple check valves of different sizes operating at different pressures in a wide variety of in situ conditions encompassing a wide range of plant-induced noise conditions. These valves should be instrumented with both wideband AE sensors and accelerometers, and locations upstream of each valve should be instrumented with low-cost sensors developing a signal proportional to flow rate. Multiple analytical techniques, including all those used in the previously described work, should be applied to this larger dataset. This would provide evaluation of the proposed monitoring technique and provide a dataset probably sufficient to develop an improved, robust monitoring technique based upon the fusion of multiple analysis results.

3.5 Task 1.5: signal data processing analyses for noise filtering and pattern recognition

Performed by SNL and KAERI (PSU and CNU)

The research goal of the project has been focused on developing a method to distinguish defect signals associated with disc wear and foreign object in check valves. This task is geared toward developing the capability of the artificial neural network (ANN) technique to provide diagnostic information useful in determining check valve aging and degradation, check valve failures and undesirable operating modes. The processing analysis starts with the data associated with the normal configuration at different flow rates to provide the baseline vibration patterns. Similar analyses were performed for each chosen abnormal configuration at different flow rates. The vibration patterns from these analyses will be baseline adjusted with those associated with normal configuration to establish a unique set of vibration patterns characteristic of the chosen abnormal configuration. This procedure provides the basic scheme of noise filtering with the quality of filtered vibration patterns, depending on the sensors and the quality of signal data themselves.

3.5.1 Sensor signal characteristics

The filters were designed to screen background noise components relevant to each sensor characteristic. FFT provides a technique to analyze the frequency characteristics. The sampling rates for AE sensor and accelerometer were 1 MHz and 50 kHz, respectively. Figure 3-84 shows the acquired AE sensor signal corresponding to two test conditions of non-leak and leak cases. Leak may occur due to foreign object interference and/or disc wear. From this figure, the useful frequency band lies between 50 kHz and 450 kHz, while the background noise components occupy the low frequency portion up to 25 kHz. In the case of accelerometer, the passband ranges from 0.5 kHz to 24 kHz. The details of background noise analysis are discussed in Appendix A, Section V.

3.5.2 Filter design and noise filtering result

The design specifications of filters were derived from the frequency characteristics of each sensor, and four band-pass filters were designed. The Butterworth filter has flat magnitude response in both passband and stopband, although the filter order is relatively large. The other Chebyshev-like filters have ripple in either passband or stopband, and both bands. Table 3-20 summarizes filter order in the frequency domain.

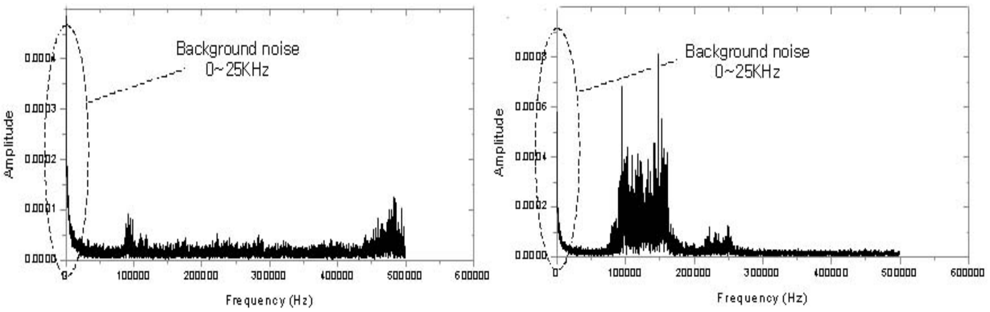

a) Non-leak (normal) **b) Leak (foreign object case)**

Figure 3-84 Acquired AE signals

Table 3-20 Filter order in the frequency domain

	Butterworth	Chebyshev-I	Chebyshev-II	Elliptic
Number of filters order	15	6	6	4

Figure 3-85 displays the noise filtering result when the Butterworth filter is applied to the raw signal of the AE sensor. Comparing these figures, the unwanted noise components in the stopband cleared out. Table 3-21 shows the comparison of the SNR for each filter. With respect to SNR and complexity, the Butterworth filter is slightly better, and so recommendable.

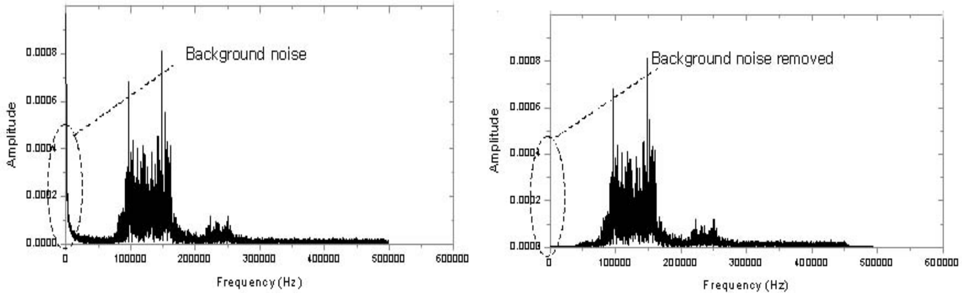

(a) Raw **(b) Filtered**

Figure 3-85 Noise filtering result

Table 3-21 Filter performance (SNR)

	Butterworth	Chebyshev-I	Chebyshev-II	Elliptic
SNR (dB)	41.1170	41.0249	32.1947	31.0939

The details of the applied DSP techniques for design of noise filtering are discussed in Appendix A, Section VI.

3.5.3 Data processing analysis of experimental signals

The details of the experimental data processing techniques are discussed in Appendix A, Section VII.

3.5.3.1 AE data analysis

The analyzed AE sensor signals are summarized in Appendix A, Section VII. The applicability of using AE sensor to monitor check valve vibration is illustrated in Figure 3-86, which shows the AE frequency spectra from a normal valve and degraded valves with disc wear and foreign object. Significant differences in leak signals were found in these three cases. There is a frequency peak of 265 kHz in normal disc. There were three different frequency peaks of 100 kHz, 280 kHz, and 510 kHz in disc wear case, and two frequency peaks of 100 kHz, and 510 kHz in foreign object case.

Although the effectiveness of the procedure for interpreting leak signals from the field has not been determined, the results of characterization of different leak sources and their behavior such as disc wear and foreign object have been demonstrated successful. It is certainly beneficial to be able to compare data from wide and narrow band frequencies in optimizing sensor position and frequency for leak detection in the field. In addition, AE RMS value may provide quantitative information, particularly at low flow rate, where the flow may be relatively unstable.

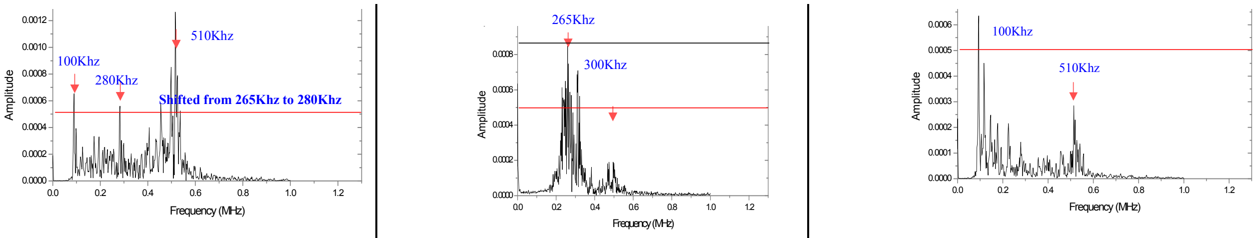

(a) Normal configuration

(b) Degraded state with disc wear

(c) Degraded state with foreign object

Figure 3-86 Spectral analysis results of AE signals

3.5.4 AE signal characteristics

Figure 3-87 shows the results between AE RMS and leak rate obtained from foreign object failure mode of the check valve data recorded September 2003. The leakage flow rate in the foreign object failure tests could not be increased about 300 liter/m, because 1 in. pipe for leakage line was very small. To solve this problem, the 1 in. piping was changed to 4 in. piping.

Figure 3-88 shows the results of actual measurement for comparing the intensity of AE RMS value by a leak in the disc wear and foreign object failure modes. As shown in Figure 3-88, AE RMS increases with an increase in the pressure (or rpm) in the same leak size. It is desirable to obtain some estimates of the leak flow rate, but this information is difficult to obtain directly from acoustic intensity data because the amplitude of the acoustic signal varies with geometry and temperature for a given flow rate. Thus, other characteristics of the signals must be examined. One possible way is to monitor the variation in the RMS value with time. Figure 3-89 shows the results between AE RMS value and flow rate obtained from the disc wear and foreign object failure modes. The leak flow rates were measured by means of an ultrasonic flow meter. As shown in Figure 3-89 (a) and (b), a linear relationship is observed. The analyses of the results suggest that acoustic signals depend on leak rate.

The frequency spectrum of the check valve leakage is illustrated in Figure 3-90, which shows the frequency spectra of leak signals at 150 kHz sensor. It can be seen that the frequency range of leak signals between disc wear and foreign object were significantly different. However, the frequency spectrum content on AE signals due to leaks indicates no significant changes with the leak rate and pressure in the same source. That is, it is significant that for the three spectra results obtained from disc wear shown in Figure 3-90 (a), all have the same general shapes, whereas the spectra results (Figure 3-90 (b)) obtained from foreign object have different shaped spectra compared with disc wear failure mode. These observations imply that the frequency spectrum profile of the disc wear and foreign object failure modes do not depend on the leak rate and pressure. It was found that signal generated by the turbulence in a disc wear failure mode is 150 to 250 kHz and in a foreign object failure mode is 100 to 150 kHz.

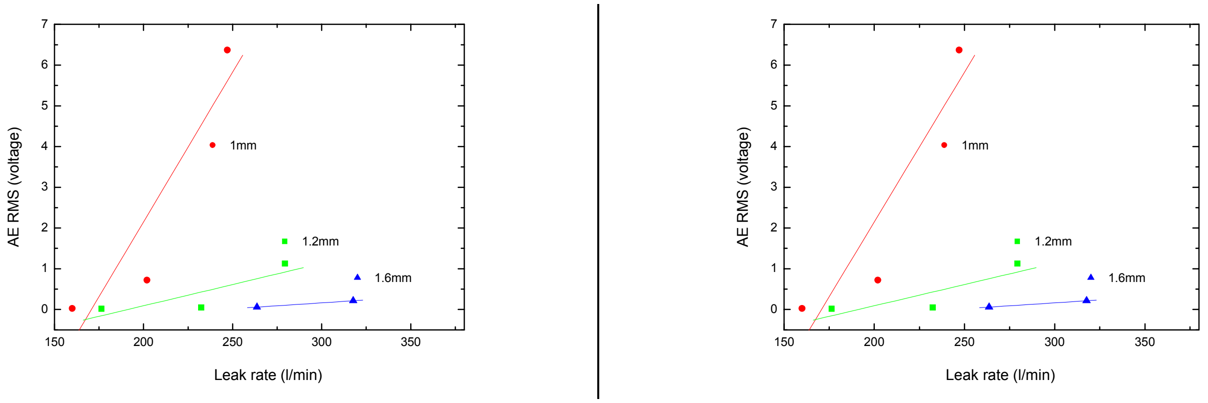

Figure 3-87 AE RMS value versus leak rate from foreign object failure mode (September 2003)

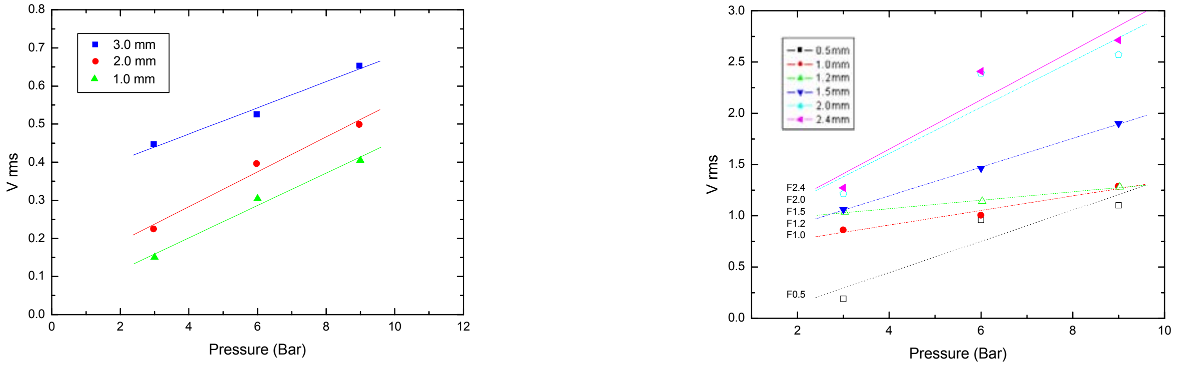

(a) disc wear (b) foreign object

Figure 3-88 AE RMS data from disc wear and foreign object failure modes (March 2004)

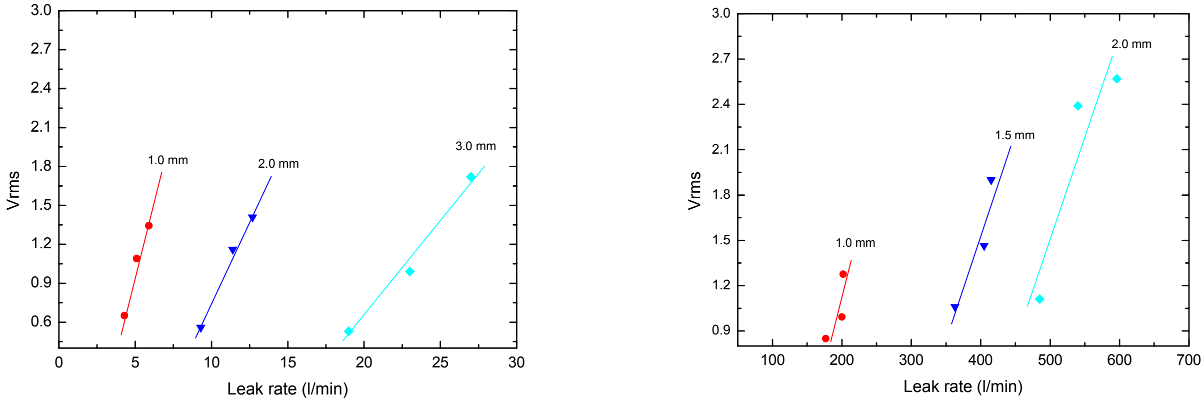

(a) disc wear (b) foreign object

Figure 3-89 AE RMS value versus leak rate (March 2004)

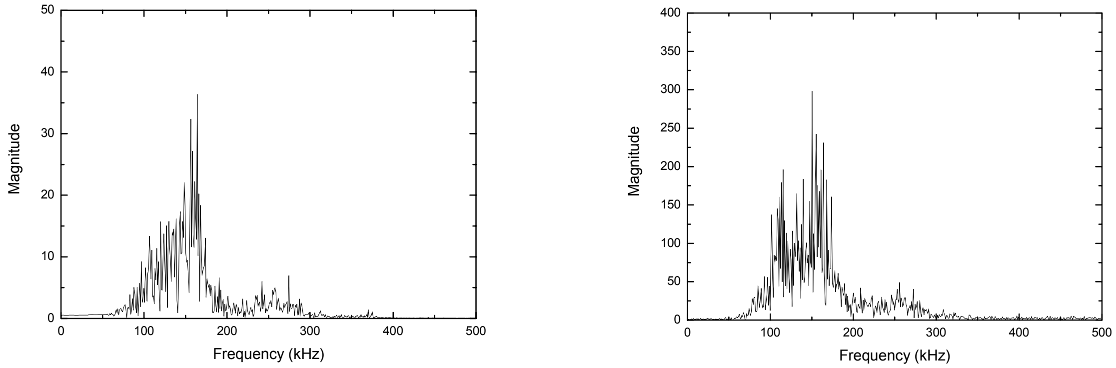

(a) disc wear **(b) foreign object**

Figure 3-90 Frequency spectrum (FFT) from different failure modes (March 2004)

3.5.5 Accelerometer signal characteristics

Several condition monitoring tests were performed on a 4 in. check valve in normal condition and with simulated degradation. In particular, vibration signal were detected by accelerometers, which respond to pressure waves over a low-frequency range (<100 kHz). Figure 3-91 shows the waveforms and corresponding spectra for the accelerometer output of initial background noise. The resulting accelerometer signature shows that the FFT is concentrated in the range of 1 to 2 kHz. Figure 3-92, which shows the waveforms and corresponding spectra from the accelerometer for foreign object failure mode, involves detecting a leak flow signal that corresponds to a diameter of leak size of about 0.85 and 1.20 mm. When comparing leakage signals (Figure 3-92) with normal signals (Figure 3-91), their frequency characteristics could not be clearly distinguished.

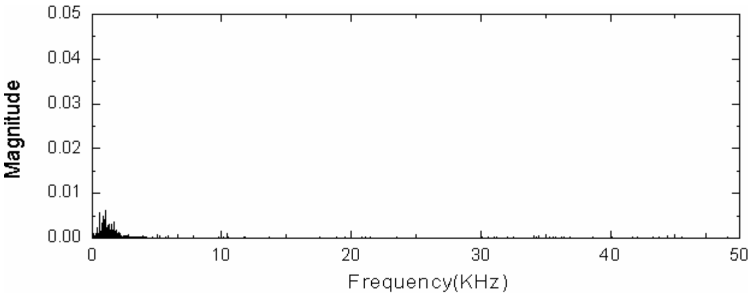

Figure 3-91 Waveform and corresponding spectra obtained from normal condition

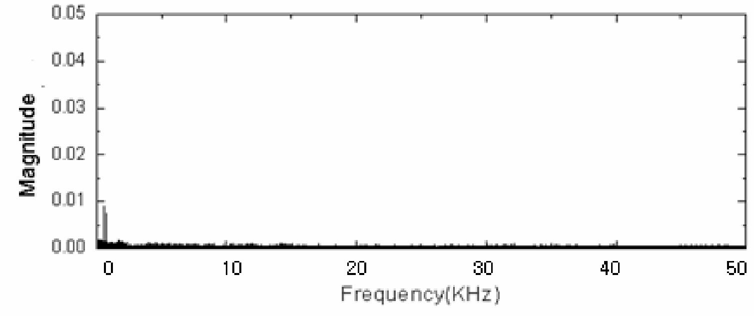

Figure 3-92 Waveform and corresponding spectra obtained from leak condition (ϕ 1.20 mm)

3.5.5.1 Ultrasonic data analysis

Ultrasonic inspection techniques can be used to detect a missing or stuck disc. Typically, one (pulse-echo) or two (pitch-catch) ultrasonic transducers were used to detect internal part of the check valve. If the disc is missing, no signal will be reflected from the disc; however, if the hinge arm remains inside the valve, its position can be verified by ultrasonic inspection techniques.

Figure 3-93 shows ultrasonic signatures acquired from a check valve at two disc positions; fully open (b) and fully closed (c) from the worn hinge pin and the improper assembly of disc. It is noted that the no signal was returned from the disc in the open position and that echo signal was returned from the disc in the closed position.

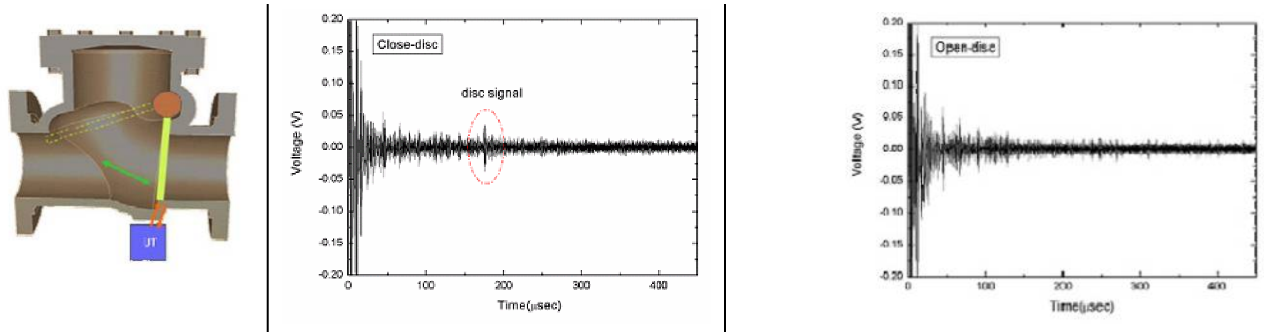

(a) ultrasonic measurement

(b) disc open

(c) disc close

Figure 3-93 UT signals obtained from disc of check valve

3.5.6 Fusion sensor monitoring

The fusion sensor combines several sensors to identify and analyze the changes of frequency response for normal and degraded check valves. The AE sensor, accelerometer, and ultrasonic device have been selected for developing the fusion sensor methodology. It has been found that the AE sensor could directly detect a high frequency acoustic wave generated from the backward leakage flow. The accelerometer would be useful for high pressure and temperature environments. Ultrasonic devices would be used for detecting the disc locations when it fails to close or open, and measuring the leakage flows. The ultrasonic flow meter can also perform a direct measurement of leakage flow. The fusion sensor method provides a more comprehensive dataset than that from any single sensor technology, and this approach can be made non-intrusive, allowing check valves to be monitored and diagnosed without being disassembled from the piping system.

Some representative experimental results in the frequency domain using the Hanning FFT analysis are shown in Table 3-22. The results show that the mechanically degraded check valves have higher frequencies above 50 kHz. The accelerometer could not contribute to easy identification of check valve failure in these experiments. It is possible to detect check valve failure at a high pressure (9 bar) with an accelerometer that is sensitive to a low frequency induced from the mechanical vibration of check valve housing. A wide range acoustic sensor attached to the backward leakage side seems to be more powerful than the other sensors in these experiments. The characteristic frequencies from the wide range AE sensors were similar for degraded check valves with disc wear or foreign object as shown in Table 3-22.

Table 3-22 Representative experiment results (frequency in kHz)

Condition Sensor	3 bar Disc wear, 2 mm	6 bar Foreign object, 1.2 mm	9 bar Disc wear, 1 mm	9 bar Foreign object, 1.0 mm
Wide A/E 2	100, 240, 280, 400, 460	110, 140, 160, 230, 280, 460	110, 200, 230, 280, 400, 480,	150 220 280, 400, 460
Wide A/E 1	100, 480, 280, 400	100, 470, 480	170, 230, 280, 400, 480	100, 17,0 230, 280, 470
NR A/E 2	100, 140, 160	95, 160	100, 150	100, 150
NR A/E 1	110, 160	120, 150	140, 160	140, 160
Accelerometer	Noise level	Noise level	9	6, 7, 10, 15

The details of the time and frequency analysis are discussed in Appendix A, Section VII.

3.5.7 Failure algorithm development using ANN technique

The details of the ANN technique are discussed in Appendix A, Section VII. The objective of an AE test is to detect the presence of emission sources and to characterize the source. The purpose of source characterization is to use the sensor output waveform to identify the sources and to evaluate their significance through qualitative and quantitative procedures. For quantitative leak evaluation, only six data features were used, including AE amplitude, RMS, pressure, signal strength (or energy), and FFT information collected from two different check valve failure modes as the input to the neural network. Table 3-23 to Table 3-25 show the neural network results obtained from disc wear and foreign object failure modes. Figure 3-94 shows the flow chart for training the neural network.

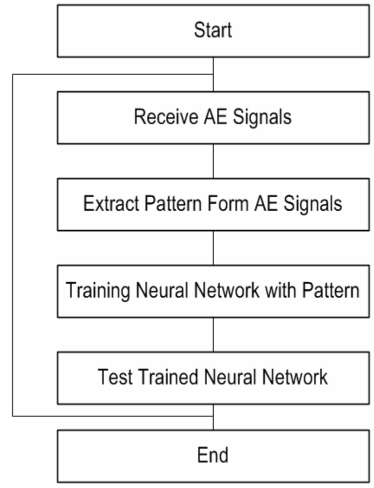

Figure 3-94 Flow chart for training neural network

The AE data were in the form of analog signals that were filtered to remove the mean value and to prevent aliasing and then digitized into time series. These data were transformed into the frequency domain, where the signals were represented through their frequency components in FFT, using data sampled at 1 MHz. The relationship between the FFT, signal amplitude, pressure, and RMS value is modeled with an ANN using time series data from a check valve. That is, the neural network was used to compute the corresponding AE parameters such as amplitude, RMS, pressure, and FFT.

Figure 3-95 shows the example of relationship between pressure and AE counts and duration time. As shown in Figure 3-95, linearity between AE parameters and pressure is not observed. However, some AE parameters such as RMS, signal strength, FFT, and amplitude have an obvious linearity with respect to the operating conditions or failure modes.

Inputs to the neural network included amplitude, RMS, signal strength, and two peak frequencies obtained from frequency spectrum and pressure. Outputs of the neural network included the failure modes for disc wear and foreign object. In the first simulation, the features of 136 cases were used for training neural network and the features of 54 cases (that were not a subset of the 136 cases) were used for testing the trained neural network. All cases of failure modes were recognized well by neural network.

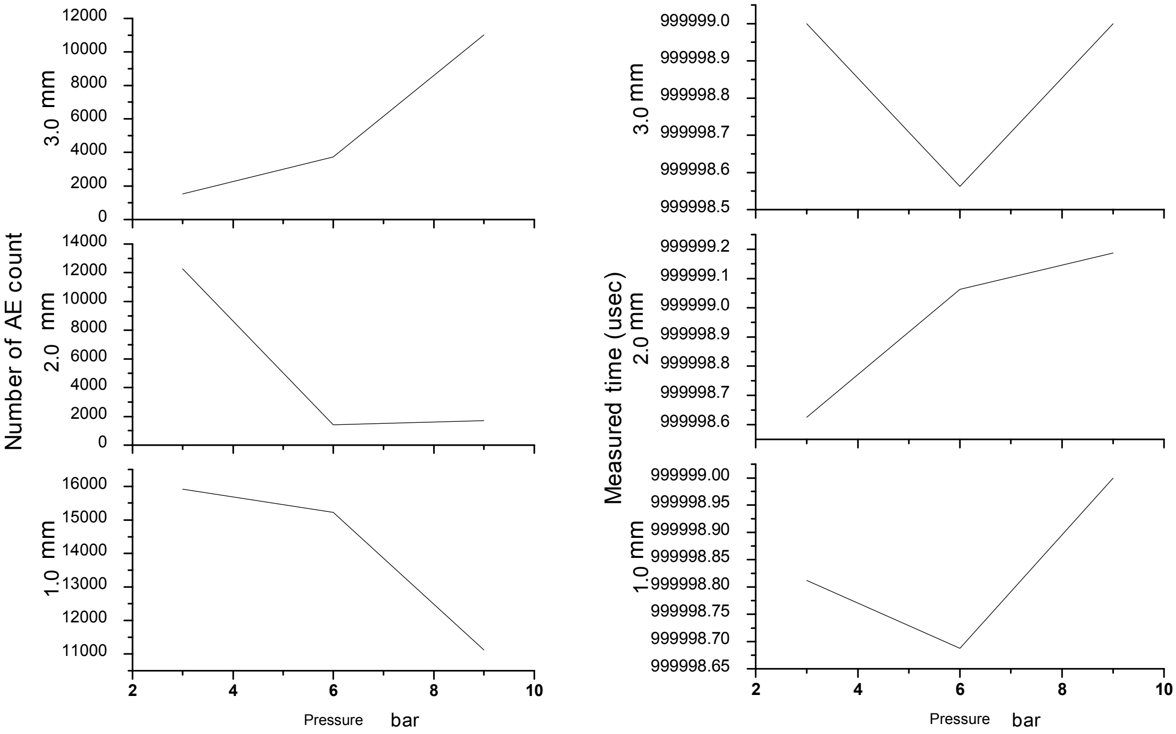

(a) AE count versus pressure **(b) AE duration time versus pressure**

Figure 3-95 The example results between AE parameters and pressure

Neural network outputs provided the correct failure mode for all cases when the 54 cases were tested. the maximum error was 6.5%, and the percentage of errors in most cases was under 1.0%; therefore, the neural network can be used to classify failure modes in check valves. Table 3-23 and Table 3-24 show the true leak size of check valves and corresponding predictions produced by the trained neural network. Sizes of disc wear and foreign object were obtained from a trained neural network after it classified failure modes.

In the case of 2.0 and 3.0 mm disc wear, all neural network output results agreed with real size; however, in the case of 1.0 mm disc wear, disc wear sizes of neural network output results for 9 bar were underestimated. That is, output results of neural network were 0.74 mm for 1.0 mm disc were at 9 bar. The neural network results showed about 26% errors in the case of leak size of 1.0 mm at pressure 9 bar.

In the case of foreign object, the maximum error was 39% and, the percentage errors in most cases was lower than 10%. Output results of neural network were 1.23 mm and 1.39 mm for 1.0 mm foreign object at 6 bar. In addition, some cases of neural network output results show overestimation in foreign object at 3 bar for 1.2 mm and at 3 bar and 9 bar for 2.0 mm. In case of foreign object

2.4 mm, output result of neural network was 2.27 mm for 9 bar. However, greater errors occur in the neural network at high pressure versus low pressure and in the foreign object failure mode versus the disc wear failure mode. This is expected due to the variation in the leak rate of the check valve.

In the second simulation, features of 1356 cases were used for training neural network and features of 216 cases were used to testing the trained neural network. The results in Table 3-25 indicate that the maximum number of errors of disc wear failure mode represented just 26% but the percentage of errors in most cases was lower than 5%. In the case of the foreign object failure mode, the maximum percentage error was about 27% but the percentage of errors in most cases was lower than 10%, therefore, as was discovered in the first simulation, the neural network is suitable for reliably classifying failure modes in check valves, and the results agree well with the actual failure modes.

The current neural network provided consistent results for the 4 in. check valve that involved AE RMS, amplitude, signal strength, and frequency. The results using the neural networks agree qualitatively with the results obtained using back propagation neural networks. In addition, it was shown that leak size could be determined with neural network. It is difficult to distinguish between different check valve failure modes.

Table 3-23 Classification of faults using neural network

Defect	Error(%)	Defect	Error(%)	Defect	Error(%)
Disc Wear (1.0mm)	1.3	Foreign Object (0.5mm)	2.7	Foreign Object (1.5mm)	0.2
	0.0		6.5		0.2
	0.8		0.2		0.2
	0.7		0.7		0.2
	0.1		0.3		0.2
	0.1		0.2		0.0
Disc Wear (2.0mm)	0.1	Foreign Object (1.0mm)	0.2	Foreign Object (2.0mm)	0.2
	0.2		0.2		0.2
	3.8		0.2		0.0
	4.0		0.2		0.0
	0.1		0.2		0.0
	0.2		0.2		0.0
Disc Wear (3.0mm)	0.0	Foreign Object (1.2mm)	0.2	Foreign Object (2.4mm)	0.2
	0.3		0.2		0.2
	1.5		0.2		0.0
	1.6		0.2		0.0
	0.1		0.2		0.0
	0.1		0.2		0.0

Input feature (6 units): amplitude, RMS, signal strength, FFT1, FFT2, and pressure
Output (2 units): disc wear, foreign object
Training data: 136 cases Testing data: 54 cases

Table 3-24 Classification of faults using neural network

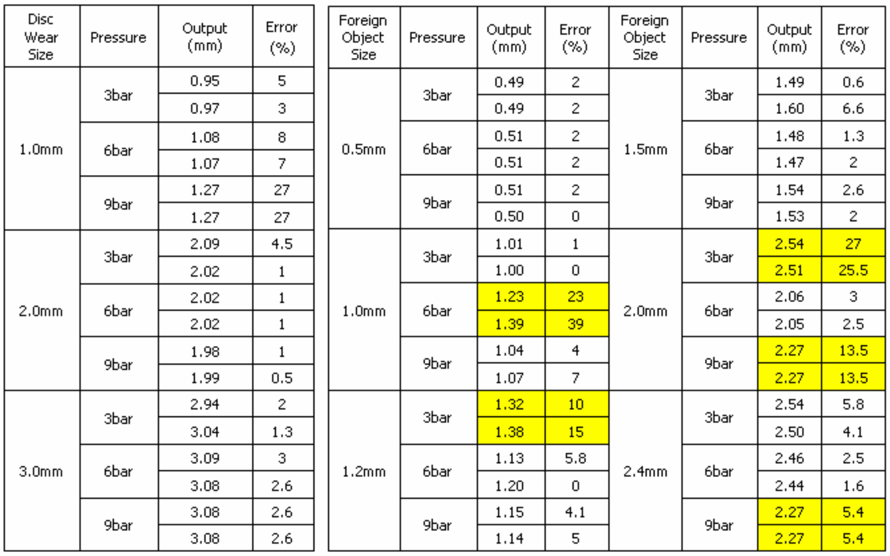

Disc Wear Size	Pressure	Output (mm)	Error (%)	Foreign Object Size	Pressure	Output (mm)	Error (%)	Foreign Object Size	Pressure	Output (mm)	Error (%)
1.0mm	3bar	0.95	5	0.5mm	3bar	0.49	2	1.5mm	3bar	1.49	0.6
		0.97	3			0.49	2			1.60	6.6
	6bar	1.08	8		6bar	0.51	2		6bar	1.48	1.3
		1.07	7			0.51	2			1.47	2
	9bar	1.27	27		9bar	0.51	2		9bar	1.54	2.6
		1.27	27			0.50	0			1.53	2
2.0mm	3bar	2.09	4.5	1.0mm	3bar	1.01	1	2.0mm	3bar	2.54	27
		2.02	1			1.00	0			2.51	25.5
	6bar	2.02	1		6bar	1.23	23		6bar	2.06	3
		2.02	1			1.39	39			2.05	2.5
	9bar	1.98	1		9bar	1.04	4		9bar	2.27	13.5
		1.99	0.5			1.07	7			2.27	13.5
3.0mm	3bar	2.94	2	1.2mm	3bar	1.32	10	2.4mm	3bar	2.54	5.8
		3.04	1.3			1.38	15			2.50	4.1
	6bar	3.09	3		6bar	1.13	5.8		6bar	2.46	2.5
		3.08	2.6			1.20	0			2.44	1.6
	9bar	3.08	2.6		9bar	1.15	4.1		9bar	2.27	5.4
		3.08	2.6			1.14	5			2.27	5.4

Input feature (6 units): amplitude, RMS, signal strength, FFT1, FFT2, pressure
output (2 units): disc wear, foreign object
Training data: 1356 cases Testing data: 216 cases

Table 3-25 Neural network results obtained from disc wear and foreign object failure modes

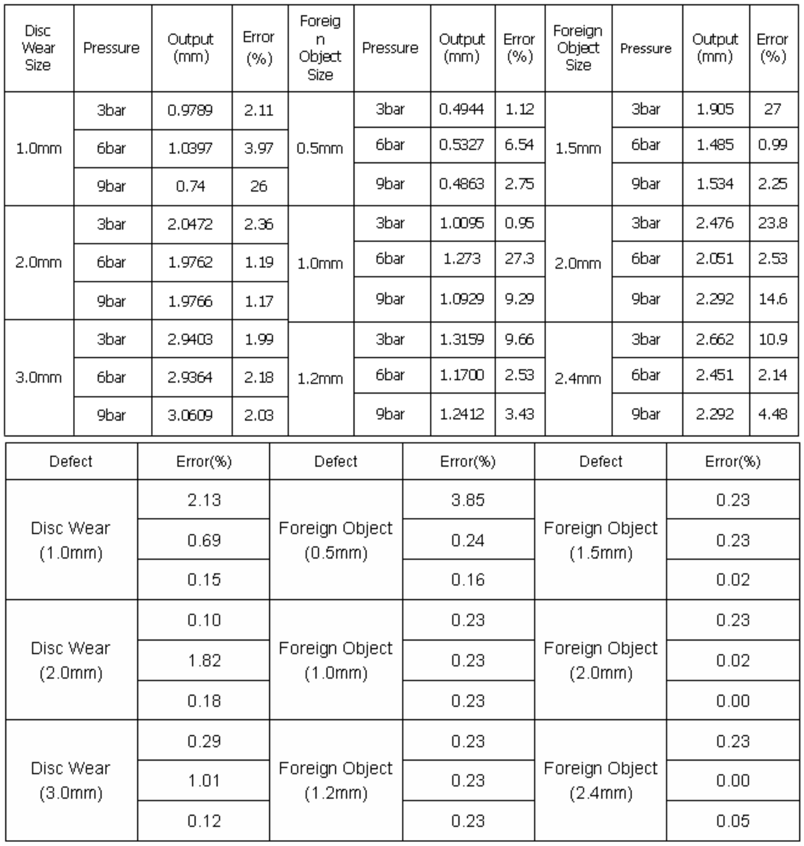

Disc Wear Size	Pressure	Output (mm)	Error (%)	Foreign Object Size	Pressure	Output (mm)	Error (%)	Foreign Object Size	Pressure	Output (mm)	Error (%)
1.0mm	3bar	0.9789	2.11	0.5mm	3bar	0.4944	1.12	1.5mm	3bar	1.905	27
	6bar	1.0397	3.97		6bar	0.5327	6.54		6bar	1.485	0.99
	9bar	0.74	26		9bar	0.4863	2.75		9bar	1.534	2.25
2.0mm	3bar	2.0472	2.36	1.0mm	3bar	1.0095	0.95	2.0mm	3bar	2.476	23.8
	6bar	1.9762	1.19		6bar	1.273	27.3		6bar	2.051	2.53
	9bar	1.9766	1.17		9bar	1.0929	9.29		9bar	2.292	14.6
3.0mm	3bar	2.9403	1.99	1.2mm	3bar	1.3159	9.66	2.4mm	3bar	2.662	10.9
	6bar	2.9364	2.18		6bar	1.1700	2.53		6bar	2.451	2.14
	9bar	3.0609	2.03		9bar	1.2412	3.43		9bar	2.292	4.48

Defect	Error(%)	Defect	Error(%)	Defect	Error(%)
Disc Wear (1.0mm)	2.13	Foreign Object (0.5mm)	3.85	Foreign Object (1.5mm)	0.23
	0.69		0.24		0.23
	0.15		0.16		0.02
Disc Wear (2.0mm)	0.10	Foreign Object (1.0mm)	0.23	Foreign Object (2.0mm)	0.23
	1.82		0.23		0.02
	0.18		0.23		0.00
Disc Wear (3.0mm)	0.29	Foreign Object (1.2mm)	0.23	Foreign Object (2.4mm)	0.23
	1.01		0.23		0.00
	0.12		0.23		0.05

3.6 Task 1.6: integrated system analyses on check valves for recommending mitigation and correction options

Performed by SNL, KAERI, and CNU

3.6.1 Data feature extraction for an algorithm development of failure diagnosis

This task describes a prototype of the check valve fault diagnosis algorithm based on the experimental data from March and April 2004. These data were divided by each set of data length of 65536 of the entire experimental data. There were 100 datasets for every case. Table 3-26 presents an example dataset for the prototype development.

Table 3-26 An experiment dataset to extract the data feature for developing algorithms

	3 Bar	6 Bar	9 Bar
Normal	100 cases	100 cases	100 cases
Disc wear 1 mm	100 cases	100 cases	100 cases
Disc wear 2 mm	100 cases	100 cases	100 cases
Disc wear 3 mm	100 cases	100 cases	100 cases
Foreign object 0.5 mm	100 cases	100 cases	100 cases
Foreign object 1.0 mm	100 cases	100 cases	100 cases
Foreign object 1.2 mm	100 cases	100 cases	100 cases
Foreign object 1.5 mm	100 cases	100 cases	100 cases
Foreign object 2.0 mm	100 cases	100 cases	100 cases
Foreign object 2.4 mm	100 cases	100 cases	100 cases

To develop the prototype of condition monitoring of check valve diagnosis system, the six previously discussed parameters (RMS, amplitude, signal strength, FFT1, FFT2, and pressure output) were extracted to identify a characteristic of the experimental data by PNU. The details of the six parameters of the specific feature characteristics of the experimental data are discussed in Appendix A, Section VII.

Failure diagnosis algorithm using neural network

This task focuses on developing an ANN method using waveforms processing method to distinguish the defect signals associated with disc wear and foreign object of check valve.

Verification of extracted data feature characteristics

WD acoustic sensor data were used to verify the extracted data feature characteristics. There were two sets of condition monitoring data for the check valve–the PNU data gathered from AE-exclusive component and KAERI data acquired by recorder. The PNU data were gathered in a very short time, appropriate to the AE exclusive components. For example, the filtered signals were gathered over 1 ms. On the other hand, the KAERI data were gathered as unfiltered signals during a long time (30 s). Figure 3-96 to Figure 3-103 show the comparisons of the feature characteristics from these two datasets. The left plots (a) in the figures are from the PNU data and the right plots (b) from the KAERI data. The results of comparison of the extracted feature characteristics were very similar between the two datasets.

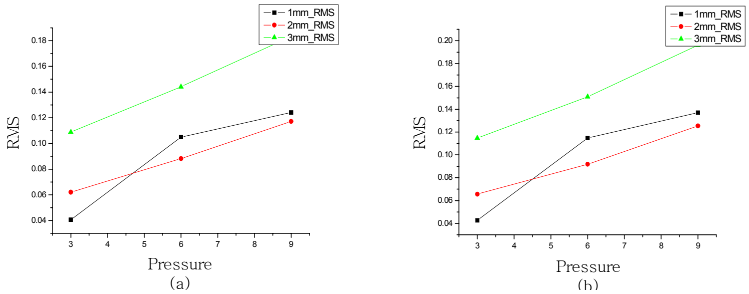

(a) (b)

Figure 3-96 Data comparison of RMS value (disc wear)

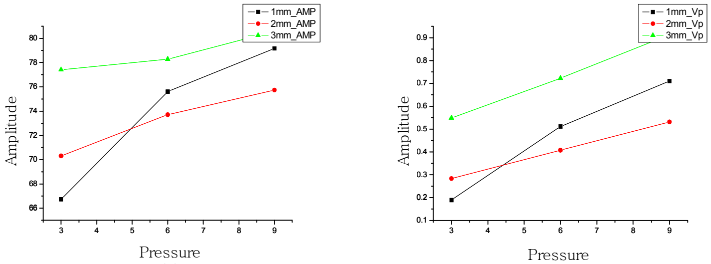

(a) (b)

Figure 3-97 Data comparison of amplitude value (disc wear)

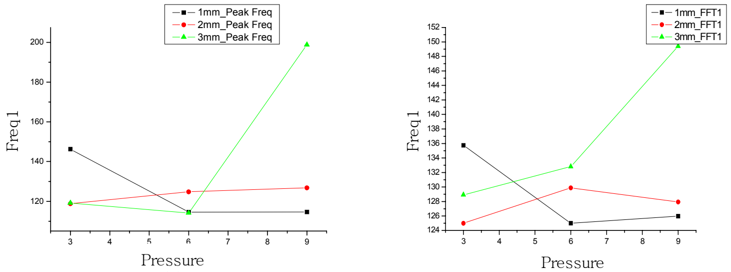

(a) (b)

Figure 3-98 Data comparison of FFT1 value (disc wear)

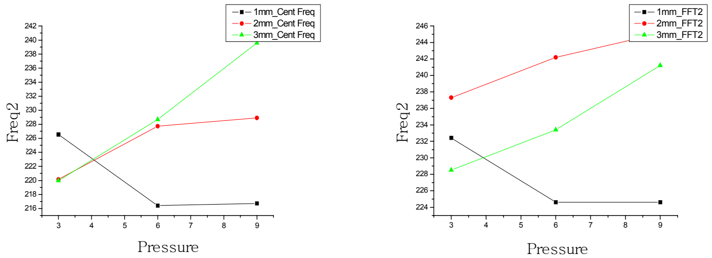

(a) (b)

Figure 3-99 Data comparison of FFT2 value (disc wear)

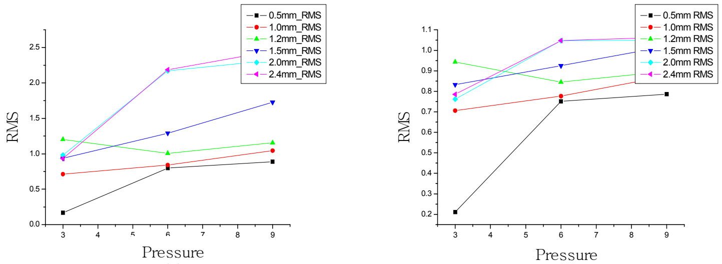

(a) (b)

Figure 3-100 Data comparison of RMS value (foreign object)

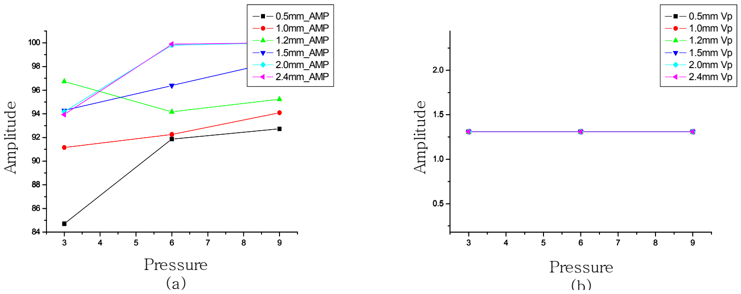

Figure 3-101 Data comparison of amplitude value (foreign object)

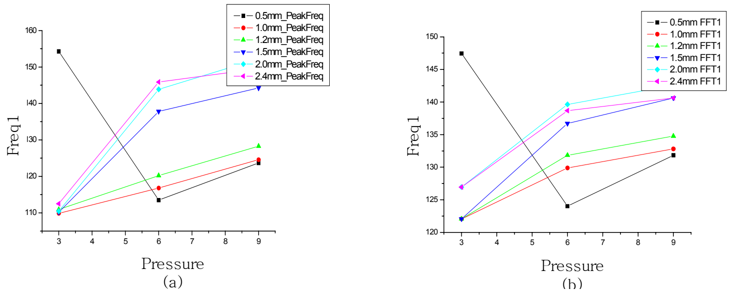

Figure 3-102 Data comparison of FFT1 value (foreign object)

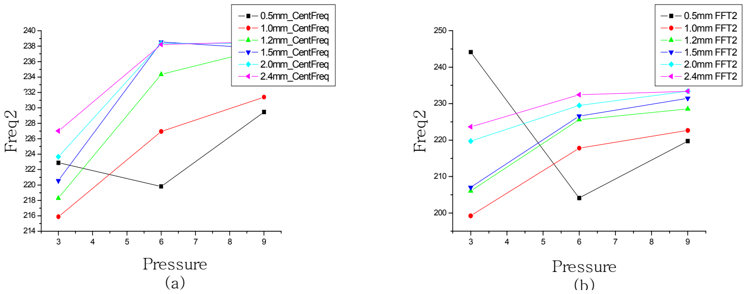

Figure 3-103 Data comparison of FFT2 value (foreign object)

Processing of failure diagnosis algorithms

The check valve failure diagnosis algorithm on check valve failure consists of three steps. The first step is a fault detection step that distinguishes a normal mode from abnormal modes. In case of abnormal modes, the failure algorithm identifies whether its failure is disc wear or foreign object. The step 2-1 and step 2-2 characterize fault types for either disc wear or foreign object and the fault size by quantifying each failure's magnitude. Figure 3-104 shows the procedure of the failure diagnosis algorithms.

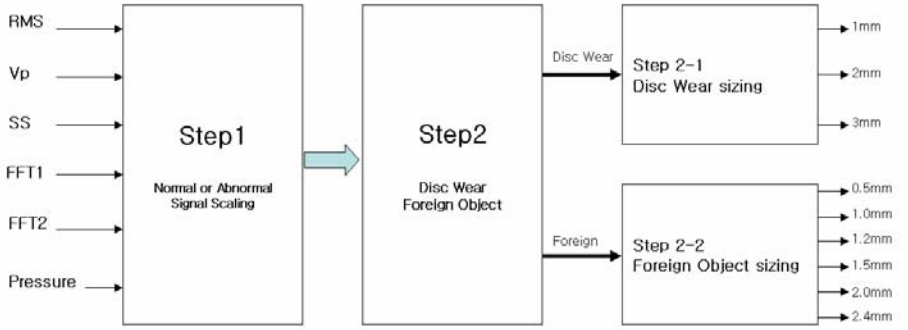

Figure 3-104 Two-step procedure of classification of the failure diagnosis algorithms

The neural network is composed of three layers; 6 input layers, 12 hidden layers, and 1 or 2 output layers. When applying the neural network, it is necessary to configure the initial parameters, and it was found that the best connection weight could be achieved with the following parameters: moment rate = 0.7, weight and threshold = 0.2, learning rate = 0.1, decline of sigmoid function = 0.7, and error rate = 0.01. The training processing for the failure classification steps using a neural network are presented in Figure 3-105.

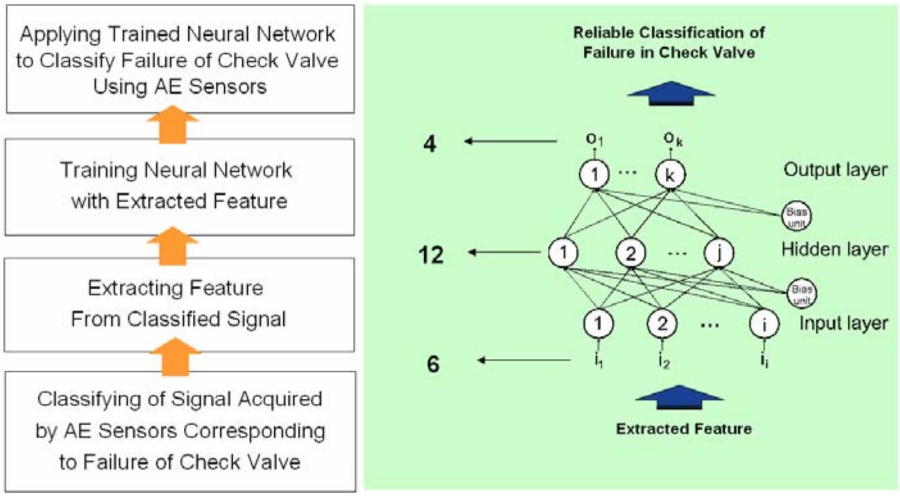

Figure 3-105 Training processing steps using a neural network

To avoid saturation of the sigmoid function and obtain identical weights of each dataset, the following ranges were assigned: input data ("0" to "1"), RMS value (0.001 to 1.06), amplitude (0.007 to 1.31), signal strength divided by 100000 (2928 to 74125), FFT1 divided by 1000 (120 to 147), FFT2 divided by 100 (198 to 244), and pressure divided by 10 (3 to 9).

Verification of trained neural network

Step 1: Distinguish between normal and abnormal conditions

The outputs of neural network are shown in Figure 3-106. The blue solid line represents the reference output and the red dots are the output of the trained neural network. The numbers of input data and experiment modes are shown on the x-axis. This figure shows that the trained neural network can distinguish between normal and abnormal modes of check valve.

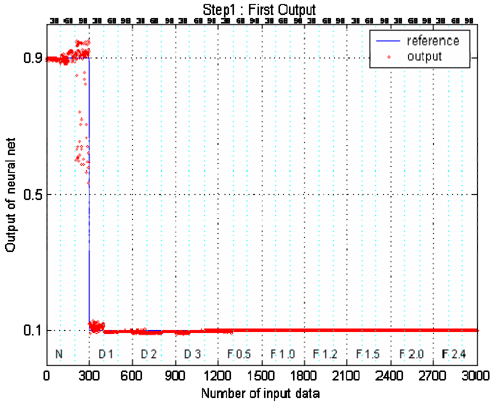

Figure 3-106 The outputs of trained neural network in step 1

Step 2: Distinguish between disc wear and foreign object

The results show that the trained neural network can distinguish between the degradation models of disc wear and foreign object, except for the case of foreign object 0.5 mm at 3 bar as shown in Figure 3-107.

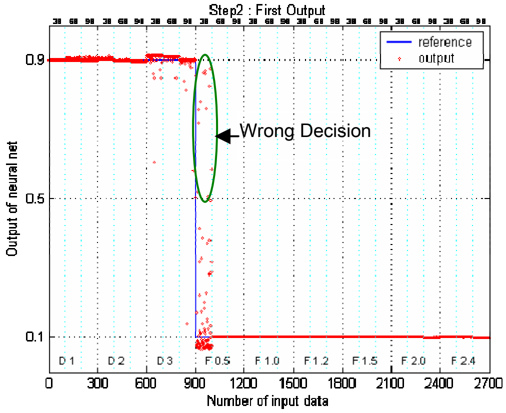

Figure 3-107 The outputs trained neural network in step 2

Step 2.1: Disc wear classification

From Table 3-27, the wrong decision mainly occurred in the case of 1 mm disc wear at 9 bar. These cases are indicated by the circle in Figure 3-108.

Table 3-27 The results of trained neural network in step 2-1

Failure size	1mm			2.0mm			3mm		
Pressure (bar)	3	6	9	3	6	9	3	6	9
Wrong Decision (%)	0	7	72	12	0	0	0	1	4

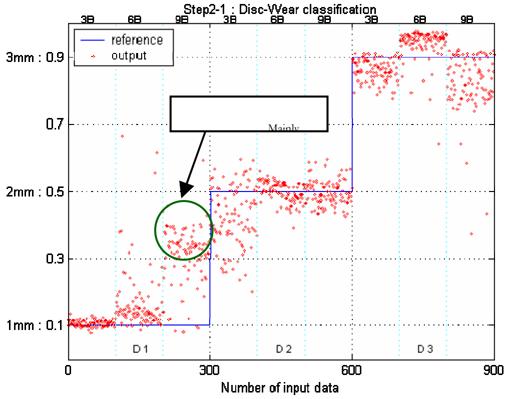

Figure 3-108 The outputs of trained neural network in step 2.1

Step 2.2: Foreign object classification

From Table 3-28, the wrong decision mainly occurred in the case of the 2.0 mm foreign object at 6 bar and 9 bar. These cases are indicated by the circle in Figure 3-109.

Table 3-28 The results of trained neural network in step 2-2

Failure size	0.5mm			1.0mm			1.2mm			1.5mm			2.0mm			2.4mm		
Pressure (bar)	3	6	9	3	6	9	3	6	9	3	6	9	3	6	9	3	6	9
Wrong Decision (%)	3	0	0	0	0	0	20	0	0	0	8	0	37	86	78	1	20	11

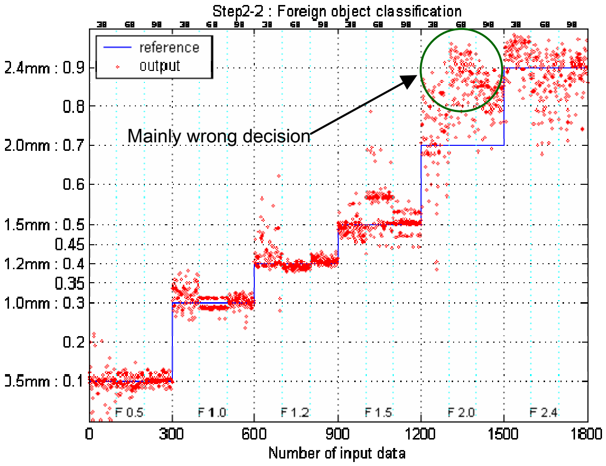

Figure 3-109 The outputs of trained neural network in step 2.2

Some conclusions can be derived from Table 3-29, which represents the wrong decision rate in each step:

- Step 1 can clearly distinguish between normal and abnormal conditions
- Step 2 can differentiate the degradation modes between disc wear and foreign object in most cases
- Step 2.1 and step 2.2 can distinguish the defect size except in some specific cases (with 1 mm at 9 bar in disc wear and 2 mm in foreign object).

Table 3-29 The results of all outputs

	Step 1	Step 2	Step 2.1	Step 2.2
Wrong decision rate (%)	0	0.37	5.33	14.68

4. TASK 2: condition monitoring of a secondary piping elbow (passive component) in a non-safety–related environment

This task focuses on investigating and developing a condition monitoring system for a secondary piping elbow in a non-safety–related environment as a passive component. The work scope includes collecting and examining existing performance data on piping systems as passive components in an aggressive erosion/corrosion environment, investigating and identifying sensors and communication options to be used in condition monitoring test loop, developing and analyzing FEMs of piping elbow, conducting condition monitoring tests, and processing signal data to establish recognizable vibration patterns.

4.1 Task 2.1: performance, failure, and inspection data on piping elbows in an accelerated erosion or corrosion environment

Performed by SNL and KAERI

Pressure vessels and heat exchangers such as steam generators have very sophisticated piping systems operating in a very aggressive erosion/corrosion environment of turbulent flow and high temperature and pressure. These adverse operating environments make a piping system very vulnerable to accelerated wear and degradation. There are on-going research efforts in environmentally assisted cracking (EAC) to investigate the failure modes and mechanisms of piping systems operating in these conditions. This task collected and reviewed a series of published papers in the EAC area and a database was organized using the Microsoft Access program to categorize these technical reports systematically.

4.1.1 Flow-accelerated corrosion (FAC)

Figure 4-1 shows a schematic of a PWR secondary coolant system referenced from Ulchin Unit 3 and 4. The following is a list of NPP systems that often experience flow-accelerated corrosion (FAC) problems:

- Single-phase systems
- Condensate and feedwater
- Auxiliary feedwater
- Heater drains
- Moisture separator drains
- Steam generator blow-down
- Reheater drains
- Other drains
- Two-phase systems
- High and low pressure extraction steam lines
- Flashing lines to the condenser (miscellaneous drains)
- Feedwater heater vents

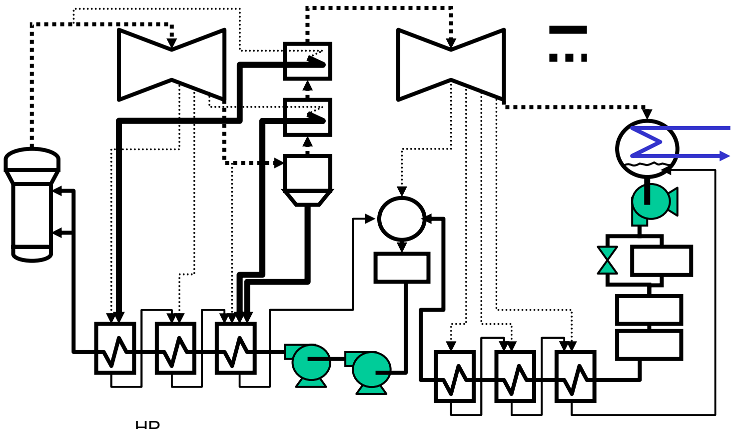

Figure 4-1 Schematic of a PWR secondary coolant system

In a PWR secondary side, moisture separator and reheater (MSR) drains were selected as a first application area of FAC monitoring system. MSR drains with single-phase flow have a high susceptibility to FAC, and its temperature and pressure are relatively low as compared with feedwater or blow-down. The maximum temperature of MSR drains is 232ºC and maximum pressure is 30 atm. The specification of sensors was tailored based on operational variables of MSR drains.

4.2 Task 2.2: sensor and communication options for test loop to obtain condition monitoring data on piping elbows

Performed by SNL, KAERI, and SNU

The project team is very interested in conducting condition monitoring tests on steam generator tube bundles in support of its inspection and maintenance procedures to safeguard its normal operations. However, the budget and schedule for such test series are far beyond the investigation scope of this project. Therefore, the project team decided to conduct a lesser scale test series on a piping elbow as a prelude to that on steam generator tube bundles. An accelerated erosion/corrosion environment was implemented and monitored in the piping elbow test loop. Three types of sensors–advanced optical fiber displacement sensors, micro-accelerometers, and a capacitance displacement sensor–were used to collect signal data. In this test series (where the piping elbow is in a benign ambient condition), it was not necessary to use the highly sophisticated sensors such as advanced optical fiber displacement sensors. These advanced sensors were chosen to allow project team members to gain operational experiences with them so that the sensors may be used in the future test series on steam generator tube bundles. The advanced optical fiber displacement sensors, in particular, were chosen because they can survive and operate in the highly erosive and corrosive environment of high pressure and temperature in a steam generator

4.2.1 Overall approach to FAC monitoring

FAC is a process whereby the normally protective oxide layer on carbon or low-alloy steel dissolves into a stream of flowing water or a water-steam mixture. The researchers at SNU analyzed the physical phenomena to extract monitoring parameter to develop the on-line monitoring system for the FAC. Since the FAC combines both erosion and corrosion processes, the monitoring parameters are classified accordingly in two categories: one is electrochemical parameters and the other is mechanical parameters.

In the mechanical processes, piping materials eroded resulting in a drastic reduction of the thickness of piping. For the electrochemical process, oxide that is formed at the material surface is easier to erode. The mechanical vibration was chosen as an indirect method to monitor the piping thickness reduction. To monitor the electrochemical condition, the SNU researchers developed ECP and pH electrodes for the high temperature applications. In addition, a high-temperature UT was used to detect the piping thickness reduction.

Since FAC is a global corrosion phenomenon, ECP and pH are major factors influencing FAC. De Bouvier et al showed some experimental results that the FAC rate changes drastically with ECP as shown in Figure 4-2 [xi]. These experimental results confirmed that ECP is an important factor and should be precisely measured during a FAC experiment.

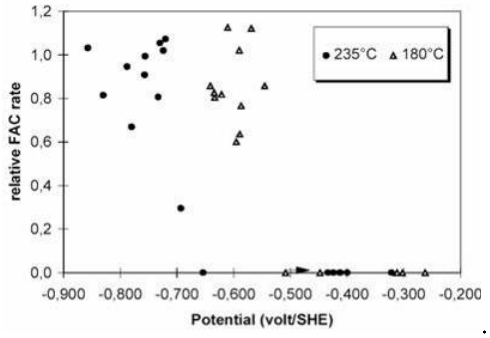

Figure 4-2 Relative FAC rate as a function of potential (From O. De Bouvier et al)

4.2.2 Sensors for monitoring FAC phenomena

4.2.2.1 Electrode sensors

The SNU researchers have developed ECP and pH electrodes for FAC monitoring in the secondary side of NPPs. The temperature range of the FAC occurrence in a PWR secondary system is from 100 to 250°C. To perform *in-situ* condition monitoring, the electrodes should operate reliably in these high temperature ranges.

The external pressure-balanced Ag/AgCl (water) electrode has been used extensively for PWR environment. The external reference electrode-PTFE (EREP) was chosen for the condition monitoring tests. The EREP design was derived from the original Danielson's electrode design, by using pure water as the filling solution and by adding a compression seal for the zirconia plug, as shown in Figure 4-3. A chloridized silver rod is sheathed with heat shrinkable PTFE tube, which is connected with a porous zirconia plug in the lower part and with a Rulon® adaptor in the upper part. The Rulon® sleeve is tightened with a stainless steel nut for preventing chloride ion from leaking through the porous zirconia plug and PTFE tube. AgCl was deposited on the silver rod by electrochemical chloridization in the HCl solution.

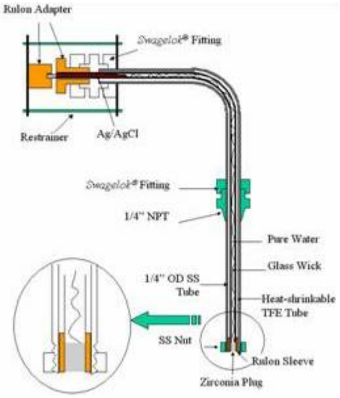

Figure 4-3 Schematic of external pressure-balanced Ag/AgCl (water) electrode

With respect to reproducibility and stability, the EREP showed very good performance in the experiment involving high temperature aqueous environment. The stability was within 15 mV during

400 hours of experiment period. The electrode-to-electrode potential variation was observed within 20 mV.

A gold-plated nickel electrode, Au Electrode-Non PTFE (AUEN), was developed as a pH sensor of the solution that can be used in temperatures above 320℃, where PTFE can no longer survive. The schematic diagram and part description of AUEN are shown in Figure 4-4. The SNU researchers solved the technical challenge of metal-ceramic brazing by adopting a commercially available feedthrough conductor, which is originally used in high temperature hermetic conditions. A nickel conductor of the feedthrough was plated with gold so that hydrogen reaction can occur on the surface. In this way, pH of the solution can be measured in a high-temperature hydrogen-reducing environment and an oxidation-reduction potential of the oxidizing or reducing agents can be determined in non-hydrogen environment. The pressure boundary was joined with a stainless steel tube by an electron beam welding or laser beam welding. The integrity of the metal-ceramic brazing on the feedthrough was monitored continuously by installing pressure transducers in the end of the stainless steel tube.

The potential stability of this electrode during 350 hours of experiment was observed within 15 mV. The potential for reproducing this kind of electrode for two manufactured electrodes was within 10 mV. The performance of this electrode is comparable to the results of an international round robin test in the aspects of the reproducibility and stability. The electrode development is discussed in detail in Appendix C, Section I.

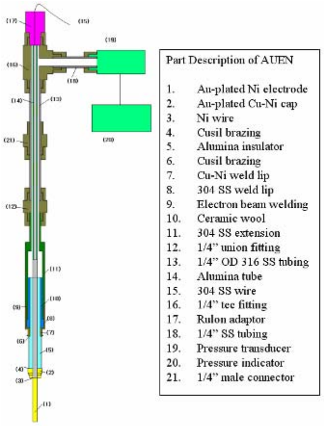

Figure 4-4 Schematic diagram and part description of gold-plated nickel electrode.

4.2.2.2 Ultrasonic thickness sensors

In addition to the electrochemical sensors, the ultrasonic sensor was used to monitor the piping thickness change in the FAC test. Figure 4-5 shows the conceptual design for the installation of ultrasonic sensor on high temperature steel piping elbow surface. As depicted in Figure 4-5, the high-temperature ultrasonic transducer was attached by using supporting structures. To get interpretable and reliable signals from UT sensor, the contact interface between the elbow surface and the transducer is very important. Couplants suitable for high-temperature application were used to enhance the physical contact at the interface.

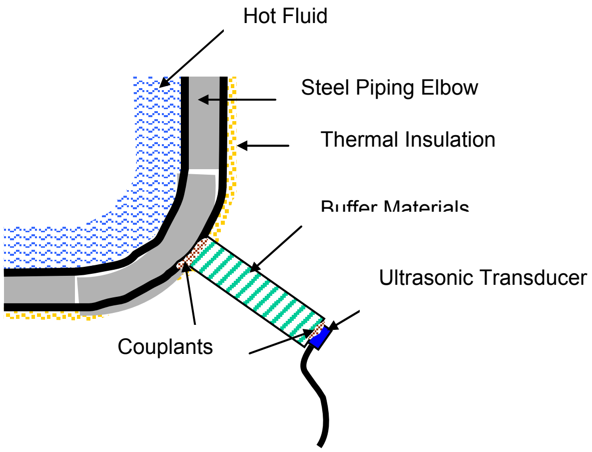

Figure 4-5 **Conceptual design for the installation of ultrasonic sensor on high temperature steel piping elbow surface**

4.2.2.3 Fiber-optic reflection displacement sensor

As shown in Figure 4-6, this sensor consists of a bundle of seven closely packed optical fibers in a tube. The face of this bundle is well polished and parallel to a reflecting surface. The central fiber is connected at its opposite end to an optical source, such as a light-emitting diode, while the surrounding six fibers are connected to a single optical detector. When light emerges from the central fiber, it reflects off the surface and into the surrounding fibers. The total optical power entering these receiving fibers is a function of the separation between the face of the bundle and the surface. Based on actual data, that function is shown in Figure 4-7 for the fibers used in this application. The sensitive and linear region to the left of the peak, extending from about 0.1 mm to 0.5 mm, is most useful. Thus, this sensor produces a large change in signal over a narrow range of displacement.

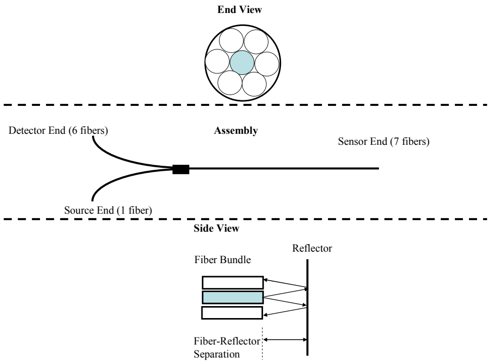

Figure 4-6 **Fiber-optic reflection displacement sensor**

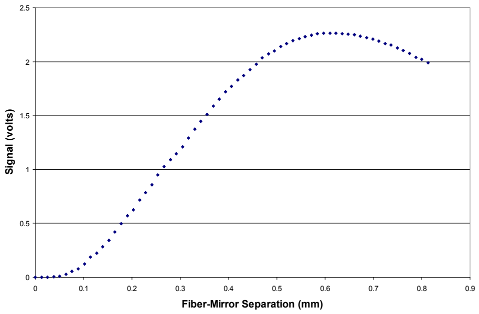

Figure 4-7 **Optical power entering receiving fibers as a function of gap between bundle face and the surface**

Figure 4-8 illustrates how the advanced optical fiber sensor might be implemented for vibration measurement in condition monitoring tests. This figure shows a cross-section of a horizontally vibrating tube. Surrounding the tube is a frame, inside of which are two bundles of optical fibers that form two displacement sensors, for which the tube is the reflecting surface. The frame is shown rigidly attached to the roof of the chamber that is a fixture. As shown, one sensor has its face coincide with the end of the left arm of the frame and the other with the right arm. As the tube vibrates, the output of one sensor increases, while the other decreases. If a difference/sum of the two signals were determined, excellent common-mode rejection would be the result if the two sensors were linked to the same optical source.

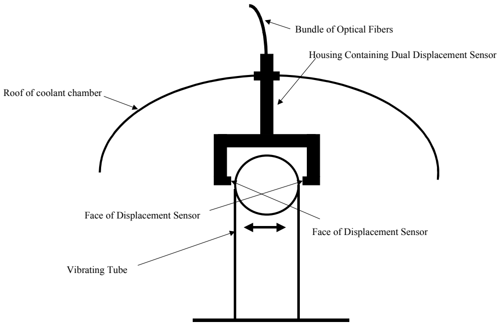

Figure 4-8 An advanced optical fiber sensor as a vibration measurement device

4.3 Task 2.3: Finite Element Analyses of piping elbow to investigate its dynamic response and to select optimal sensor locations

Performed by SNL

4.3.1 Modal analysis of U-section of piping elbow

Condition monitoring tests were conducted to evaluate the feasibility of various types of selected sensors to passively detect local thinning in a piping elbow caused by corrosion degradation. This task focused on monitoring changes in the piping system vibration response under flow conditions where corrosion is present in the elbow. Since the flow-induced vibrations are expected to be small, it is important that the test loop be configured so that the corrosion will cause an appreciable difference in the vibration characteristics of the system. Therefore, a U- section of piping was added to the main loop as shown in Figure 4-9 to amplify the changes in vibration response of the portion of the test loop subjected to corrosion. The two elbows at the end of this section closest to the supports would experience corrosion resulting in a relatively great effect on the vibration response of this section. This modification also has the advantage that it geometrically resembles a steam generator U-tube, making the results of this test more applicable to systems to monitor the condition of steam generator U-tubes.

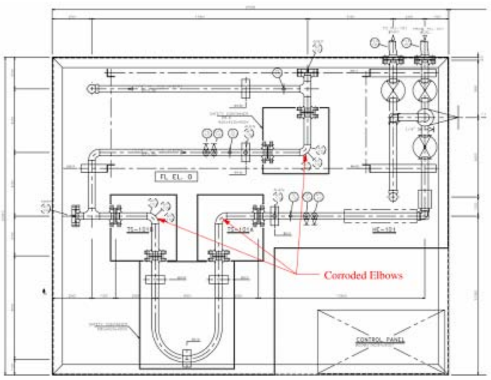

Figure 4-9 Modified piping elbow test loop

Modal analyses of the original elbow test segment and the U-shaped segment of piping were performed using the ABAQUS™ (Version 6.3-1) FEA software to demonstrate the effects of corrosion in the elbows on the vibration characteristics of the system. The modal analyses produced a series of mode shapes, along with their corresponding fundamental frequencies. The sections of piping near the corroded elbows were modeled with 3D solid elements, while the rest of the system was modeled with beam elements. Figure 4-10 shows the detailed view of U-section of piping modeled by 3D solid elements. To save computational effort, the effects of water have been accounted for by adding mass to the steel. The effects of the internal pressure on the system have been demonstrated to be minor, and have thus not been included in the model. It should be noted that no damping is used in these models.

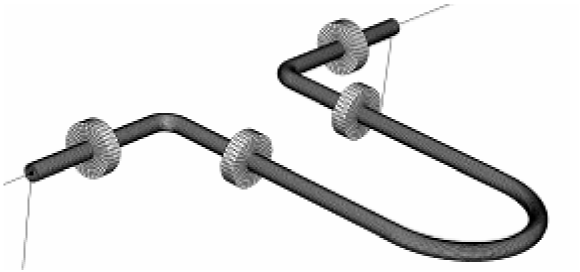

Figure 4-10 Detailed view of region modeled with solid elements in U-shaped pipe model

Since solid brick elements are used to model the local region of the elbow to be corroded, the most reasonable way to model the removal of material due to corrosion is to reduce the thickness of these elements by moving nodes along the inside surface of the pipe away from the pipe centerline. In the first stage of this analysis effort, the piping elbow was simply corroded a uniform amount. Later, a more refined approach, in which the pipe was corroded more along the outside curve of the elbow, was used.

The FEMs of the original (without the U-section) and the U-section elbow designs were executed to compute the fundamental frequencies and mode shapes of the first 200 vibration modes. Different levels of corrosion degradation of the piping elbow were investigated in the analyses. Variations in modal frequencies of the original and U-section elbow designs are depicted in Figure 4-11 and Figure 4-12, respectively, for both uniform and non-uniform thinning of the elbow. The analysis results demonstrate that greater changes in the modal frequencies due to corrosion are expected in the U-shaped test section than in the original elbow test section. This will improve the likelihood that the condition monitoring sensors will be able to detect the presence of corrosion in the piping elbows.

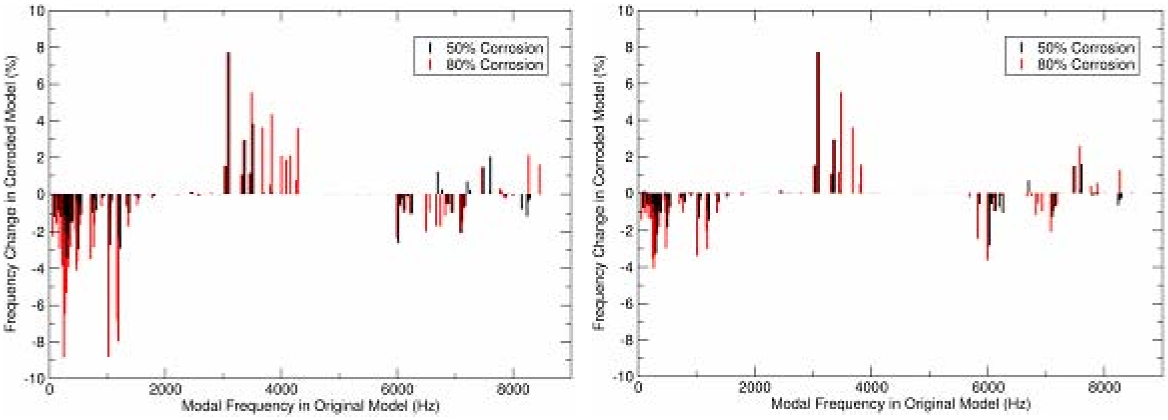

(a) Uniformly thinned cases **(b) Non-uniformly thinned cases**

Figure 4-11 Modal frequency change for original elbow design

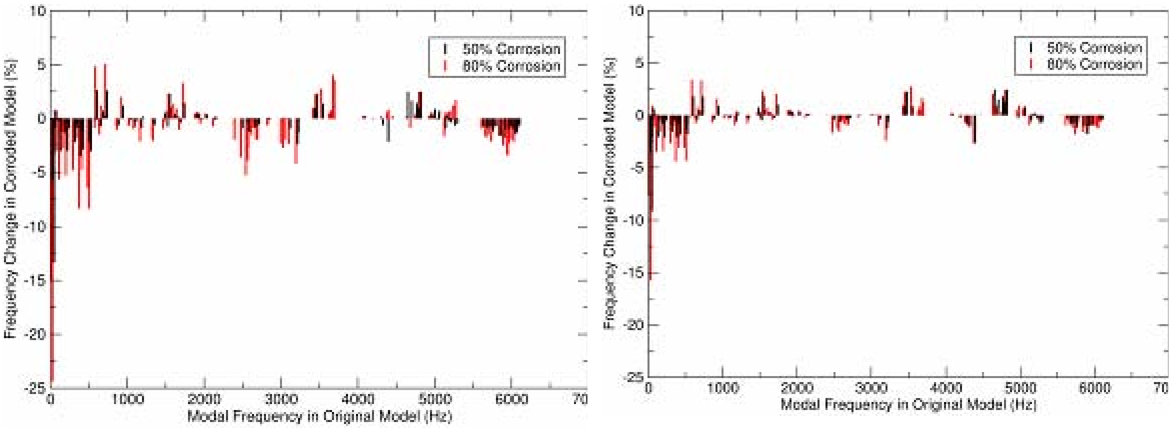

(a) Uniformly thinned case **(b) Non-uniformly thinned cases**

Figure 4-12 Modal frequency change for U-shaped section

4.3.2 CFD modeling of pipe elbow flow

In addition to the modal analyses of the piping elbow structure previously summarized, CFD models were used to predict the characteristics of the flow within the piping elbow. The flow characteristics are important for estimating the amount of corrosion expected to occur. Figure 4-13 shows a diagram of the piping section under consideration. Flow enters the pipe at the lower left hand corner of the figure and passes around a 90° elbow. In some of the test loop elbows, an AUEN chemical sensor is located downstream of the elbow, with the support bracket crossing the pipe approximately 200 mm from the downstream end of the elbow.

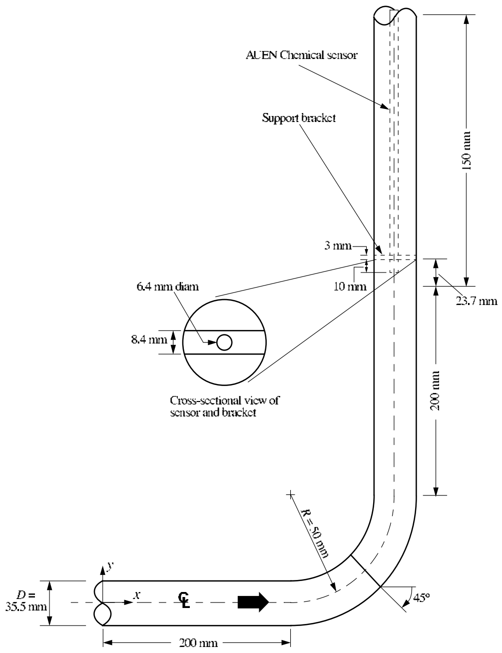

Figure 4-13 Pipe elbow model geometry (not to scale)

Assuming a flow velocity of 5 m/s averaged across the inlet cross-section, the Reynolds number is approximately 5.4x10^5, which indicates that the flow is expected to be fully turbulent. Turbulent flows are decomposed to consist of a steady mean flow velocity field onto which a turbulent fluctuating velocity field is superimposed. Computational methods such as DNS and Large Eddy

Simulation (LES) can be used to compute the transient turbulent fluctuations, but due to high computational costs, are still not considered practical for flows of typical engineering interest.

To simplify the analysis procedure, a turbulence model, which relates the magnitude of the turbulent fluctuations to the mean flow variables, is used to achieve a steady state solution for a turbulent flow. One of the most widely used turbulence models is the two-equation k-ε model developed by Launder and Spalding. It is so named because it introduces an additional pair of partial-differential equations (PDEs) for predicting the turbulent kinetic energy per unit mass, k, and its rate of dissipation, ε. The model incorporates several constants whose values have been determined from experiments with both air and water for fundamental turbulent shear flows.

The turbulence model used in this project is a modification of the k-ε model that uses a more rigorous statistical technique known as ReNormalization Group (RNG) theory. This technique results in an analytical derivation of the values of the model constants, and introduces new terms into the transport equations for k and ε that allow them to compute more accurately turbulent flows involving swirl. The reduced dependence on empiricism, and the inclusion of the additional terms make this so-called RNG k-ε model more accurate and reliable for a wider class of flows than the standard k-ε model.

The Navier-Stokes equations, which express the conservation of mass and momentum, and the transport equations for k and ε used in the turbulence model, form a coupled set of nonlinear PDEs. The FLUENT (Version 6.0) software was used in this study to solve these equations. FLUENT uses a finite-volume discretization to convert the PDEs to a set of nonlinear algebraic equations, which are solved iteratively. Figure 4-14 shows the analysis results in terms of regions of high shear stresses and kinetic energy. In this figure, the regions of high shear stress and kinetic energy appear at different locations from those expected to experience local thinning in the FAC test.

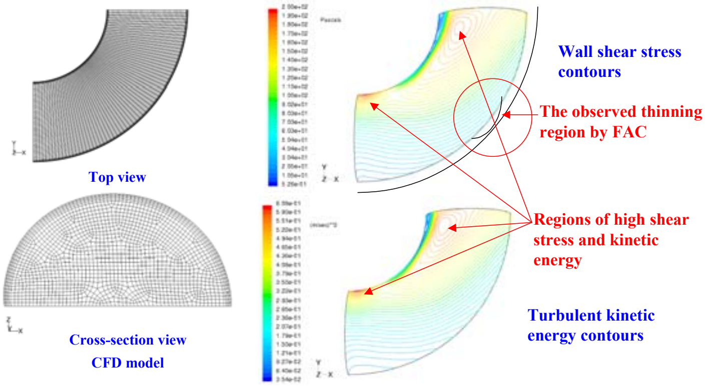

Figure 4-14 CFD analyses of piping elbow

4.4 Task 2.4: Tests with the test loop at SNU to obtain condition monitoring data on piping elbows using selected sensors

Performed by KAERI and SNU

4.4.1 FAC test loop design

The SNU researchers developed the simulation loop to test advanced monitoring system for the FAC process. Since this test loop simulates the secondary side of an NPP, operating temperature and pressure were determined according to the NPP condition. Test temperature was about 150ºC, and pressure was about 20 bar. Both charging and circulation pumps ware installed. To minimize the vibration effect of pumps, the loop was constructed as two skids: one with pumps and the other with a circulation loop. Flexible cable connected the two skids. The test loop includes an elbow pipe and a U-shaped pipe similar to a steam generator tube as test specimens to maximize the effect of FAC and thus vibration. Figure 4-15 shows the developed test loop. The left side shows the test loop and the right side shows the monitoring program (upper image) and the test specimen covered with a safety box (lower photo).

Figure 4-15 Developed FAC test loop and test specimen

4.4.2 Test matrix for vibration sensors

In this task, the test loop was designed to monitor both electrochemical parameters and mechanical parameters. The SNU researchers tested electrodes and identified that ECP and pH were good parameters to corrosion monitoring. However, confirmatory tests are needed to demonstrate that vibration is a good monitoring parameter of local thinning of piping. Two tests were performed to address this issue. First, pull-down tests on U-section were performed to obtain a basic understanding of the vibration characteristics of the relationship between force and induced vibration. In these tests, an electromagnet was installed and different vibration modes of the U-section were measured by changing the relative position of the electromagnet to the U-section.

Second, simulated FAC tests were designed to identify the effect of the pipe thickness reduction on the vibration response of the U-section. There were three sets of simulated FAC tests. The first simulated uniform thinning of the piping system by replacing the original pipes with pipes having different thicknesses. The second test simulated non-uniform thinning of the piping system after the outer and inner portions of the elbow were ground down to the same thickness. The emphasis of this test series was to investigate the change in vibration characteristics of U-section due to local pipe thinning. The third test simulated a real FAC condition in a continuous test sequence with well-controlled water chemistry and flow velocities.

4.4.2.1 Magnetic pull-down test

The pull-down tests were performed to obtain baseline data. To provide a basic understanding on the vibration characteristics of the U-section, the pull-down tests generated forced vibration with specific direction and measured the change of vibration modes of the U-section. In these tests, an electromagnetic force was applied onto the U-section that was set in vibratory motions upon release of this force. Different vibratory modes were tested including up-down, right-left, and rocking modes. Figure 4-16 shows the installation of electromagnet for these tests.

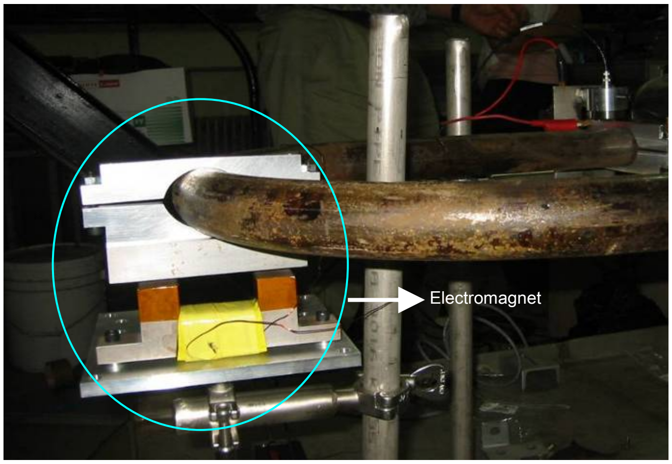

Figure 4-16 Installation of electromagnet for the pull-down test

The pull-down tests were performed at room temperature at a pressure of ~20 bar, with elbow and U-sections made of carbon steel having SC40 of thickness. Five types of sensors were installed around elbow and U-section: a fiber-optic displacement sensor, a 3-axis accelerometer, a capacitance sensor, a fiber-optic accelerometer, and a piezoelectric accelerometer. These five sensors are shown in Figure 4-17.

Sensor locations were adjusted to find optimal positions to maximize sensor signals. The operation range of fiber-optic displacement sensor is only a few tenth of millimeters and very sensitive to the change. Four of these sensors were installed around the straight part of U-section and elbow. The capacitance sensor, which has an operation range around a few millimeters, was installed in the U portion that was expected to have the largest vibration amplitude. The 3-axis accelerometer has a wide operation range and can thus be installed anywhere. Two accelerometers were installed: one in the U portion and the other in the straight part of U-section. One piezoelectric fiber-optic sensor was used to measure background noise. In addition, the fiber-optic accelerometer was removed from the tests because it was too sensitive to background noise.

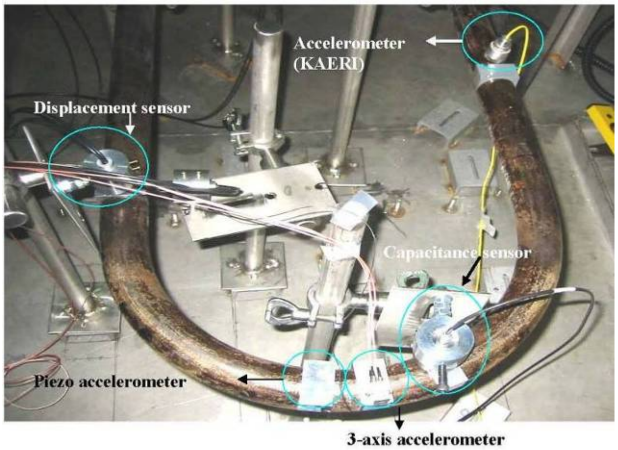

Figure 4-17 Sensor installation for the pull-down test

Description of the magnetic pull-down apparatus

This apparatus was used to induce a particular mode of vibration of the U-section by pulling on it at one or two points and releasing it, allowing the structure to ring downward. In its basic form, the apparatus, shown in Figure 4-18, consisted of an electromagnet and a keeper, both of which were made of high-purity annealed iron. The heavy line indicates the predominant path (that is, ignoring fringe effects) of the magnetic induction produced by current through the windings. When current is sent through the windings, regardless of direction, the keeper is attracted to both pole faces of the electromagnet. The symbols G, A, X, N, and I stand for the initial gap, the area of the pole faces, the displacement of the keeper, the number of turns, and the current through the windings. Since the cross section of the pole face was a square 1 in. on a side, A = (1/1600) m^2.

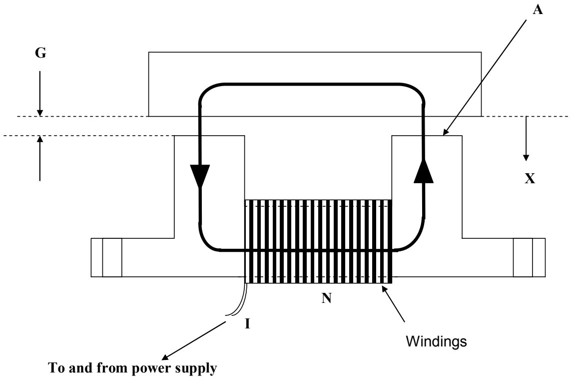

Figure 4-18 Magnetic pull-down apparatus

To displace the U-tube, the keeper must be attached to it by bolting the keeper to an aluminum clamp that is squeezed around the U-section by other bolts. This arrangement is shown in Figure 4-19, along with the electromagnet. The electromagnet was designed to be securely bolted to a mounting plate.

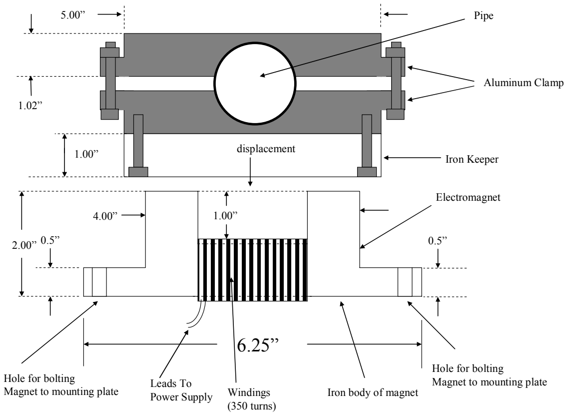

Figure 4-19 Keeper arrangement

Analysis of the magnetic pull-down apparatus

The fundamental question for this arrangement is related to the amount of deflection as a function of the current and the initial gap. This question can be addressed by equating the required force, F_{mech}, to a small deflection, X, in the U-tube in a linear fashion,

$$F_{mech} = KX \tag{1}$$

where K is the force constant of proportionality.

The magnetic force, F_{mag}, which generates the mechanical force in Equation 1, is calculated by using Ampere’s Circuital Law to arrive at the following equation,

$$F_{mag} = (NI)^2 A \mu_0/[2(G–X) + L/\mu_R]^2, \tag{2}$$

where μ_0 and μ_R are the permeability of free space and the relative permeability, respectively, and L is the length of the iron around the loop in Figure 4-19, which is 10”. The relative permeability of iron was chosen to be 5000 for these calculations.

Figure 4-20 is a plot of the magnetic force versus displacement for this system. A constant current of 5 amps is assumed, along with an initial gap of slightly over 0.5 cm. A relative permeability of 5000 was also assumed. It should be noted that the force increases rapidly with displacement until about 0.45 cm, at which point the force remains constant until the gap is closed. This occurs because the magnetic induction in the iron has been increasing with deflection, at constant current, until it reaches saturation at 2.1 Tesla.

Figure 4-21 is a graphical solution for the deflection of the U-tube. For currents less than 5.75 amps, there are two points of intersection, or two possible deflections: a stable point A and an unstable point B. If the U-section is perturbed toward lower deflections, the magnetic force drops below the mechanical force needed to maintain its position and its deflection drops to point A, where it is stable. If it is perturbed toward higher deflections, the magnetic force is greater than needed and the deflection increases until the keeper contacts the pole face. Figure 4-22 is a graph of the achievable deflection versus current for an initial gap of 0.508 cm. Figure 4-23 is a graph of the achievable deflection versus initial gap for a fixed current of 5 A. For small gaps, the deflection is equal to the gap because the magnetic force in Figure 4-21 always lies above the necessary mechanical force. At a gap of about 0.45 cm, the magnetic force has dropped sufficiently that two the curves begin to intersect. Thereafter, the achievable deflection drops precipitously.

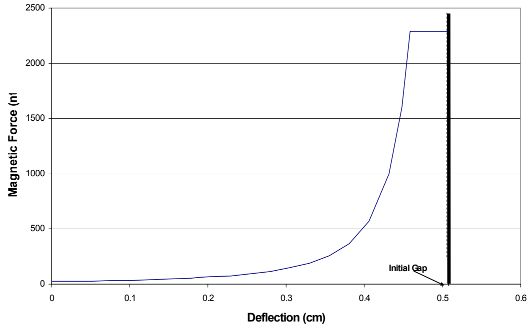

Figure 4-20 Magnetic force versus deflection for winding current of 5 A and initial gap 0.508 cm

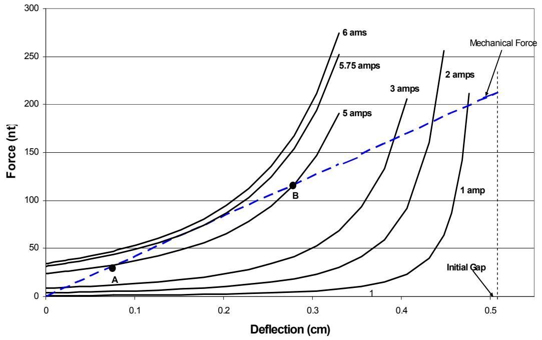

Figure 4-21 Mechanical and magnetic forces versus deflection for various winding currents. *Initial gap 0.508 cm (0.2 in.); force constant = 41,818 Nt/m.*

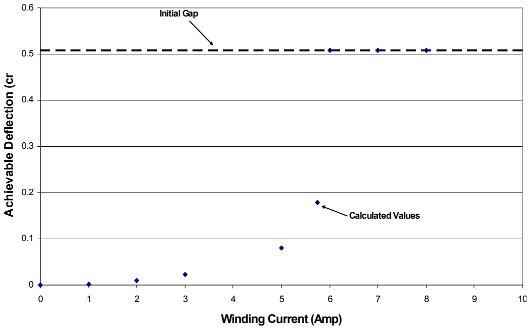

Figure 4-22 Achievable deflection versus winding current for initial gap 0.508 cm

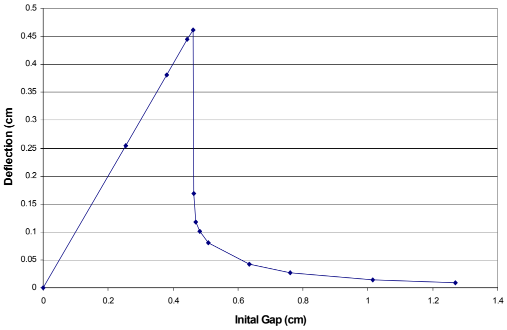

Figure 4-23 Achievable deflection versus initial gap for fixed current 5 A

4.4.2.2 Simulated FAC test 1 (uniform thinning)

The simulated FAC tests were repeated with pipes of different wall thickness to check the signal consistency between tests. These test utilized four fiber-optic displacement sensors, a capacitive sensor, and two 3-axis accelerometers. The test conditions included using specimens with three different thicknesses: SCH 10S (2.77 mm), SCH 20S (3.0 mm), and SCH 40S (3.56 mm). The tests were conducted at 20 bar pressure and ambient temperature with the pump turned on and off.

Figure 4-24 shows the sensor locations for simulated FAC test 1. The test objectives are to investigate the frequency change associated with fluid induced vibration caused by uniform thinning of different thickness pipes and verify the results of computational modal analysis. Table 4-1 represents a list of test description of the simulated FAC test 1.

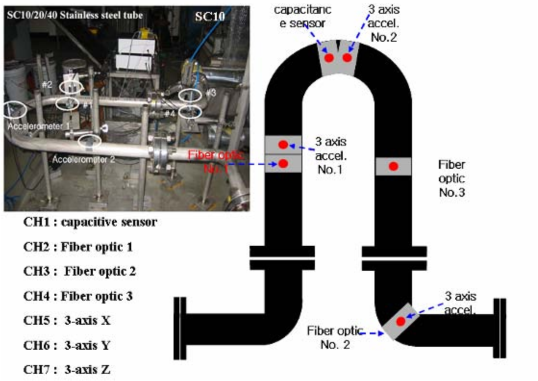

Figure 4-24 Sensor location for simulated FAC test 1

Table 4-1 A list of test description of simulated FAC test 1

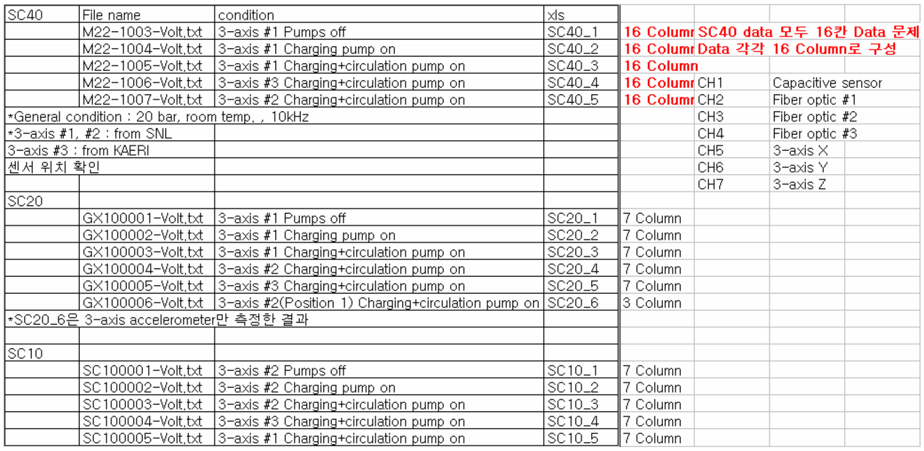

SC40	File name	condition	xls				
	M22-1003-Volt.txt	3-axis #1 Pumps off	SC40_1	16 Column	SC40 data 모두 16칸 Data 문제		
	M22-1004-Volt.txt	3-axis #1 Charging pump on	SC40_2	16 Column	Data 각각 16 Column로 구성		
	M22-1005-Volt.txt	3-axis #1 Charging+circulation pump on	SC40_3	16 Column			
	M22-1006-Volt.txt	3-axis #3 Charging+circulation pump on	SC40_4	16 Column	CH1	Capacitive sensor	
	M22-1007-Volt.txt	3-axis #2 Charging+circulation pump on	SC40_5	16 Column	CH2	Fiber optic #1	
*General condition : 20 bar, room temp., , 10kHz					CH3	Fiber optic #2	
*3-axis #1, #2 : from SNL					CH4	Fiber optic #3	
3-axis #3 : from KAERI					CH5	3-axis X	
센서 위치 확인					CH6	3-axis Y	
					CH7	3-axis Z	
SC20							
	GX100001-Volt.txt	3-axis #1 Pumps off	SC20_1	7 Column			
	GX100002-Volt.txt	3-axis #1 Charging pump on	SC20_2	7 Column			
	GX100003-Volt.txt	3-axis #1 Charging+circulation pump on	SC20_3	7 Column			
	GX100004-Volt.txt	3-axis #2 Charging+circulation pump on	SC20_4	7 Column			
	GX100005-Volt.txt	3-axis #3 Charging+circulation pump on	SC20_5	7 Column			
	GX100006-Volt.txt	3-axis #2(Position 1) Charging+circulation pump on	SC20_6	3 Column			
*SC20_6은 3-axis accelerometer만 측정한 결과							
SC10							
	SC100001-Volt.txt	3-axis #2 Pumps off	SC10_1	7 Column			
	SC100002-Volt.txt	3-axis #2 Charging pump on	SC10_2	7 Column			
	SC100003-Volt.txt	3-axis #2 Charging+circulation pump on	SC10_3	7 Column			
	SC100004-Volt.txt	3-axis #3 Charging+circulation pump on	SC10_4	7 Column			
	SC100005-Volt.txt	3-axis #1 Charging+circulation pump on	SC10_5	7 Column			

A 1-axis accelerometer was located on the pumps (charging and circulation pump) to acquire their dynamic data directly. These pump data were used to characterize flow induced vibration caused by pump and to filter and reduce pump noise signals.

4.4.2.3 Simulated FAC test 2 (non-uniform thinning)

Local areas of the target specimen were grinded in order to distinguish characteristic vibration mode change from global and local variations. First, outer surface of top part of the U-section and elbow was grinded. Only one 3-axis accelerometer was used to monitor the vibration change cause by local degradation. In the case of the outer surface of the top part of U-tube with an initial diameter of 40.4 mm, gradual grinding took place every 0.5 mm until the final measurement of 39.2 mm. In the case of the outer surface of the top part of elbow with an initial diameter of about 43 mm, similar gradual grinding also took place every 0.5 mm until the final measurement of about 41.5 mm. Since the original thickness of the piping is approximately 3.7 mm, a total 1.5 mm was grinded resulting in a 40% of thickness reduction. Figure 4-25 shows the grinding locations at the outer surfaces.

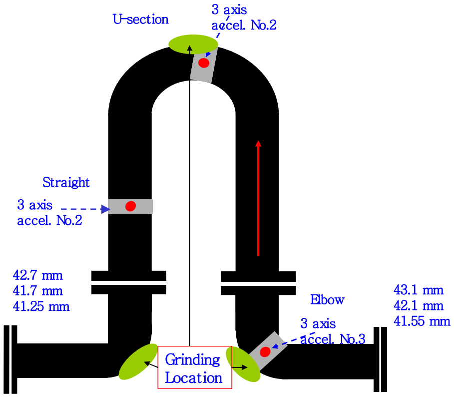

Figure 4-25 Grinding locations at outer surfaces

Second, inner surface of top part of elbow was ground, starting with an initial elbow thickness of elbow of about 3.9 mm and gradually grinding every 1.0 mm until a final measurement of 0.67 mm. The grinding process resulted in a 82% of the thickness reduction. Figure 4-26 shows the grinding locations at the inner surface. 3-axis accelerometers were used in this test series.

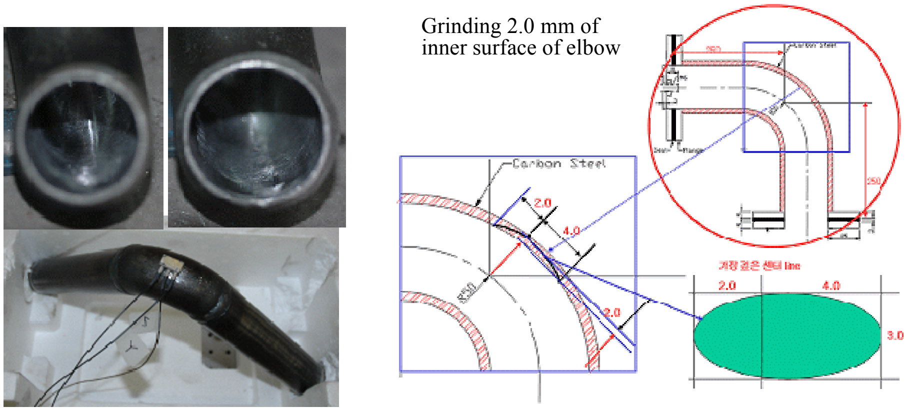

Figure 4-26 Grinding locations at the inner surface

4.4.3 FAC chemical testing

The operating conditions for the chemical test series are described in Table 4-2.

Table 4-2 Operating conditions for chemical test series

	Temp.(°C)	Flow velocity (m/s)	Cr content (%)	pH	
				calculated	monitored
1st trial	120	1.1	0.4	4	5-6
2nd trial	110	3.2	0.4	3.7	5-6
3rd trial	100	3	0.01	3.4	4-5

4.4.3.1 Environmental condition

There is a group of parameters affecting the FAC rate. These parameters including temperature, flow velocity, material composition and also ECP and pH of water were investigated in the test loop of piping elbow. Relations between these parameters and the FAC rate are shown in Figure 4-27, Figure 4-28, Figure 4-29, and Figure 4-30:

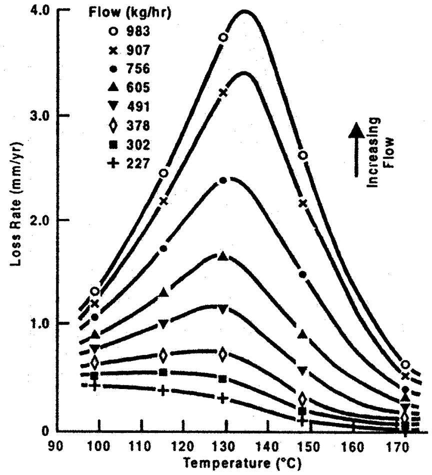

Figure 4-27 Temperature and flow velocity dependency of FAC rate

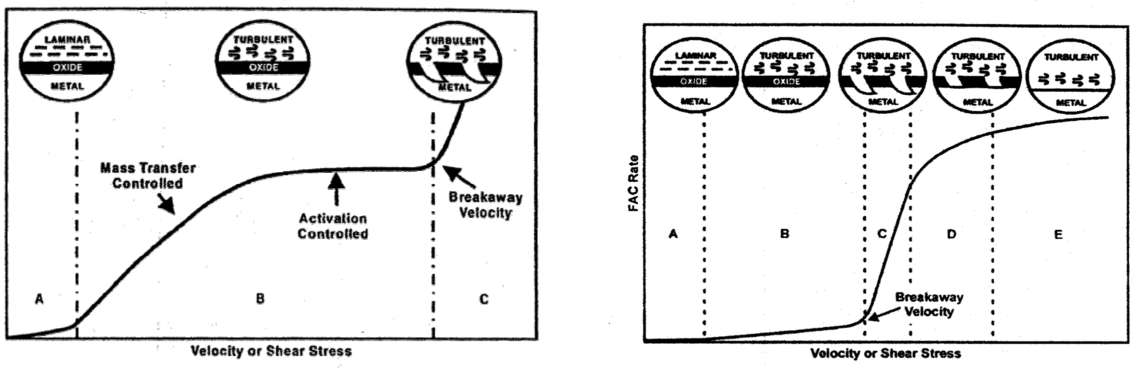

Figure 4-28 Schematic diagram of FAC rate with changing flow velocity

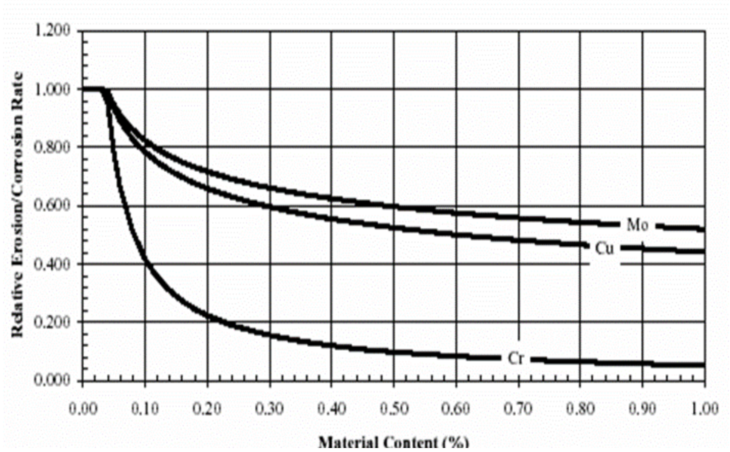

Figure 4-29 Effect of alloy content on erosion/corrosion rate.

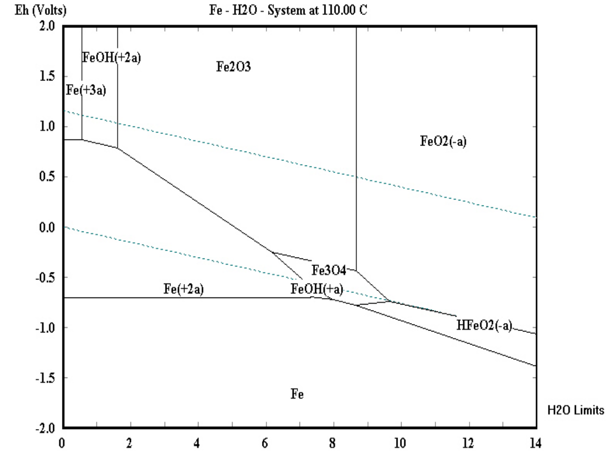

Figure 4-30 Pourbaix diagram at 110°C

4.4.3.2 Mechanical vibration conditions

A realistic FAC condition was simulated to control the corrosive condition for piping system, elbow, and U-section. Non-uniform local thinning on the inner surface of elbow and U-section occurred due to corrosion. The piping system wall thinning induced a change of fluid dynamics, resulting in a change of vibration mode in terms of frequency and amplitude. The operating conditions for the FAC tests are described here:

- Sensors: 3-axis accelerometer
- Measurement condition: 20 bar at 120°C
- Chemical condition: pH 4~5
- Flow velocity: 3.3 m/s (for corrosion), 1.3 m/s (measuring vibration)
- With charging pump (charging rate at 40 cc/min) and circulation pump on.

4.4.3.3 Analysis of wearing rate

ECP and pH are the main monitoring parameters in the test series. The MULTEQ code was used to calculate the proper amount of chemicals needed to obtain the required pH level. To control the ECP, the oxygen inside the test loop was removed by 5% hydrogen bubbling. The Sanchez-Caldera model, which is a theoretical model that can predict the rate of materials reduction induced by FAC, was used to calculate the corrosion rate in the test series.

$$\frac{dm}{dt} = k_g \frac{\theta(C_e - C_\infty)}{\frac{1}{k} + (1-f)\left[\frac{1}{h_D} + \frac{\delta}{D}\right]} \tag{1}$$

where $\frac{dm}{dt} = \text{wear rate}[\text{kg/m}^2\text{s}]$

$k_g = \text{geometrial factor}$

$C_e = \text{equilibrium concentraion of iron species}[\text{kg/m}^3]$

$C_\infty = \text{iron species concentraion in the bulk water}[\text{kg/m}^3]$

$\theta = \text{porosity}$

$k = A\exp(-Q/RT)$, the reaction rate constant[m/s]

$f = \text{fraction of oxidized metal converted into magnetite at the metal-oxide interface}$ (constant $f = 0.5$)

$h_D = \text{mass transfer coefficient}\ [\text{m/s}]$

$\delta = \text{oxide thickness}[\text{m}]$

$D = \text{diffusion coefficient of the dissolved ferrous species}[\text{m}^2/\text{s}]$

The original Sanchez-Caldera model does not include the geometrical factor. To apply this model, which considers straight pipe condition only, to complex geometry, such as piping elbow, geometrical factor, k_g was introduced. All the parameters are determined from calculations, and almost of the values are chosen from the theoretical data book. The analysis of wearing rate is discussed in detail in Appendix C, Section II.

Development of pre-amplifier

The pre-amplifier was designed to measure chemical sensor signals related to the erosion of the piping elbow. The pre-amplifier was custom-made for this chemical test series because it is essential to use a differential amplifier that can detect differences AUEN and EREP sensors. The pre-amplifier is composed of differential amplifier logic, as shown in Figure 4-31. In this figure, R2 is variable resistor to prevent output that might occur by resistor error under no input condition. In addition, R1 is composed of variable resistor so that the amplifier gain is regulated correctly. The power supply used a series regulator to reduce noise and ripple that might be associated with a switching power. The test loop has two amplifiers linked by a connector for easily change when composition is out of order. The cable is an insulated wire to help prevent noises. Pre-amplifier was installed on each of the two AUEN and EREP sensors. The AUEN was supplied 350 mV and the EREP 1V. Figure 4-32 shows the inside view of the developed amplifier.

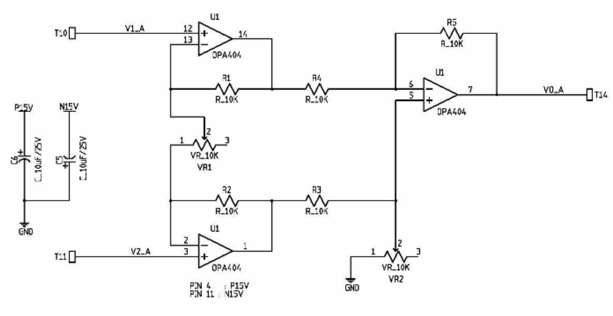

Figure 4-31 Circuit layout showing the differential amplifier logic

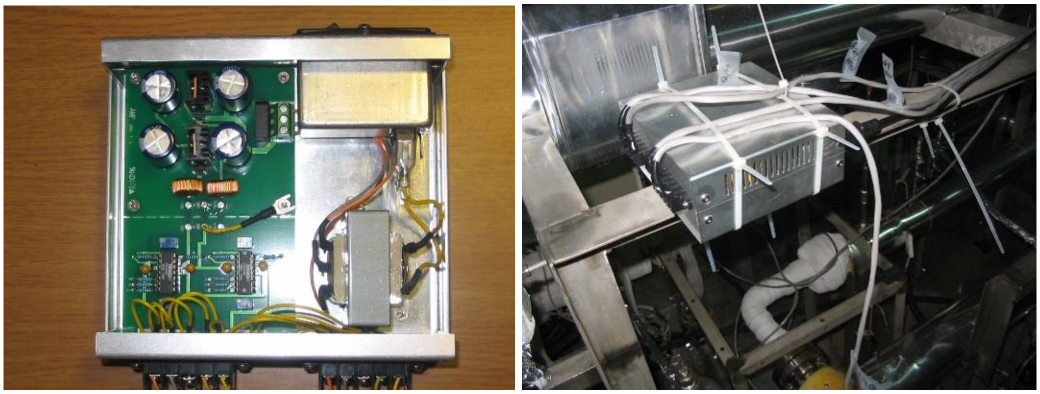

Figure 4-32 Inside of amplifier and installed amplifier on test loop

4.4.4 Test results and discussion

4.4.4.1 Characteristics of frequency

Magnetic pull-down tests

The purpose of the magnetic pull-down test is to provide as simple and clean an experiment as possible to study the performance of selected sensors, the DAS, and the effect of wall-thinning of the U-section of piping on its vibration characteristics,. The test series was conducted with the pump off and on to avoid unwanted vibrations.

The frequency response characteristics of the signals from the pull-down tests have been evaluated. An accelerometer and a capacitance displacement sensor were used to acquire vibration signals and compare them to those from the fiber-optic sensor. The 3-axis accelerometer was the Endevco model 65HT-10 and its resonance frequency was 25 kHz. The capacitance displacement sensor was the part # DT 6100 by Micro Epsilon.

Figure 4-33 shows the results of the frequency response of the fiber-optic displacement sensor in comparison with the signals of an accelerometer and a capacitance displacement sensor from the pull-down test in a rocking mode There were the dominant peaks at about 8 Hz and 16 Hz, which seem to be the natural frequency, harmonic motions in piping system itself. These test findings are not in good agreement with the finite element analysis results that predicted the first mode at 16 Hz. The peak from the fiber optic sensor was clearer and sharper than that from the other sensors.

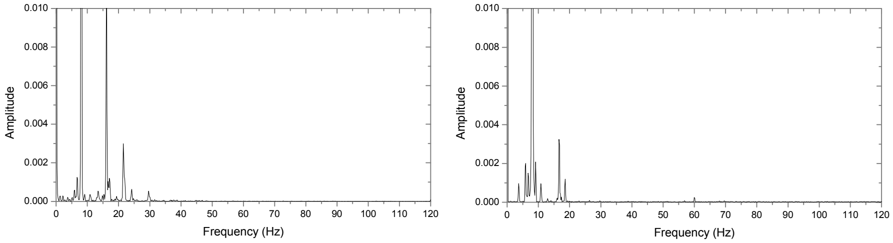

a) Fiber Optic Displacement sensor b) Capacitance Displacement sensor

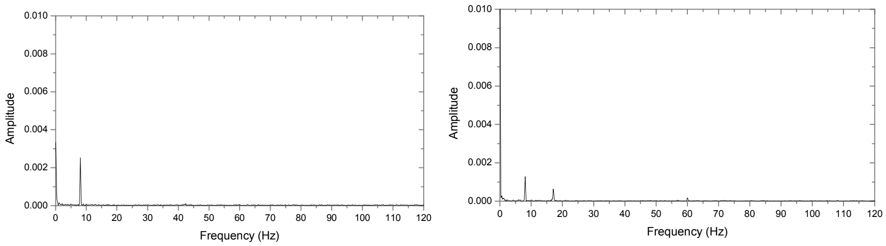

c) Z-axis Accelerometer d) Y-axis Accelerometer

Figure 4-33 Sensitivity comparison

There were dominant peaks in the vicinity of 8 Hz and 22 Hz in the low frequency range for the cases of the pump off and a charging pump on, respectively. The more dominant peaks were found at about 40 Hz and 90 Hz with the circulating pump on. In addition, there was an electrical noise at 60 Hz and 120 Hz. In the case of the pump on, the amplitude of the peak was larger and new peaks appeared. Figure 4-34 illustrates the frequency shift from 21 Hz to 16 Hz, due to operating the circulation pump.

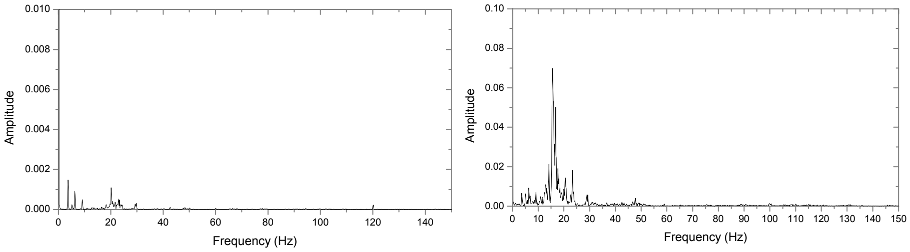

a) No Pump b) Circulation Pump on

Figure 4-34 Frequency shift by pump on

Figure 4-35 illustrates the results of the frequency response of a low and high frequency at the steady condition of a pull-down test. There were dominant peaks near 8 Hz and 22 Hz in the case of the pump off and a charging pump on. In the low frequency, less than 350 Hz, the response of signals of the optical sensor is very sensitive. The spectrum shows that the dominant frequency of piping elbow appears around 350 Hz when flow exists, as shown in Figure 4-35. In the high frequency, there were several mode changes of frequency around 1350, 2000, 3400, 3700 Hz. On the other hand, there were several mode changes of frequency around 1600, 2550, 3100, 3600 Hz from the model analysis results. Their result is coincident with a prediction about a change of vibration mode by modal analysis, especially, in the range of less than 50 Hz, there is a very sensitive change in the modal frequencies. For the frequency range of the piping elbow, the greatest shift in response was to occur in the range of 250 Hz and 1000 Hz.

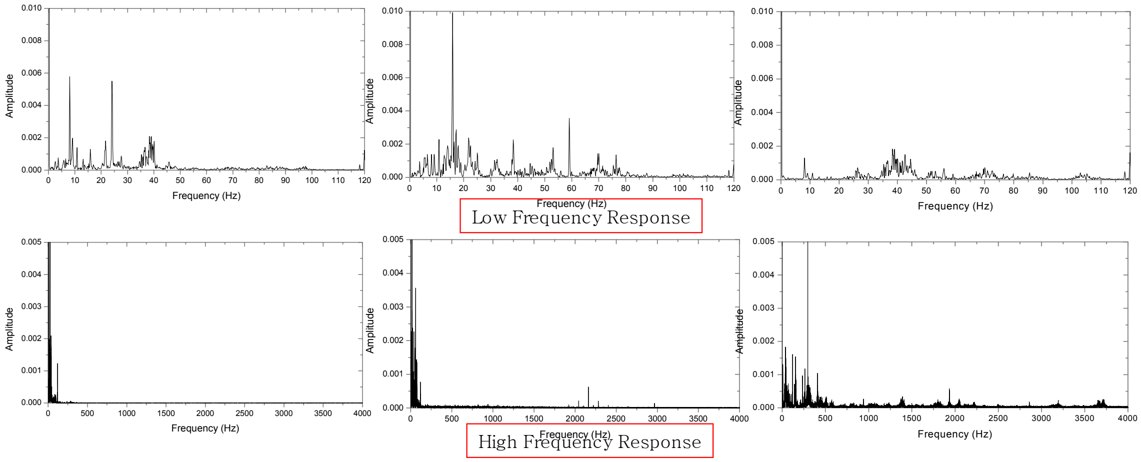

a) Fiber Optic Displacement sensor
b) Capacitance Displacement sensor
(SC40_CH_CIR_PW_24.2_Yt_1)
c) Z-axis Accelerometer

Figure 4-35 Frequency response on the low and high frequency ranges

Pump noise and simulated FAC test 1 (uniform thinning)

It is important to predict the mechanical behavior and vibration signal properties from pump. In general, there is a resonance frequency from the pump impeller. There are two kinds of pump in the FAC test loop, charging pump and circulation pump. Figure 4-36 shows a frequency response of signals measured in the test loop. In case of charging pump on, its signals are identical with no pump. In addition, their signals are identical in case of circulation pump on and both charging pump and circulation pump on. The noise signals from charging pump are to be isolated to minimize their effect on the fluid dynamics in the test loop. A frequency response of signals directly measured on the charging pump (up) and circulation pump(down) is shown in the left side of Figure 4-37. The right side of this figure shows a frequency response of signals of the charging pump (up) and circulation pump (down) indirectly measured on the elbow in the test loop. It also shows that dynamics from charging pump do not affect fluid dynamics in the test loop. In case of circulation pump on in the bottom of the figure, it seems that dynamics from circulation pump affects fluid dynamics in the test loop. However, it is important to identify the signal from circulation pump because fluid dynamics from circulation pump are responsible for the flow-induced vibration in the test loop.

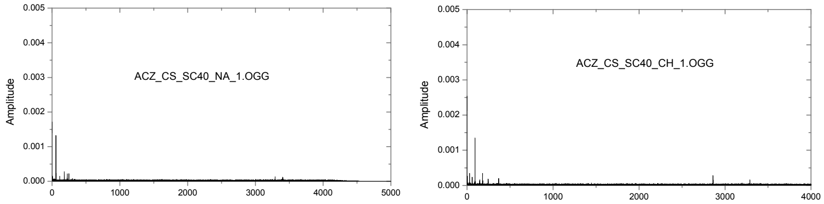

a) No pump
b) Charging pump on

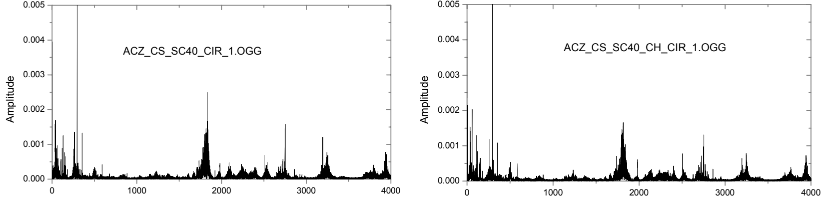

c) Circulation pump on
d) Charging & Circulation pump on

Figure 4-36 Frequency responses of signals measured in the test loop

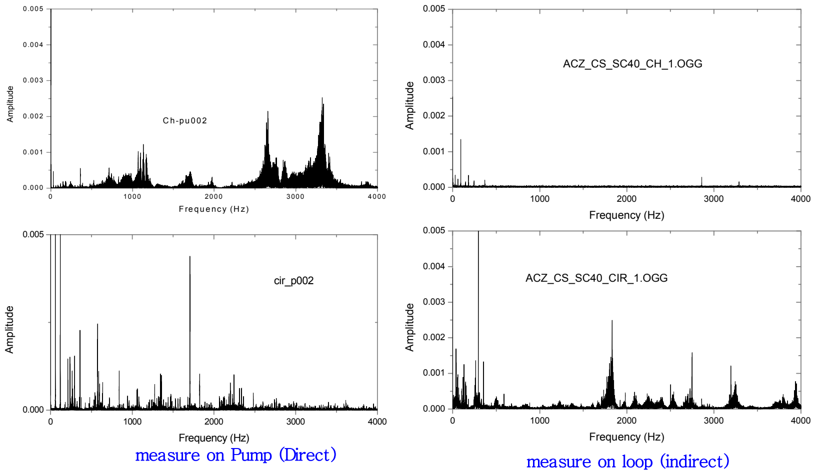

Figure 4-37 Frequency responses of signals directly and indirectly measured

There are two reasons for a vibration mode change in the inner wall of piping system. One is a change of mass of piping system, and another is a change of the fluid dynamics in the piping system. Figure 4-38 shows the result of frequency response of simulated FAC test 1. It simulated uniform thinning of piping system for three different thickness specimens, SCH 10S (2.77 mm), SCH 20S (3.0 mm), SCH 40S (3.56 mm). The top portion of Figure 4-38 shows a result of FFT (Fast Fourier Transform), and the bottom shows a result of MUSIC tool. The data was measured from the top of elbow. As predicted, a change of mass of piping system caused a change of frequency responses. From the result of frequency response of simulated FAC test 1, a mode change of vibration due to FIV for three different thickness pipes can be distinguished effectively, but cannot observe a frequency shift.Table 4-3 4-3 represents a summary of frequency responses of simulated FAC test 1.

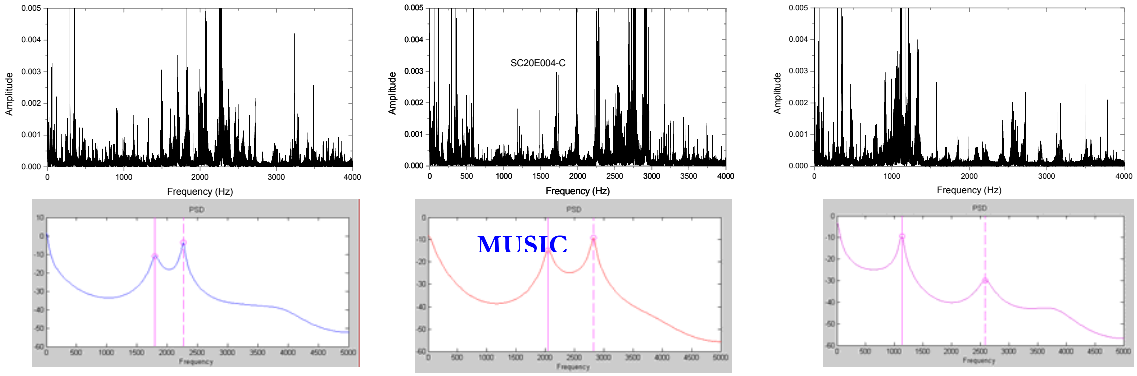

a) SC 10 Elbow Pipe

b) SC 20 Elbow Pipe

c) SC 40 Elbow Pipe

Figure 4-38 A result of frequency response of simulated FAC test 1

Table 4-3 A summary of frequency responses of simulated FAC test 1

Specimen	1st Peak	2nd Peak	3rd Peak	Specimen	1st Peak	2nd Peak	3rd Peak
SC40 Elbow	1100	2600	3800	SC40 U-sec	3000	1150	3700
SC20 Elbow	2800	2050		SC20 U-sec	950	2050	3850
SC10 Elbow	2250	1600	3850	SC10 U-sec	3130	2150	4030

MUSIC algorithm: Eigen Pseudo Spectrum (EPST) have two desirable characteristics: a response to the degree of variance of a signal regardless of the degree of harmonic content within signal, and a response to low power components of signal. The MUSIC algorithm estimates the pseudo-spectrum from a signal or a correlation matrix using Schmidt's eigen-space analysis method. The algorithm performs eigen-space analysis of the signal's correlation matrix to estimate the signal's frequency content. Because of these benefits, MUSIC algorithm for spectrum estimation was used to find the particular frequency of flow-induced vibration. Unfortunately, most of FAC test data had a very low SNR (signal to noise ratio). Therefore, analytical techniques that are less influenced by SNR are possibly promising for use in fault classification. Among the existing techniques, eigen-decomposition methods are applied to produce a pseudo-spectrum to monitoring the vibration mode changes due to thinning of piping elbow. The FFT can be computed for each eigenvector of the correlation matrix and then the squared magnitudes can be summed to allow the complicated peaks in FFT to be simply represented to a few peaks by the MUSIC algorithm. Figure 4-39 shows the results using the MUSIC algorithm of test data measured on SC40 elbow.

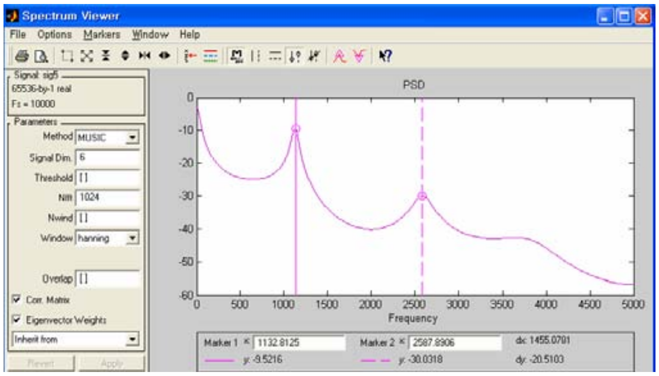
Signal: sig5
65536-by-1 real
Fs = 10000
Parameters
Method: MUSIC
Signal Dim.: 6
Threshold: [ ]
Nfft: 1024
Nwind: [ ]
Window: hanning
Overlap: [ ]
☑ Corr. Matrix
☑ Eigenvector Weights
Inherit from
Marker 1 x: 1132.8125 y: -9.5216
Marker 2 x: 2587.8906 y: -30.0318
dx: 1455.0781
dy: -20.5103

Figure 4-39 Results using MUSIC algorithm for SC40 elbow

Time-frequency analysis: A time frequency representation (TFR) method, the Wavelet-Vaguelette deconvolution (WVD) and Exponential Distribution, for an analysis of wall-thinning data, was explored to confirm the temporal variation of the spectral characteristics of a non-stationary signal of simulated-FAC Test 1. In applying the TFR method, a total of 65536 measured data was divided to the data groups with 1024 data. 10th, 20th, 30th, 40th, 50th and 60th data groups of these data groups were analyzed using the TFR method. Figure 4-40 shows the analyzed results of signal characteristics. The particular frequency was shown around 1.7, 1.9, 2.1 and 2.3 kHz. Its frequency keeps, to some degree, on a steady peak in the time domain. Therefore, test signals were confirmed to be stationary to some degree.

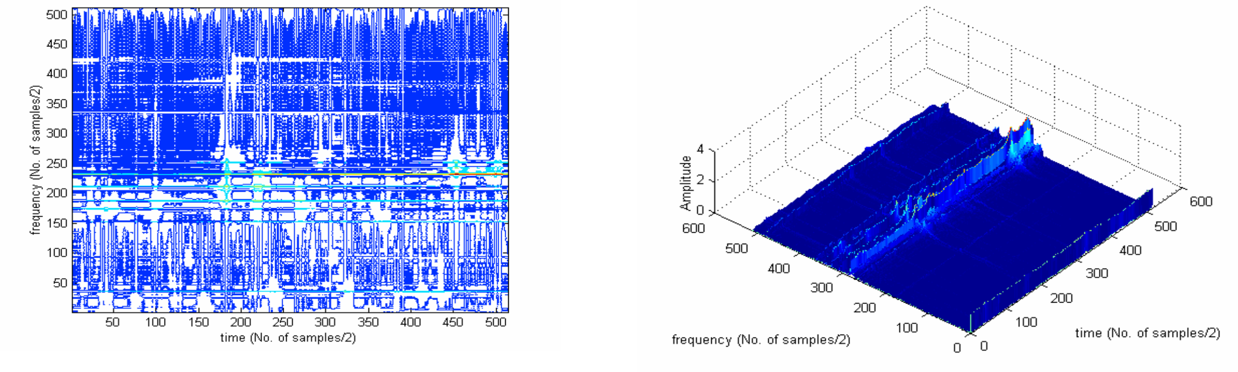

SC10E005-C

(a) 30th Contour **(b) 30th Mesh**

Figure 4-40 Results of signal characteristics using TFR method

Simulated FAC test 2 (non-uniform thinning)

In general, the corrosion/erosion process does not cause uniform degradation in a piping system because the fluid dynamics varies along the course of the piping system. Piping elbow and U-section are usually subjected to a higher degree of degradation because of the rapid change of local flow profile. To simulate non-uniform thinning of piping system, outer wall of elbow and U-section of SCH 40S (3.56 mm) specimen was grinded. The original piping thickness is 3.7 mm and a total of 1.5 mm of wall thickness was grinded to represent a 40% of total thickness reduction. Figure 4-41 shows the results of frequency response of simulated FAC test 2 for non-uniform thinning of piping system. The sampling frequencies were 20 KHz. The top portions of figures are data for no grinding condition, middle portions are data for 1.0 mm grinding condition, and bottom portions are data for 1.5 mm grinding condition. These plots indicate that the changes in frequency and vibration mode caused by non-uniform thinning of pipes cannot be distinguished effectively. Possible explanation of this observation may be that there was only a small amount of mass reduction due to non-uniform thinning of pipes and the local fluid dynamics was not affected because grinding took place on the outer pipe surface. Table 4-4 represents a summary of frequency responses of simulated FAC test 2, acquired at the straight portion of U-section.

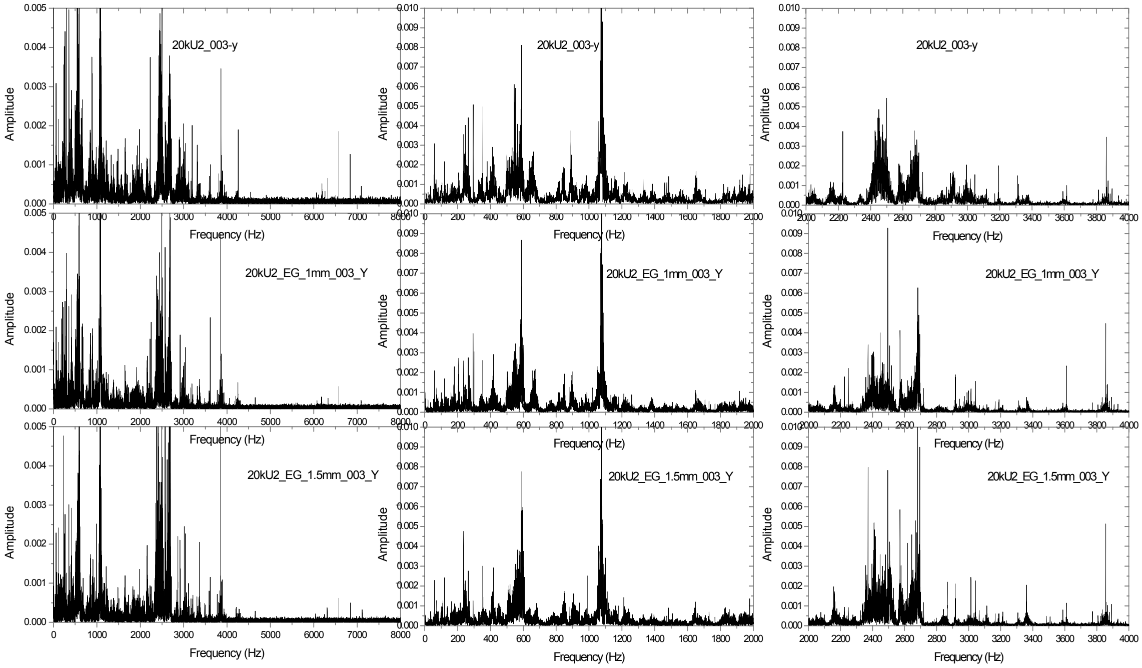

Figure 4-41 Frequency response of simulated FAC test 2 for non-uniform thinning

Table 4-4 Summaries of frequency responses of simulated FAC test 2

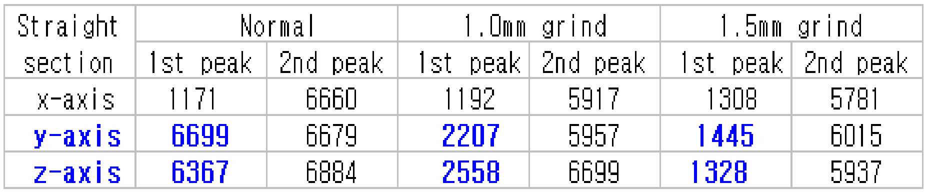

Straight	Normal		1.0mm grind		1.5mm grind	
section	1st peak	2nd peak	1st peak	2nd peak	1st peak	2nd peak
x-axis	1171	6660	1192	5917	1308	5781
y-axis	**6699**	6679	**2207**	5957	**1445**	6015
z-axis	**6367**	6884	**2558**	6699	**1328**	5937

Lesson learned for improvement of monitoring environment

From the experiences accumulated from the magnetic pull-down tests, and the simulated FAC tests, the project team learned that it was more beneficial to use 3-axis accelerometers and install them at strategic locations shown in Figure 4-42.

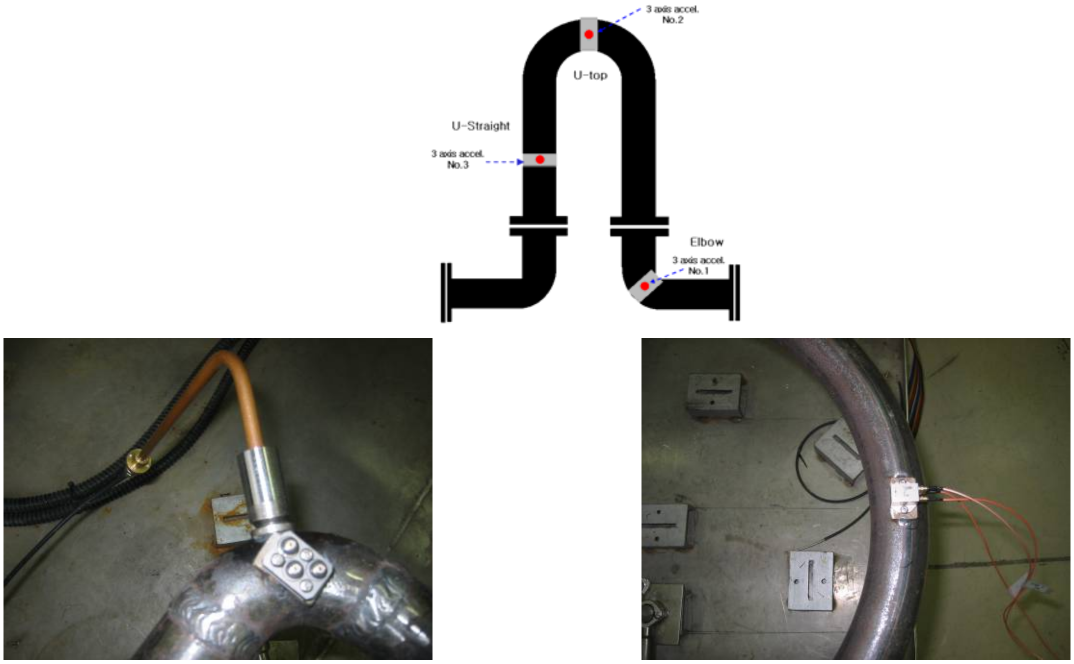

(a) Sensor installed at elbow **(b) Sensor installed at U-top**

(c) Sensor installed at straight section **(d) Signal conditioner**

Figure 4-42 Locations of 3-axis accelerometer installation

4.5 Task 2.5: signal data processing analyses for noise filtering and pattern recognition

Performed by SNL, PSU, and CNU

4.5.1 Integrated approach with fusion sensor concept

FAC a chemical process whereby the normally protective oxide layer on carbon or low-alloy steel dissolves into a stream of flowing water or a water-steam mixture. FAC consists of two main processes. The first process is to form soluble ferrous ions at the oxide film/solution interface and followed with the second process of diffusion of those ions to the solution. One of the main FAC rate controlling steps is the diffusion of ferrous ions through the boundary layer. Figure 4-50 shows this diffusion boundary layer near the oxide film. Generally, a laminar flow is formed at the inner boundary layer and a turbulent flow at the outer boundary layer. As the flow velocity increases, the width of the laminar layer decreases and the diffusion rate of the ferrous ion increases. A chain of these processes brings about the wall thinning of piping system, especially elbow and u-section pipe. Piping degradation mechanism is related to FAC process and flow rate. The U-section and piping systems are operating in a very aggressive erosion/corrosion environment of turbulent flow and high temperature and pressure. These adverse operating environments make a piping system very vulnerable to accelerated wear and degradation.

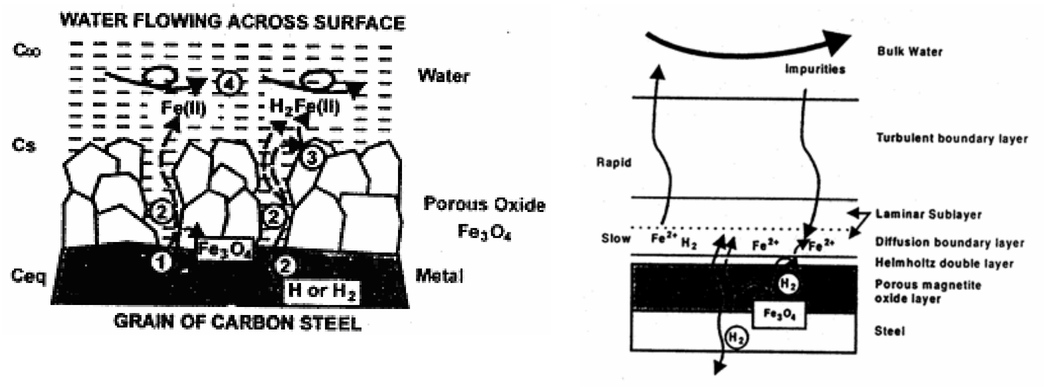

Figure 4-43 FAC corrosion phenomenon

Since FAC is a global corrosion phenomenon, wide spread wall thinning takes place inside the piping system. There are usually changes in local vibration frequencies and modes associated with changes in fluid dynamics caused by pipe wall thinning. However, the changes in vibration characteristics are small and thus very difficult to detect and identify owing to small amounts of degradation of piping. The task of acquiring clear recognizable vibration signals becomes increasingly challenging in a noisy background vibration due to pump and/or support fixtures. Therefore, an array of parameters must be monitored to detect and identify FAC phenomenon. Integrated approach using the fusion sensor concept was adopted to monitor these parameters to acquire a cohesive set of sensor data. Figure 4-44 shows the integrated approach with the fusion sensor concept, which consists of the following key components:

1. Electrochemical electrodes to monitor chemical conditions: ECP and pH
2. Mechanical sensors to monitor vibration characteristics
   - Flow induced vibration - using micro accelerometer, optical fiber sensor, and capacitance sensor
   - Thickness affected vibration - using ultrasonic devices
3. Application of new signal processing algorithm to amplify signal output with special sensor
   - Neural Network
   - Time-Frequency Distribution
   - Wavelet

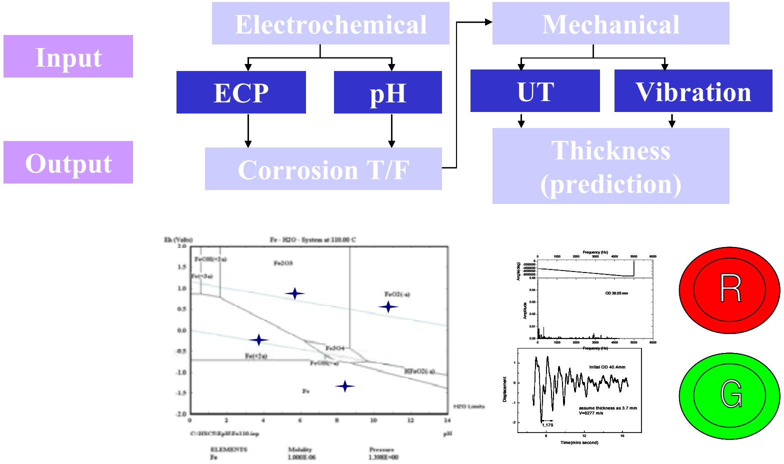

Figure 4-44 Integrated approach with fusion sensor concept

4.5.1.1 UT monitoring

The ultrasonic technique is widely used to evaluate the material integrity in the industry at ambient temperature. Since the UT has good directionality and easily reflects at the boundary of different medium, it is very convenient to use to measure local thickness. Recently, a UT was used in the NPPs to inspect defects during overhaul. Therefore, it cannot only validate the vibration monitoring by direct measurement of pipe wall thickness, but it can also be employed as an alternative for on-line monitoring. In this project, the applicability of the 5 MHz Krautkramer Branson USD15 UT at high temperature was examined. This UT was implemented with a special shoe to protect the piezoelectric element from exposure to high temperature.

In the FAC tests, the high temperature UT (HTUT) was installed with a screw thread at the corner of the carbon steel elbow where the maximum reduction of thickness is assumed to occur. However, it is very difficult to discriminate the signal of the target specimen from that of HTUT shoe. Figure 4-45 shows the measured HTUT signal from first FAC test. In each trial, UT shows similar behavior, which means most of ultrasonic signals may not be transmitted to specimen but reflected at the boundary of HTUT and elbow. Figure 4-46 shows the signal reflected at the shoe surface. There are two possible explanations for this observation. First, the reflected ultrasonic wave from the carbon steel pipe wall is weakened through the HTUT shoe. As it is an intrinsic effect, it has no room for improvement of a signal. Second, the point contact of HTUT (flat surface) and the corner of elbow (round surface) were too limited to transmit a sufficient ultrasonic signal. Therefore, a better signal could be achieved through improving the attachment of HTUT to an elbow.

Two methods were examined to improve the attachment of UT to elbow. One is to use an acrylic wedge, the other is to flatten the corner of round elbow to increase the contact area at the interface and make airtight contact. Acrylic wedge method is generally used in the curved-surface measuring.

Figure 4-47 shows the HTUT equipped with wedge. Since acrylic is very sensitive to temperature, it is not suitable as an online monitoring sensor for a long time but it may be possible to provide thickness information during the short measuring time. Unfortunately, in the case of HTUT, however, reflected signals were extremely attenuated, as shown in the Figure 4-48.

A trial test was conducted to measure the thickness of an attachment plate to investigate the effect of shoe thickness on the UT signal the capability of measuring thickness. Figure 4-49 shows the results of direct measurement of plate to demonstrate the excellent performance of HTUT with the attachment plate. Therefore, the second option was adopted in the FAC tests by flattening the carbon steel elbow with a milling machine. Figure 4-50 and Figure 4-51 show the installed HTUT at the flattened elbow and the distinguishable signals from this setup, respectively. A test on large-radius piping similar to the main steam line (MSL) in the NPP was conducted to examine the application of this monitoring technique. Since the MSL has a large radius, it has a flat surface to allow thickness measurement without machining the surface. Figure 4-52 shows the direct measurement of MSL.

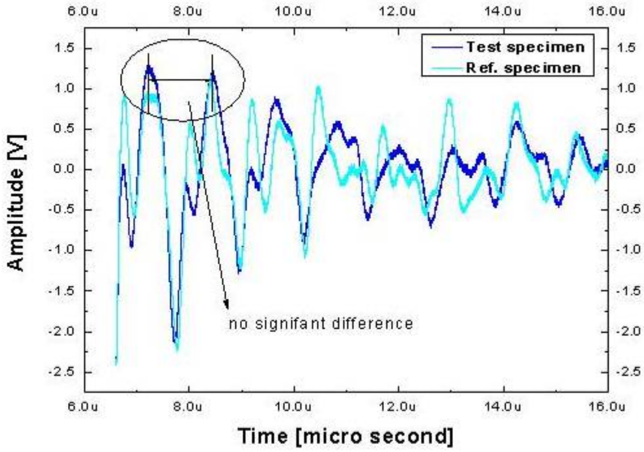

Figure 4-45 Result of HTUT monitoring from first FAC test

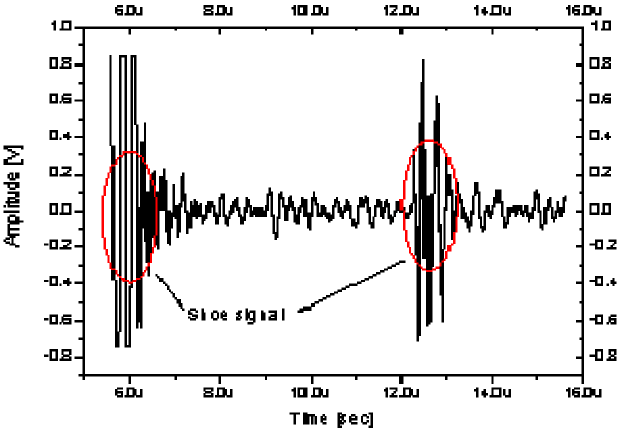

Figure 4-46 UT signal reflected on the shoe surface

(a) Acrylic wedge (b) Installation the HTUT using acrylic wedge

Figure 4-47 Acrylic wedges

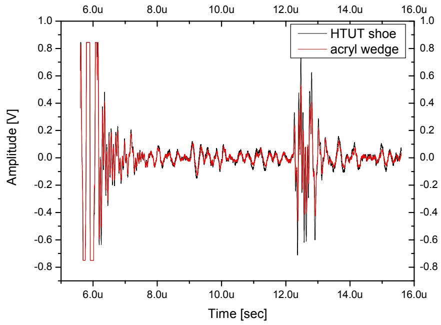

Figure 4-48 Comparison of UT signals with and without wedge

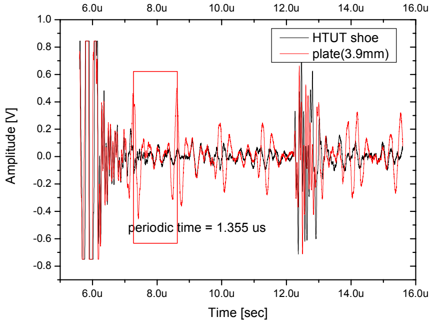

Figure 4-49 Direct measurement of attachment plate

Figure 4-50 Flattened surface of elbow

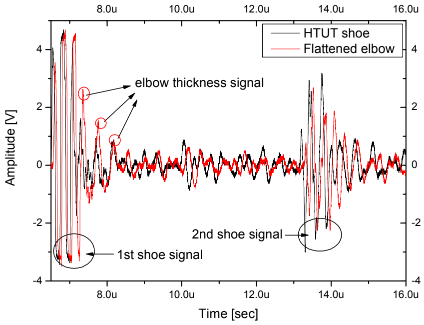

Figure 4-51 Signal from the flattened elbow

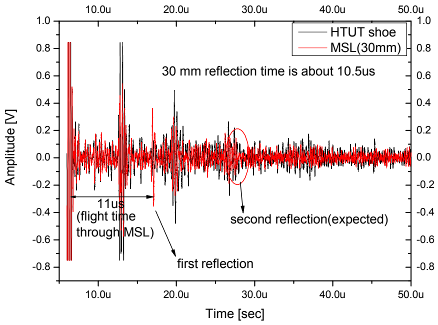

Figure 4-52 Direct measurement of MSL

4.5.2 FAC test results

The integrated approach with fusion sensors was adopted in the FAC tests. The details of the test conduct and sensor data are discussed in the following subsections.

4.5.2.1 First FAC test

After all preliminary tests, all selected sensors were installed in the test loop to conduct on-line monitoring performance at the high temperature condition and to confirm whether FAC susceptibility could be quantitatively correlated with ECP and pH. In this test, reference electrodes, Ag/AgCl water-filled electrode and gold-plated Ni electrode for ECP and pH measurements were developed for high temperature.

Figure 4-53 shows the expected chemical reactions in the specific regions. After 12 days of operation, the graphs for ECP/pH and the corresponding Pourbaix diagram was obtained, as shown in Figure 4-54. Figure 4-55 shows the FFT analysis results for the monitored vibrations.

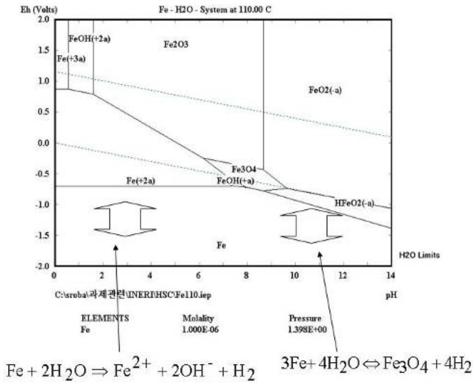

Figure 4-53 Expected chemical reactions

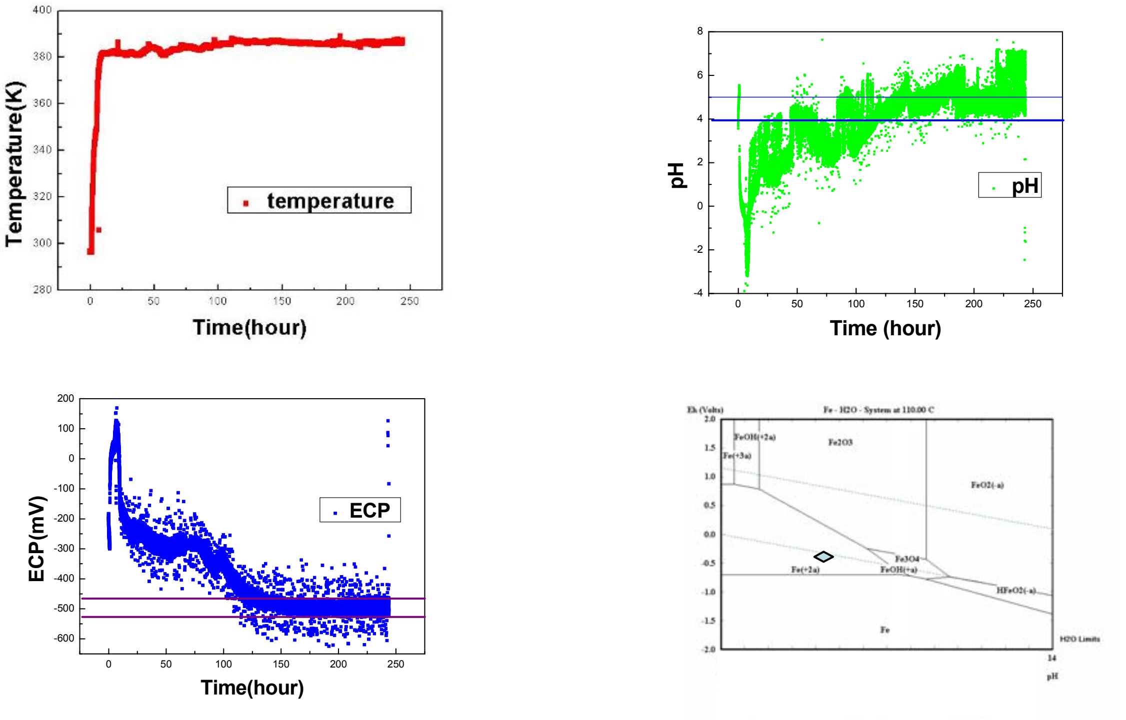

Figure 4-54 Temperature, pH, ECP, and the corresponding Pourbaix diagram

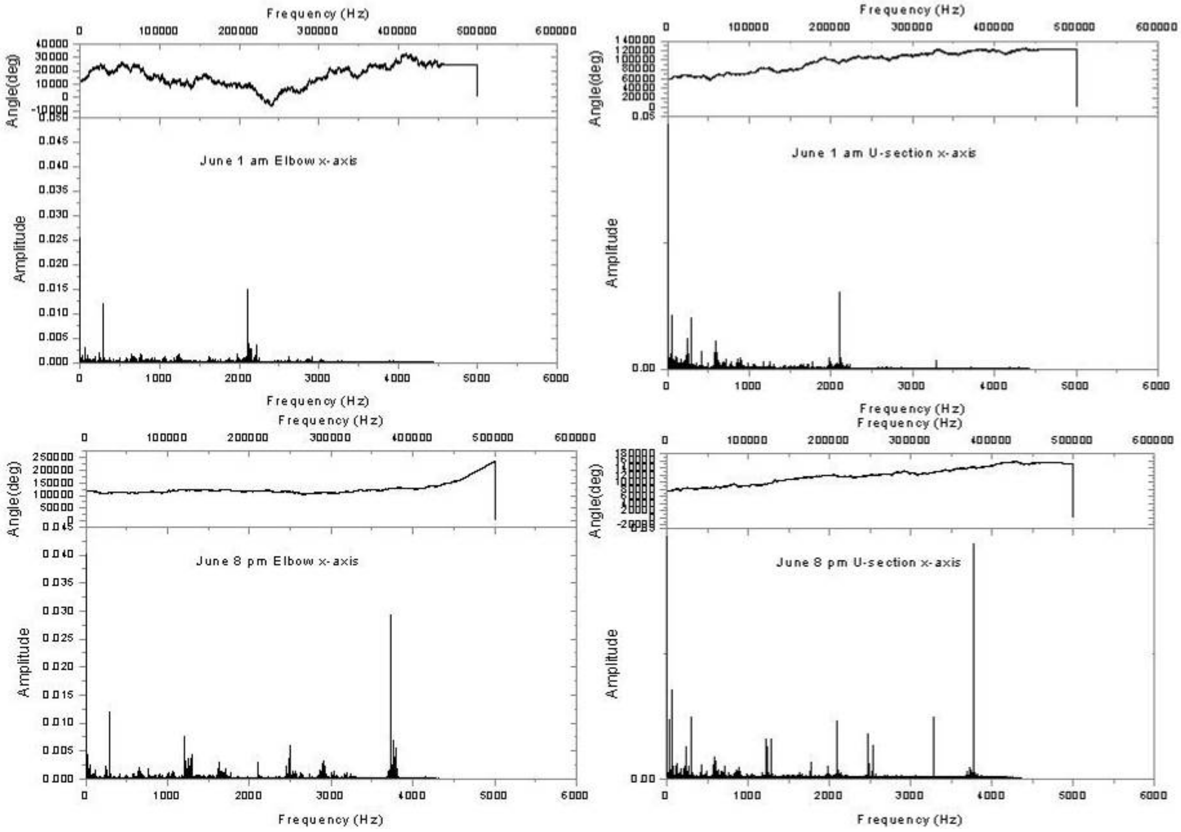

Figure 4-55 Vibration mode change after 12 days of operation

Test results are summarized as follows:

- Verify performance and functionality of selected sensors
- Electrochemical parameters show clear evidence of corrosion
- UT signal does not show clear thickness reduction.

4.5.2.2 Second FAC test

In the second test series, additional protection of signal wires for the vibration sensors was installed, accelerometers were anchored with bolts, and the flow velocity was increased by three times. The FFT method was applied to analyze signals from accelerometers to detect changes in vibration modes of the piping system due to a reduction of its thickness during the test. Figure 4-56 and Figure 4-57 show the FFT analysis results for top and straight portions of the U-tube, respectively. In these plots, the test results demonstrate vibration mode changes of the piping system, similar to those from the first test, but the changes are small indicating that the local pipe thinning is less than expected.

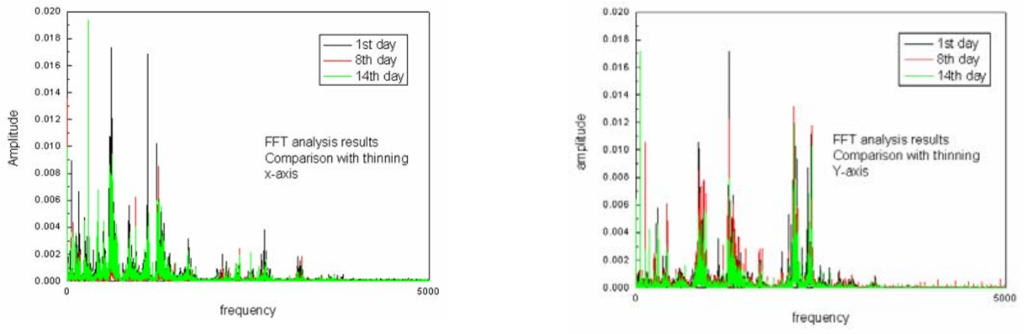

(a) FFT analysis results in x-axis

(b) FFT analysis results in y-axis

Figure 4-56 FFT analysis results of top portion of U-tube

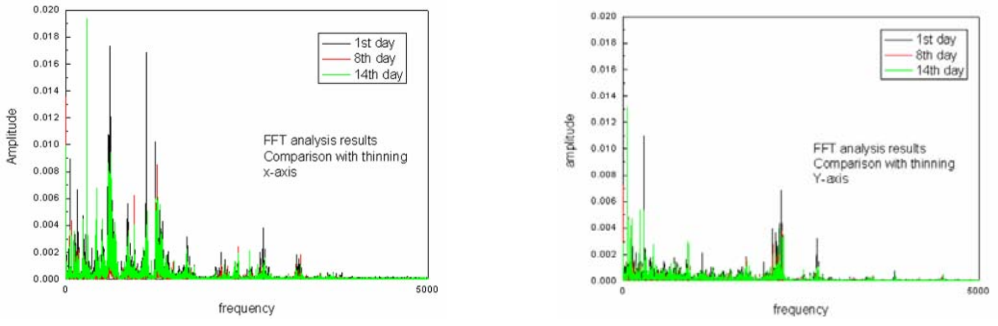

(a) FFT analysis results in x-axis

(b) FFT analysis results in y-axis

Figure 4-57 FFT analysis results of straight portion of U-tube

4.5.2.3 Third FAC test

During the first two tests, test specimen did not erode as much as expected. Detailed examination of the test conduct yielded the following improvements to the test conditions:

- First, the test specimen contained more chromium than specified; therefore, new elbows were manufactured with carbon steel of less chromium content. In the third test, only one elbow is carbon steel and the other elbow is stainless steel for safety reasons.
- Second, the test temperature range was lower than that required for the higher FAC rate. The third test series was conducted at around 120°C to 130°C.

- Third, the flow velocity was too low and it was increased from 1.2 m/s to 3 m/s in the third test series.

During the first two tests, there was an observed gradual increase in pH as the test proceeded with additional release of Fe^{2+} ions. Figure 4-58 show the increase of pH with Fe^{2+} ions concentration. Accordingly the pH of inlet water was reduced to maintain a better pH control.

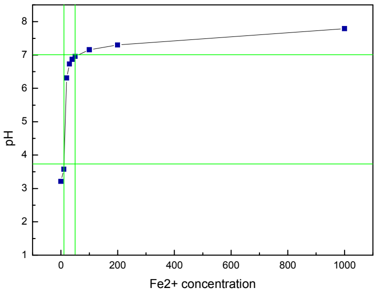

Figure 4-58 pH change with Fe^{2+} ion concentration

In the third test, the vibration data from three 3-axis accelerometers and the UT thickness measurement were acquired once every day. In the test duration, the pH became lower and the test specimens were susceptible to degradation. The FAC test was executed continuously for three weeks resulting in 30 to 40 % of thickness reduction in carbon steel elbow. All the monitored signals were integrated to evaluate the environmental test condition.

Test results-electrochemical parameters

Figure 4-59 shows the monitored environmental test conditions of temperature, pressure, dissolved oxygen, and the variation of monitored ECP and pH with time. Post-test examination of the test elbow was also conducted. Figure 4-60 shows the dissected elbow revealing corrosion and erosion at its inside surfaces with reduced thickness.

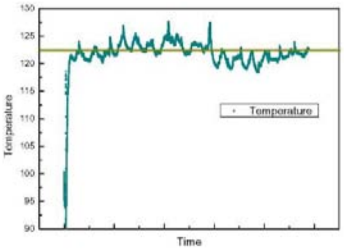

(a) Temperature during the test

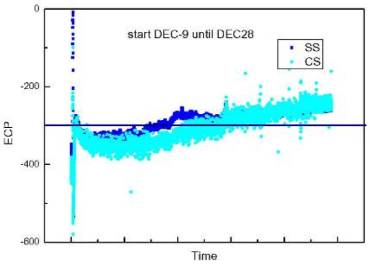

(b) Monitored ECP change during the test

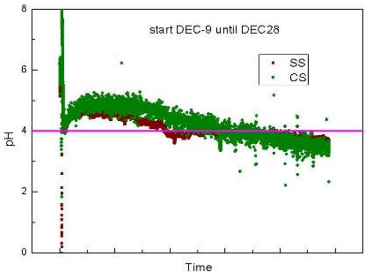

(c) Monitored pH change during the test

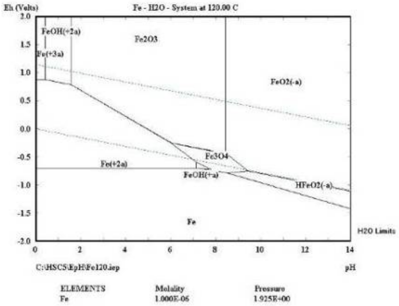

(d) ECP-pH diagram of the test

Figure 4-59 Monitored temperature, ECP, and pH plotted separately versus time with ECP-pH diagram

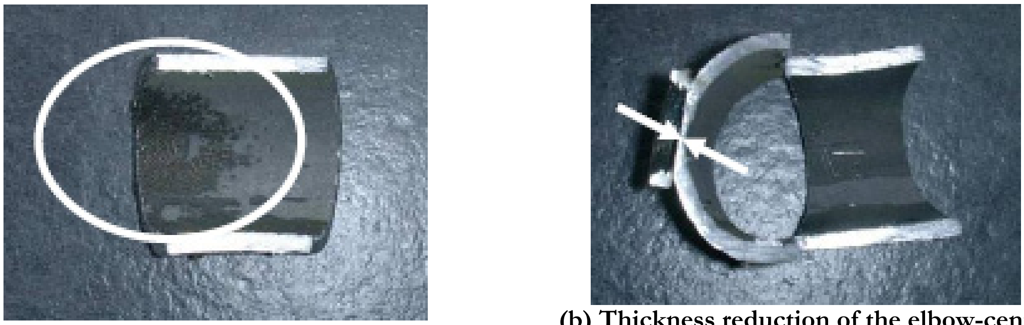

(a) Inner surface of the elbow-center **(b) Thickness reduction of the elbow-center**

(c) Inner surface of the bare piping taken with stereoscope **(d) Inner surface of the piping experienced FAC for 3 weeks (magnification of (a))**

Figure 4-60 Dissected elbow details

Test results-UT

The pipe wall thickness, measured by UT, can be calculated from the ultrasonic flight time between first and second reflection signal (peak). The wall thickness can be correlated directly with the flight time between peaks (reciprocation time of ultrasonic) using the following equation:

$$thickness = \frac{5700}{2} \cdot \Delta t \times \frac{1}{1000}$$

Where
Thickness = wall thickness of pipe (in mm)
Δt = reciprocation f
Velocity of ultrasonic: ~5700 m/s in carbon steel

The daily HTUT measurement results are summarized in Table 4-5. In addition, Figure 4-62 shows the UT signals of pipe wall thickness reduction with the progress of the FAC test. The calculated thickness reductions during FAC test were plotted with the dissolved oxygen in Figure 4-62.

Table 4-5 UT monitoring results during third FAC test

Date	1st peak	2nd peak	Elapse time	Thickness	Difference
1	7.35132	7.76132	0.41	1.1685	
2	7.35072	7.75557	0.40485	1.1538	-0.0147
3	7.57941	7.98841	0.409	1.1657	0.0118
4	7.57003	7.92703	0.357	1.0175	-0.1482
5	7.55566	7.91766	0.362	1.0317	0.0142
6	7.56765	7.92165	0.354	1.0089	-0.0228
7	7.58768	7.94068	0.353	1.0061	-0.0028
8	7.57484	7.92584	0.351	1.0004	-0.0057
9	7.58173	7.87373	0.292	0.8322	-0.1682
10	7.54168	7.82568	0.284	0.8094	-0.0228
11	7.5447	7.8347	0.29	0.8265	0.0171
12	7.52644	7.80544	0.279	0.7952	-0.0314
13	7.52791	7.82491	0.297	0.8464	0.0513
14	7.51128	7.80128	0.29	0.8265	-0.0199
15	7.51753	7.81852	0.30099	0.8578	0.0313
16	7.53769	7.8217	0.28401	0.8094	-0.0484
17	7.51616	7.79816	0.282	0.8037	-0.0057
18	7.50992	7.79793	0.28801	0.8208	0.0171
19	7.51519	7.78819	0.273	0.7781	-0.0428
units		(µs)			(mm)
the velocity of ultrasonic is assumed to be constant (5700 m/s) in carbon steel pipe					

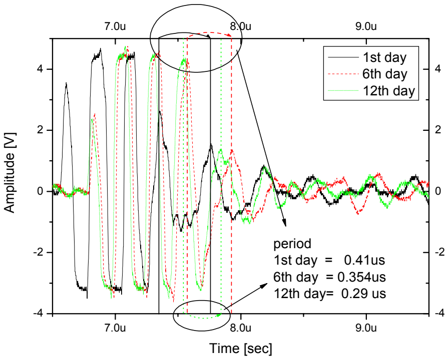

Figure 4-61 UT signal shows thickness reductions during FAC test

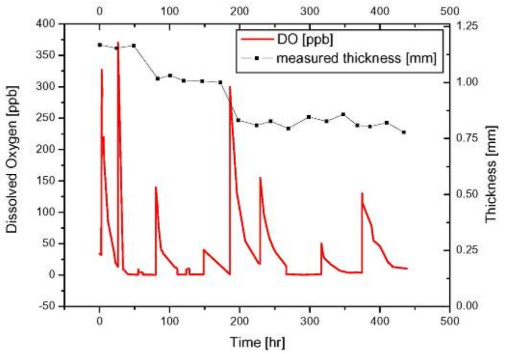

Figure 4-62 Thickness reductions during FAC test plotted with dissolved oxygen

In summary, Table 4-6 shows the comparison of pipe elbow thickness between UT monitoring and direct measurement. The initial thickness of the reference specimen (elbow) was 2.87 mm.

Table 4-6 Summary of thickness

Initial thickness of the elbow	
Direct measurement with micrometer	1.27 mm
UT monitoring	1.2 mm
After 3 weeks of FAC experiments	
Direct measurement with micrometer	0.94 mm
UT monitoring	0.8 mm

Test results-vibration

In the FAC tests, the change of vibration characteristics induced by flow dynamics on elbow, top and straight portions of U-section was monitored once everyday. Figure 4-63 shows a result of frequency response in the chemical FAC test in which corrosion of the interior metal surface of the piping system occurred resulting in its mass reduction and local thinning of elbow and u-section. Consequently, these changes were expected to alter the characteristics of fluid induced vibration. However, test results indicated that since the amount of mass reduction of the thinned wall was relatively small, it was very difficult to detect vibration mode changes of the piping system. Nonetheless, a vibration mode change or a shift of frequency in X-axis and Z-axis of pipe elbow was observed at 4th and 9th days. Table 4-7 represents a summary of frequency data at straight portion of U-section using MUSIC tool in the chemical FAC test.

Table 4-7 Summary of frequency data of chemical FAC test

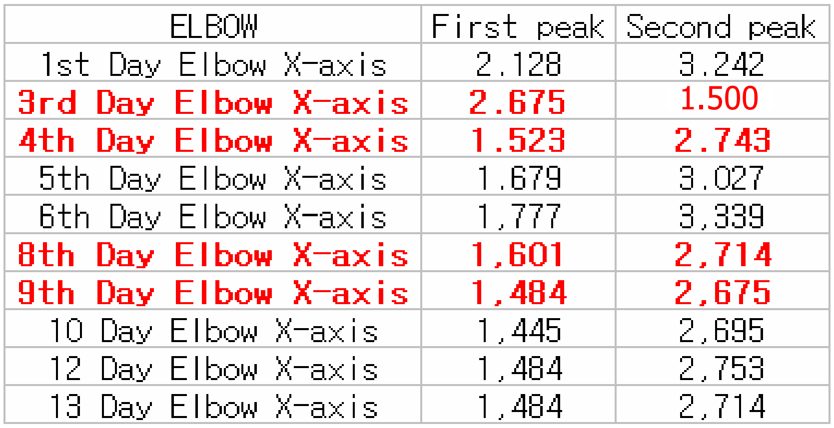

	ELBOW	First peak	Second peak
12/ 9	1st Day Elbow X-axis	2.128	3.242
12/11	**3rd Day Elbow X-axis**	**2.675**	1.500
12/13	**4th Day Elbow X-axis**	**1.523**	**2.743**
12/14	5th Day Elbow X-axis	1.679	3.027
12/15	6th Day Elbow X-axis	1,777	3,339
12/16	**8th Day Elbow X-axis**	**1,601**	**2,714**
	9th Day Elbow X-axis	**1,484**	**2,675**
	10 Day Elbow X-axis	1,445	2,695
	12 Day Elbow X-axis	1,484	2,753
	13 Day Elbow X-axis	1,484	2,714

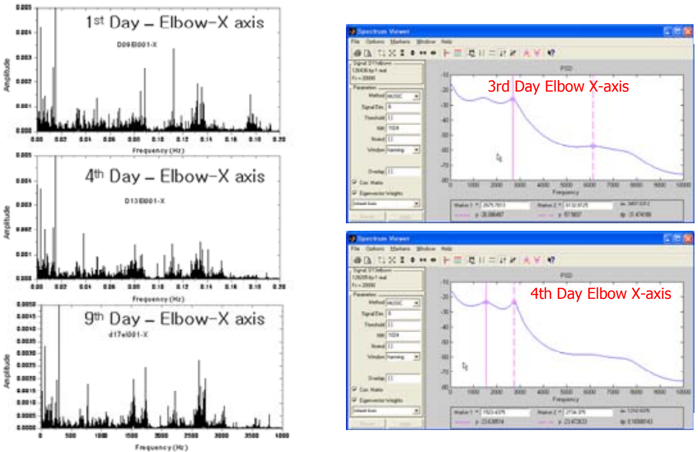

Frequency Analysis (FFT) Frequency Analysis (MUSIC)

Figure 4-63 Frequency response of chemical FAC test

To simulate the non-uniform thinning of piping system and additional mass reduction on the thinned wall, a total of 3.2 mm of thickness, corresponding to 82% of its initial thickness, was grinded at the interior portion of the elbow. Figure 4-64 shows the result of frequency response of the grinded elbow, indicating a small amount of frequency response shift. However, it was still difficult to detect a vibration mode change.

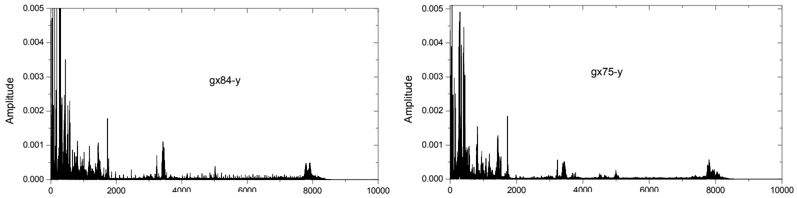

No Grinding 1 mm Grinding

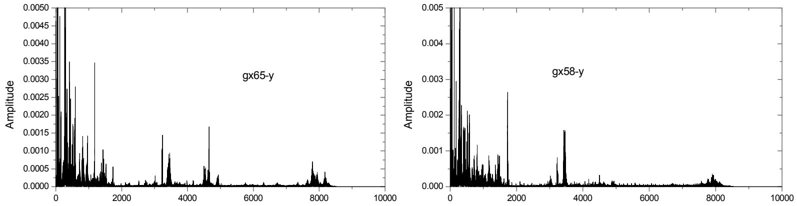

2 mm Grinding 3 mm Grinding

Figure 4-64 Frequency response of grinded elbow

4.6 Task 2.6: integrated system analyses on piping elbow for recommending mitigation and correction options

Performed by KAERI, SNU, CNU, and SNL

This task was performed after completing the condition monitoring testing of the piping elbow and analyzing the sensor signals.

4.6.1 Algorithm development for FAC phenomena monitoring

Figure 4-65 shows the strategy of the monitoring algorithm for the FAC test loop. The two electrochemical electrodes, AUEN and EREP, were used to monitor the ECP and pH of water chemistry. If the electrochemical data indicated that the test loop was in the active region, the mechanical signals were checked to make sure that the pipe thickness was still within the safe region. These mechanical signals included data from the UT, vibration monitoring sensors, and the correlation from the wearing rate model.

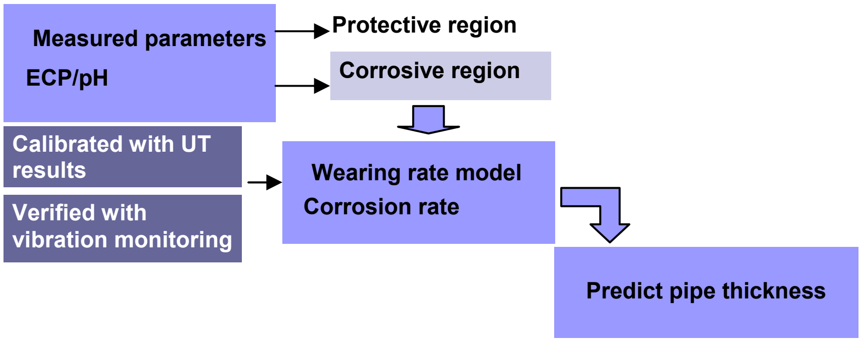

Figure 4-65 Strategy for the monitoring algorithm

Figure 4-66 shows the monitoring screen. Monitored values were converted to the real ECP and pH values directly to support operators to evaluate the water chemistry in the piping system. Figure 4-67 shows the ECP-pH diagram.

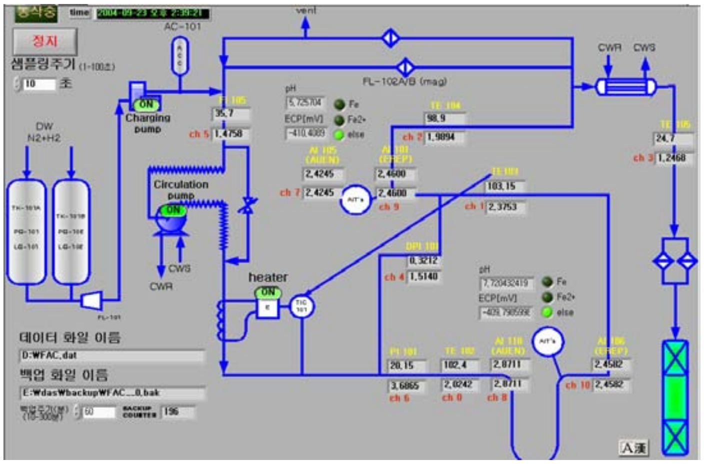

Figure 4-66 Monitoring screen of the test loop

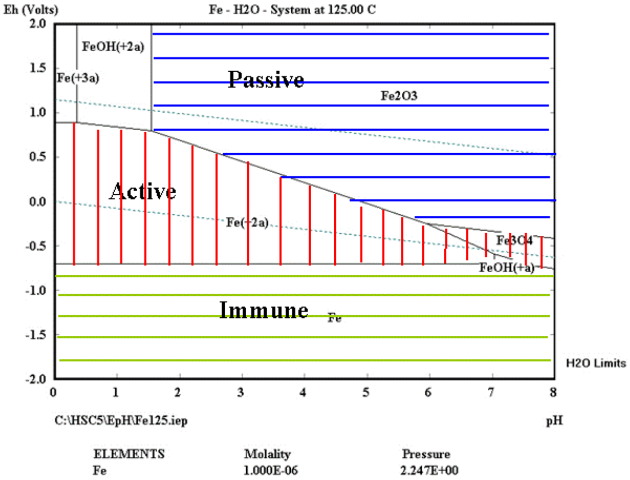

Figure 4-67 ECP-pH diagram for each section

4.6.2 Prototype of FAC condition monitoring system for a secondary piping elbow

The condition monitoring system computed the ECP and pH values from the AUEN and EREP sensor signal and temperature. These computed results helped to identify the electrochemical state in the piping system. The safe regions of FeOH and Fe_2O_3 are indicated in Figure 4-68 by diagonal lines. Figure 4-69 represents safe region using Cartesian coordinate.

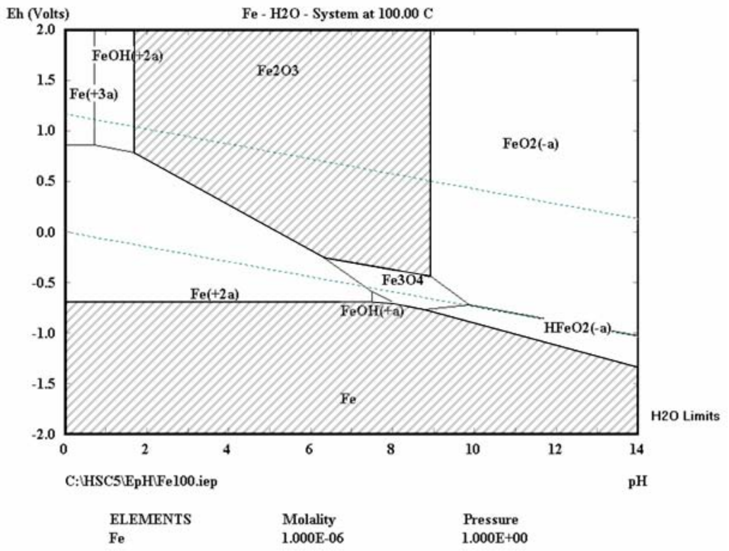

Figure 4-68 The safe regions of FeOH and Fe_2O_3

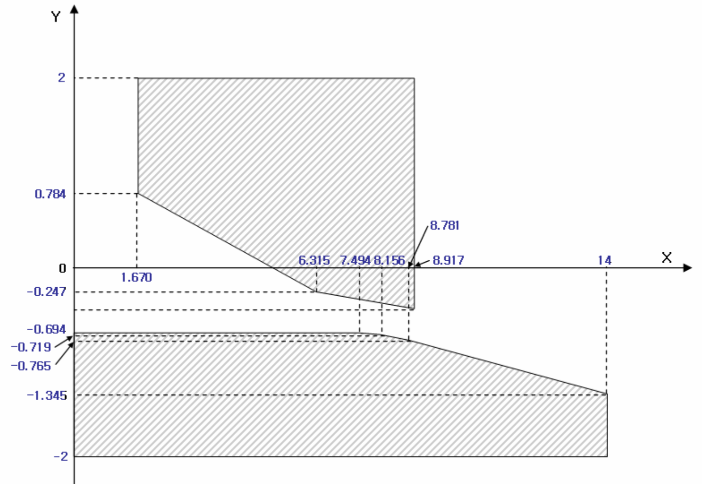

Figure 4-69 Representation of safe regions using Cartesian coordinate

The actuated procedures of data processing algorithm are as follows:

1. Measure AUEN and EREP data using preamp (gain of 3 dB).
2. Calculate the value of ECP and pH using temperature and acquired AUEN and EPER data.
3. Select table which indicate current temperature.
4. Distinguish between safe or non-safe region using inequalities and show front panel.

Figure 4-70 shows the program display of ECP, pH values and regions of current states on the front panel of piping elbow condition monitoring system.

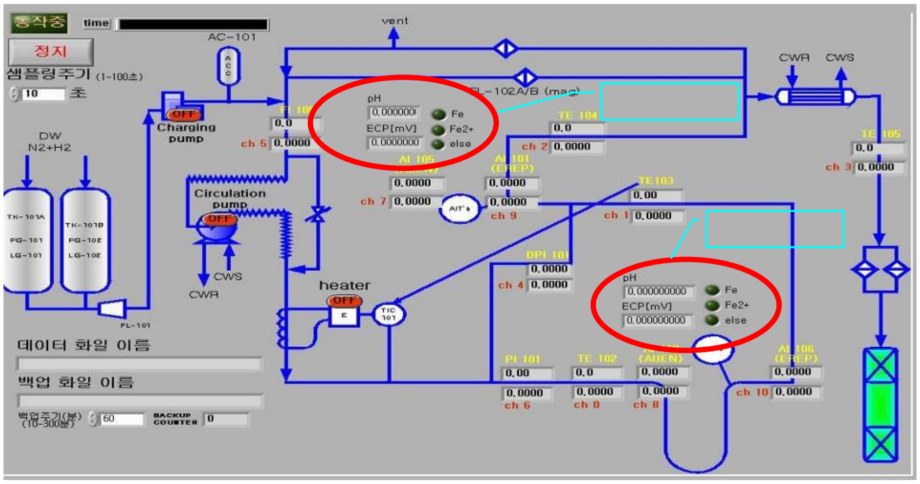

Figure 4-70 Front panel of piping elbow condition monitoring system

5. TASK 3: condition monitoring of an assembly of tubesheet and tube bundle in a steam generator

This task focused on investigating and developing a methodology for condition monitoring of an assembly of tubesheet and tube bundle in a steam generator as a passive component in a safety-related environment. The work scope included collecting and examining existing data on this passive component in an aggressive erosion/corrosion environment, investigating and identifying sensors and communication options, developing a demonstration scenario, investigating and designing test options to acquire condition monitoring data, and developing and performing finite element analyses of the steam generator tube assembly.

5.1 Task 3.1: performance, failure, and inspection data on steam generator assembly

Performed by SNL and KAERI

A systematic survey of performance, failure, and inspection data of steam generators in Korea and the United States from plant operators and manufacturers were performed to investigate the broad spectrum of degradation and failure of steam generator tubes. The investigation addressed critical agents in highly erosive and corrosive environments, such as water chemistry, high temperature, high pressure, and turbulent flow, which accelerate the degradation process in steam generator tubes. Particular attention focused on the failure modes and mechanisms of tubes and their frequency of occurrence.

A database was prepared using the Microsoft Access program to document the survey findings in the United States. A collection of 27 reports, published in mid-1984 to early 2002, was surveyed. Technical issues discussed in these reports include steam generator tube degradation and integrity issues, steam generator operation experiences, validation of failure and leak-rate correlations for stress corrosion cracks in steam generator tubes, and evaluation of eddy-current array probes for steam generator tube inspection.

The degradation of steam generator tubes in PWRs, and in particular, the stress corrosion cracking (SCC) of steam generator tubes, continues to be a serious problem. Figure 5-1 shows the worldwide causes of steam generator tube plugging [xii]. Figure 5-1 clearly indicates that in recent years, outer-diameter stress corrosion cracking and intergranular attack (ODSCC/IGA) and, to a lesser extent, primary-water stress corrosion cracking (PWSCC), have become the predominant identifiable causes of tube plugging. PWSCC is commonly observed at the roll transition zone, at U-bends and tube denting locations, and occasionally in plugs and sleeves. ODSCC/IGA commonly occurs near tube support plate crevices, near the tubesheet in crevices, or under sludge piles, and occasionally in the free span. There are particular concerns on the increasing occurrence of axial and circumferential cracking at the roll transition zone on both the primary and secondary sides.

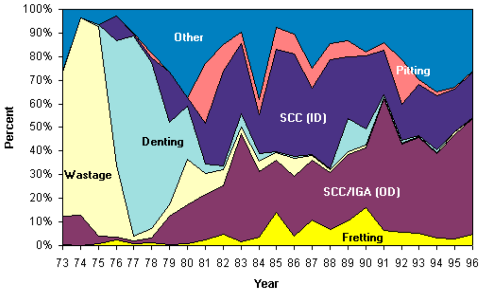

Figure 5-1 Causes of steam generator tube plugging (from Dow's work)

5.2 Task 3.2: scenario to demonstrate condition monitoring for a steam generator tube assembly

Performed by SNL and KAERI

After completing the survey of the performance, failure, and inspection database on the steam generator tube assembly in Task 3.1, different degradation scenarios involving the most frequent tube failure modes and mechanisms were identified. Probable degradation scenarios of steam generator tubes were explored to determine the feasibility of implementing them in a condition monitoring test loop. Because most of the tube degradation and failure occurred in highly erosive and corrosive environments, it is very difficult to duplicate some of the important agents in these hostile environments in laboratory test loops due to limited budgetary resources and physical feasibility. There are additional technical complications in developing specialty sensors that can survive and function in these environments. Therefore, we chose to conduct condition monitoring of a piping elbow in Task 2 to advance technology development as a prelude to conduct condition monitoring of steam generator tubes.

5.3 Task 3.3: design options for a steam generator tube assembly test loop

Performed by SNL, KAERI, and SNU

Different designs of steam generators (straight tubes and U-tubes) were investigated, including those associated with Generation IV reactors with different operating media and temperature and pressure environments. In addition, steam generators with both conventional and helical coil tube assemblies were considered. Various design options of test loops for performing condition monitoring of steam generator tubes were explored to ensure that the designed test loop includes all identified tube failure scenarios, and the proposed test program fits within the budget and schedule constraints.

Most of the tube degradation and failure have been found near a tubesheet or a U-turn portion. As discussed in Task 2, normal and degraded tubes are expected to exhibit different vibratory responses that may be detected with advanced sensors such as optical fiber, accelerometer, and AE devices. In addition, specialty chemical sensors have been developed to monitor water chemistry and temperature; therefore, the sensor and computational technologies developed and demonstrated in this project may provide the backbone for the future designs of a test loop for a steam generator tube assembly. The prohibitive barrier for such a test loop might be the high costs and technical challenge in assembling a test loop in a highly erosive and corrosive environment.

5.4 Task 3.4: Sensor and communication options for test loop to obtain condition monitoring data on steam generator tube assembly

Performed by SNL, KAERI, and CNU

Various advanced sensors including optical fiber displacement sensors and AE devices have been evaluated to participate in condition monitoring of steam generator tube assembly. The mounting fixtures for these sensors were anchored at various locations on the interior end of the tubesheet to allow them to monitor the vibration response of nearby tube sections. Likewise, they were mounted on structures close to the U-turn portion of the tube bundle to obtain condition monitoring data on these tube sections. A few selected tubes at strategic locations were plugged to provide anchorage of mounting fixtures to allow condition monitoring of tubes at the middle of the tube bundle. Both options of wired and wireless communication have also been examined.

5.5 Task 3.5: Fluid and FEAs of steam generator assembly to investigate dynamic response characteristics

Performed by SNL

Fluid and FEMs of steam generator tubes are developed to investigate their vibration response caused by the fluid-structure interaction phenomenon.

5.5.1 The Use of the FLUENT LES turbulence model for steam generator tube flow-induced vibration analysis

The prediction of unsteady fluid forces on structures such as steam generator tubes due to vortex shedding phenomena is a difficult task. CFD codes are just beginning to address this issue. Traditional approaches that use two-equation turbulence models (such as unsteady Reynolds-Averaged Navier-Stokes) have met with limited success due to fundamental limitations in the averaging process. More recent approaches (such as LES) that filter the Navier-Stokes equations to resolve the large-scale motions with subgrid-scale turbulence models have been much more successful.

The most widely used CFD code in the world, FLUENT CFD code [xiii], has recently enhanced its LES capability, including associated numerical enhancements [xiv]. Validations for fully developed channel flow, flow over a square cylinder, and flow over a sphere have shown good accuracy (Kim's work). Because of our experience with FLUENT, we have investigated flow over an isolated circular cylinder as an initial validation problem for the steam generator tube application.

5.5.1.1 Validation

To assess flow over an isolated tube, two sets of data were readily available; one for a Reynolds number of 3900 [xv] and one for a Reynolds number of 140,000 [xvi]. Both datasets were in the subcritical vortex shedding regime (300<Re<150,000) [xvii]. Breuer [xviii] has successfully simulated each of these datasets using the LES approach and his own code.

Flow over steam generator tubes results in Reynolds numbers of ~10,000 to 20,000. We chose Ong and Wallace's data for a Reynolds number of 3900 for the initial validation of FLUENT because of the close value of its Reynolds number with that expected for steam generator tubes. The Cantwell and Coles data could be used for further validation of FLUENT at higher Reynolds numbers.

Ong and Wallace

Ong and Wallace performed experiments in a wind tunnel for air flow over a 14.3 mm (0.0143 m) diameter circular cylinder. The free stream velocity of the approaching air was about 4.2 m/s, resulting in a Reynolds number of about 3900. Measurements included the measured vortex shedding frequency of about 64 Hz, or a Strouhal number ($S = f_s D/U$) of 0.21, which is in good agreement with other experimental data as summarized in Blevins' work. Additionally, average velocity and turbulent shear stresses were measured.

For LES calculations, the mesh should be fine enough to simulate the larger eddies in the flow. Guidance from Fluent [xix] indicates that the first mesh point should be at a y^+ distance of about 1 from the wall, where y^+ is a dimensionless distance ($y^+ = y\, u^*/\nu$), or well within the laminar or viscous sublayer [xx].

A mesh was generated for an isolated circular cylinder of 14.3 mm diameter. The domain was very large (10 m in the flow direction, 6 m normal to the cylinder) to eliminate any boundary effects. Consistent with Breuer's results, the spanwise dimension of the mesh was about 3 tube diameters. The spanwise boundaries were modeled as periodic boundary conditions with zero pressure gradients. The boundaries normal to the flow direction were symmetrical and the boundaries in the flow direction were inlet and outlet. The total mesh size was 624,000 cells (160 x 130 x 30), where the first number was the number of points around the tube, the second number was the number of radial points, and the third dimension was the spanwise value.

The subgrid scale turbulence model was the dynamic Smagorinski model (described in Kim's reference), which gave the best solution according to Breuer. The simulation was run with dimensionless time steps of 0.029 ($\Delta t_{dim} = \Delta t\, U_{inf}/D$). The PRESTO discretization scheme was used for pressure and central differencing was used for momentum. The non-iterative time advancement scheme using the fractional-step method was selected.

The simulation was run for 4 s as the flow developed and reached equilibrium. Statistics and forces on the cylinder from vortex shedding were determined from fully developed conditions between 3 and 4 s, or over about 60 vortex shedding cycles. The y^+ values for the simulation are 0.3 (maximum) on the upstream side and 0.159 (generally) on the downstream side of the tube including the wake region. These values are well within the recommended values discussed previously.

Data-model comparisons are given for the mean streamwise velocity on the centerline and the total u and v velocity fluctuations, or resolved Reynolds stresses. In addition, the mean lift and drag coefficients and the dominant vortex shedding frequency were compared to data.

Figure 5-2 shows the results of the simulation. Figure 5-2 (a) presents the contours of velocity magnitude at 4.0 s, the end of the simulation. The vortex shedding behavior is clearly seen. In this snapshot, the velocity is higher below the cylinder, which leads to vortex shedding from that side. At other times, the velocity is higher at the top of the cylinder. The alternating vortex shedding behavior is shown downstream of the cylinder. Figure 5-2 (b) shows the time-averaged velocity magnitude averaged over 1 s. Although the time averaged velocity magnitude is symmetrical about the cylinder, the instantaneous velocity is obviously not as shown earlier in Figure 5-2 (a).

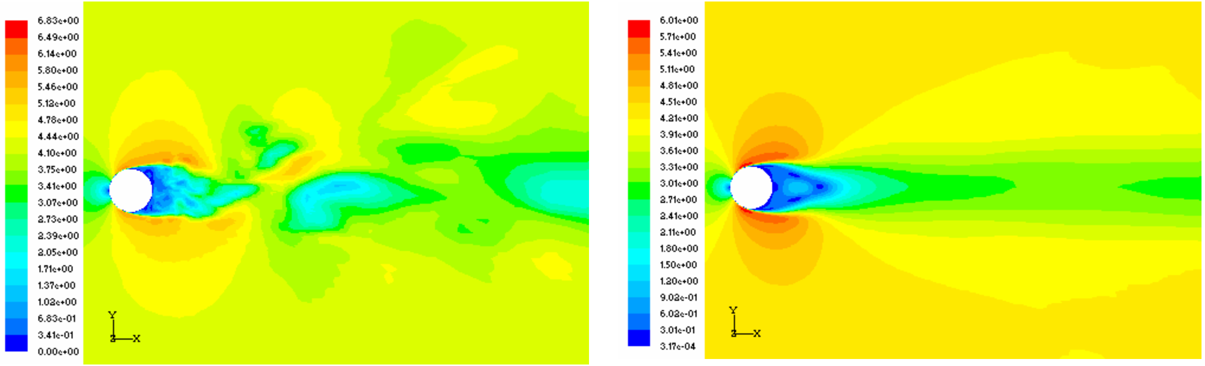

(a) Velocity magnitude at 4.0 s **(b) Time-averaged velocity magnitude**

Figure 5-2 Contours of velocity magnitudes

Figure 5-3 shows the mean streamwise velocity prediction from FLUENT downstream of the tube along the centerline as well as experimental data from Ong and Wallace and Lourenco and Shih [xxi], where x is the distance downstream from the center of the cylinder. The results show a recirculation zone downstream of the cylinder that extends 1.1 diameters downstream of the cylinder, which compares well with the experimental value of 1.33±0.2 as given by Breuer. The shape of the centerline velocity compares reasonably well with the experimental data.

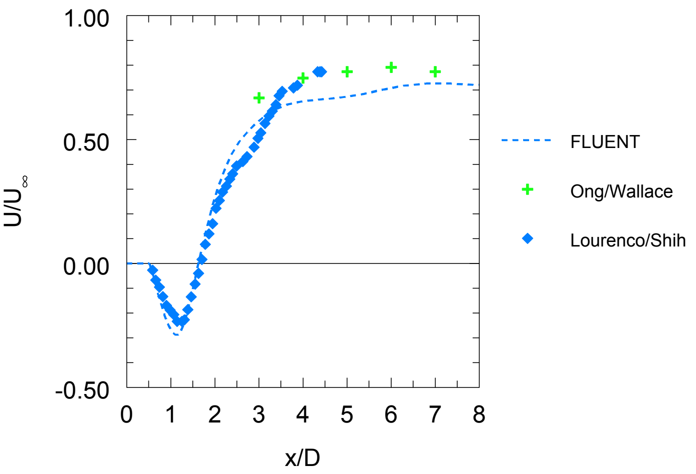

Figure 5-3 Data-model comparison for mean streamwise velocity along the centerline

Figure 5-4 (a) gives the u velocity fluctuations or Reynolds shear stress ($\overline{u'u'}$), at a downstream distance (x/d) of 1.54, or just downstream of the recirculation zone, as a function of distance away from the centerline. The shape and magnitude of the Reynolds shear stress predictions compare very well with the experimental data. Figure 5-4 (b) shows the v velocity fluctuations, or Reynolds shear stress ($\overline{v'v'}$), at the same location with similar good data-model comparison.

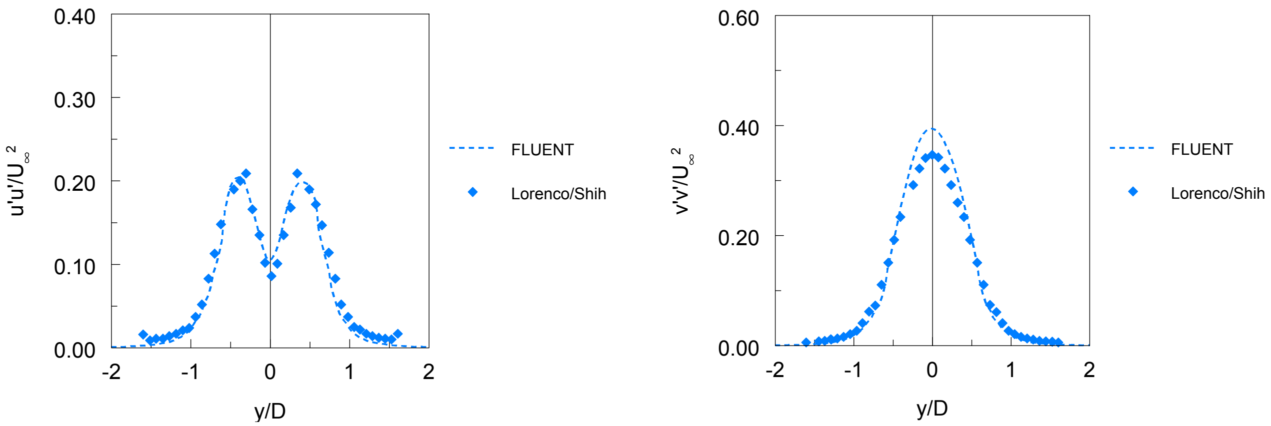

(a) Resolved Reynolds stress $\overline{u'u'}$ at x/D = 1/54 **(b) Resolved Reynolds stress $\overline{v'v'}$ at x/D = 1.54**

Figure 5-4 Resolved Reynolds stress

The lift and drag coefficient values are shown in Figure 5-5 (a) and (b). For reference, the lift and drag forces for a circular cylinder are given by the following:

$$F_L = C_L \frac{1}{2} \rho U^2 D L$$

$$F_D = C_D \frac{1}{2} \rho U^2 D L$$

where the product DL (diameter times length) is the area normal to the direction of flow, and U is the upstream, undisturbed velocity. In this case, ρ is 1.225 kg/m^3, U is 4.2 m/s, and D is 0.0143 m.

Over the sampling period from 3 to 4 s, the mean lift coefficient was -0.0109 with a variance of 0.103 and RMS value of 0.32; a correlation from Norberg [xxii] indicates that the lift coefficient RMS magnitude should be about 0.083 at this Reynolds number. It is not clear why the predicted lift coefficient is so much larger than the Norberg correlation. Note that Breuer shows a “typical” lift coefficient variation for the Re=3900 case that is about half the magnitude of that predicted by FLUENT, although the conditions (mesh, discretization scheme, and subgrid turbulence model) are not identified.

The difference in lift coefficients may be due to the spanwise dimension of the simulation. A spanwise dimension of 3 tube diameters, which is consistent with the Breuer model, has been used for the present calculation. However, Norberg implies that the spanwise correlation length is about 10 diameters at this Reynolds number. A larger spanwise dimension would lower the lift coefficient because some of the forces will cancel each other out.

The predicted drag coefficient from the FLUENT simulations is 1.079±0.009; experimental data summarized by Breuer indicate a range of 0.98±0.05. The drag is overpredicted by about 10%. A larger spanwise dimension should lower the drag coefficient as discussed previously for the lift coefficient.

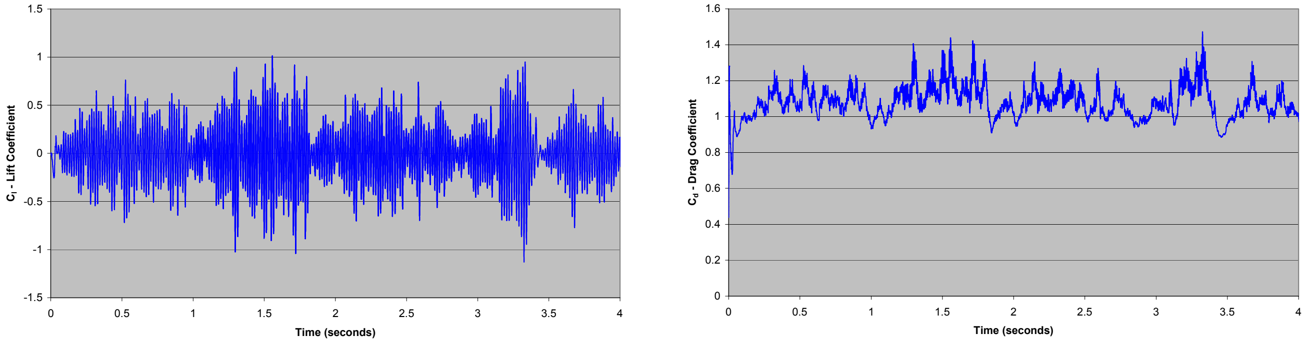

(a) Predicted lift coefficient **(b) Predicted drag coefficient**

Figure 5-5 Predicted (a) lift and (b) drag coefficients

The frequency distributions of the drag and lift are important in the determination of flow-induced vibrations. The lift and drag coefficients were filtered through the FFT process to determine the frequency behavior as shown in Figure 5-6. The dominant frequencies for lift and drag are 58.8 and 115.4 Hz, respectively. The frequencies for drag are approximately twice that of lift The dominant lift frequency of 58.8 Hz results in a Strouhal number of 0.20 compared to an experimental value of 0.21.

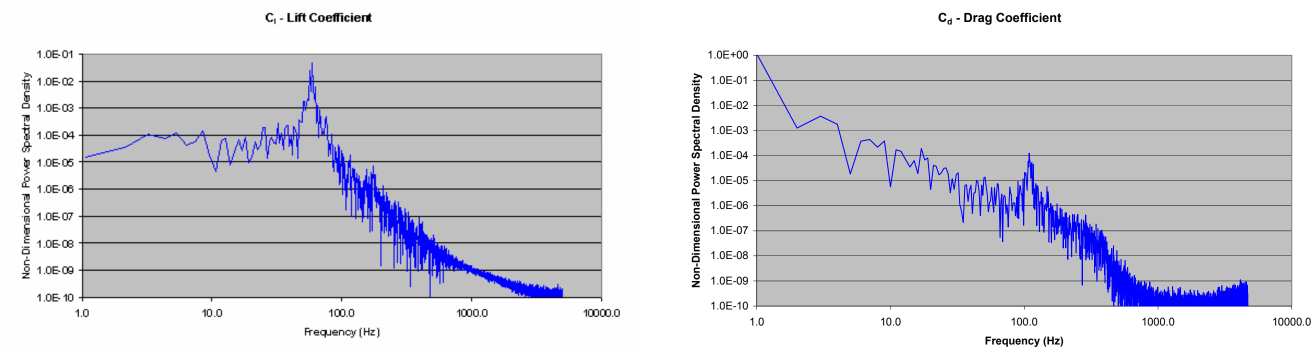

(a) FFT of predicted lift coefficient **(b) FFT of predicted drag coefficient**

Figure 5-6 FFT of predicted (a) lift and (b) drag coefficients

LES simulations need significant computational resources. These calculations take about 100 CPU-hr for every second of simulation time on a 3.0 GHz Pentium 4 computer. Thus, the 4.0 s simulation time for the validation problem requires about 400 CPU-hr of computer time.

Overall, the FLUENT simulations provide reasonable agreement with the available experimental data. Although the lift coefficient is not as accurate as desired, it may be due to the limited computational domain. The general characteristics of the flow (mean velocity and turbulent stresses) are correct. Therefore, FLUENT can be confidently used to predict the general characteristics of flow-induced vibrations over steam generator tubes.

Steam generator tube analysis

With the successful validation of FLUENT for the prediction of forces from vortex shedding over a circular cylinder, it has been used to predict the transient forces over a typical steam generator tube. An isolated tube has been used in this initial simulation for simplicity. The conditions chosen are for water flow over a single isolated tube with a diameter of 17.46 mm (0.01746 m) and an upstream freestream velocity of 0.47 m/s. The Reynolds number (Re = $\left(\frac{\rho U D}{\mu}\right)$) in this case is about 8200.

The Strouhal number at this Reynolds number is expected to be about 0.21 as given by Blevins 2001 work, so the dominant vortex shedding frequency is expected to be about 5.7 Hz. Figure 5-7 shows the lift and drag coefficient predictions for a single isolated steam generator tube as a function of time. Figure 5-8 shows the FFT of these results for the full period from 10 to 20 s. The dominant frequencies are 5.24 and 10.5 Hz for the lift and drag coefficients, respectively. The Strouhal number for the lift coefficient is 0.195.

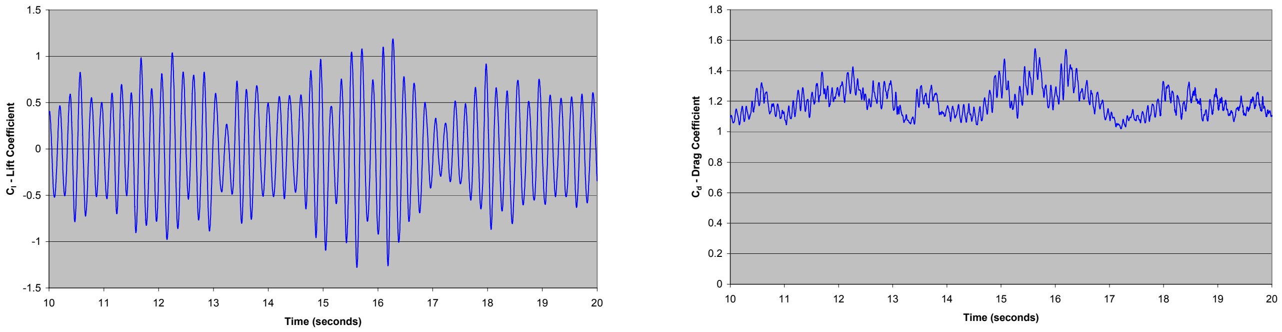

(a) Predicted lift coefficient **(b) Predicted drag coefficient**

Figure 5-7 Predicted (a) lift and (b) drag coefficients for steam generator tube

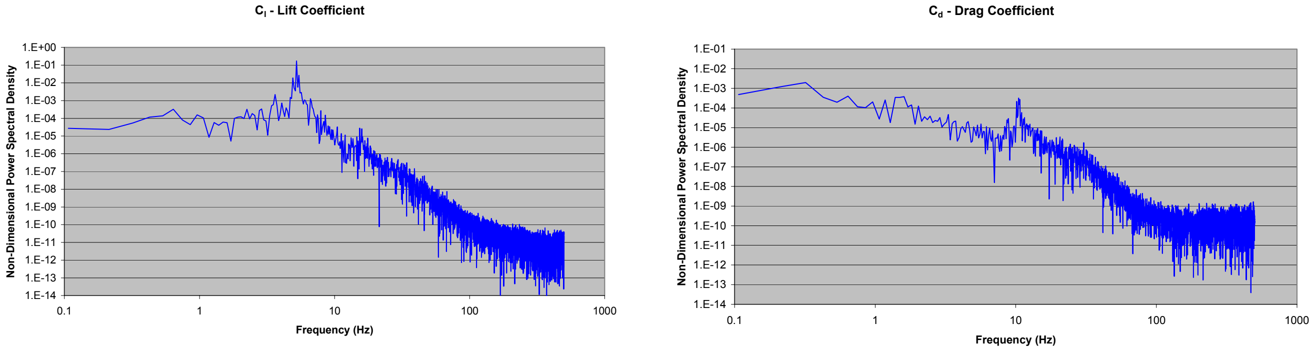

(a) Predicted lift coefficient **(b) Predicted drag coefficient**

Figure 5-8 FFT of (a) predicted lift and (b) drag coefficients for steam generator tube

5.5.1.2 Conclusions

The FLUENT code has been used to predict the vortex shedding forces on isolated circular cylinders. The FLUENT model has been validated by comparison to experimental data for flow over an isolated circular cylinder at a Reynolds number of 3900 including mean velocity, Reynolds stresses, and Strouhal number with reasonable overall agreement. Subsequently, FLUENT has been applied to predict the transient vortex shedding forces over an isolated steam generator tube.

Additional validation of FLUENT should consider flow in tube bundles as exemplified by the experimental data of Simonin and Barcouda [xxiii], who obtained velocity and Reynolds stress data in a staggered tube bundle at a Reynolds number of about 20,000. Once successful data-model comparisons are available for this tube bundle, application to an actual steam generator tube bundle problem can be confidently performed.

Future work should also consider the feedback between the fluid forces and tube vibrations. In the present simulations, a rigid tube is assumed. FLUENT's moving deforming mesh capability is currently being coupled with ABAQUS to allow for feedback between the fluid forces and a moving structure. This feedback may significantly increase the drag coefficient as discussed by Blevins' 2001 work. Coupled simulations would allow for more accurate modeling of fluid-structure interactions for the steam generator tube problem and other applications.

5.5.2 Flow-induced vibration analysis of a steam generator tube

Structural analyses were performed on a 90 in. long straight tube with a 0.854 in. diameter using the ABAQUS, Inc. EXPLICIT™ code. The ends of the tube were fixed against displacement and rotation. Forces were applied to the tube along the middle 72 in. (9 in. at the tube ends have no applied load). The lift and drag forces were determined as a function of time from an LES using the FLUENT code. Forcing functions were supplied for both air and water acting on a single straight tube. Three analyses were performed using the air-based forcing function; a shell element model with the drag and lift forces distributed around the circumference, a shell element model with the drag and lift force applied as concentrated loads, and a beam element model. For the water-based forcing functions, the second and third analyses were performed.

These analyses demonstrated a methodology of applying forcing functions calculated by the FLUENT code to a structural tube model using the ABAQUS code. The tube length, tube diameter, and boundary conditions are not necessarily representative of actual steam generator tubes.

5.5.2.1 Tube and material properties

Single tube

Length = 90 in (2.286 m)
Diameter = 0.854 in (21.7 mm)
Thickness = 0.05 in (1.27 mm)
Elastic modulus = 30,000 ksi (206.7 GPa)
Poisson's ratio = 0.3
Steel density = 7.324E-4 lb-s^2/in.^{4} (7827 kg/m^3)

Air

Velocity = 165.4 in/s (4.2 m/s)
Density = 1.21E-7 lb-s^2/in.^{4} (1.29 kg/m^3)

Water

Velocity = 18.5 in/s (0.47 m/s)
Density = 9.34E-5 lb-s^2/in.^{4} (998.2 kg/m^3)

Forcing functions (air and water)

The equations for the drag and lift forces are the following:

$$F_{drag} = 0.5 \ \rho \ C_d V^2 DL$$

$$F_{lift} = 0.5 \ \rho \ C_l V^2 DL$$

where ρ denotes the density of the flowing medium, C_d and C_l denote the coefficients of drag and lift, V denotes the velocity, D denotes the tube diameter, and L denotes the tube length. Based on FLUENT analyses, the forcing functions are shown Figure 5-9 and Figure 5-10 for both air and water at the velocities stated previously.

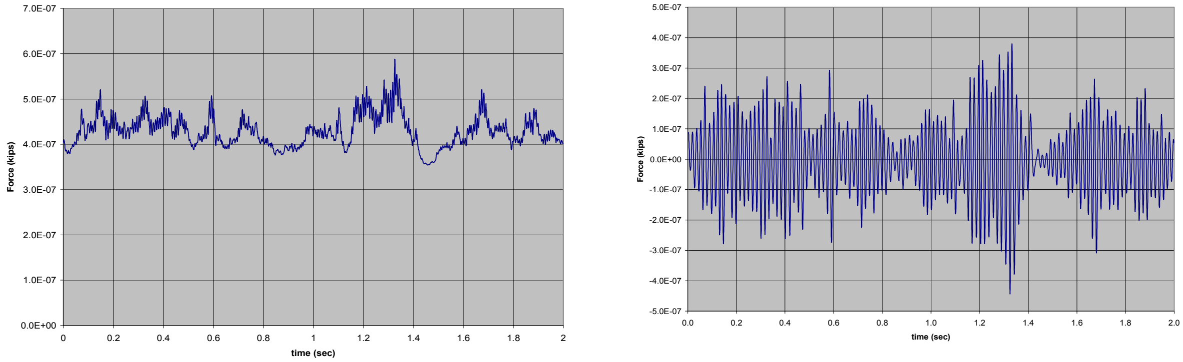

(a) Drag force time history using air **(b) Lift force time History using air**

Figure 5-9 Drag and lift force time histories using air

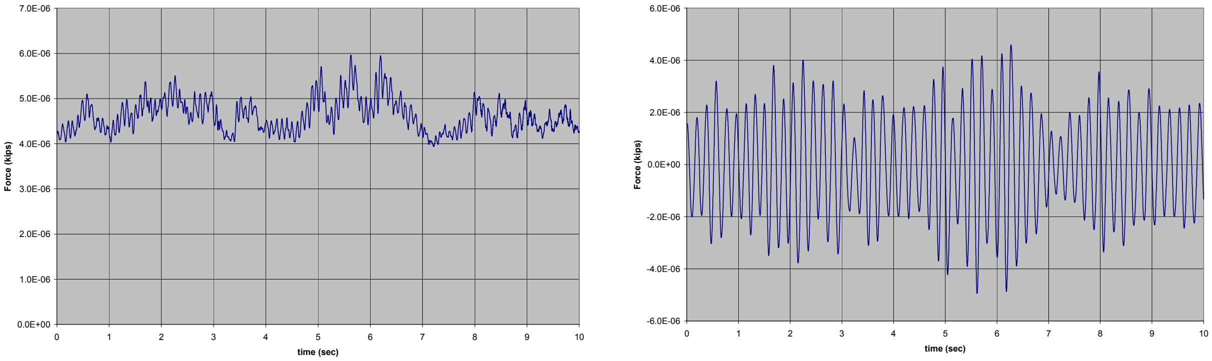

(a) Drag Force time history using water **(b) Lift force time history using water**

Figure 5-10 Drag and lift force time histories using water

5.5.2.2 FEM

Two FEMs were analyzed: a shell element model and a beam element model, as shown in Figure 5-11.

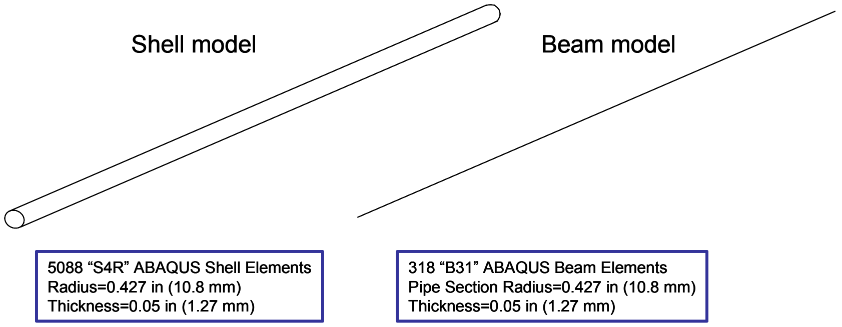

Figure 5-11 Shell and beam models

For both the beam and shell element models, the drag and lift forces were applied to the middle 80% (72 in., 1.829 m) of the tubes length as shown in Figure 5-12. Both ends of the tube were constrained against displacement and rotation.

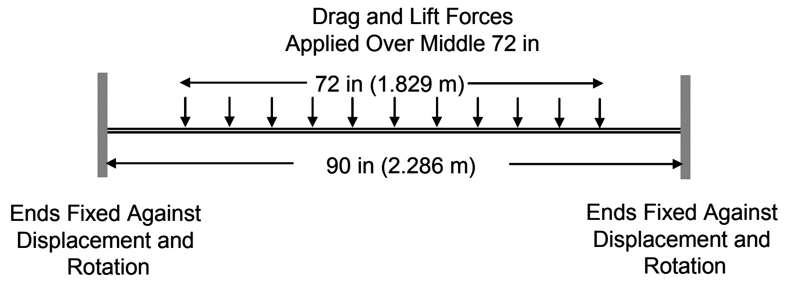

Figure 5-12 Load distribution over tube length and boundary conditions

Two methods were investigated to distribute to drag and lift forces around the circumference of the tube for the shell model. Figure 5-13 illustrates the distributed force method, where a sinusoidal distribution was employed to divide the total drag and lift forces into components for each of the 16 nodes. Figure 5-14 shows the concentrated force method, where the drag and lift forces were divided in half and applied at two nodes each. For the air flow analysis, we found that identical displacements resulted from both methods; therefore, only the concentrated method is shown in the results and used in the water flow analysis.

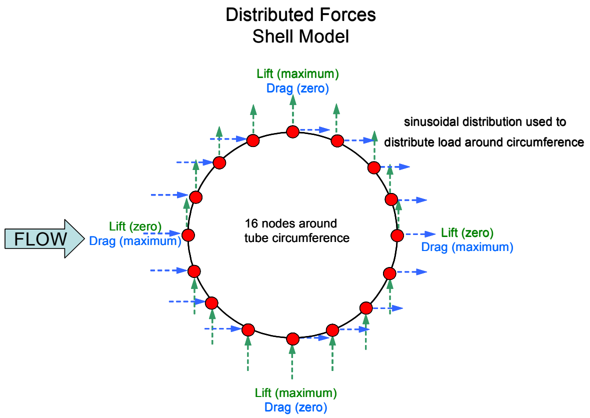

Figure 5-13 Distributed force illustration

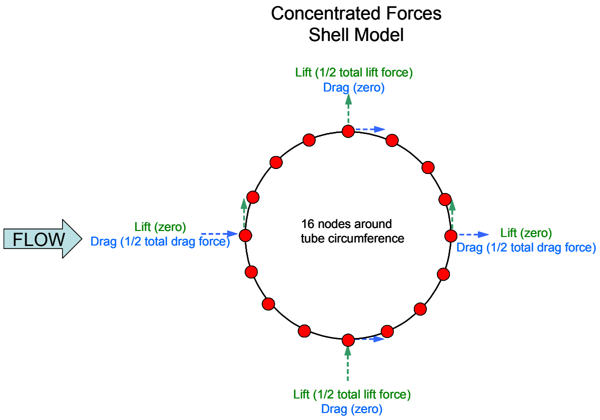

Figure 5-14 Concentrated force illustration

5.5.2.3 Analysis results

The first 10 natural frequencies, which have been computed for the 90 in. tube, are shown in Table 5-1.

Table 5-1 Natural frequencies

Mode	Beam Model (Hz)	Shell Model (Hz)
1	25.26	24.78
2	25.26	24.78
3	69.51	68.18
4	69.51	68.18
5	136.0	133.4
6	136.0	133.4
7	224.2	219.9
8	224.2	219.9
9	333.8	327.4
10	333.8	327.4

The displacement time histories in the drag and lift directions at the tube's midspan are shown in Figure 5-15 and Figure 5-16 for the beam and shell analyses with air flowing.

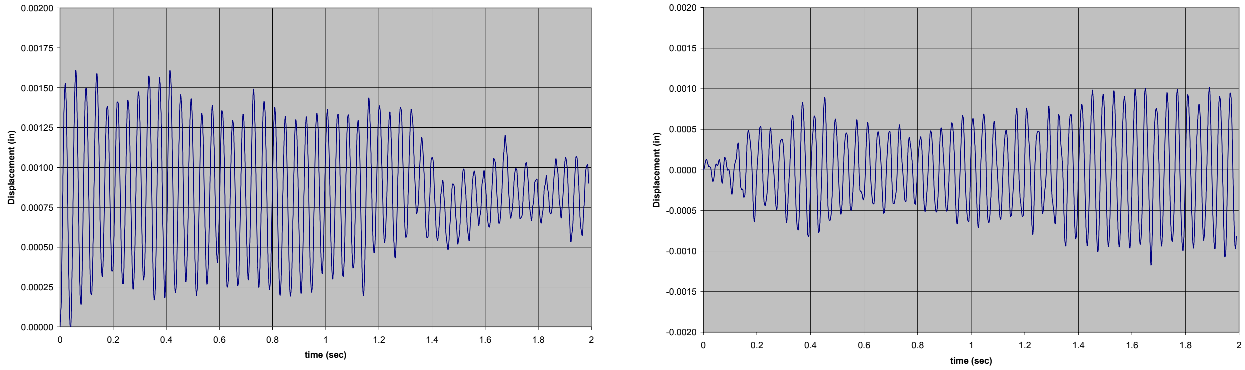

(a) Drag direction (b) Lift direction

Figure 5-15 Beam model midspan displacement using air

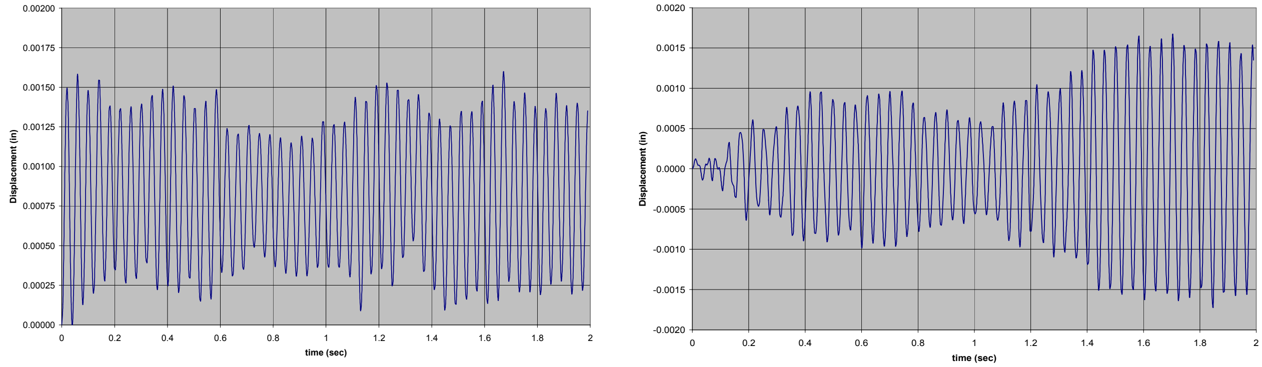

(a) Drag direction (b) Lift direction

Figure 5-16 Shell model midspan displacement using air

The displacement time histories in the drag and lift directions at the tube's midspan are shown in Figure 5-17 and Figure 5-18 for the beam and shell analyses with water flowing.

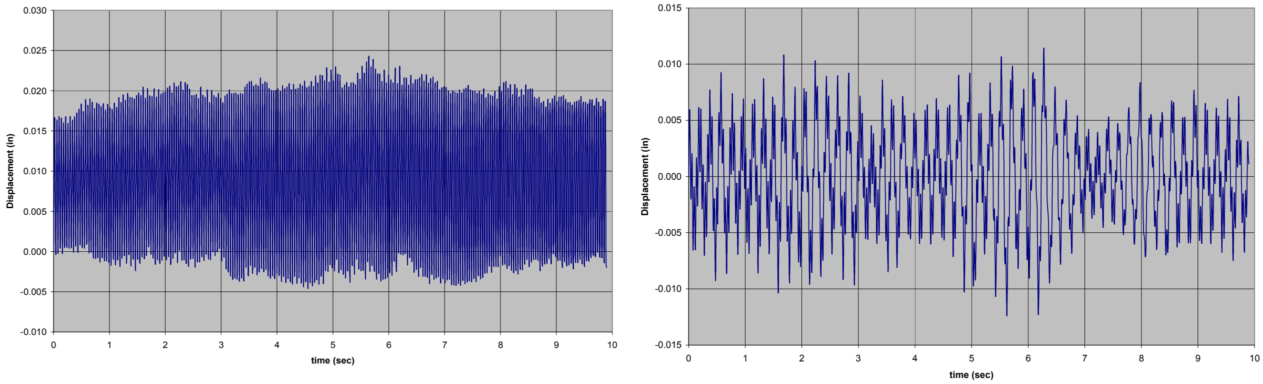

(a) Drag direction **(b) Lift direction**

Figure 5-17 Beam model midspan displacement using water

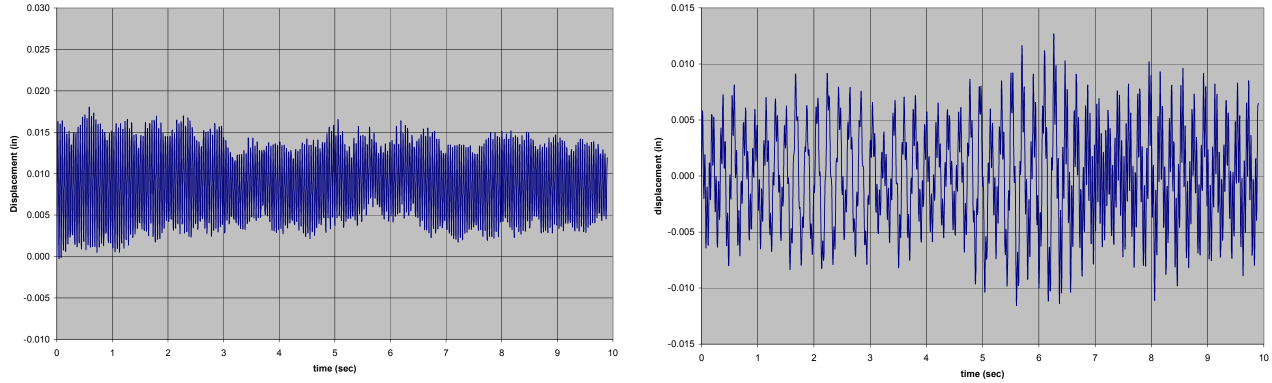

(a) Drag direction **(b) Lift direction**

Figure 5-18 Shell model midspan displacement using water

5.5.2.4 Conclusion

The midspan displacement time histories for the beam and shell models appear to be significantly different. The air flow analysis shows larger displacements for the shell model, but the water flow analysis shows larger displacements for the beam model. One possible explanation is the significantly higher frequency forcing function for the air flow analysis. Because the beam element model produces larger displacements for the water flow analysis, beam element will be used in future parametric analyses.

The beam element model was used to reduce the computational time. The vibration model might be used for follow-up parametric studies. Variables to be studied include the boundary conditions at the tube ends, the tube length, addition of intermediated boundary conditions to represent the baffle plate, and the forcing function application length. In addition, the forcing function from a tube bundle was applied to the tube models and compared with the single tube forcing function analyses. These analyses will help develop the tube vibration structural modeling methodology. Shell or solid model analysis may be necessary to study the local behavior of the tube at the baffle plate and end locations.

6. TASK 4: technical task reports and deliverables

6.1 Task 4.1: condition monitoring technologies report

Performed by KAERI and SNL

The Condition Monitoring Technologies Report, as a part of the final project report, was prepared to document the findings and the lessons learned from conducting the two suites of condition monitoring tests with the check valve and piping elbow test loops.

6.2 Task 4.2: advanced sensor technologies report

Performed by SNL and KAERI

The performance characteristics of all advanced sensors participated in the two condition monitoring test loops of check valve and piping elbow was documented in this final project report.

6.3 Task 4.3: erosion and corrosion monitoring data

Performed by KAERI, SNU, and SNL

The erosion and corrosion data on the piping elbow from the FAC test series was documented in this final project report.

6.4 Task 4.4: baseline software using operational and laboratory data

Performed by KAERI and SNL

The developed baseline software packages based on operational and laboratory data were documented in this final project report.

6.5 Task 4.5: signal processing and smart communications technologies report

Performed by KAERI, CNU, SNL, and PSU

There are sections in this final project report to document all findings related to signal processing and smart communications technologies.

6.6 Task 4.6: final technical project report on methods and results of prototype demonstrations

Performed by KAERI and SNL.

The Final Technical Project Report was prepared to document all technical findings and lessons learned at the end of this joint research project.

Table 6-1 Project milestone and deliverable summary

	Milestone/Deliverable Description	Planned Completion Date	Actual Completion Date
Task 1.1	Performance, failure, and inspection data on check valves in Korea and the US	August 31, 2002	May 31, 2002
Task 1.2	Sensor and communication options for data acquisition for condition monitoring of check valves	November 30, 2002	Sept. 30, 2002
Task 1.3	FEAs of selected check valve designs to investigate dynamic response and to select optimal sensor locations	Oct. 15, 2002	August 31, 2003
Task 1.4	Tests with the KAERI DVI test loop and ARL test bed to obtain condition monitoring data on check valves using selected sensors	June 30, 2003	June 30, 2004
Task 1.5	Signal data processing analyses for noise filtering and pattern recognition	Mar. 31, 2004	Sept. 30, 2004
Task 1.6	Integrated system analyses on check valves for recommending mitigation and correction options	Oct. 15, 2004	Dec. 15, 2004
Task 2.1	Performance, failure, and inspection data on piping elbows in an accelerated erosion or corrosion environment	Oct. 31, 2002	Oct. 31, 2002
Task 2.2	Sensor and communication options for test loop to obtain condition monitoring data on piping elbows	Dec. 15, 2002	May 31, 2003
Task 2.3	FEAs of piping elbow to investigate its dynamic response and to select optimal sensor locations	Mar. 31, 2003	Dec. 31, 2003
Task 2.4	Tests with the test loop at SNU to obtain condition monitoring data on piping elbows using selected sensors	Feb. 28, 2004	Sept. 30, 2004
Task 2.5	Manufacturing and installation of selected sensors and DASs to test loop of piping elbow	May 31, 2003	August 30, 2003
	Signal data processing analyses for noise filtering and pattern recognition	Mar. 31, 2004	Dec. 15, 2004
Task 2.6	Integrated system analyses on piping elbow for recommending mitigation and correction options	Oct. 15, 2004	Dec. 15, 2004
Task 3.1	Performance, failure, and inspection data on steam generator assembly	Apr. 30, 2003	May 30, 2003
Task 3.2	Scenario to demonstrate condition monitoring for a steam generator tube assembly	June 30, 2003	November 30, 2003
Task 3.3	Design options for a steam generator tube assembly test loop	Sept. 30, 2003	Dec. 15, 2003
Task 3.4	Sensor and communication options for test loop to obtain condition monitoring data on steam generator tube assembly	Oct. 31, 2003	March 31, 2004
Task 3.5	Fluid and FEAs of steam generator assembly to investigate dynamic response characteristics	Dec. 31, 2003	Dec. 15, 2004
Task 4.1	Condition monitoring technologies report	May 15, 2003	May 31, 2005
Task 4.2	Advanced sensor technologies report	Feb. 15, 2004	May 31, 2005
Task 4.3	Erosion and corrosion monitoring data	Feb. 28, 2004	May 31, 2005
Task 4.4	Baseline software using operational and laboratory data	August 31, 2004	May 31, 2005
Task 4.5	Signal processing and smart communication technologies report	Oct. 31, 2004	May 31, 2005
Task 4.6	Final technical project report on methods and results of prototype demonstrations	Dec. 31, 2004	May 31, 2005

Publications

The project team members prepared the following papers, which have been submitted for publication to document the technical findings from this joint research project:

For SMiRT17

1. Na Young Lee, Chi Bum Bahn, Si Hyoung Oh, Il Soon Hwang, Jung Taek Kim, Vincent K. Luk, Condition Monitoring of Flow-Accelerated Corrosion of a Simulated Low Alloy Steel Piping Elbow using Electrochemical and Vibration Sensors, SMiRT17, Prague, Czech Republic, August 2003.
2. J. H. Lee, M. R. Lee, J. T. Kim, J. S. Kim, V. K. Luk, Condition Monitoring of a Check Valve for Nuclear Power Plants by Means of AE Technique, SMiRT17, Prague, Czech Republic, August 2003.

For 11th Asia-Pacific Conference on Non-Destructive Testing

1. Jung-Taek Kim, Won-Man Park, Cheol-Kwon Lee, S. Hur/Korea Atomic Energy Research Institute (Korea), Jonathan Weiss, V. Luk/Sandia National Laboratories (US), Sang-Jeong Lee/Chung-Nam National University (Korea), I. S. Hwang/Seoul National University (Korea), Displacement Measurement Using Optical Sensors, 11th Asia-Pacific Conference on Non-Destructive Testing, Jeju, Korea, November 2003.
2. Na Young Lee, Chi Bum Bahn, Ji Hyun Kim, Tae Hyun Lee, Il Soon Hwang, Joon Hyun Lee, Jung Taek Kim, Vincent K. Luk, Development of an On-line Ultrasonic System to Monitor Flow-Assisted Corrosion of Piping in Nuclear Power Plants, 11th Asia-Pacific Conference on Non-Destructive Testing, Jeju, Korea, November 2003.
3. Seung-Hwan Seong, Jung Soo Kim, Seop Hur, Jung Tak Kim, Won Man Park/KAERI (Korea), The Development of Fusion Sensor Techniques for Condition Monitoring of Check Valve, 11th Asia Pacific Conference on Non Destructive Testing, Jeju, Korea, November 2003.
4. Seop Hur, S.H. Seong, W. M. Park, S. H. Nam, D. B. Cha, J. T. Kim/KAERI (Korea), S. J. Lee/Chung-Nam National University (Korea), I. S. Hwang/Seoul National University (Korea), Measurement of Piping Elbow Integrity Using Fiber-Optics Technique, 11th Asia-Pacific Conference on Non-Destructive Testing, Jeju, Korea, November 2003.
5. Cheol kwon Lee, J.T. Kim, J.S. Kim, S.J. Lee/Korea Atomic Energy Research Institute (Korea), J. Yoo/Chungnam National University (Korea), Condition Monitoring of Check Valve Using Time-Frequency Representation, 11th Asia-Pacific Conference on Non-Destructive Testing, Jeju, Korea, November 2003.
6. Joon-Hyun Lee, Min-Rae Lee/Pusan National University (Korea), Jung-Teak Kim, Jung-Soo Kim/Korea Atomic Energy Research Institute (Korea), Analysis AE Signals for Condition Monitoring of Check Valve at Nuclear Power Plants, 11th Asia-Pacific Conference on Non-Destructive Testing, Jeju, Korea, November 2003.

For ANS'03 Fall Meeting

1. Na Young Lee, Chi Bum Bahn, Il Soon Hwang, Jung Taek Kim, Vincent K. Luk, FAC Monitoring through Advanced Sensors, ANS winter meeting, New Orleans, US, November 2003.
2. Seop Hur, S.H. Seong, J. T. Kim/KAERI (Korea), S. J. Lee/Chung-Nam National University (Korea), Condition Monitoring Methods using the Fiber-optic Techniques for Nuclear Power Plants, NPIC&HMIT2004, ANS, September 2004.
3. Seung-Hwan Seong, Jung Soo Kim, Seop Hur, Jung Taek Kim, Won Man Park/KAERI (Korea), The Development of Condition Monitoring Technology for a Check Valve Using Acoustic Emission Sensor, NPIC&HMIT2004, ANS, September 2004.

For Key Engineering Materials

1. Jung-Taek Kim, Won-Man Park, Cheol-Kwon Lee, S. Hur/Korea Atomic Energy Research Institute (Korea), Jonathan Weiss, V. Luk/Sandia National Laboratories (US), Sang-Jeong Lee/Chung-Nam National University (Korea), I. S. Hwang/Seoul National University (Korea), Fiber-Optic Displacement Sensor to Detect the Vibration of the Thinned U-section by FAC, Key Engineering Materials(SCI), vol. 270-273, June 2004.
2. Na Young Lee, Chi Bum Bahn, Ji Hyun Kim, Tae Hyun Lee, Il Soon Hwang, Joon Hyun Lee, Jung Taek Kim, Vincent K. Luk, Development of an On-line Ultrasonic System to Monitor Flow-Assisted Corrosion of Piping in Nuclear Power Plants, Key Engineering Materials(SCI), vol.. 270-273, June 2004.
3. Seung-Hwan Seong, Jung Soo Kim, Seop Hur, Jung Taek Kim, Won Man Park/KAERI (Korea), The Development of Fusion Sensor Techniques for Condition Monitoring of Check Valve, Key Engineering Materials(SCI), vol. 270-273, June 2004.
4. Seop Hur, S.H. Seong, W. M. Park, S. H. Nam, D. B. Cha, J. T. Kim/KAERI (Korea), S. J. Lee/Chung-Nam National University (Korea), I. S. Hwang/Seoul National University (Korea), Measurement of Piping Elbow Integrity Using Fiber-Optics Technique, Key Engineering Materials(SCI), vol. 270-273, June 2004.
5. Cheol kwon Lee, J.T. Kim, J.S. Kim, S.J. Lee/Korea Atomic Energy Research Institute (Korea), J. Yoo/Chungnam National University (Korea), Signal Analysis for the Condition Monitoring of a Check Valve Using a Time-Frequency Representation, Key Engineering Materials (SCI), vol. 270-273 June 2004.
6. Joon-Hyun Lee, Min-Rae Lee/Pusan National University (Korea), Jung-Teak Kim, Jung-Soo Kim/Korea Atomic Energy Research Institute (Korea), Analysis AE Signals for Condition Monitoring of Check Valve at Nuclear Power Plants, Key Engineering Materials(SCI), vol. 270-273, June 2004.

For Korea Nuclear Society (KNS)

1. Seung-Hwan Seong, Jung Soo Kim, Seop Hur, Jung Taek Kim, Won Man Park/KAERI (Korea), Development of a Diagnostic Algorithm with Acoustic Emission Sensors and Neural Networks for Check Valves, Korea Nuclear Society, Vol 36, no. 6, December 2004.
2. Jung-Taek Kim, Cheol-Kwon Lee, S. Hur/Korea Atomic Energy Research Institute(Korea), Sang-Jeong Lee/Chung-Nam National University (Korea), I. S. Hwang/Seoul National University (Korea), Condition Monitoring through Advanced Sensor and Computational Technology, Korea Nuclear Society, ANS 2004 Fall Meeting, October 2004.

Appendix A: Condition monitoring of check valve

I. License issues and failure analysis of components

The licensing issues and failure analysis[1] *of components in NPPs in the US*

There are 103 NPPs in the US, two thirds of which (about 70 NPPs) have been in operation for more than 25 years. In these NPPs, the performance of structures and components related to safety were evaluated as “outstanding,” but their failure rate tends to increase with the age of the NPP. Figure 1, which shows the number of degradation occurrences of passive structures and components, indicates that the number of NPP stoppages due to deterioration of passive components increased steadily with the age of NPP. The average of these occurrences is 27 per year. Figure 2 shows the distribution of degradation occurrences by age of NPPs per year for different NPP vintages. Although the actual number of occurrences is not high, this curve demonstrates that as the age of NPPs increases, the number of occurrences per NPP per year also increases. The actual number of occurrences over a 14 year period shows a growth of almost four times from about 0.065 to 0.24 (NPP operation year).

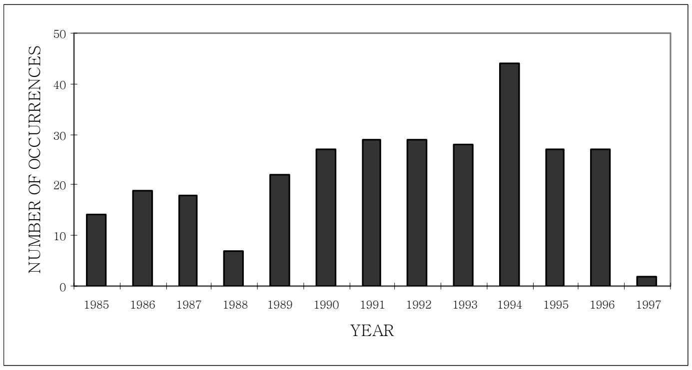

Figure 1 **Degradation occurrence distributions of passive structures and components versus year (1985 to 1997)**

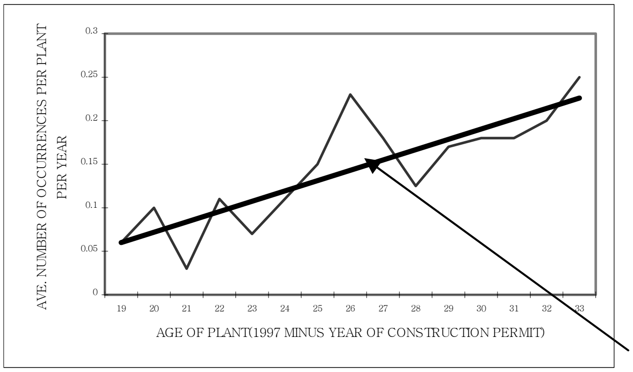

Best fit

Figure 2 **Degradation occurrence distribution of passive structures and components versus age of NPPs**

A further detailed investigation into the failure occurrence at the sub-component level indicates that a very high number of occurrences (greater than 80 items during 1985 to 1997) is associated with piping and tubing failures. Figure 3 shows the detailed breakdown of this finding.

---

[1] This section includes details for license issues and failure analysis that are introduced in Section 3.1.

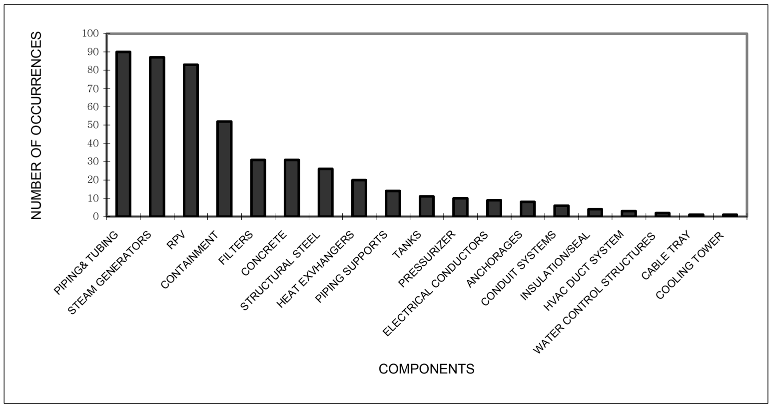

Figure 3 Degradation occurrences of passive structures and components at sub-component level

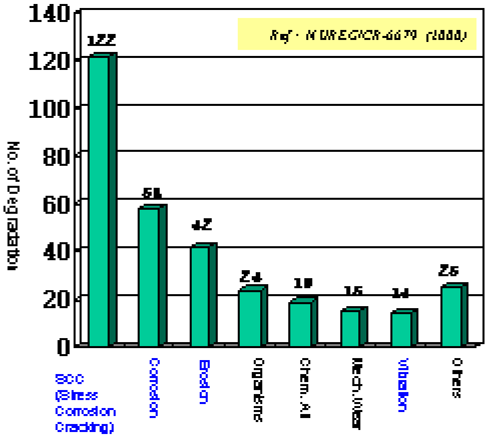

Figure 4 Degradation occurrence distribution by aging mechanisms

Figure 4 shows the distribution of degradation occurrences of the passive components by aging mechanisms. The predominant aging mechanisms, in descending order, are SCC, corrosion, erosion, organisms, chemical attack, mechanical wear, and vibration.

Concerning component failures, the NRC published reports such as GL-89-10 (on motor-operated valves), GL-89-04 (on check valves), and SOER 86-3 (on check valves) to document the diagnosis of components during normal operation. The NRC plans to enforce the in-service inspection during operation period by enlarging the inspection range of important components such as the valves or pumps in operational NPPs.

In essence, NRC recommended the utilities to establish the predictive maintenance procedure (testing and inspection) to confirm early failure occurrences of pumps and valves. In addition, Institute of Nuclear Power Operation (INPO) recommended utilizing the diagnosis equipment to find faulty components without disassembling them. Electric Reactor Power Institute (ERPI) and Nuclear Inspection Commission developed a program to detect the performance of components through checking or disassembling processes.

Operating & Maintenance (OM) Part 10 described the in-service testing of valves in light-water reactors. The leakage test of valves was performed once every two years according to procedures in 10 CFR 50 Ap. J. The leakage test should be performed under similar conditions to the differential pressure during normal operation. It was recommended that Category C valve should meet the requirement of Part 1 in case of safety and pressure valves.

The report, *INPO 86-03*, described the failure occurrence of check valves from 1984 to 1986 in the US. This report identified the main failure mechanisms of check valves, including the over-pressurization of low-pressure systems, water hammer, steam binding, loosening of nuts and bolts, failure of internal components, and stoppage of flow caused by internal failure. Table 1 provides the details of these failure mechanisms.

Table 1 Main failure mechanisms of valves

Failure Mechanism	Number
Internal leakage	376
External leakage	160
Fail to close	86
Fail to open	9
Very slow closing	1
Hinge pin wear	28
Total	672

The licensing issues and failure analysis of components in NPPs in Korea

In Korea, the in-service testing of safety-related valves (*MOST Notice 1994-10*) and the inspection and testing at normal operation of NPPs (*MOST Notice 1995-01*) do not require the safety valves to satisfy the criteria nor apply the specific testing recommended by the criteria. Instead, utilities could apply alternative criteria or guides. In addition, the alternative criteria should be executed within a practical range, at least not to obstruct the reliability of equipment or the integrity of a related facility. The MOST Notice that contains the adopted criteria since 1995 is based on the American Society of Mechanical Engineers (ASME) requirements in the US.

Analysis of failure modes of components in Korea

This project focuses on analyzing failure data on pumps or valves (active components). The survey was targeted at operating PWR NPPs (except the Canadian deuterium uranium [CANDU] type). The survey method, which separated all NPPs into two main categories of operating duration either below or above 10 years, analyzed the maintenance database at overhaul period and failure reporting data at each NPP. The failure modes of valves are assembled in Table 2.

In Table 2, the left chart describes the total number of failure modes and the right chart illustrates the leak position of valves. This table identifies leakage as the main failure mode of valves (above 40% of the total failure occurrences) and gasket and gland packing as the predominating failed component part (above 50% of the total failures). However, the failure database of check valves in the US indicates that the disc support bar was frequently broken within the design life of each check valve; therefore, it is necessary to develop a condition monitoring technique to detect premature failure of check valves.

Table 2 **Failure modes of valves at all NPPs.** *(Left) failure modes (right) valve leak position.*

Total Failure	906	%	leak position of failure	729	%
leak	427	47.13	gasket	229	31.41
packing change	249	27.48	gland packing	201	27.57
drive failure	72	7.95	internal leak	85	11.66
over pressure	31	3.42	stem	64	8.78
hadnle broken	20	2.21	diapharm	52	7.13
flow change	14	1.55	ring	34	4.66
crack	13	1.43	flange	19	2.61
change filter	10	1.10	line	9	1.23
fan belt change	8	0.88	bonnet	9	1.23
pin hole	8	0.88	external leakage	6	0.82
flange change	8	0.88	connection line	5	0.69
O/H inspection	7	0.77	muffler	3	0.41
blocking	5	0.55	pin hole	3	0.41
hose installation	5	0.55	welding	3	0.41
line change	4	0.44	sealing	3	0.41
stem fault	4	0.44	pump body	2	0.27
VRC change	4	0.44	nut, bolt	1	0.14
check valve failure	3	0.33	york	1	0.14
boron cleaning	3	0.33			
low pressure	2	0.22			
increase level	2	0.22			
inapprobriate pipe size	2	0.22			
motor borken	1	0.11			
change moisture-proof	1	0.11			
broken pipe	1	0.11			
oil	1	0.11			
install lag	1	0.11			

The valve failure modes were surveyed at each NPP. Figure 5 shows the status of failure modes of valves during 20 years of NPP operation. In this figure, the packing and gasket account for more than 60% of all failure occurrences. Leakage was identified as the main failure mode. Figure 6 shows the status of failure modes of valves during 10 years of NPP operation. The database in Figures 5 and 6 were surveyed from January 2000 through December 2001.

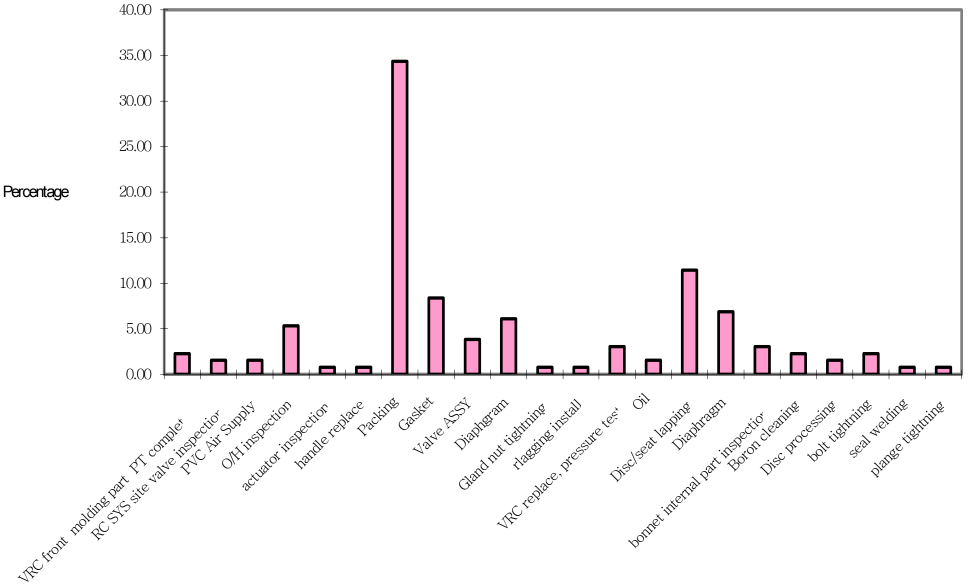

Figure 5 Status of failure modes of valves during 20 years of NPP operation

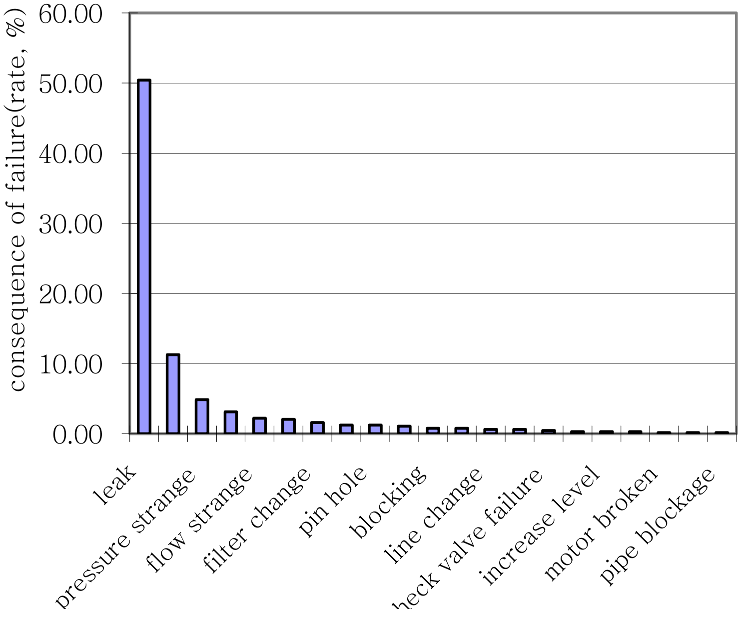

Figure 6 Status of failure modes of valves during 10 years of NPP operation

The failure modes of valves are illustrated in Figure 7, which identifies leakage as the primary failure mode and mechanical problems, such as failure of flange, as the secondary failure mode.

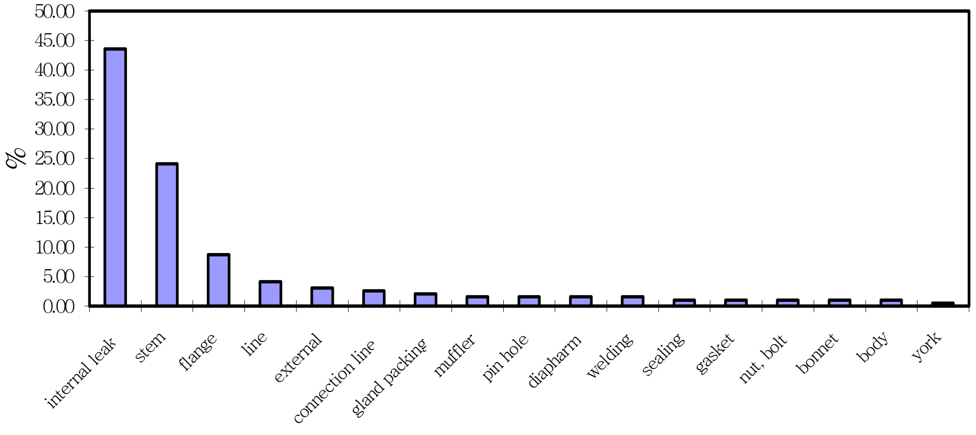

Figure 7 **Failure modes of valves**

In summary, internal leakage was identified as the main failure mode of valves, as indicated in Figures 5 to 7. In addition, there were more failure occurrences in NPPs with 20 years of operation than those with 10 years of operation. Therefore, the failure occurrence of components increases with the operating age of NPPs. It is important to point out that the leakage failure can be prevented if early detection device were available; therefore, a condition monitoring technique is needed to detect early malfunctioning of components during normal NPP operation. The NPP operator can be informed of the health status of components in time to take proper actions to remedy any potential problems.

II. Signal characteristics for check valve failures

The specifications of input and output signal on DASs as well as the characteristics of sensors used in the check valve test loop are discussed here.[1]

AE monitoring

AE is detected by sensors, such as piezoelectric-type accelerometers or microphones, which respond to pressure waves over a wide range of frequencies. Analyses of AE signals obtained from check valves can be used to monitor check valve disc position, movement, and mechanical condition, as well as internal flow/leakage through the valve. Various methods of obtaining and analyzing data are available, including filtering, FFT, and pattern recognition techniques.

In this project, AE monitoring was used to detect check valve disc movement and to evaluate valve degradation, such as disc and hinge pin wear. The check valve AE testing was performed under controlled flow-loop conditions and with the introduction of various implanted defects to simulate severe aging and service wear. The specifications of input characteristics and output signal on DASs for the AE sensors are as follows:

- Physical Acoustic Corporation®: R15
- Frequency range: 50 to ~200 kHz, central frequency: 150 kHz
- Physical Acoustic Corporation: WD
- Frequency range: 100 to ~1000 kHz, central frequency: 650 kHz, 100 to ~1200 kHz (BPF)

The AE sensor was used for the following operational conditions:

- Valve with normal configuration and artificially disc wear: 1 mm, 2 mm, and 3 mm depth half-circle
- Valve with normal configuration and artificially hinge pin wear: 1 mm, 2 mm, and 3 mm depth hinge pin cutting

---

[1] This section includes details of sensor characteristics that are introduced in Section 3.2.1.4.

- Valve with normal configuration and artificial leakage: 1.0 mm, 1.2 mm, and 1.6 mm foreign object interference between body and disc
- Valve with improper assembly: separating disc from disc arm by loose disc pin
- Loop operation condition (steady state, transient operation at 0, 3, 6, and 9 bar).

To get the baseline data from typical wearing such as disc wear, hinge pin wear, and foreign object interference, the leak tests were conducted for condition monitoring of check valves at the DVI test loop. The AE sensor data were taken at various pressure levels on a normal check valve, and then an artificial defect was induced, such as a foreign object interface, disc wear, and a loose hinge pin. These data were analyzed with various data processing techniques.

The specifications of input characteristics and output signal on AE DASs are listed in Table 3. Figure 8 and 9 show examples of artificially degraded check valves.

Table 3 **Frequency ranges of AE sensor and preamplifier**

Type	Frequency Range	Center Frequency	Filter (BPF)
WD	100 to 1000 kHz	650 kHz	100 to 1000 kHz
R15 (resonance)	50 to 200 kHz	150 kHz	100 to 300 kHz

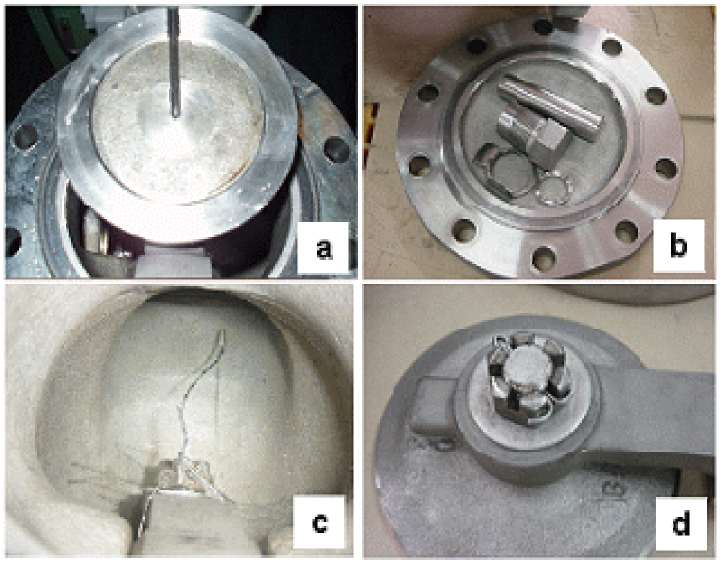

Figure 8 **Four different kinds of artificial defects of check valve.** *(a) Disc wear (b) hinge pin wear (c) foreign object (d) improper assembly*

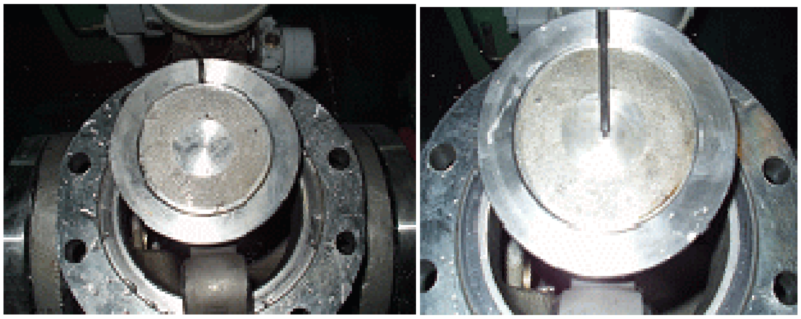

(a) 1.0 mm (b) 3.0 mm

Figure 9 **Example of artificial disc wear of check**

valve

Ultrasonic monitoring

Ultrasonic measurement involves introducing high-frequency sound waves into a test part and analyzing the characteristics of the reflected beam. Typically, one or two ultrasonic transducers are used to provide both transmission and receiving capabilities. The ultrasonic signal is injected from outside the valve at the transmitting transducer and passes through the valve body, where it is reflected by an internal part (such as the disc or hinge arm) back toward the receiving transducer.

The ultrasonic technique is used to produce a time waveform display from which disc position and movement may be determined. It can also be used to detect a missing or stuck disc. For example, if the disc is missing, no signal will be reflected; therefore, disc wear can be detected by ultrasonic technique by monitoring the motion of both the disc and hinge arm using ultrasonic transducers. The specifications of input characteristics and output signal on DASs for ultrasonic sensors are as follows:

Input frequency range for the ultrasonic device:

- 2 MHz angle beam transducer, 0.25 in. element diameter (Techsonic, USA®)
- 5 MHz angle beam transducer, 0.25 in. element diameter (Techsonic, USA)
- 20°, 30°, 45°, 60°, and 70° wedges (Techsonic, USA)

Frequency of ultrasonic data to be stored by the DAS:

- Oscilloscope (LeCroy® 9310A, DUAL 400 MHz)

Accelerometer monitoring

Accelerometers are used to detect vibration signals from pressure waves over a low-frequency range (<100 kHz) when strapped to the valve body. The specifications of input and output signals on DASs for the accelerometers are as follows:

- Wilcoxon Research®: model 736 (serial no. 11173)
- Frequency range: 5 Hz to ~24.5 kHz, central frequency: 52 kHz, sensitivity: 98 mV/g
- Wilcoxon Research: model 736 (serial no. 11174)
- Frequency range: 5 Hz to ~24 kHz, central frequency: 52 kHz, sensitivity: 100 mV/g

III. Data transmission and smart sensor techniques[1]

Realization of wired communication

The preprocessed sensor signals are transmitted to the remote analysis computer via wired communication. Since the bandwidth of AE sensor signal is about 400 kHz, the sampling rate must be at least 1 MHz. A data transmission scheme was developed and implemented via the fieldbus called DeviceNet. There are a few advantages of using the fieldbus as the communication network. It supports bi-direction communication and it can reduce more cost of wiring than the existing point-to-point communication method because it uses a single transmission medium. In addition, it can reduce the effect of noise more effectively than the existing analogue method because of application of digital signal. Therefore, fieldbus can improve the overall control performance of systems with added flexibility. The DeviceNet, which is an industrial networking protocol based on the Controller Area Network (CAN), was selected to facilitate higher-level communication features by allowing industrial devices from different vendors to operate on the same network

Wireless communication

One of the tasks of this research project is to develop and demonstrate advanced wireless communication technology for continuous monitoring for the condition of components, structures, and systems in NPPs.

---

[1] This section includes details for the KAERI/CNU prototype using wireless communication, which is introduced in Section 3.2.2.2.

Figure 59 shows a schematic wireless communication system for condition monitoring of check valves. The basic requirements for this system include:

- Low-power system
- High level security
- Embedded system for field-testing
- Low maintenance and repair costs
- Wired equivalent credibility
- Digital technology of measuring instrument
- Multi-drop mode for master system
- Real-time monitoring system

The development of the embedded Linux and wireless LAN (IEEE 802.11b) technology will facilitate meeting these requirements.

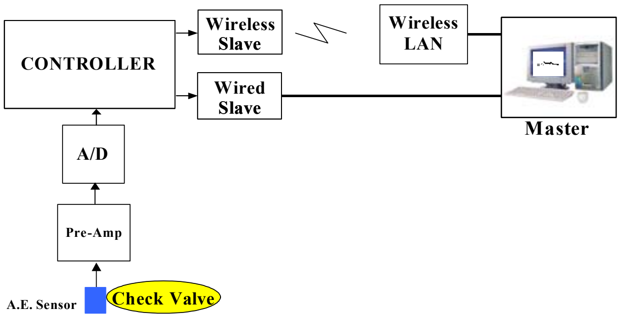

Figure 59 **A schematic wireless communication system for check valve condition monitoring**

An IEEE 802.11 LAN is based on a cellular architecture where the system is subdivided into cells, where each cell is controlled by a Access Point (AP). Although a wireless LAN may consist of a single cell with a single access, most installations are formed by several cells, where the AP are connected through some kind of backbone, typically Ethernet, and in some cases wireless itself. The whole interconnected wireless LAN including the different cells, their respective AP and the distribution system, is shown in Figure 60.

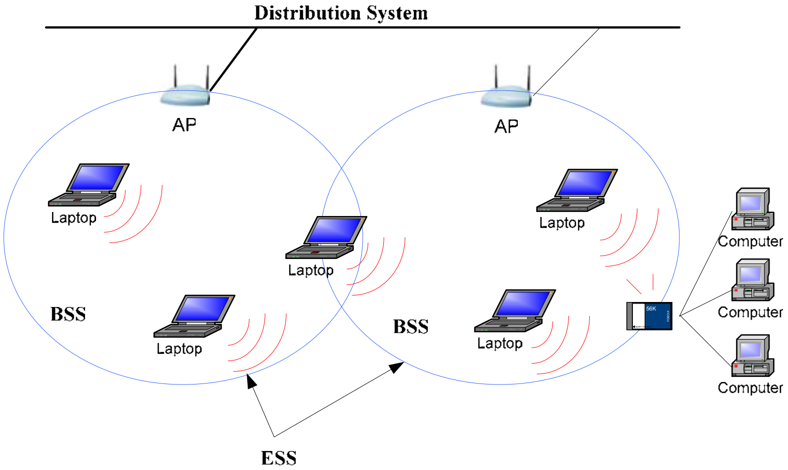

Figure 60 **Typical 802 11 LAN**

Data are transmitted in wireless LAN through sockets that allow reading and writing data to the storage device by opened files. The socket permits one application to communicate with another application that is plugged in network by "plug in" process to network. Data, written by one host application can be read by other host application and vice versa.

An embedded development environment was constructed for the wireless communication network. The Linux kernel structure, shown in Figure 61, was chosen to provide the communication architecture.

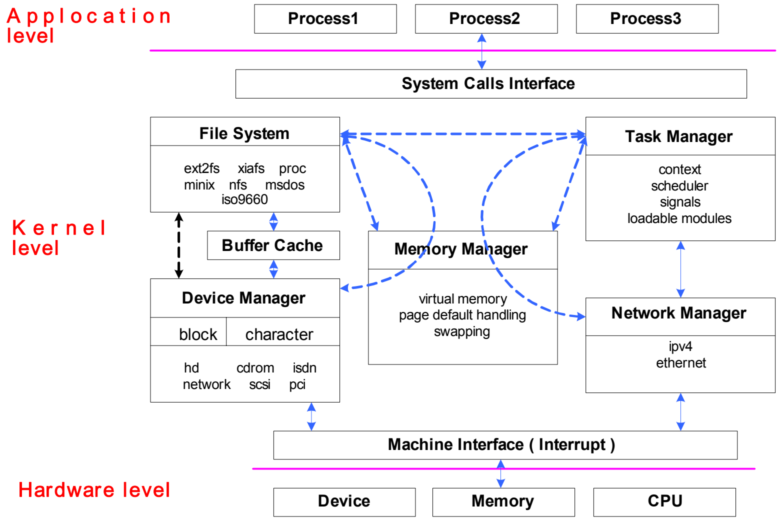

Figure 61 **Internal structure of Linux kernel**

In this figure, the internal structure of Linux kernel is divided into various logical elements, including task manager, memory manager, file system, network manager and device manager:

- Task manager: task generation and execution, state transition, scheduling, signal processing, and inter-process communication
- Memory manager: virtual memory, address translation, and handling page absence fault
- File system: file generation, access control, and mode and directory management
- Network manager: socket interface
- Device manager: composed of driver for disc, terminal, CD, and network card

In the Linux system, the device manager is implemented in the coherent structure. The device manager is an internal function of the kernel that performs the communication between device and system memory.

IV. Experimental setup[1]

This experiment planned to collect baseline data on the background noise and leakage flow of selected check valves. This experiment was performed with three sensor devices: AE, ultrasonic, and accelerometer. Figure 10 provides a simplified drawing that illustrates the basic operation of the condition monitoring. Figure 11 and 12 show the attached sensor positions schematically and in photographs, respectively.

---

[1] This section includes details for the check valve test loop experimental setup, which is introduced in Section 3.4.1.3.

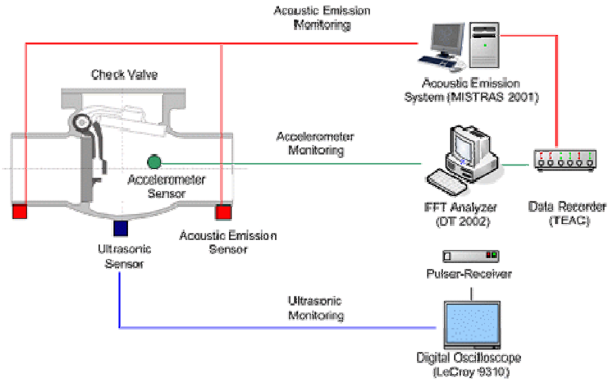

Figure 10 Schematic diagram of the condition monitoring test

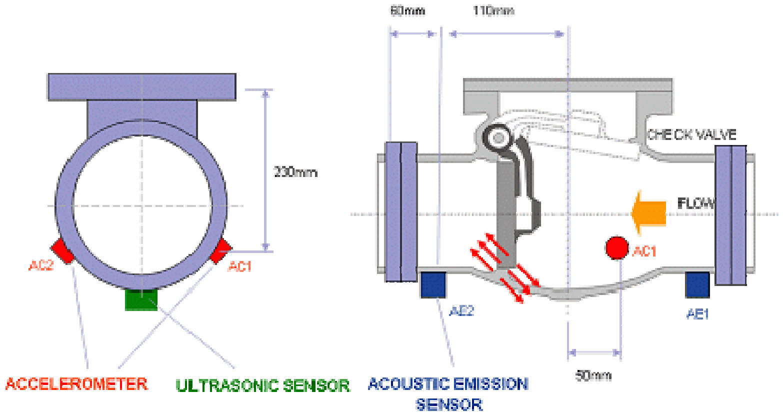

Figure 11 Typical attachment points for each sensor

Figure 12 Photograph of experimental setup

V. Background noise analysis[1]

The first experiment

In this project, the characteristics of advanced fusion sensors were evaluated. Fusion sensors combine the signals from different types of sensors and apply them to extend the measurement range, accuracy, or application of a single type of sensor. Fusion sensors can also reduce the noise and uncertainties of signal origin or data association for single sensors. Advanced fusion sensors integrated with AE, ultrasonic, and accelerometer sensors are applied for condition monitoring of check valves. To get baseline condition monitoring data of check valves, the first experiment was performed with the original DVI test loop at KAERI, shown in Figure 13, and the second one was performed with the modified DVI test loop.

Figure 13 Schematic diagram for condition monitoring of check valve at KAERI

Results and discussion

Figure 14 shows the typical AE waveform and corresponding spectra obtained from background flow noise. As shown in the figure, the FFT is concentrated in the range of 100 kHz; however, Figure 15 shows the waveform and corresponding spectra for the accelerometer output. The resulting accelerometer signature shows that the FFT is concentrated in the range of 0.2 and 2.4 kHz.

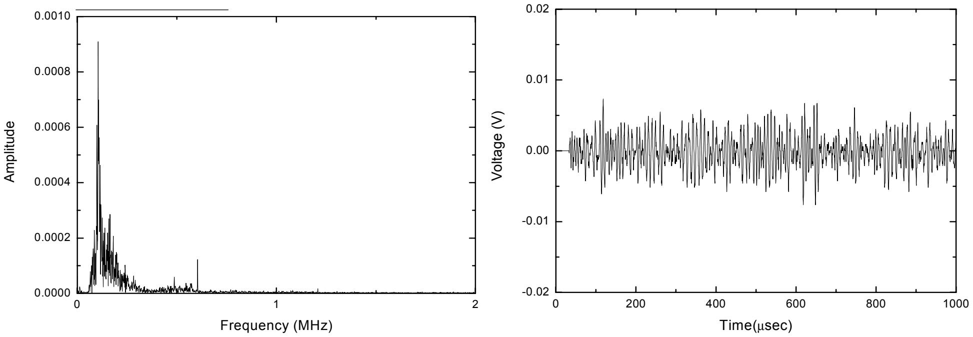

(a) Waveform (b) FFT

Figure 14 AE waveform and corresponding spectra from background flow noise

---

[1] This section includes details for background noise analysis, which is introduced in Section 3.5.1.

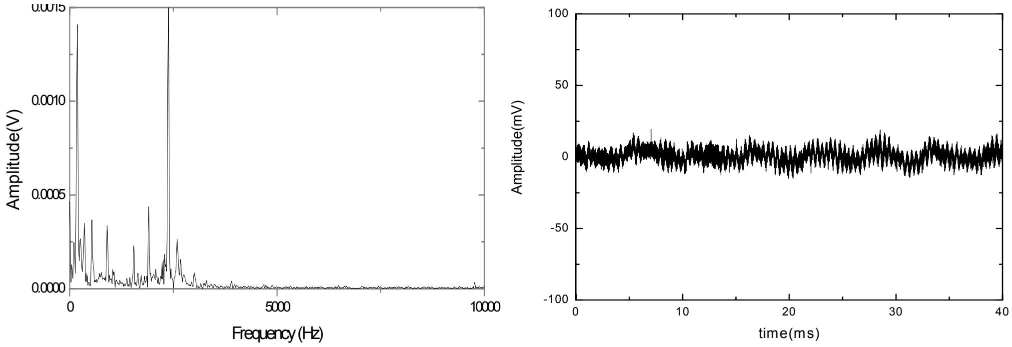

(a) Waveform (b) FFT

Figure 15 **Accelerometer waveform and corresponding spectra from background flow noise**

The second experiment

In this experiment, the AE signals were detected with sensors attached to the center of the check valve. The AE data were collected and compared to data from accelerometer and ultrasonic sensors and for different operating conditions. Figure 16 shows the schematic diagram of the installation for this test, with accelerometers on the side and an ultrasonic transducer (1 MHz) on the bottom of the check valve body. Figure 17 shows a photograph of the condition monitoring.

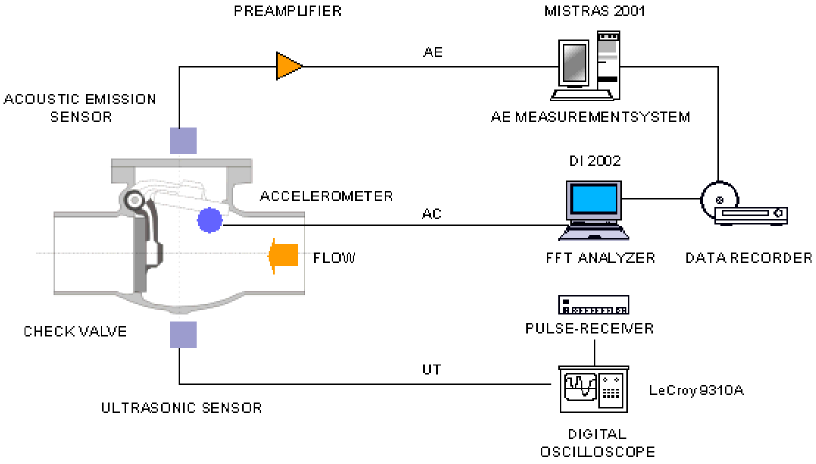

Figure 16 **Schematic diagram of modified DVI test loop at KAERI**

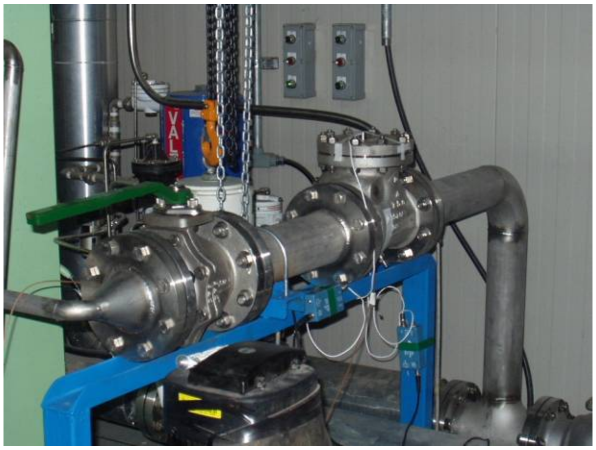

Figure 17 **Photograph of modified DVI test loop at KAERI**

Results and discussion

Three check valves–A, B, and C–were investigated in this test series. Figure 18 shows the typical AE waveform and corresponding spectra obtained from background flow noise in valve B. Figure 19 shows the typical AE waveform and corresponding spectra obtained from leak flow signal in check valve B. Comparison of data in these two figures indicates that a leak is detected on the basis of the significant difference in the leak signal and the background signal.

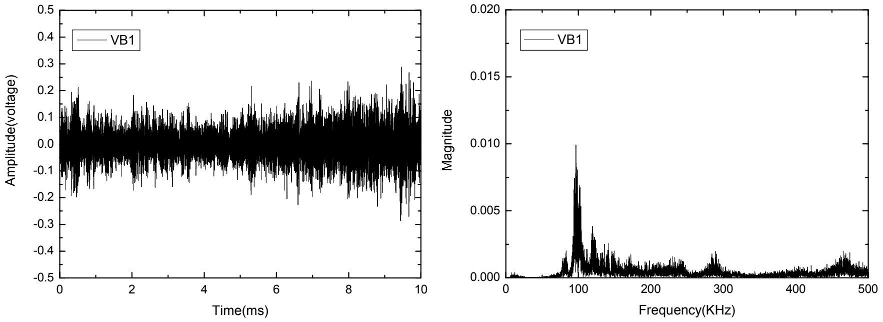

(a) Waveform (S_1)   (b) FFT (S_1)

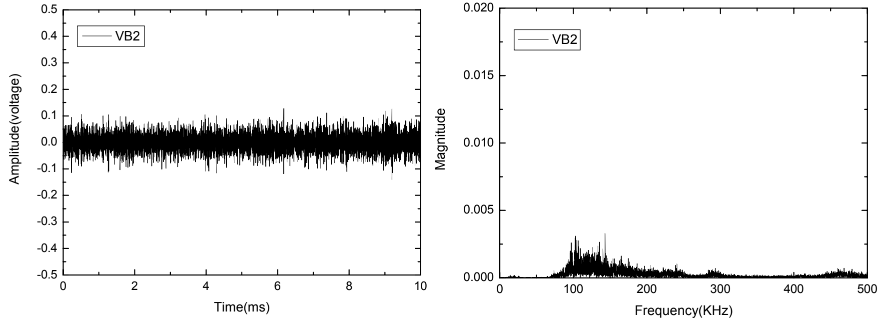

(a) Waveform (S_2)   (b) FFT (S_2)

Figure 18 AE waveform and corresponding spectra from initial background noise (valve B)

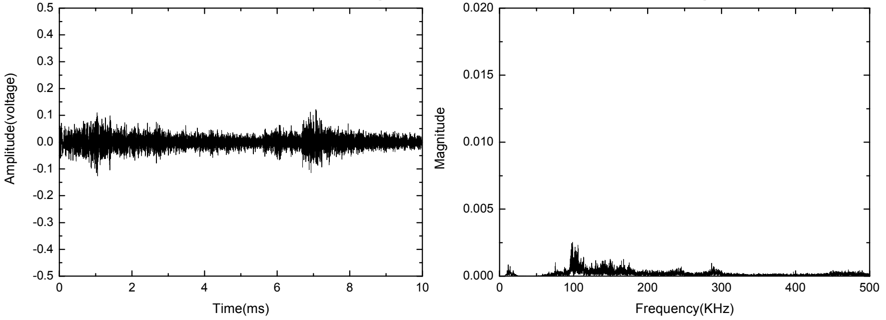

(a) Waveform (S_1)   (b) FFT (S_1)

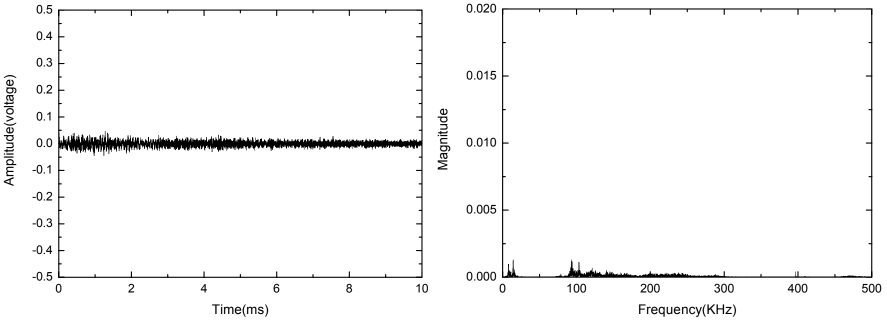

(a) Waveform (S_2)   (b) FFT (S_2)

Figure 19 AE waveform and corresponding spectra from leak valve (leak valve B)

The AE amplitude results are shown in Figure 20. As shown, the signal levels normally increased with the pressure and most of the AE threshold level of the check valve having high amplitude (75 to 80 dB) were observed, which suggests that the AE signals are the result of mechanical disturbances (such as vibration of the pipe line). However, some AE signals of the burst type were detected and it was confirmed that the AE signals were associated with the leakage.

Figure 21 (a) and (b) present a typical oscillogram of the open and closed traces captured by the UT sensors during operation, respectively. As shown in these figures, it seems that disc position was detected near the bottom of the check valve. Comparison of results between the two signals suggests that it is possible to detect the disc location of the check valve.

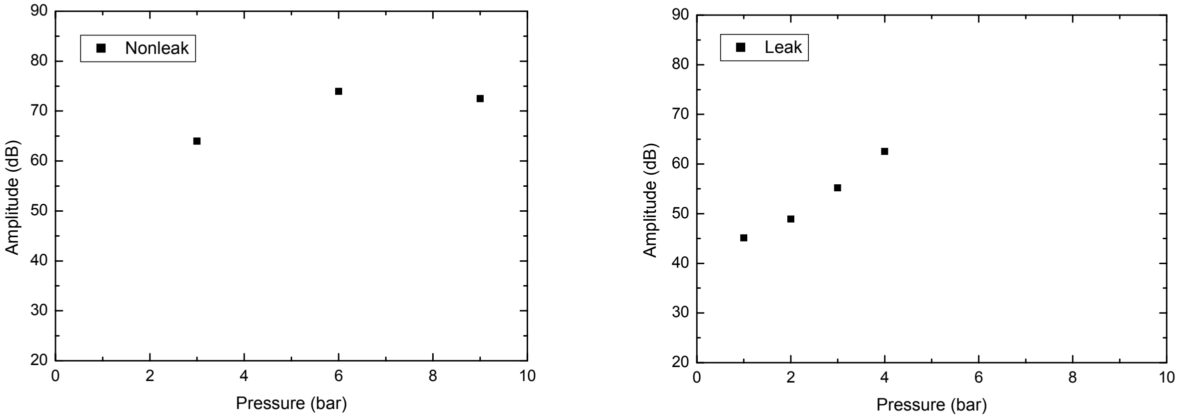

(a) AE amplitude during non-leak (b) AE amplitude during leak

Figure 20 AE amplitude versus pressure

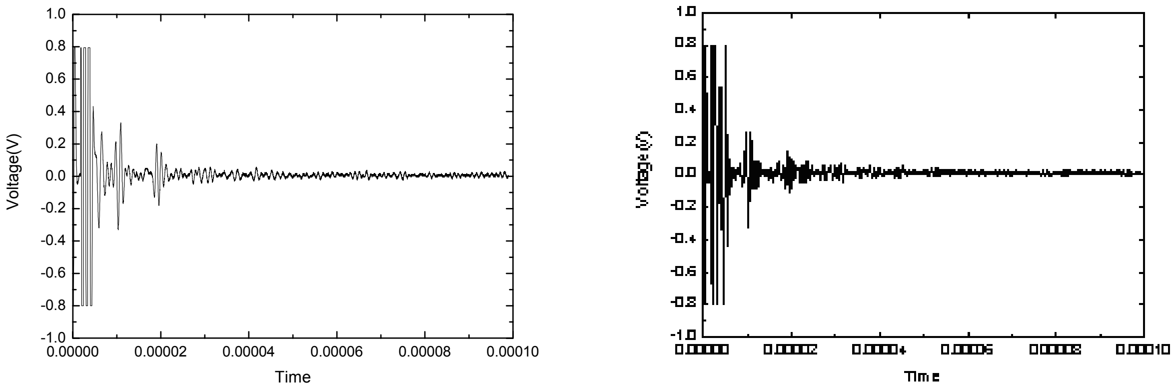

(a) Disc open (b) Disc close

Figure 21 UT signals obtained from disc of check valve

The third experiment

Experimental setup. The AE signals are detected with AE Sensor 1 attached to the center of the bottom of the check valve and AE Sensor 2 to the pipeline of test loop. The AE data were compared to data from an accelerometer and an ultrasonic transducer under different operating conditions.

Figure 22 shows the installed sensor positions for condition monitoring. Accelerometers were strapped to the body of the check valve and an ultrasonic transducer (1 MHz) was attached to its bottom as shown in Figure 22. Figure 23 shows a photograph of the sensor setup for the test. The test valves were swing-type check valves (A, B, C, and D). The AE testing of check valves was conducted under controlled flow-loop conditions and with the introduction of various artificial defects that simulated severe aging and service wear. The AE check valve monitoring was performed with the following operational conditions:

- Valve with new and artificially worn disc (slit thickness 0, 1, 2, and 3 mm)
- Valve with artificially leakage (implanted defects diameter of 0, 85, 1, and 2 mm)
- Loop condition (steady state, at operating pressures 0, 3, 6, and 9 bar)

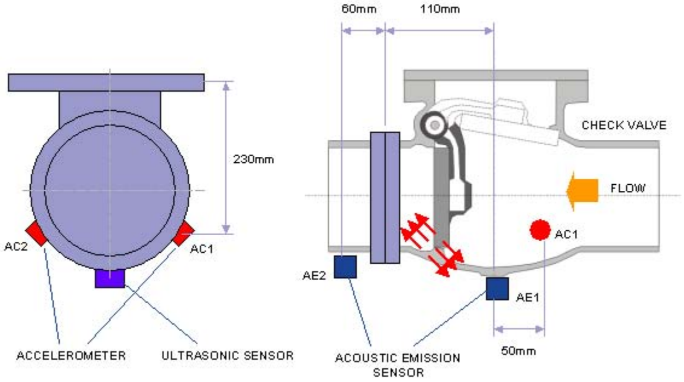

Figure 22 **Sensor positions for modified DVI test loop @ KAERI**

Figure 23 **Photograph of sensor positions for on-line condition monitoring test**

Results and discussion

Figure 24 shows the typical AE waveform and corresponding spectra obtained from background flow noise (valve D). In this case, the sampling rate is 100 kHz, and threshold level is 0 dB, data acquisition time is 0.5 s. This figure indicates that the typical AE_1 waveform is similar to AE_2 waveform. However, it was not found that the FFT is concentrated in the range of 100 to ~500 kHz because of the limit of sampling rate of 100 kHz. In this case, the lowest possible low sampling rate was chosen for the maximum data acquisition time.

On the other hand, Figure 25 shows that the typical AE spectra were not found from the leak flow signal of check valve D (which had a leak diameter of ~0.85 mm); rather, the leak was detected on the basis of the significant difference in the leak and background signals. Figure 26 shows the typical AE waveform and corresponding spectra obtained from the leak flow signal of check valve D (which had a diameter of 1.20 mm implanted defect size). In this test series, the signal amplitude increases with increased leak size.

Figure 27 shows the typical AE waveform obtained from check valve D with worn disc having slit thicknesses 1, 2, and 3 mm. As shown, the signal amplitude increases with the increasing slit thickness of worn disc. However, the amplitude of AE_2 signals appeared higher than that of AE_1 signals. Leak was detected on the basis of the significant difference in the leak and background signals.

The waveforms and corresponding spectra for the accelerometer output of initial background noise (valve D) are discussed in detail later in this appendix. The typical accelerometer waveform obtained from check valve D with worn disc having slit thicknesses 1, 2, and 3 mm are discussed in detail later in this appendix.

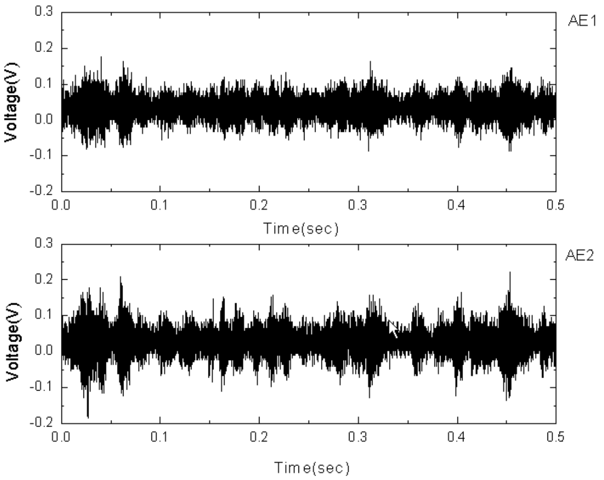

Figure 24 AE waveform and corresponding spectra from initial background noise (Valve D)

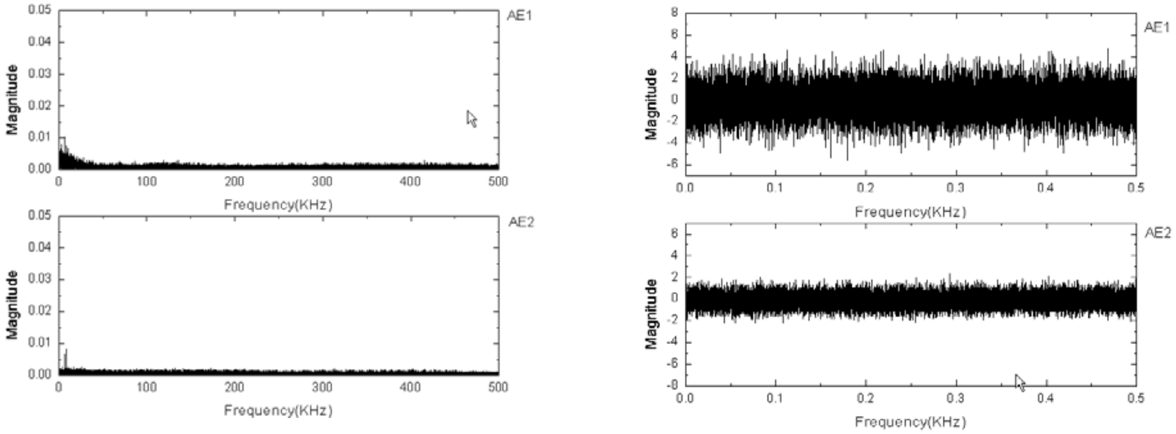

(a) ϕ 0 mm

(b) ϕ 0.85 mm

Figure 25 AE waveform and corresponding spectra from leaked valve

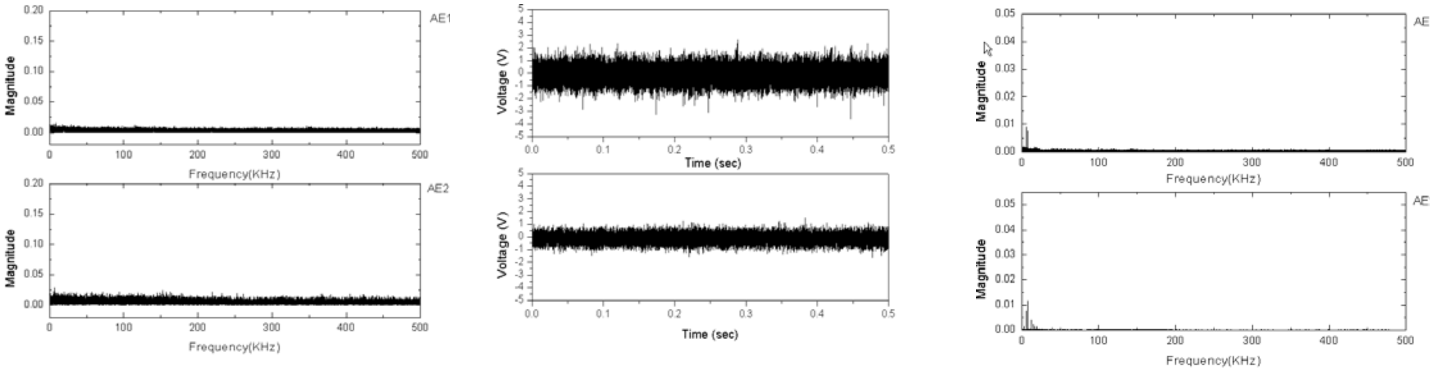

Figure 26 AE waveform and corresponding spectra from leaked valve (ϕ 1.20 mm)

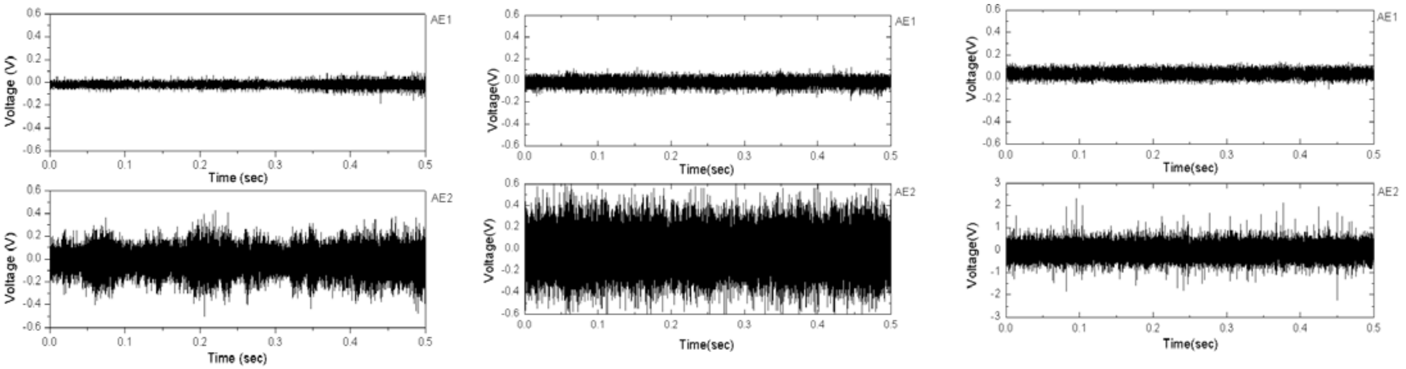

(a) slit 1 mm (b) Slit 2 mm (c) Slit 3 mm

Figure 27 AE waveform and corresponding spectra from worn disc

VI. Digital signal-processing techniques[1]

Digital signal-processing techniques are divided into two types: noise filtering and pattern recognition involving signal analysis and validation.

Noise-filtering techniques

Several noise filters were used in the time and frequency domains to effectively isolate the background noises.

Design in the time domain:

- Moving window average method. It has been known that the moving window average method can estimate slowly time-varying offset or bias. The moving average operation is very simple and calculates the mean value from sampled values at the center point of a specific interval. The moving average method, which acts like a low-pass filter, can eliminate the background noise of high-frequency components.
- Kalman filter. The Kalman filter is designed as the state estimation method in the time domain with real-time implementation because of Infinite Impulse Response (IIR) structure expressed in linear recursive type. However, the Kalman filter contains the divergent possibility caused by modeling error to calculate errors. Identification of the background noise characteristics has to precede applying the Kalman filter when the background noise model is not available.
- Finite Impulse Response (FIR) filter/smoother. In many cases, the FIR structure (although inefficient in computation) is often used instead of the IIR structure because it has built-in Bounded Input/Bounded Output (BIBO) stability, robustness to parameter changes and round-off errors, and has a linear phase property. As in the case of the Kalman filter, the background noise model is required before applying the FIR filter/smoother.

The background noise-reduction techniques in the time domain are summarized in Table 4.

Table 4 Background noise-reduction techniques in time domain

Method	Advantage	Disadvantage
Moving window average	Simple structure	Sensitive to window size
Kalman filter	Possible real-time implementation because of recursive type	Possible to diverge due to modeling error
FIR filter/smoother	Build-in BIBO stability Robustness to parameter change and round-off error	Requires significant processing

Design in the frequency domain:

---

[1] background noise analysis

- Butterworth filter. The transfer function of the Butterworth filter offers maximally flat amplitude. Selectivity is better than Bessel filters but the delay and phase linearity are worse. The Voltage Standing Wave Ratio (VSWR) at center is extremely good. Butterworth filters, in most instances, are the least sensitive to changes in element values.
- Chebychev I, II filter. The transfer function of the Chebychev I, II filter is derived from Chebychev I (II) equal ripple function in the pass band (stop band) only. These filters offer performance between that of elliptic function filters and Butterworth filters. For the majority of applications, Chebychev I, II is the preferred filter type because it offers improved selectivity (compared to Butterworth filters) and result in simpler networks (compared to elliptic function filters).
- Elliptic function filter. The transfer function of the elliptic function filter is derived by using Jacobian elliptic functions. The amplitude is equal ripple in both pass band and stop band. This type of filter offers the most selectivity per pole but has the worst delay and phase linear performance. These filters can sometimes be designed wider than Butterworth or Chebychev filters, thereby offering reduced insertion loss.
- Bessel Filter. The transfer function of the Bessel filter is derived from a Bessel polynomial, which yields a filter having a maximally flat time delay but has poor selectivity. This type of filter is close to a Gaussian filter. It has poor VSWR and loses its maximally flat delay properties at wider bandwidths.

The background noise-reduction techniques in the frequency domain are summarized in Table 5.

Table 5 Background noise-reduction techniques in frequency domain

	Delay and Phase Linearity	**Selectivity**
Butterworth	Good	Poor
Chebychev	Poor	Good
Elliptic	Worst	Best
Bessel	Best	Worst

Pattern-recognition techniques

Signal-analysis technology. Traditional signal analysis by Fourier transform has many alternative methods. The necessity of their application is provoked by non-stationary characteristics of the signals being analyzed. Most published methods are short-time Fourier transform (STFT), discrete wavelet transform (DWT), and Wigner-Ville distribution (WVD). The signal analysis techniques are summarized in Table 6.

- STFT. The STFT, also known as windowed Fourier transform, was developed to overcome the lack of information on time locality in Fourier analysis. It is a compromise between the time and the frequency view of a signal; therefore, it is better suited for analysis of non-stationary signals than the ordinary Fourier transform. The STFT provides some information on both time locality and frequency spectra, but the precision of information is limited and determined by the size of the window.
- DWT. The DWT is based on local sums and differences. The procedure for implementing the DWT is to shift a copy of the signal by 1 sample and subtract the modified copy from the original signal. In terms of the sums and differences, the results are down-sampled by a factor of two to correct for the generated redundant values.
- WVD. The WVD is the Fourier transform of the signal's autocorrelation function with respect to the delay variable. It can also be thought of as an STFT in which the windowing function is a time-scaled and time-reversed copy of the original signal. The WVD is a popular tool in the electrical engineering community for time-frequency analysis because it generally has much better resolution than the STFT method.

Table 6 Signal analysis techniques

	Characteristics
STFT	The disadvantage of the STFT is that all signal frequencies are analyzed using the same resolution. One specific size of window is chosen as a compromise between requirements of time and frequency resolution, and this window is then used to analyze every signal frequency.
DWT	The advantage of the DWT over the STFT is the shorter computation time, but the disadvantage is the poor frequency resolution.
WVD	The WVD has two notable limitations: Cross-term calculations may artificially give rise to negative energy Aliasing effect may distort the spectrum such that a high-frequency component may be misidentified as a low-frequency component The WVD has many attractive mathematical properties. One of the most important is that the transformation produces a function of real values (in other words, it does not have imaginary components as does the STFT).

Signal-validation technology. Signal validation addresses the binary decision of whether or not there is a condition outside the scope of normal system operation and refines information (such as nature, location, and root cause) of a condition known to be a fault. In general, signal validation methods can be grouped into model-based, knowledge-based, and signal-based methods.

- Model-based approaches are grouped into those using quantitative and qualitative models. Their detection methods are based on using analytical rather than physical redundancy
- Knowledge-based approaches utilize deep understanding of the process structure, functions, and qualitative models under various faulty conditions
- Signal-based methods (such as spectral analysis, which do not incorporate any model) can be used for fault detection and even diagnosis.

Recent developments in empirical modeling (such as the use of neural networks) have broadened the scope of quantitative modeling to include "data-based" models in addition to traditional models based on physical principles. The signal validation techniques are summarized in Table 7.

Table 7 Signal-validation techniques

Name	Approach	Advantage	Disadvantage
Parity space	Signal based	Supply fault occurrence time and magnitude	Require hardware redundancy
Neural network	Data based	Evaluate without need for numerical model	Require huge training data
Generalized Likelihood Ratio	Model based	Supply fault occurrence time and magnitude	Require information of fault type
Separate Bias Estimation	Model based	Supply fault occurrence time and magnitude	Difficult to fault detection under threshold region

Application to the AUEN sensor data

The background noise-reduction methods have been applied to the AUEN sensor data and the pre-amplifier circuit for data acquisition was designed. Figure 28 shows the original voltage signal measured between AUEN and EREP#2 through the pre-amplifier board. This signal has a very slow time-varying bias with noise of ~40 mV, so the moving window average and the low-pass filter (which can be implemented without a numerical model) are used for canceling the background noise. Figure 29 and Table 8 show the filtering results. It should be noted that the moving window average method works best with SNR 49.284 dB.

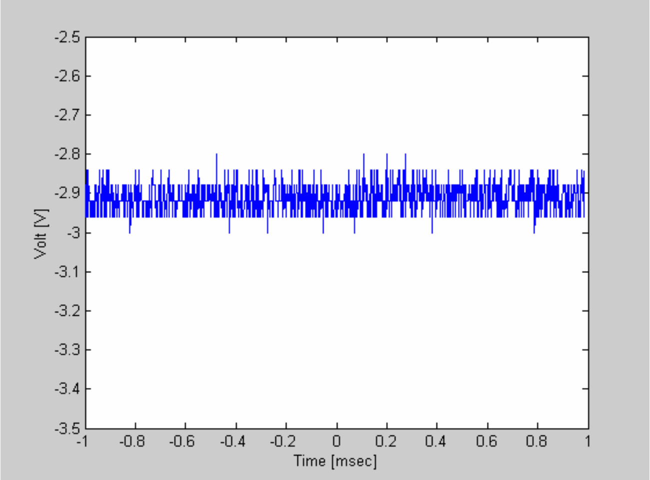

Figure 28 **Voltage signal measured between AUEN and EREP#2**

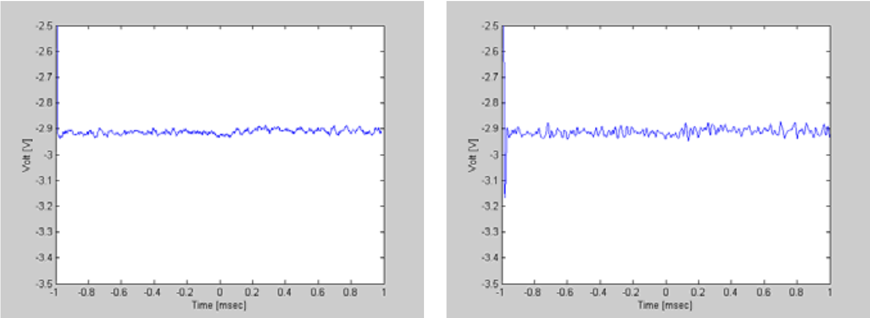

(a) Moving window average (b) Butterworth filter

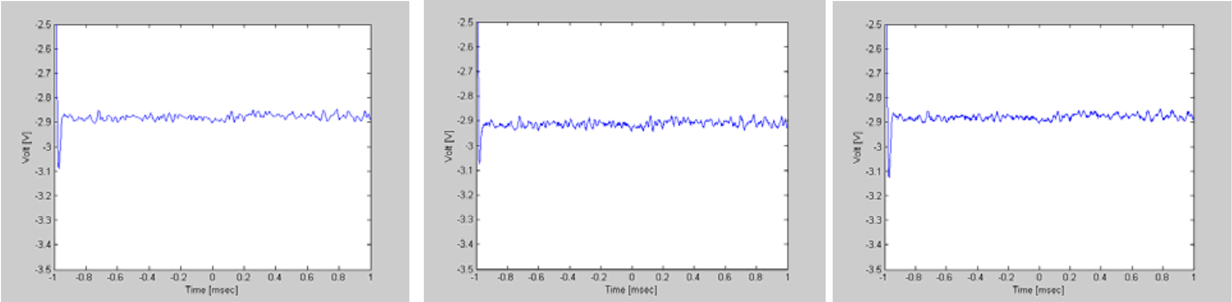

(c) Chebyshev I filter (d) Chebyshev II filter (e) Elliptic filter

Figure 29 **Results of each noise-reduction filter**

Table 8 **SNR of each noise-reduction filter applied in AUEN sensor data**

	Moving Average	Butterworth	Chebyshev I	Chebyshev II	Elliptic
SNR (dB)	49.284	43.299	37.112	44.785	36.939

The result of applying the signal-processing techniques to eliminate background noise

AE sensor signal. AE sensors detect the fluid and leakage flow while the check valve disc is moving. Figure 30 shows the time and frequency signals from the check valve test loop using the AE sensor with normal and degraded configurations (foreign object and disc wear). From Figure 30, the characteristic point can be detected from the frequency signal but not from the time signal. Figure 31, which shows the filtered signals using the moving window average technique for different valve configurations, indicates that the background noise (0 to ~200 Hz) level decreases substantially compared to the raw signal.

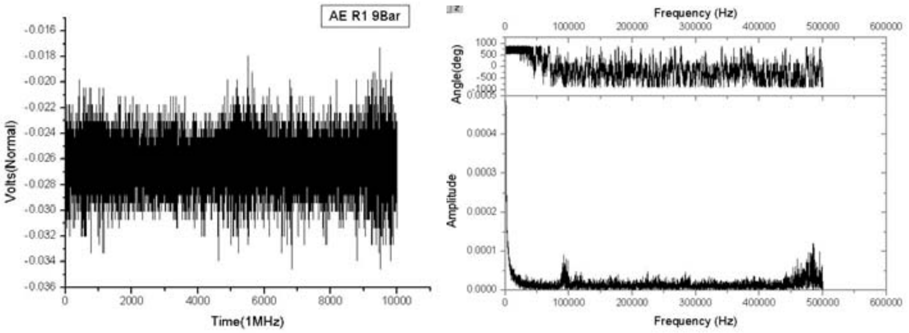

a) Normal configuration (9 bar, R1, 1007 rpm)

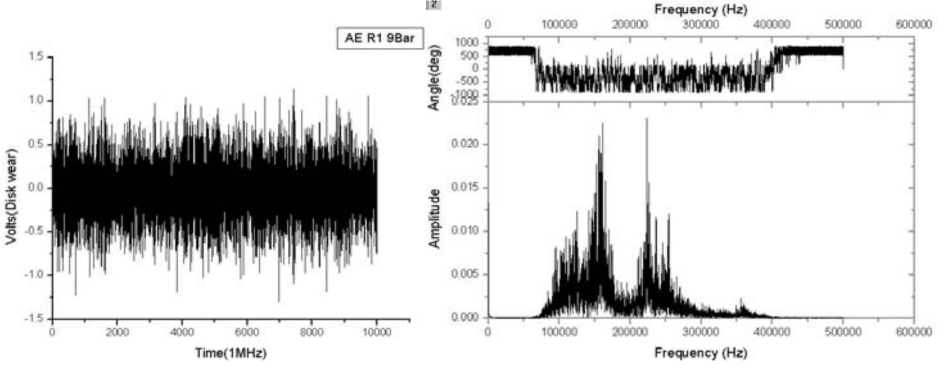

b) Disk wear (9 bar, R1, 1070 rpm)

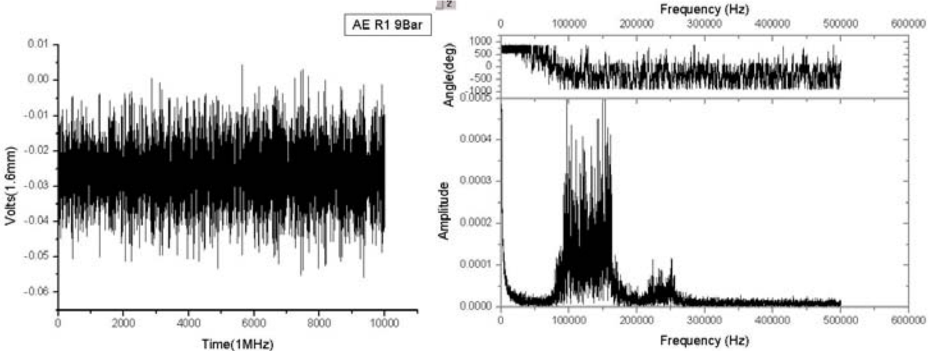

c) Foreign object (9 bar, R1, 1712 rpm)

Figure 30 **Comparison of time and frequency signals with AE sensor**

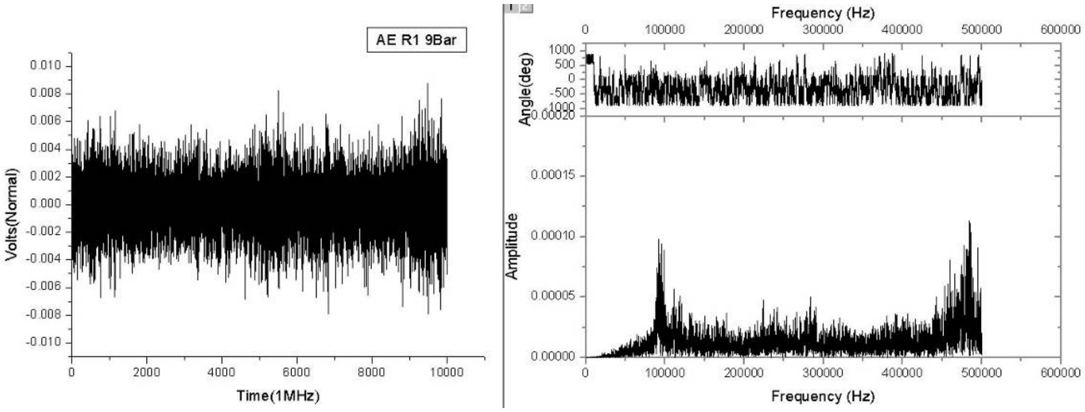

(a) Normal configuration

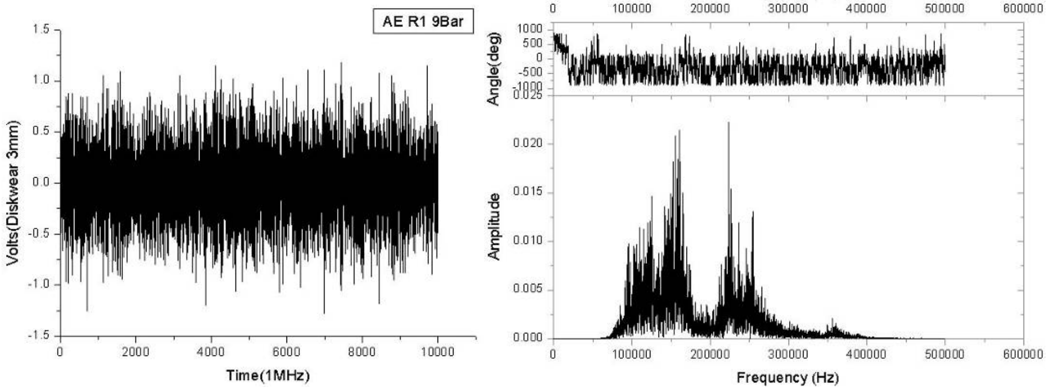

(b) Disc wear

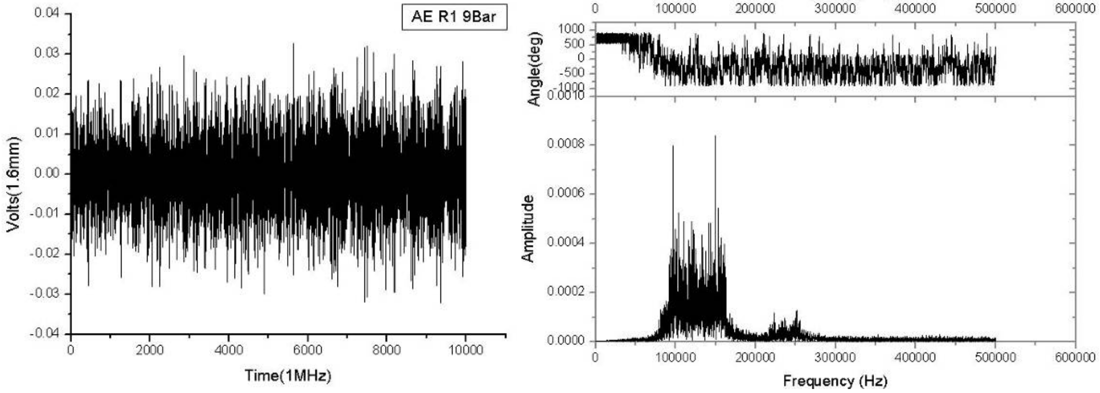

(c) Foreign object

Figure 31 Filtered AE signal using the moving window average technique

Accelerometer sensor signal. The accelerometer detects the vibration signal in the lower frequency domain not covered by the AE sensor. Figure 32 shows the time and frequency signals from the check valve test loop using the accelerometer for normal and degraded configurations (foreign object and disc wear). The figure shows that, unlike the AE signal, the time and frequency signals cannot differentiate between the different test configurations. Figure 33 shows the filtered accelerometer signals using the moving window average technique for different valve configurations.

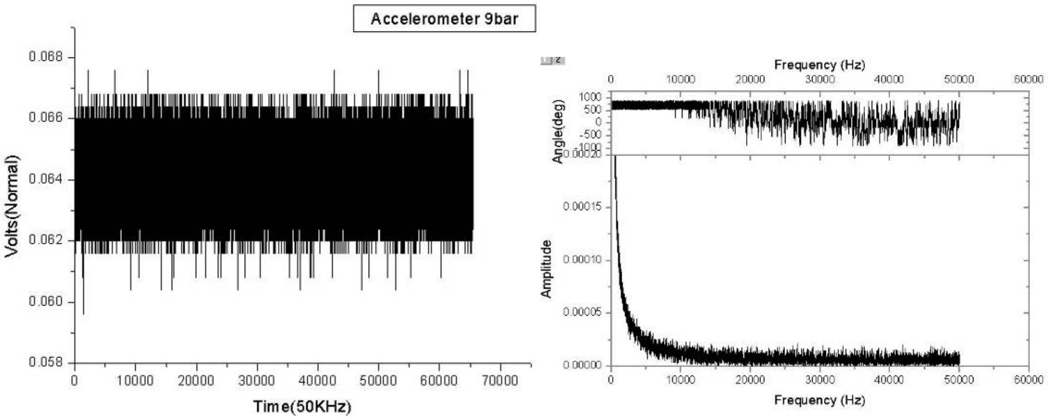

(a) Normal configuration (9 bar, R1, 1707 rpm)

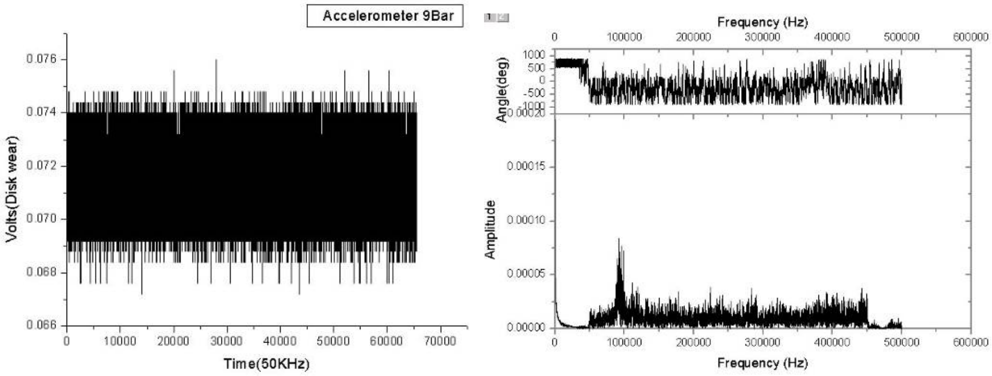

(b) Disc wear (9 bar, R1, 1710 rpm)

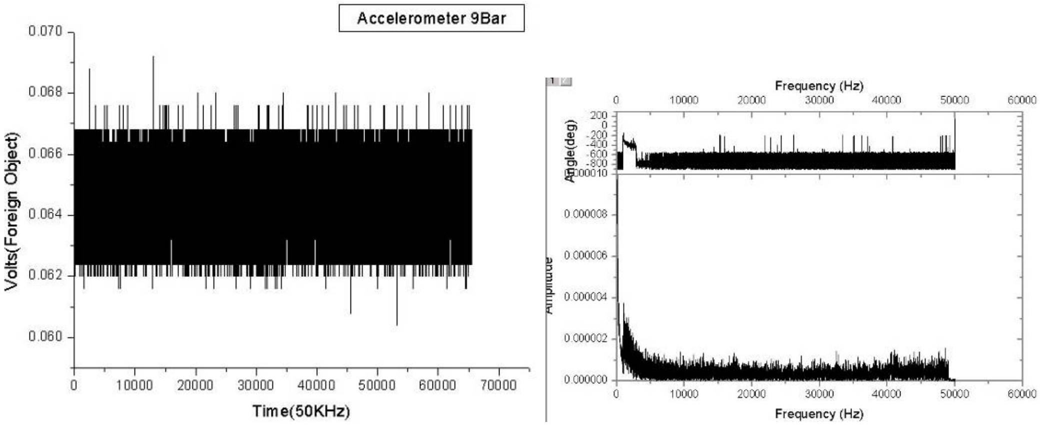

(c) Foreign object (9 bar, R1, 1705 rpm)

Figure 32 **Comparison of time and frequency signals with accelerometer**

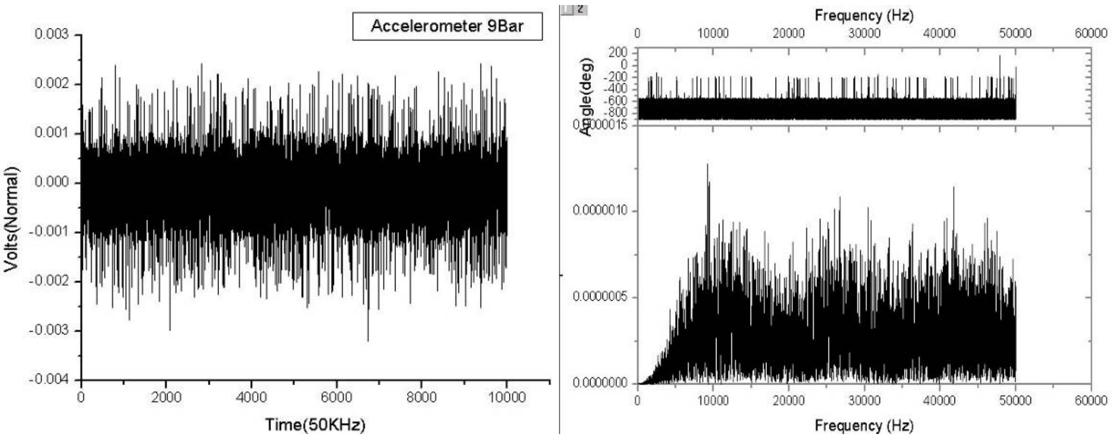

(a) Normal configuration

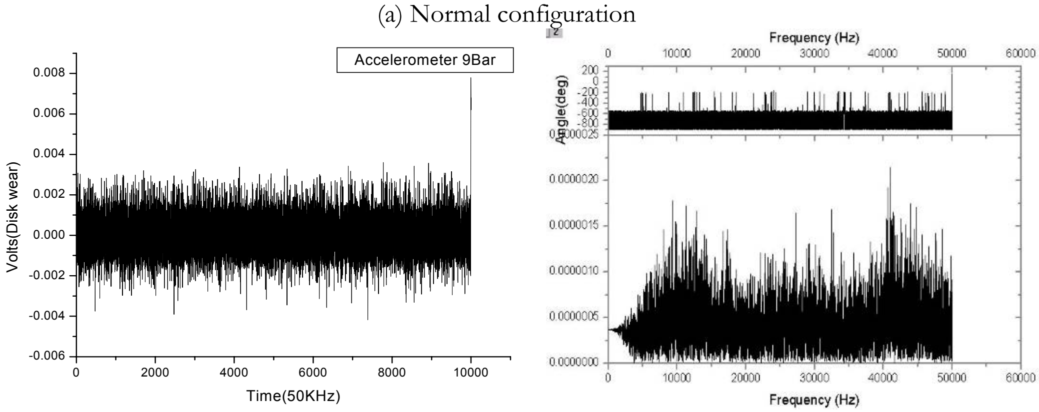

(b) Disc wear

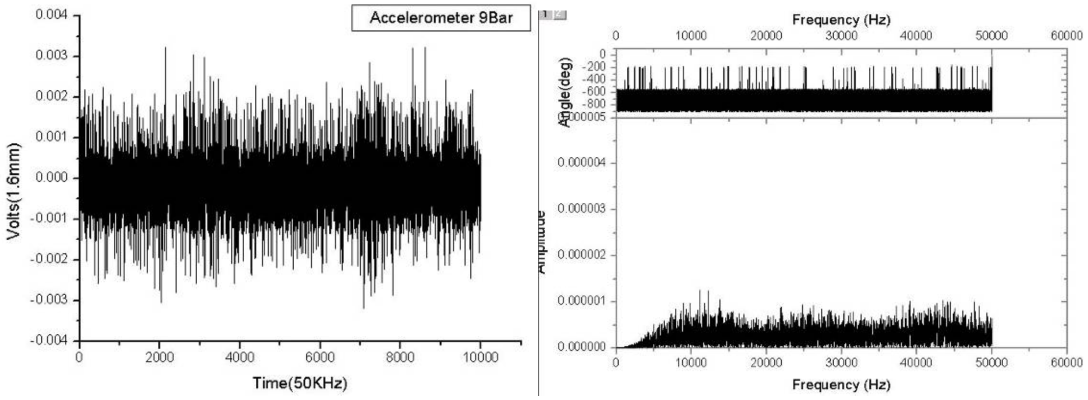

(c) Foreign object

Figure 33 Filtered accelerometer signal using the moving window average technique

Performance comparison

Generally, the frequency domain filters do not have time delay problems over communication networks; therefore, a decision was made to filter sensor signals in the frequency domain.

VII. Data processing analysis of experimental signals[1]

AE data analysis

In the following waveform analysis, 20 waveforms of 1024 data points per waveform were averaged in the time domain. Figures 34 and 35 show the typical AE RMS results and corresponding pressure obtained from check valve A's degraded configurations of disc wear and foreign object, respectively.

In Figures 34 and 35, the signal energy is stabilized over the 1 min recording period to allow time for the transient effect due to pump pressure change to stabilize before data recording. The AE RMS results increase with pressure for the same leak size because leak rate increases with pressure. Figure 36 (a) and (b) show the relationship between AE RMS results and leak rate obtained from disc wear and foreign object, respectively. The AE RMS value increases linearly with leak rate.

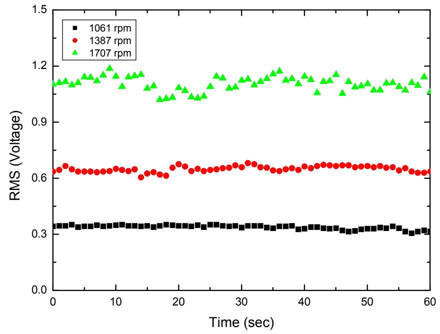

(a) Disc wear 1.0 mm

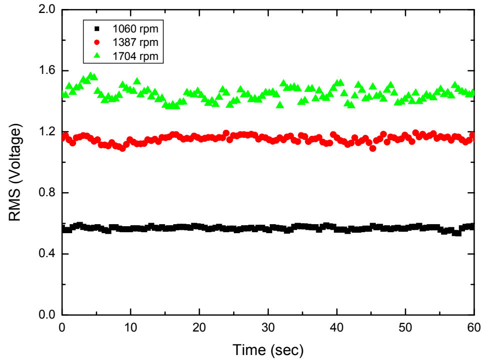

(b) Disc wear 2.0 mm

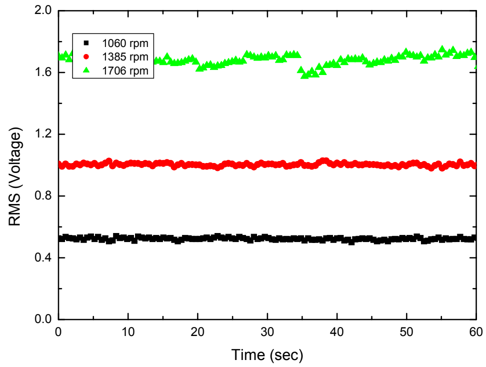

(c) Disc wear 3.0 mm

Figure 34 **The AE RMS value obtained from disc wear**

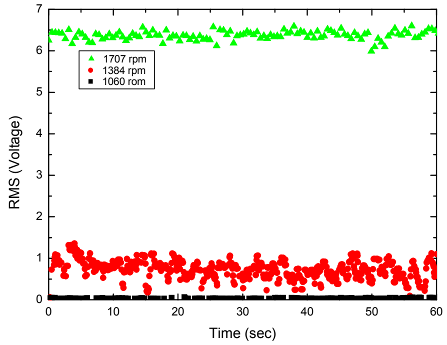

(a) Foreign object 1.0 mm

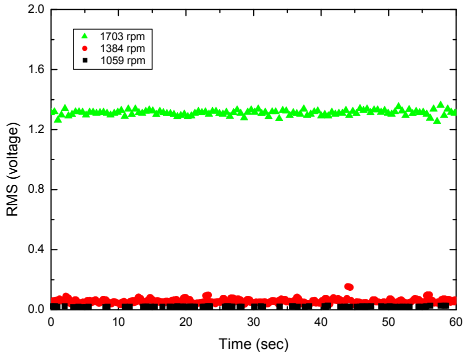

(b) Foreign object 1.2 mm

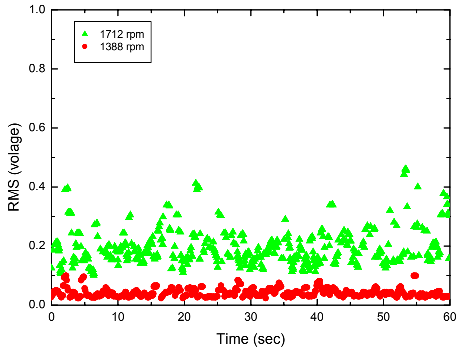

(c) Foreign object 1.6 mm

Figure 35 **The AE RMS value obtained from foreign object**

---

[1] This section includes details of experimental data processing techniques, which is introduced in Section 3.5.3.

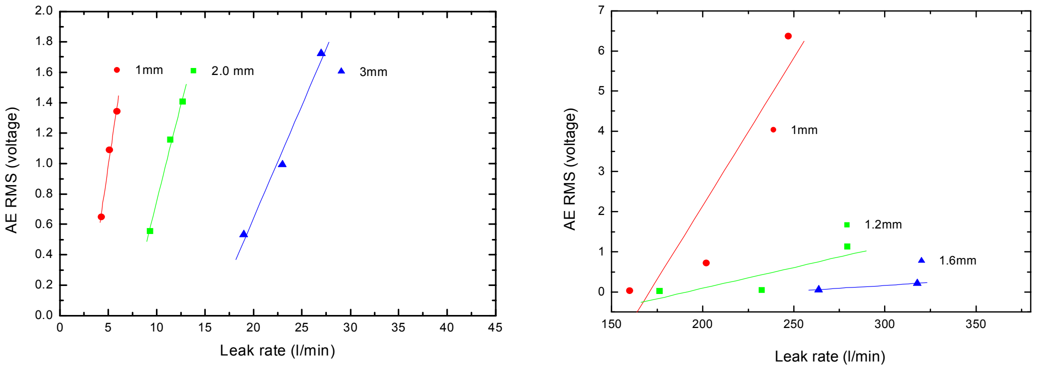

(a) Disc wear (1.0, 2.0, 3.0 mm)

(b) Foreign object (1.0, 1.2, 1.6 mm)

Figure 36 AE RMS value versus leak rate

Although it is desirable to develop a procedure to estimate the leak rate, this information is difficult to obtain directly from acoustic intensity data because the amplitude of the acoustic signal varies with geometry and temperature for a given flow rate. Thus, other signal characteristics must be examined. One possible way is to monitor the variation in the RMS signal with time. Figure 37 shows the actual measurement results of AE RMS value for a leak in the disc wear failure mode. As shown in Figure 38, the intensity of AE RMS value obtained from resonance-type sensor (R15) is the highest. Figure 37 shows the difference in the intensity of AE RMS values caused by a fluid leak from the foreign object failure mode between the resonance-type and WD-type sensors.

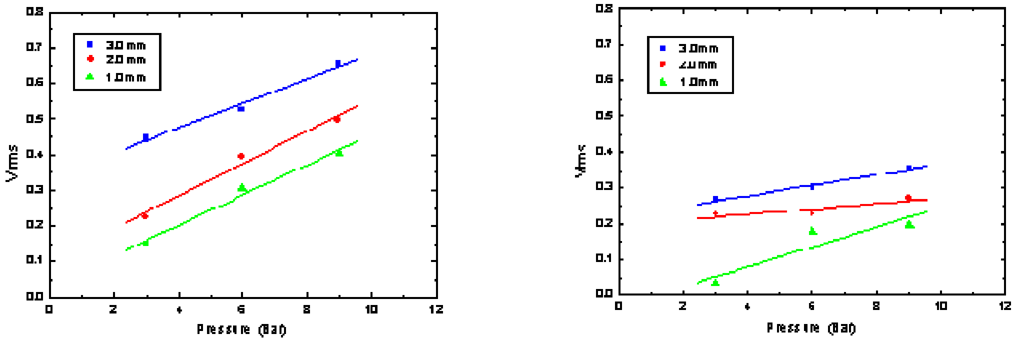

(a) R15 sensor (150 kHz)

(b) R6 sensor (60 kHz)

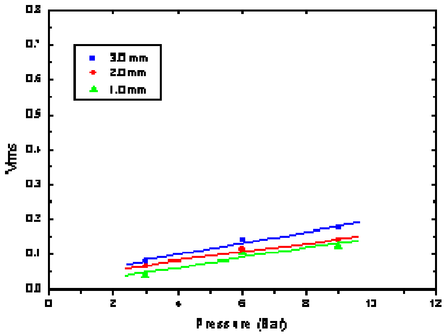

(c) WD sensor (1.2 MHz)

Figure 37 AE RMS data obtained from each sensors (disc wear)

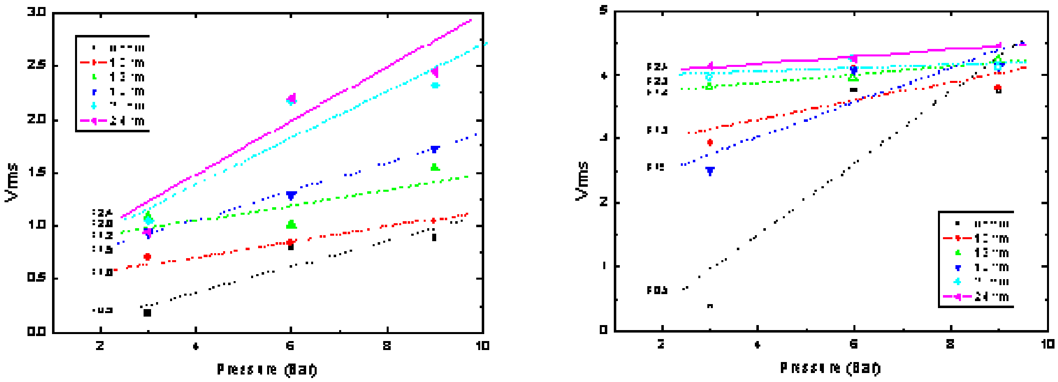

(a) R15 sensor (150 kHz) (b) R6 sensor (60 kHz)

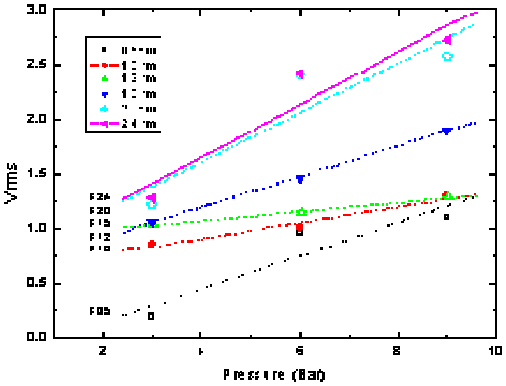

(c) WD sensor (12 MHz)

Figure 38 AE RMS data obtained from each sensor (foreign object)

In the case of both failure modes, the AE RMS values increase linearly with pressure. The plots of signal RMS value versus the pressure for the three sensors are shown in Figure 39. The AE RMS values of the 150 kHz sensor are greater than that of the others, suggesting that the signals of 150 kHz sensor are more sensitive to the leakage. The leakage flow was monitored to investigate the variation of the AE RMS values with the leak rate, the pressure, and leak geometry. Figure 40 shows the variation of AE RMS value for the 150 kHz sensor with pressure for each failure mode. The important aspect of the data is that the AE RMS values increase linearly with leak rate and pressure. In addition, the critical flow occurs at 4.5 bar. It is expected that the discontinuity occurs due to the chocking discharge rate at the critical flow condition; therefore, the AE RMS value is a more sensitive indicator of the leak rate.

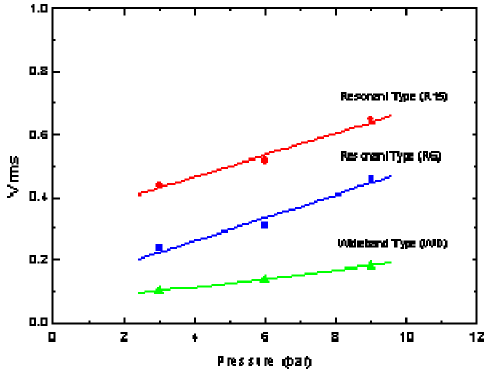

Figure 39 Plot of AE RMS values versus pressure for each sensor

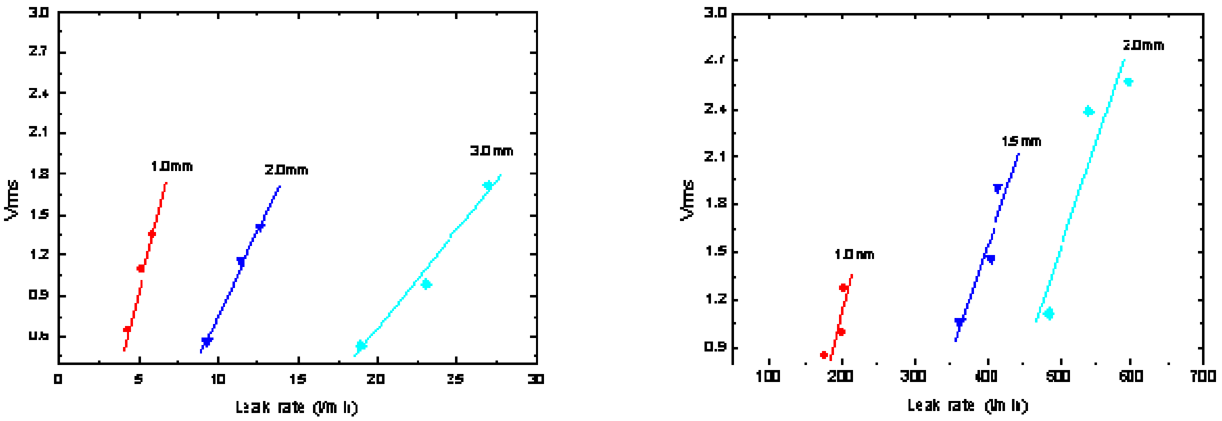

(a) Disc wear failure mode (b) Foreign object failure mode

Figure 40 AE RMS level versus leak rate

The frequency spectra of the check valve leakage is illustrated in Figure 41 and 42. Figure 41 shows the frequency spectra of leak signals with the 150 kHz sensor. The frequency range of leak signals between disc wear and foreign object are significantly different. However, the frequency spectrum content of AE signals due to leaks indicates no significant changes with the leak rate and pressure; that is, it is significant that for the three spectra results obtained from disc wear shown in Figure 41 (a), all have the same general shapes, whereas the spectra results (Figure 41 (b)) obtained from foreign object have different-shaped spectra compared with the disc wear failure mode. These observations imply that the frequency spectrum profile of the disc wear and foreign object failure modes do not depend on the leak rate and pressure. It was also found that the turbulence sound in a disc wear failure mode was detected at 150 kHz to 250 kHz and in a foreign object failure mode at 100 kHz to 150 kHz.

Figure 42 shows the frequency spectra of leak signals at the WD (<1.2 MHz) sensor. The frequency range of leak signals between disc wear and foreign object failure modes are also significantly different. The spectra of disc wear and foreign object failure modes are readily identified in the frequency range from 100 to 600 kHz, whereas the peaks that are present only in the disc wear spectra are revealed in the frequency at 300 kHz.

The PSD function was computed for the snapshot using an FFT of n=2048 with Hanning window of n=2048 to suppress side lobe leakage, and a 50% overlap. The frequency resolution for this computation is 122 kHz per bin. The signal was normalized to a zero mean before processing. The results of the R15 data shown in Figure 43 indicate that the PSDs of leak signals between disc wear and foreign object failure modes are also significantly different.

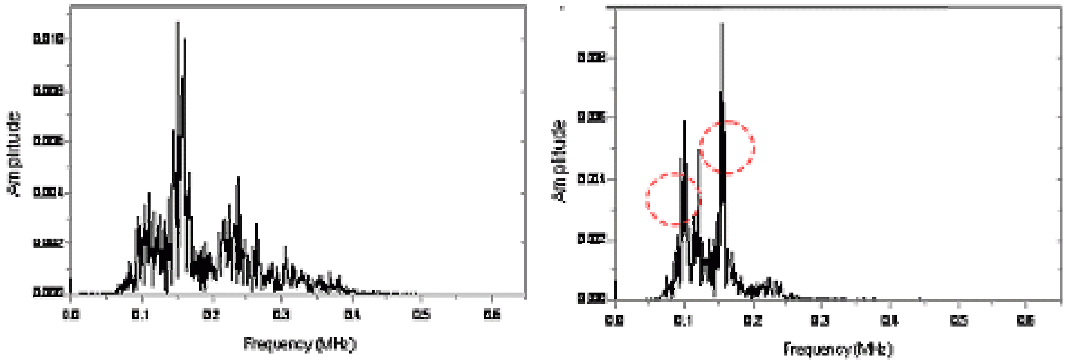

(a) Disc wear (1.0 mm)　　(a) Foreign object (1.0 mm)

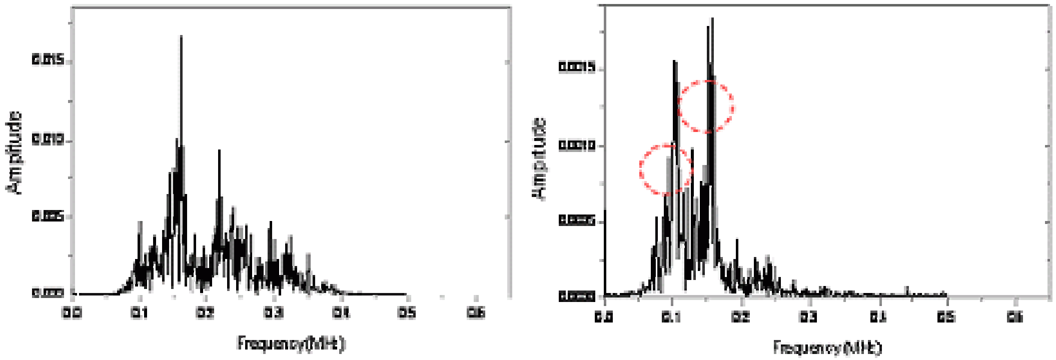

(b) Disc wear (2.0 mm)　　(b) Foreign object (1.5 mm)

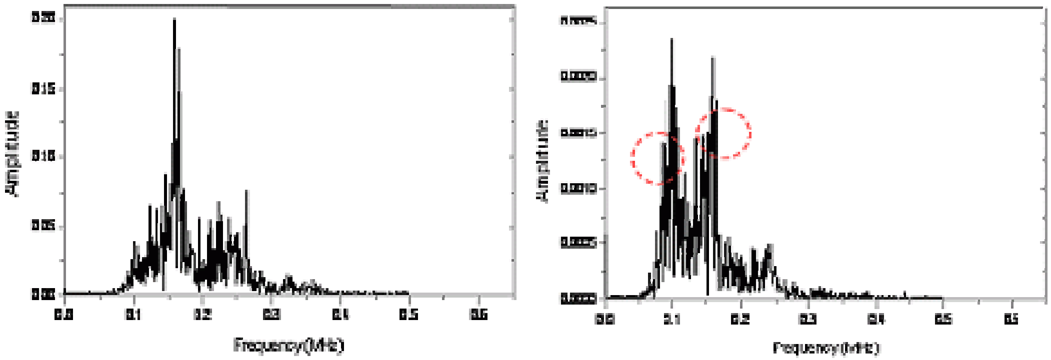

(c) Disc wear (3.0 mm)　　(c) Foreign object (2.4 mm)

Figure 41 **Frequency spectra of leak signals with 150 kHz sensor**

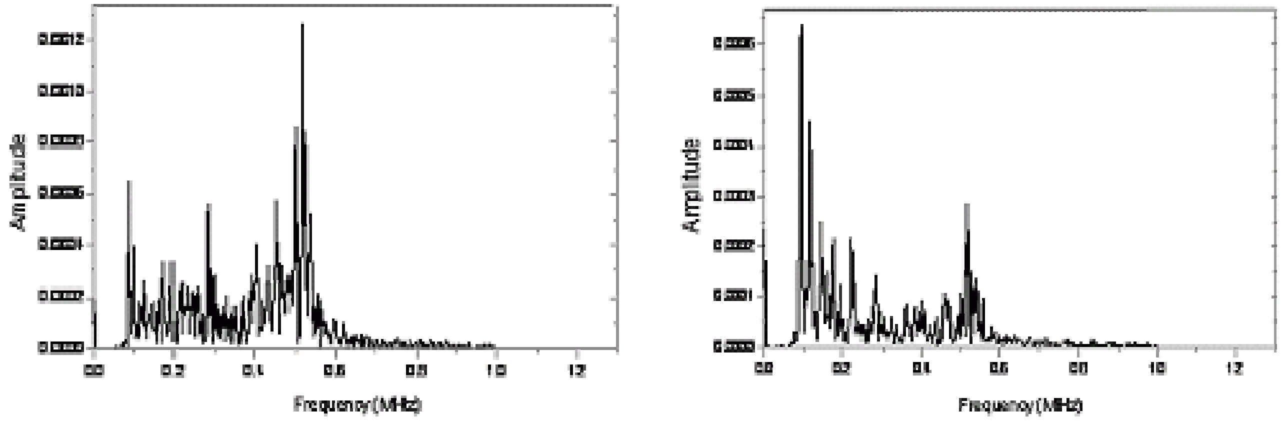

(a) Disc wear (1.0 mm)

(a) Foreign object (1.0 mm)

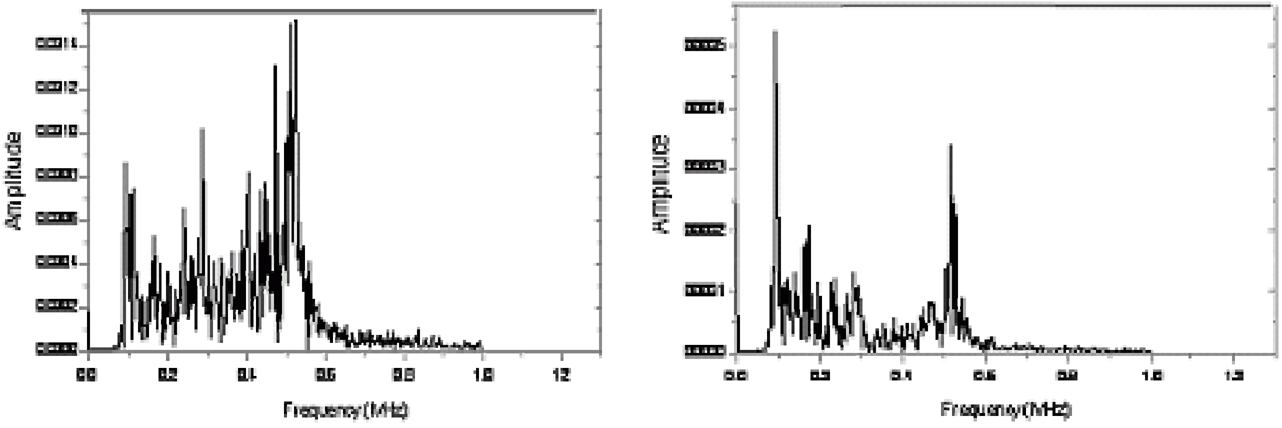

(b) Disc wear (2.0 mm)

(b) Foreign object (1.5 mm)

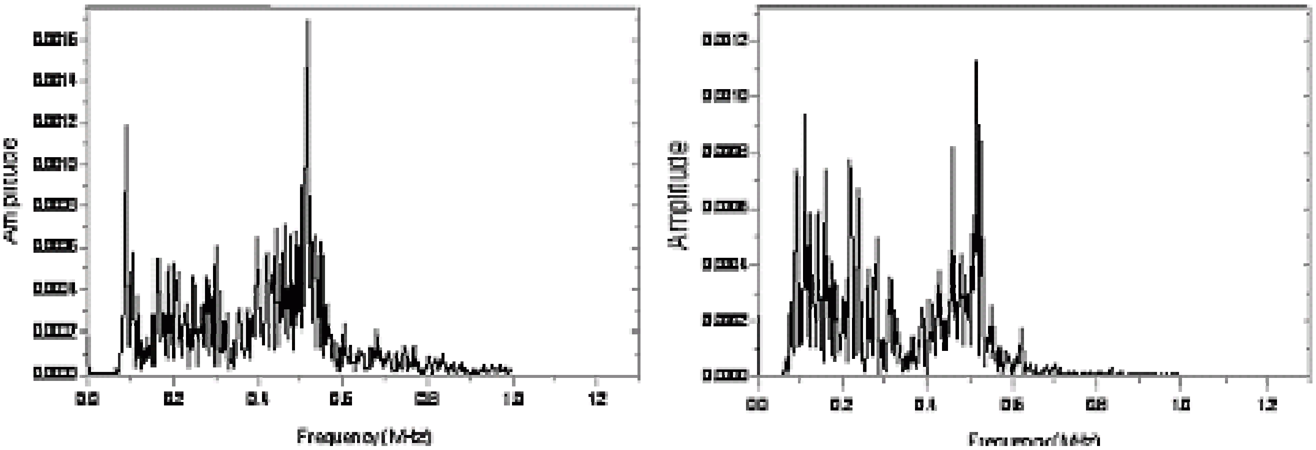

(c) Disc wear (3.0 mm)

(c) Foreign object (2.4 mm)

Figure 42 **Frequency spectra of leak signals with WD sensor**

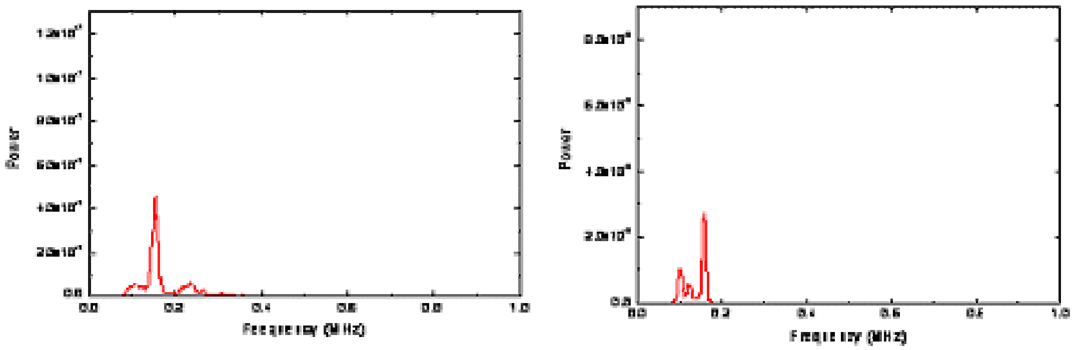

(a) Disc wear (1.0 mm)

(a) Foreign object (1.0 mm)

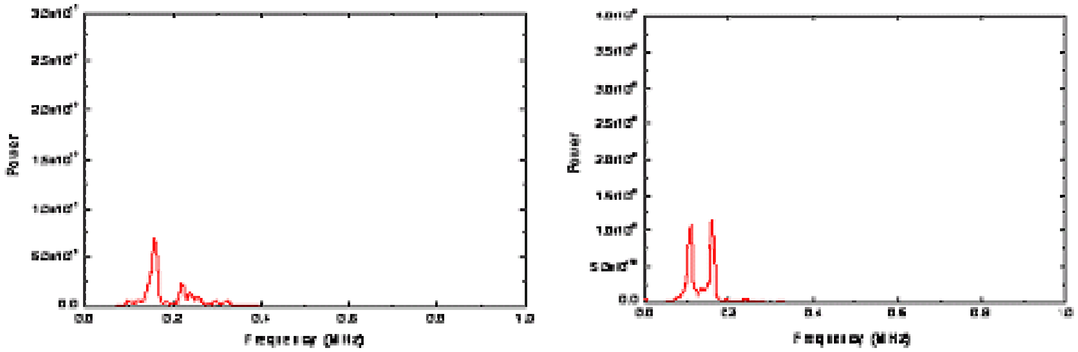

(b) Disc wear (2.0 mm)

(b) Foreign object (1.5 mm)

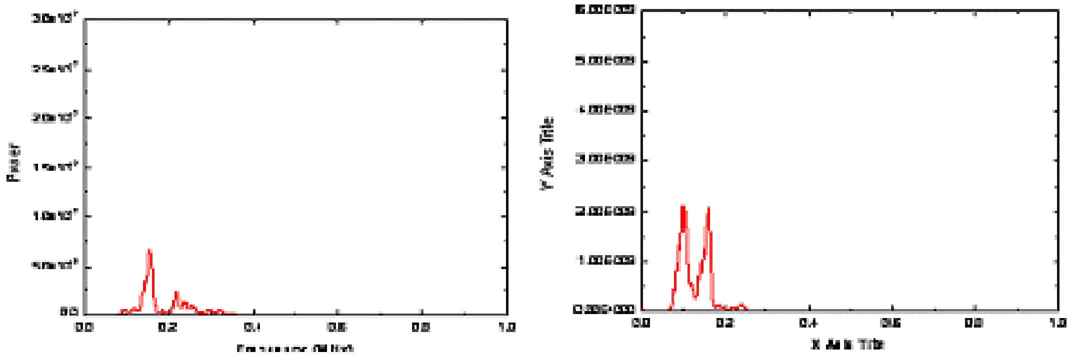

(c) Disc wear (3.0 mm)

(c) Foreign object (2.4 mm)

Figure 43 **PSD with 150 kHz sensor**

Ultrasonic data analysis

Usually, ultrasonic inspection techniques can be used to detect a missing or stuck disc. One (pulse-echo) or two (pitch-catch) ultrasonic transducers are used to detect internal parts of the check valve. For example, the ultrasonic signal is injected from outside the valve by the transmitting transducer and passes through the valve body, where it is reflected by an internal part, such as disc or hinge arm, back to the receiving transducer. In this study, one transducer is used in a pulse-echo mode, providing both transmitting and receiving capabilities.

If the disc is missing, no signal will be reflected; however, if the hinge arm remains on the valve, the hinge arm position can be verified by ultrasonic inspection techniques.

In this study, disc wear can be detected by ultrasonic inspection by monitoring the motion of the disc using an ultrasonic transducer.

Figure 44 shows ultrasonic signatures acquired from a swing-type check valve at two disc positions; fully open and fully closed. Disc motion signatures are acquired with an ultrasonic transducer (2 MHz). The open signatures are shown in Figure 44 (a) and closed signatures in Figure 44 (b). Note that no signal was reflected from the disc in the open position and that a echo signal was returned from the disc in the closed position. As shown in Figure 44, it was found that the disc movement was clearly detected using the ultrasonic method.

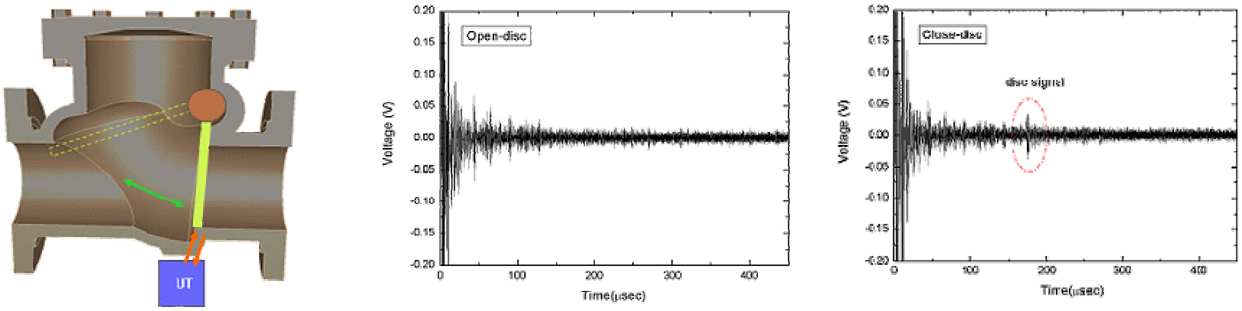

(a) Ultrasonic measurement (b) Disc open (c) Disc closed

Figure 44 UT signals obtained from disc of check valve

Accelerometer data analysis

Background noise accelerometer monitoring

Figure 45 shows the typical frequency spectrum (FFT) comparing the normal valve to the degraded valve with disc wear and foreign object obtained from the accelerometers. However, the accelerometer spectra of valve leak signals are measured at frequencies up to 20 kHz. Background noise spectra are readily identified in the frequency range from about 4 to 20 kHz. As shown in the figure, no significant spectral power was observed at frequencies above 30 kHz in all tests.

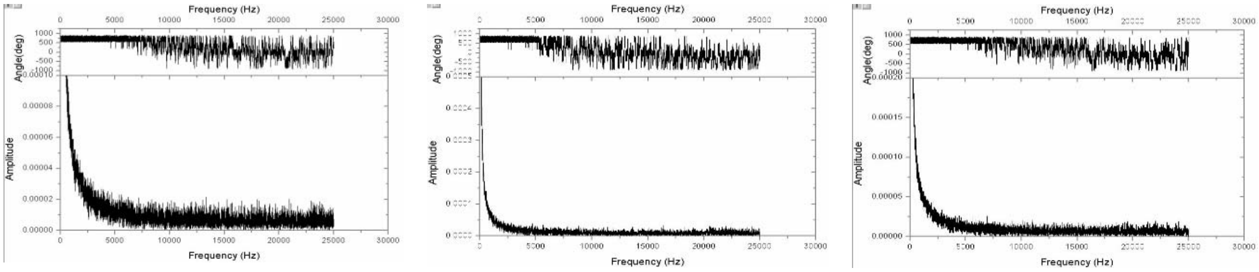

(a) Normal (b) Disc wear (3 mm, 09 bar) (c) Foreign object (1.6 mm, 9 bar)

Figure 45 Frequency spectra (FFT) from accelerometers

Figure 46 shows the waveforms and corresponding spectra for the accelerometer output of initial background noise (valve D). The resulting accelerometer signature shows that the FFT is concentrated in the range of 1 to 2 kHz. In this case, the amplitude of ACC_1 signals appeared higher than that of ACC_2 signals.

Accelerometer data analysis

Figure 47 involves the detection of leak flow signal with leak diameter of about 0.85 and 1.20 mm. Leak is detected on the basis of the significant difference in the leak signal and background signal. In addition, the amplitudes of ACC_2 signals appear greater than those of ACC_1 signals.

Figure 48 shows the typical accelerometer waveform obtained from check valve D with worn disc having slit thicknesses 1, 2, and 3 mm (results from the third experiment). As shown, the signal amplitude increases with the increasing slit thickness of a worn disc. The amplitude of ACC_2 signals appeared higher than that of ACC_1 signals; therefore, sensor position was found to be very important for detecting leak signals in this test.

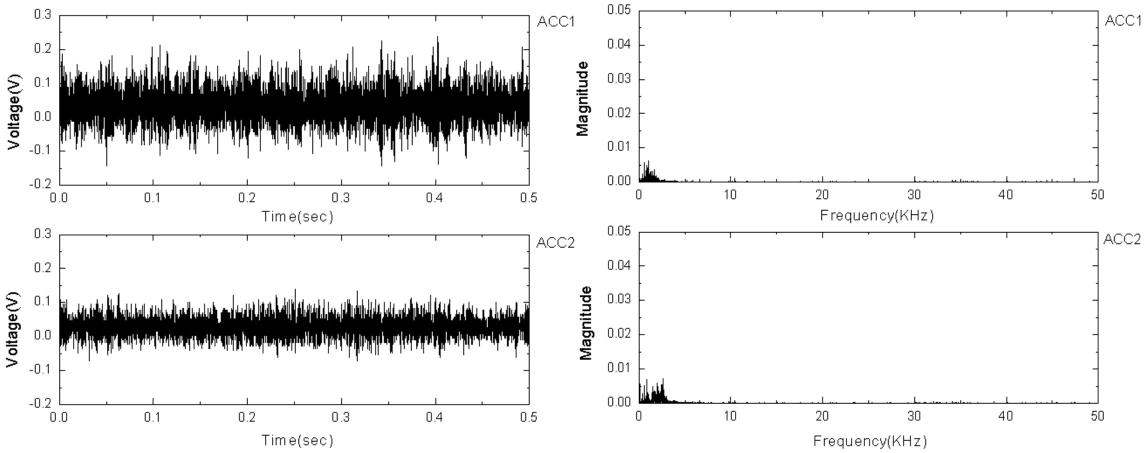

Figure 46 **Accelerometer waveform and corresponding spectra obtained initial background noise**

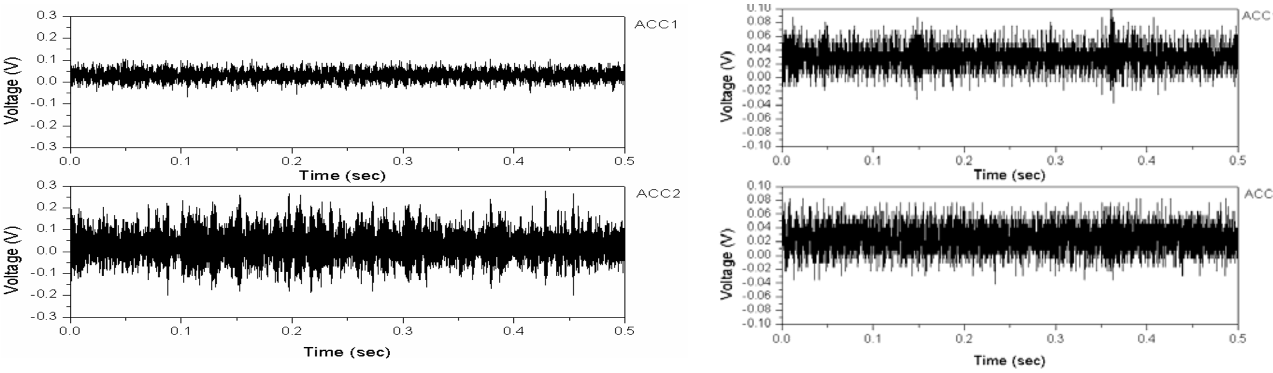

(ϕ 0, 85 mm) (ϕ 1.20 mm)

Figure 47 **Accelerometer waveform and corresponding spectra obtained leak valve**

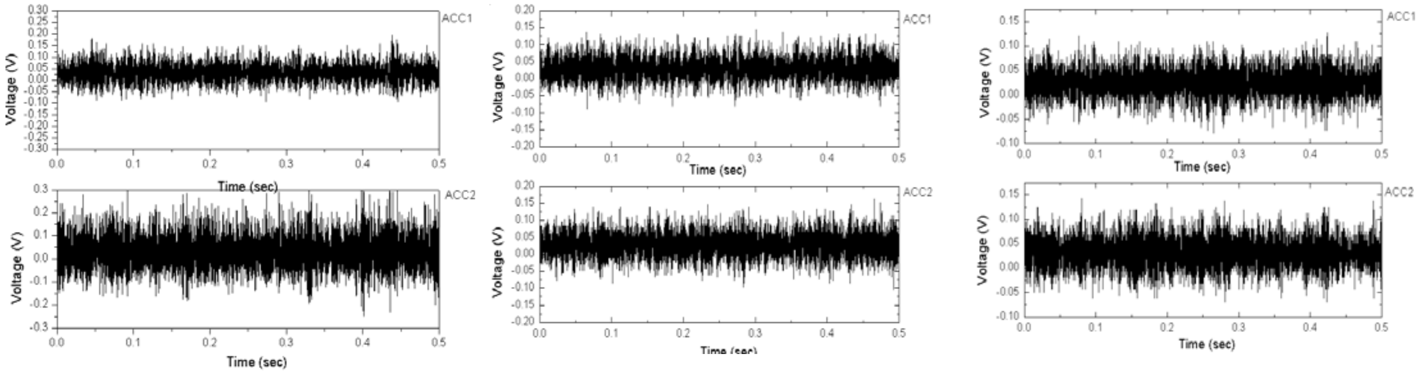

(a) Slit 1 mm (b) Slit 2 mm (c) Slit 3 mm

Figure 48 **Accelerometer waveform and corresponding spectra obtained worn disc**

Time and frequency analysis[1]

---

[1] This section includes details for time and frequency analysis, which is introduced in Section 3.5.6.

For conventional spectral analyses based on the Fourier transform, it is in general known to lose a part of the information–a temporal variation of the spectral characteristics of a non-stationary signal–because it is assumed that a signal is stationary. Figure 49 (a) shows a detected time signal and its frequency spectra at 9 bars in the normal configuration. Figure 49 (b) is for the 3 mm disc wear at 9 bars and Figure 49 (c) for the 1 mm size of a foreign object insertion at 9 bars. As indicated in Figure 49 (a), the signal amplitude at the normal configuration is so small that there is no detectable background signal. Figures 49 (b) and 49 (c) show that it is not easy to classify these two failures from only the difference of the spectra amplitude without a characterized spectral property because the spectra appear in all the frequency bands from 100 to 500 kHz. Therefore, additional information is needed for failure diagnosis.

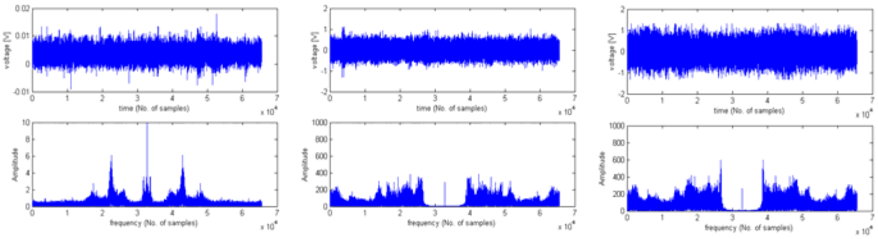

(a) Normal (b) Disc wear (c) Foreign object

Figure 49 Time signals (above) and spectra (below) for different check valve configuration

Time frequency representation (TFR)

The TFR will provide the information lost from other conventional methods. The WVD, one of the TFR methods, is interpreted as a function that indicates the energy distribution (ED) of a signal over time and frequency. To obtain it at a particular time, the pieces made up of the product of the signal at a past time are added up into the future. The WVD has a better time and frequency resolution than the other TFR methods such as instantaneous frequency, STFT, and wavelet transform (WT), even though it has a drawback of containing the cross or interference term between the different components of a signal caused by signal overlapping in its calculation.

Let *x(t)* be a complex continuous time analytic signal and *X(f)* be its FT. The WVD of *x(t)* in the time and frequency domains are defined as following:

$$W_x(t,f) = \int_{-\infty}^{\infty} x(t+\frac{\tau}{2})x^*(t-\frac{\tau}{2})e^{-j2\pi f\tau}d\tau \qquad (1)$$

$$W_X(t,f) = \int_{-\infty}^{\infty} X(f+\frac{\xi}{2})X^*(f-\frac{\xi}{2})e^{-j2\pi t\xi}d\xi \qquad (2)$$

where, *x (t)* is a time analytic signal, *f* represents frequency, and $x^*(t)$ is a complex conjugate of *x (t)*. The WVD with a windowed signal can be solved as below and the Hanning window is applied here.

$$W_{xw}(t,f) = \int x(t+\frac{\tau}{2})\,x^*(t-\frac{\tau}{2})\,w(\tau)\,e^{-j2\pi f\tau}d\tau \qquad (3)$$

ED. The general class of TFRs in the following was introduced by Cohen:

$$C_f(t,w,\phi) = \frac{1}{2\pi}\iiint e^{-j(\xi\mu-\tau\omega-\xi t)}\,\phi(\xi,\tau)\,f(\mu+\frac{\mu}{2})f^*(\mu-\frac{\mu}{2})d\mu d\tau d\xi\ . \qquad (4)$$

where $f(\mu)$ is a time-analytic signal and $f^*(\mu)$ is its complex conjugate. ϕ is a kernel function that determines the distribution and its properties. The WVD described previously has the kernel $\phi(\xi,\tau)=1$, and each distribution has its own kernel function. The ED is developed to reduce the cross-term and it has the kernel function $\phi(\xi,\tau)=e^{(-\xi^2\tau^2/\sigma)}$; therefore, the ED is obtained as shown here from the equations for the general class distribution and the kernel function:

$$E_f(t,\omega)=\int_\tau e^{-j\omega\tau}\left[\int_\mu \frac{1}{\sqrt{4\pi\tau^2/\sigma}}\exp(-\frac{(\mu-t)^2}{4\tau^2/\sigma})f(\mu+\frac{\tau}{2})f^*(\mu-\frac{\tau}{2})d\mu\right]d\tau \tag{5}$$

$$E_f(t,\omega)=\frac{1}{2\pi}\int_\tau e^{-j\xi\tau}\left[\int_\mu \frac{1}{\sqrt{4\pi\xi^2/\sigma}}\exp(-\frac{(\mu-\omega)^2}{4\xi^2/\sigma})F(\mu+\frac{\xi}{2})F^*(\mu-\frac{\xi}{2})d\mu\right]d\xi \tag{6}$$

where *F(w)* is a Fourier transformation of *f(t)*. For implementation in the computer, the ED for the discrete time signals is derived by the following.

$$E_f(n,\theta)=2\sum_{\tau=-\infty}^{\infty} e^{-j2\theta\tau}\left[\sum_{\mu=-\infty}^{\infty}\frac{1}{\sqrt{4\pi\tau^2/\sigma}}\exp(-\frac{(\mu-n)^2}{4\tau^2/\sigma})f(\mu+\tau)f^*(\mu-\tau)\right] \tag{7}$$

In the ED, the choice of scaling factor $\sigma\ (\sigma \rangle 0$ should be optimized for each application.

Signal analysis by TFR

WVD. Figure 50 depicts the WVDs for each failure condition of the check valve. The distribution has a good resolution in time and frequency, but it is not easy to extract the distinct diagnostic information for each failure due to the cross-terms. It was concluded that although the window function is used in WVD, it is not sufficient to reduce the cross-terms.

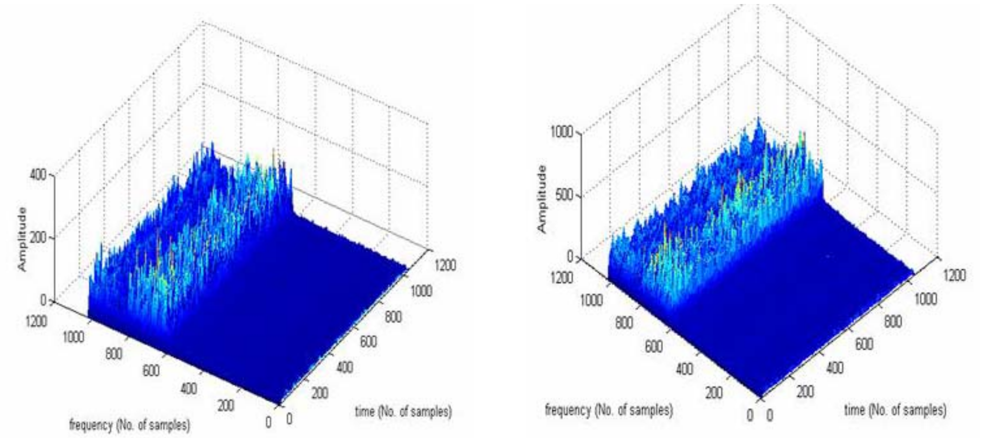

Figure 50 WVDs for the disc wear (left) and the foreign object (right) conditions

ED. Figure 51 depicts the EDs for each failure condition of the check valve. For the distributions, we chose $\sigma = 1$. The EDs show the frequency characteristic (energy density) with the variation of time as indicated by circles in the figure. They are the additional information that the conventional method cannot provide.

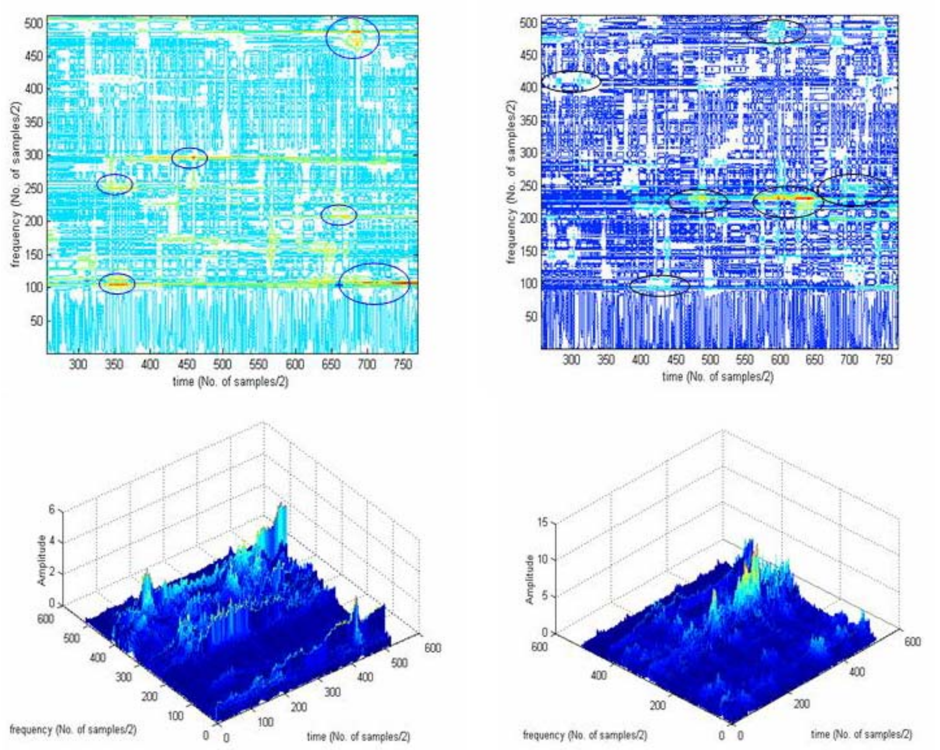

(a) Contour (above) and mesh (below) (b) Contour (above) and mesh (below)

Figure 51 EDs for the disc wear (left) and the foreign object (right) conditions (sigma = 1)

ANN technique

The appropriate check valve monitoring technique would involve using one or more sensors attached externally to the valve with simple signal-processing units connected to a small general-purpose (or specially designed) computer. In this research, classical signal-processing techniques and ANNs are integrated to identify waveforms associated with different faults. Time and frequency domain signals are used for the quantitative nondestructive evaluation utilizing a neural network.

In this research, the features are extracted from acquired AE signals from the check valve. Then, the extracted features of the same cases are used in training the neural network and the features of the other cases are used to test the trained neural network by comparing output-layer unit values and real values. The multi-layer perception neural network, which is constructed with the input layer, hidden layer, and output layer, is used to output the quantitative leak size.

When $i_l(l = 1,2,3...i)$ are the values of the input-layer unit and $y_n(n = 1,2,3...k)$ are the values of the output-layer unit, Equation (8) represents the hidden-layer unit values, $x_m(m = 1,2,3...j)$ and Equation (9) represents the output-layer unit values, $O_n(n = 1,2,3...k)$.

In these equations w is the weight on the connection, θ is the bias weight and function $f()$ is the sigmoidal function. In Equation (8), the input-layer unit values i_l product each weight on the connections w_{ml}^h, then summations of these and bias θ_m^h will be hidden-layer unit values through sigmoidal function $f()$.

$$net_m^h = \sum_{l=1}^{i} w_{ml}^h i_l + \theta_m^h$$

$$x_m = f_m^h(net_m^h) \tag{8}$$

In the same way, the summation of bias θ_n^o and the values of the hidden-layer unit values x_m product each weight on the connection w_{nm}^o will be output layer unit values through sigmoidal function $f()$, as shown in Equation (9). In this study, this sigmoidal function $f()$ of the output the layer generates the leak size and as the output vector

$$net_n^o = \sum_{m=1}^{i} w_{nm}^o x_m + \theta_n^o$$

$$O_n = f_n^o(net_n^o) \tag{9}$$

Equation (10) defines the error function E, which represents the error value between real values and output unit values.

$$E = \frac{1}{2}\sum_{n=1}^{k}(y_n - o_n)^2 \tag{10}$$

It is the training of a neural network that the weight on the connection, w values are corrected so that the value of the error function E of Equation (10) approaches zero. This means that the output-layer unit values approach real values through the back propagation algorithm.

The weights on the output-layer are updated by Equation (11) during the training of the neural network. When α is the learning-rate parameters.

$$w_{nm}^o(t+1) = w_{nm}^o(t) - \alpha \frac{\partial E}{\partial w_{ml}^h(t)} (0 < \alpha < 0.25) \tag{11}$$

In addition, the weights on the hidden-layer are updated by Equation (12) during training neural network.

$$w_{ml}^h(t+1) = w_{ml}^h(t) - \alpha \frac{\partial E}{\partial w_{ml}^h(t)} \tag{12}$$

In this study, the features are extracted from acquired acoustic signal. Then, the extracted features of same cases are used in the training of the neural network and the features of the other cases are used to test the trained neural network by comparing output-layer unit values and real values.

Time domain signals and frequency domain signals are used for the quantitative nondestructive evaluation utilizing a neural network in this research. The multi-layer perception neural network was used to output the quantitative leak size.

This neural network is constructed with the input-layer, hidden-layer and output-layer as shown in Figure 52. First, the AE signal is classified from AE data acquired by fusion sensors corresponding to failure of check valve. The features are extracted from classified AE signals of check valve. Then, the extracted featured of same cases are used in the training of the neural network and the features of the other cases are used to test the trained neural network by comparing out-layer unit values and real values.

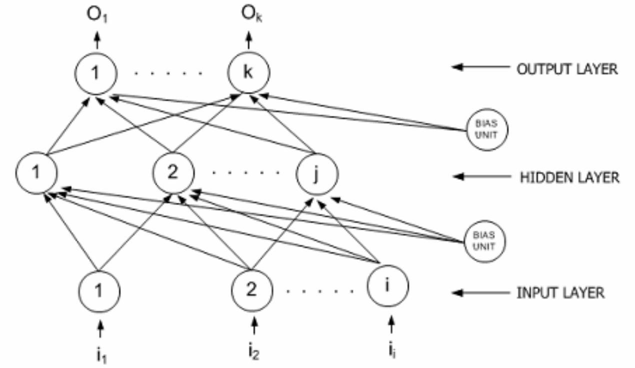

Figure 52 **Architecture of ANN**

Data feature extraction for algorithm development for failure diagnosis

Experimental data were received on March and April 2004. The acquired data were divided by each set of data length of 65536 of the whole experimental data. 100 data sets were used in each case. Table 9 presents a data set for the prototype development.

Table 9 **Experimental data set**

	3 Bar	6 Bar	9 Bar
Normal	100 cases	100 cases	100 cases
Disc Wear 1 mm	100 cases	100 cases	100 cases
Disc Wear 2 mm	100 cases	100 cases	100 cases
Disc Wear 3 mm	100 cases	100 cases	100 cases
foreign object 0.5 mm	100 cases	100 cases	100 cases
foreign object 1.0 mm	100 cases	100 cases	100 cases
foreign object 1.2 mm	100 cases	100 cases	100 cases
foreign object 1.5 mm	100 cases	100 cases	100 cases
foreign object 2.0 mm	100 cases	100 cases	100 cases
foreign object 2.4 mm	100 cases	100 cases	100 cases

Feature extraction and validation[1]

The task focused on developing the prototype of condition monitoring of check valve diagnosis system. The AE exclusive component is compared with the developed system, and common features are selected including RMS, Amplitude, Signal Strength, FFT1, FFT2, and pressures. The characteristic points are explained here.

RMS. The root mean square or RMS is a statistical measure of the magnitude of a varying quantity. It can be calculated for a series of discrete values to measure signal power.

The RMS for a collection of N values $\{V_1, V_2,. , V_N\}$ is:

$$RMS = \sqrt{\left(\frac{1}{N}\sum_{i=0}^{N} V_i^2\right)} = \sqrt{\frac{V_1^2 + V_2^2 + \ldots + V_N^2}{N}} \qquad (13)$$

N is number of acquisition data. (N = 65536)

---

[1] This section includes details for the six parameters of specific feature characteristics of the experimental data, which are introduced in Section 3.6.1.

Figure 53 shows the validation of acquired feature point. The x-axis is a number of feature points and y-axis is a real value of feature points. In this figure, each data set makes a distinction with the pressure level.

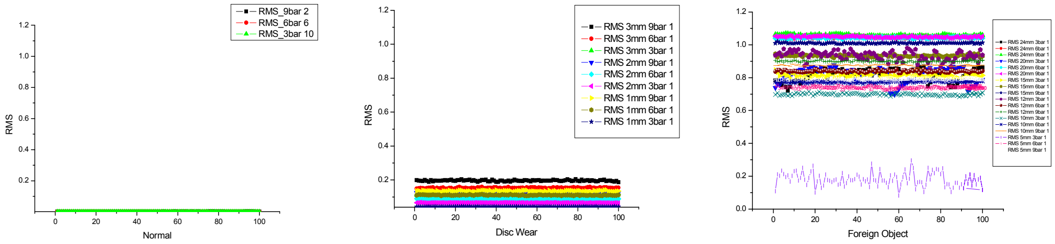

Figure 53 Distribution of RMS values

Amplitude. The amplitude of a wave is the measure of the magnitude of the maximum disturbance in the medium during one wave cycle. The amplitude for a collection of N values {V$_1$, V$_2$,. , V$_N$} is:

$$V_P = \frac{\{Max(V_1 \sim V_m) + Max(V_{m+1} \sim V_{2m}) + \ldots + Max(V_{N-m} \sim V_N)\}}{N/m} \tag{14}$$

In Figure 54, m = 8 was selected. In this figure, each data set makes a distinction related with pressure level.

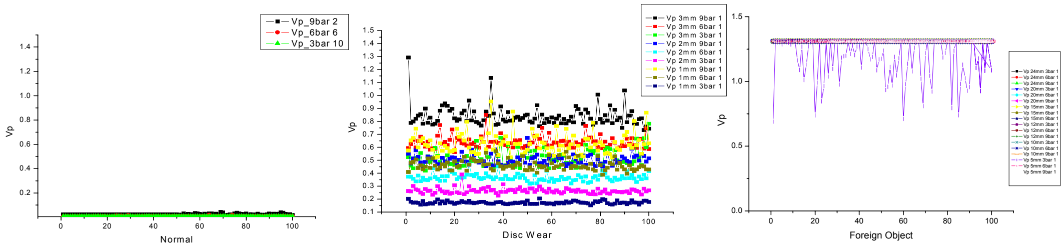

Figure 54 Distribution of amplitude values

Signal strength. Typically, signal strength is measured as voltage per square area. Power is expressed in volts per square meter (V/m^2).

$$E_{AE} = \frac{1}{R}\sum_{i=0}^{N} V_i^2 \tag{15}$$

R is a constant and selected as 1 in this case study. Figure 55 shows the signal strength distinguishes the failure at each mode.

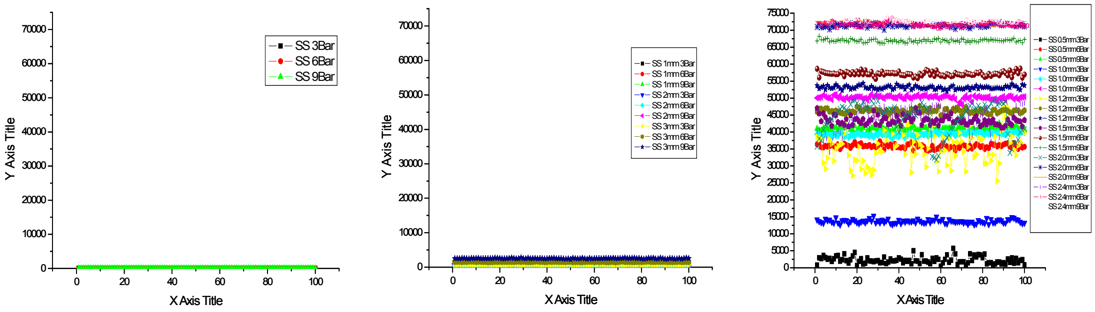

Figure 55 Distribution of signal strengths

FFT1 & FFT2. FFT1 and FFT2 are the particular frequency of acquired signal. The MUSIC algorithm was used for spectrum estimation to find the particular frequency. The MUSIC algorithm estimates the pseudo-spectrum from a signal or a correlation matrix using Schmidt's eigenspace analysis method. The algorithm performs eigenspace analysis of the signal's correlation matrix to estimate the signal's frequency content. This algorithm is particularly suitable for signals that are the sum of sinusoids with additive white Gaussian noise.

$$MUSIC = \frac{1}{e^H(f)\left(\sum_{k=p+1}^{N} v_k v_k^H\right)e(f)} \tag{16}$$

where N is the dimension of the eigenvectors and v_k is the k-th eigenvector of the correlation matrix. The integer p is the dimension of the signal subspace, so the eigenvectors v_k used in the sum correspond to the smallest eigenvalues and also span the noise subspace. The vector e(f) consists of complex exponentials, so the inner product $V_k^H e(f)$ amounts to a Fourier transform. The FFT is computed for each v_k and then the squared magnitudes are summed. FFT1 is first peak value that was calculated by the MUSIC algorithm and FFT2 is second one. Figure 56 shows the FFT1 and FFT2 using the MUSIC algorithm.

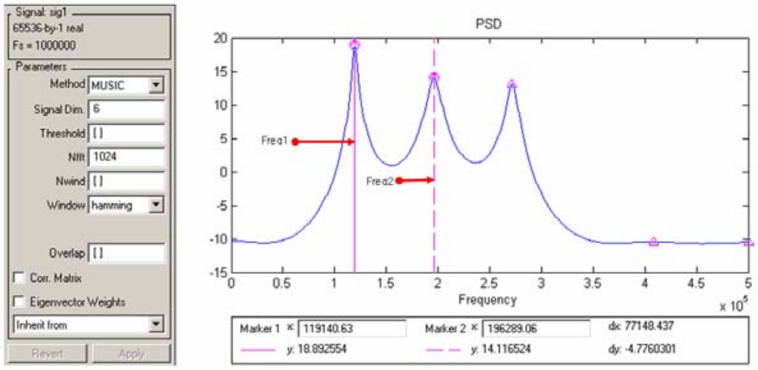

Signal: sig1
65536-by-1 real
Fs = 1000000

Parameters
Method: MUSIC
Signal Dim.: 6
Threshold: []
Nfft: 1024
Nwind: []
Window: hamming
Overlap: []
☐ Corr. Matrix
☐ Eigenvector Weights
Inherit from

Marker 1 x: 119140.63 y: 18.892554
Marker 2 x: 196289.06 y: 14.116524
dx: 77148.437
dy: -4.7760301

Figure 56 **Characteristic points.** *FFT1 and FFT2 from MUSIC algorithm.*

Figures 57 and 58 show the distributions of FFT1 and FFT2, respectively. In each case, different distributions of characteristic frequency FFT1, FFT2 are exhibited.

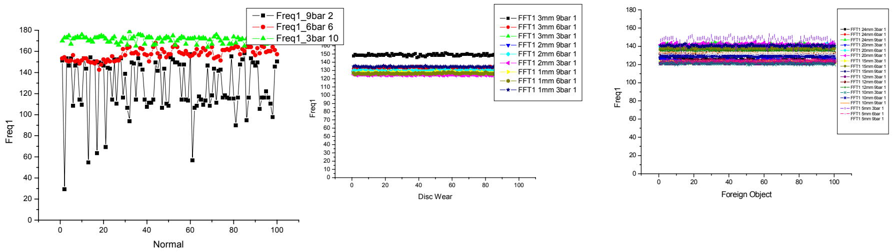

Figure 57 **Distribution of FFT1**

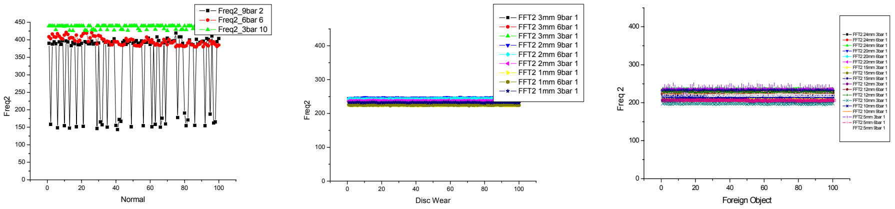

Figure 58 **Distribution of FFT2**

Appendix B: Wireless technologies

In this section, wireless standards relevant to wireless sensors are examined. These standards include Institute of Electrical and Electronic Engineers (IEEE) 802.11a [1,2], 802.11b [3], 802.11g [4], 802.15.1 (Bluetooth) [5], 802.15.3 (Ultrawideband) [6], 802.15.4 (ZigBee) [7], and from the European Telecommunication Standards Institute (ETSI), HiperLAN/2 [8].

802.11a

IEEE approved the specification for IEEE 802.11a (and 802.11b) in September of 1999. The 802.11a standard operates in 300 MHz of bandwidth that the FCC has allocated for unlicensed operation in the 5 GHz block: 200 MHz from 5.15 MHz to 5.35 MHz, and 100 MHz from 5.725 MHz to 5.825 MHz. The spectrum is split into three sections with different FCC mandated operating conditions. The first 100 MHz is restricted to a maximum power output of 50 mW, the second 100 MHz is limited to 250 mW, and the top 100 MHz is more suited to outdoor purposes, allowing up to 1 W power output. In contrast, 802.11b cards can output up to 1 watt in the United States throughout its entire frequency range.

As such, the total bandwidth available in the 5 GHz is nearly four times that of the 2.4-GHz industrial, scientific, and medical (ISM) band used by the other standards. The ISM band allows 83 MHz of spectrum, while the newly allocated Unlicensed National Information Infrastructure band at 5 GHz allows 300 MHz. The 2.4 GHz spectrum is shared with wireless phones, microwave ovens, and several wireless technologies. In contrast, 802.11a's spectrum is relatively free of interference.

The properties of the 802.11a standard are derived in large part from the higher frequencies at which it operates. In general, the frequency of a signal maintains an inverse relationship with its radiated power and range. Therefore, moving up to the 5-GHz spectrum from 2.4 GHz results in shorter distances when using the same radiated power and encoding scheme. On the other hand, by rotating and manipulating the signal, vendors can encode more information in the same time slice. To ensure that a target can decode these more complex signals, more power must be used by the sender to compensate for signal distortion. In any case, more power would be used anyway to add to the shortened range of the 5 GHz signal.

Unfortunately, simply increasing the power is not enough to maintain 802.11b-like distances using 802.11a technology. Vendors have compensated for this by designing a new physical-layer encoding system to improve upon the direct-sequence technology used by other technologies. This technology, called Coded Orthogonal Frequency Division Multiplexing (COFDM), was developed specifically for indoor use and easily outperforms the standard spread-spectrum designs. COFDM separates one data carrier into several lower-speed subcarriers, which are then transmitted in parallel. The 20 MHz wide data carrier is broken up into 52 subchannels, each approximately 300 kHz wide. COFDM uses 48 of these subchannels for data, while the remaining four are used for error correction. Through this technique, COFDM allows higher data rates and superior multipath reflection recovery.

Binary phase shift keying (BPSK) encodes 125 kbps of data per channel, resulting in a 6 Mbps data rate. Quadrature phase shift keying doubles the amount of data encoded to 250 kbps per channel, enhancing the data rate to 12-Mbps. Finally, using 16-level quadrature amplitude modulation, which encodes 4 bits per cycle, results in a data rate of 24 Mbps. The 802.11a standard requires all 802.11a-compliant products to support these basic data rates. The standard also allows the possibility of extending the modulation scheme past 24 Mbps. Even so, as the encoding system becomes more complicated, the signal becomes more susceptible to data loss in transit unless more power is used to generate the signal.

Pioneers of the 802.11a technology claim it to support data rates of 6 Mbps, 12 Mbps, 24 Mbps, 36 Mbps, 48 Mbps and 54 Mbps. As such, the de facto standard for 802.11a networking seems to be 54 Mbps. Data rates of 54 Mbps are achieved by using 64-level quadrature amplitude modulation, yielding 8 to 10 bits per cycle, up to 1.125 Mbps per 300- kHz subchannel. Using 48 subchannels, a 54 Mbps data rate is the result.

Proprietary modes that use two carriers in parallel may boost the data rate to 108 Mbps, with an expected data rate of 72 Mbps.

The 802.11a standard will run into some trouble overseas as certain military and government installations use parts of the 5-GHz space for ground tracking stations and satellite communications. To ensure that 802.11a products do not interfere with these signals, the ETSI has required two protocols to be implemented before products may be distributed in Europe. These protocols, Dynamic Frequency Selection (DFS) and (Transmit Power Control, dynamically respond to radio interference by changing channels, using lower power modulation, or attempt both solutions. These techniques ensure that the government signals get first priority when 802.11a signals coexist with them.

802.11a security

The 802.11a protocol has two methods available for securing communications. First, there is the relatively insecure Wired Equivalent Privacy (WEP) protocol that can be used or the more secure WPA protocol can be used. These two methods are outlined below:

WEP security

WEP is the standard security protocol for 802.11 communications. WEP depends on several components to maintain secure transmissions. The first component is a secret key known by the endpoints of the network. This key, generally a 40 bit or 104 bit code, is inputted manually by the network administrator as either a set of hexadecimal values or an encoded password. WEP also uses an integrity checksum (one's complement addition of eight-byte segments of the original text) to ensure that the message has not been corrupted or changed in transmission. The final component is an initialization vector (IV) that the sending computer creates for each message.

Although better than nothing, WEP has several well-known and severe security flaws [9]. First, a 40 bit secret key (specified by the WEP standard) is short enough to be broken using a simple brute force attack. This flaw is perhaps the most minor because nearly all devices also support 104 bit codes or higher, which make brute force attacks impractical.

Perhaps the major flaw in security arises from the inevitable reuse of initialization vectors. In the first place, the WEP standard does not require the IV to be changed in every message. Secondly, even if the IV is changed for every message, WEP only allocates 24 bits for the IV. A fast, busy access point can repeat the same IV several times a day even if it uses the entire space. The problem with reusing initialization vectors is that two intercepted messages with the same IV can be used to decrypt one another. More specifically, the XOR of the two encrypted messages produces the XOR of the two unencrypted messages. The messages are encrypted using the message M XOR the RC4 algorithm using the IV and the key. So:

This result can be analyzed using a variety of techniques, such as frequency analysis, to break the XORed message into the two original components. Further, as the listener gathers more messages with the same IV the messages become easier to break.

While IV reuse allows intruders to listen to network traffic, another security flaw allows unauthorized users to alter messages in transit. The integrity checksum was implemented to prevent this very problem, but does so ineffectively. Since the encryption method applies a linear algorithm (RC4) and the checksum is a linear addition, it is possible to determine how to alter the encrypted checksum so that it matches with the altered message when decrypted. Thus, an intruder can alter a message and then alter its checksum so it appears to be perfectly valid.

Not only can an intruder alter a message, but also after using some of the above techniques the intruder may be able to create new messages that appear valid. If an intruder has intercepted enough messages to determine the entire plain text corresponding to a ciphered message, the keystream for that particular IV is the simple XOR of the two messages. Since the checksum is a simple public algorithm, intruders can make a checksum for a new message of their choice, and then encrypt the message using the keystream. Because IVs can be reused, an access point must accept any IV at any time, so the message will be accepted and treated as a normal message. For sensor networks, this means an intruder can not only listen to transmitted data but also change and/or spoof sensor data.

Because of these flaws, WEP cannot be considered a secure mechanism for important purposes. Understanding this, IEEE began the 802.11i initiative, which aims to provide robust security for 802.11 systems. Although the 802.11i standard has not been ratified yet, several pre-standard security measures have been released that only incorporate portions of the proposed 802.11i standard.

Wi-Fi Protected Access (WPA) security

Wi-Fi Protected Access (WPA) is based off many of the security measures that have gone into the 802.11i standard. In fact, WPA has claimed that it will be forward-compatible with 802.11i, presumably via firmware upgrades. WPA still uses the basic mechanisms of WEP security. However, WPA fixes problems with the secret keys, the initialization vectors, and the weakness of the integrity checksums.

First, WPA has two authentication options: 802.1X authentication or Pre-Shared Key (PSK). 802.1X authentication requires users of a network to authenticate themselves via a RADIUS Server. If a RADIUS Server is not available, PSK Key mode allows each node of the network to use a password, much like WEP. For robust security, however, it is very important that the password used for the PSK be over 20 characters and immune to dictionary attacks (using numbers, symbols, varying case, etc.) This is the one security hole that has been discovered to date in WPA; if an intruder gets the PSK, all of the extra security in WPA is worthless.

To alleviate the problem with WEP initialization vectors, WPA implements a protocol called the Temporary Key Integrity Protocol (TKIP). TKIP works by changing the encryption key for every frame. It also gives each authenticated client a different starting key. Whereas the WEP secret keys were constant and could be broken eventually, WPA's keys constantly change. TKIP also uses 48 bit IVs, which repeat far less often than WEP's 24 bit IVs. Not only do IVs repeat less often, but when they repeat they will likely have a different secret key attached. This effectively nullifies the attacks described in the section on WEP security.

WPA also implemented measures to support the faulty checksum mechanism of WEP. A new protocol called Michael adds a Message Integrity Code (MIC) between the message and the checksum. The MIC is only 8 bits, compared to the 32 bit checksum. Michael is not nearly as easy to alter to match a message, and it contains a frame counter so an intruder cannot simply flood the system by repeating previously intercepted message.

Unfortunately, WPA is still vulnerable to Denial of Service (DOS) attacks. If an intruder sends two or more packets per second using an incorrect encryption key, then the access point will shut down for an entire minute. This defense prevents unauthorized access to the protected side of the network, but prevents authorized clients from using the network as well. For use in the critical sense and control systems this feature will need to be modified to allow for communications even during a DOS attack.

Advantages: The 5 GHz bandwidth allows a much higher bit rate than 802.11b and Bluetooth. It also allows more channels to be used concurrently, and more users per access point. It uses 152 bit WEP (Wired Equivalent Privacy) that offers more security than 802.11b (128 bit WEP,) but it is still not perfect.

Disadvantages: The high frequency requires more power to operate which is usually a limiting factor when it comes to designing monitoring devices. It also has shortened range, and is less resistant to obstruction. Although its high bit rate naturally lowers latency, it has no inherent QoS support. Finally, because of a lack of popularity, equipment is likely to be more expensive.

802.11b

IEEE approved the specification for IEEE 802.11b (and 802.11a) in September of 1999[3]. IEEE 802.11b uses a 2.4-GHz carrier wave with a theoretical range of 1,000 feet (and a practical limitation of less than 350 feet). Most systems encode 802.11b data using direct-sequence spread-spectrum technology (DSSS). DSSS takes the data (a stream of 0s and 1s) and modulates it with a second pattern based on complementary code keying (CCK). Finally, DSSS modulates the CCK data with quadrature-phase shift-keying (QPSK) to yield 22 MHz of frequency bandwidth. The 802.11b specification targets a theoretical throughput of 11 Mbps.

802.11b uses the carrier sense multiple access with collision avoidance (CSMA/CA) media access control (MAC) protocol. In this protocol, a wireless station listens to the network before sending a frame. If the network is being used by another station, the wireless station calculates a random backoff delay and attempts another transmission after that time period elapses. By instituting a random delay, multiple stations that are waiting to transmit do not end up repeatedly trying to transmit at the same time. Even using CSMA/CA, collisions can occur and might not be detected by the transmitting nodes. To remedy this problem, 802.11b uses a Request to Send (RTS)/Clear to Send (CTS) protocol with an Acknowledgment (ACK) signal to ensure that a frame is successfully transmitted and received.

IEEE 802.11 defines two operating modes: ad hoc mode and infrastructure mode. Using the ad hoc mode, that is, peer-to-peer mode, clients communicate directly with each other without the need for a wireless access point. Two or more wireless clients using ad hoc mode form an Independent Basic Service Set (IBSS). In infrastructure mode, at least one wireless access point and one wireless client must be available. The access point handles all network traffic, both to other wireless nodes and to a wired network.

One or more wireless clients using a wireless access point constitute a Basic Service Set (BSS). Two or more wireless access points connected to the same wired network composes an Extended Service Set (ESS). An ESS is a single logical network segment (also known as a subnet), and is identified by its Service Set Identifier (SSID). If the coverage areas of the wireless access points in an ESS overlap, then a wireless client can roam between the access points while maintaining a connection. This mechanism, as well as mobile Internet Protocol (IP), will allow for communication between mobile and stationary sensory nodes.

802.11b security

IEEE 802.11b has essentially the same options as 802.11a for security. For tighter security, WPA is compatible with all versions of 802.11.

Advantages: The 2.4 GHz frequency allows greater range for less power than 802.11a and HiperLAN/2. Its popularity has stimulated research on improving performance and lowered the cost of hardware. Although slower than 802.11a, 11 Mbps is generally satisfactory for sensor communications. As noted later, 802.11b devices are compatible with 802.11g devices.

Disadvantages: It allows a relatively low number of concurrent channels and half the users/access point than 802.11a. It is slower than HiperLAN/2 and 802.11a/g. 802.11b has no inherent support for Quality of Service (QoS). Finally, it has less standard security encryption than the other solutions: only 128 bit WEP.

802.11g

802.11g is a third wireless LAN architecture, attempting to merge the advantages of 802.11a and 802.11b. It uses the 2.4 GHz frequency range, but it utilizes special techniques to boost the bit rate up to the speed of 802.11a at close range. At greater distances, 802.11g manages to match the speed of 802.11b.

IEEE 802.11g encodes bits onto radio waves in such a way as to fit up to 54 Mbps across a single channel. This new encoding method is called Orthogonal Frequency Division Multiplexing (OFDM), and is similar to the way Digital Subscriber Line encodes data in a wired network.

Like most theoretical network figures, the net throughput of real data–the actual contents of files or transactions–falls quite short of the theoretical number; it actually lies somewhere between 20 and 30 Mbps.

This relationship between theoretical numbers and actual performance is consistent among all networking technologies, however. For instance, 802.11b's 11 Mbps theoretical throughput generally functions at 4 to 6 Mbps at best, and even less as the distance from the access point increases [4,10].

802.11g includes full backwards compatibility with 802.11b. This compatibility is not optional for manufacturers; it's a mandatory part of the specification. 802.11g also has several intermediate steps for speed, so the data rate just drop from 54 Mbps all the way down to 11 Mbps.

One of 802.11g's advantages over 802.11b is that it handles signal reflection better which will be very important in enclosed spaces. A radio signal is broadcast in all directions, and can reflect off many surfaces. As such, the same signal reaches a target at different times via different paths. A receiver must be able to reconcile all the different reflections into a single frame. 802.11g (like 802.11a) separates the spectrum in a simpler way that mitigates the effects of signal reflection. This is an important feature required for smart sensor since they are generally located in confined spaces with numerous propagation paths to an access point.

802.11g security

IEEE 802.11g has the same options as 802.11b for security. 802.11g allows for 152 bit WEP security, except when communicating with 802.11b nodes. The larger key size still has most of the same weaknesses as the smaller variety. For a closer look at WEP security, see the section on 802.11a security. For tighter security, WPA is compatible with all versions of 802.11, including 802.11g. For more information about WPA, see the section on 802.11a security.

Advantages: 802.11g is compatible with 802.11b systems. When not used with 802.11b, 802.11g uses special techniques to boost itself to about the speed of 802.11a while maintaining the range benefit of the 2.4 GHz frequency. In most ways, 802.11g combines the best features of both 802.11a and 802.11b. It uses 152 bit WEP security.

Disadvantages: One disadvantage remains from its utilization of the 2.4 GHz frequency band: the limited number of access points in a given range due to the low number of concurrent channels. As with the other 802.11 wireless standards, no inherent support for QoS is provided. In addition, when used in concert with 802.11b nodes, the 802.11g essentially becomes an 802.11b node, with lower bit rate and less security.

802.15.1–Bluetooth

Bluetooth is the name given to the IEEE standard 802.15 [5,11,12,13]. Like 802.11b and 802.11g, Bluetooth operates on the 2.4 GHz ISM band. Unlike the 802.11 standards, however, Bluetooth was designed to operate at short range with low power consumption. Bluetooth does not use access points; it can only form ad hoc networks called "piconets." The device that forms the piconet is the master, and all other devices connected to the piconet are slaves. A single piconet can contain 1 master with up to seven slaves. A single device can be in several different piconets, as either master or slave as necessary, using time-division multiplexing. The phenomenon of having multiple piconets in the same area is called a "scatternet." A scatternet is a flexible and powerful network, making Bluetooth useful for many different situations in wireless sensor applications.

In a piconet, binary data is translated into a radio wave using Gaussian frequency-shift keying (GFSK). In GFSK, a positive frequency change from the base frequency represents a 1, and a negative change represents a 0. Unfortunately, the ISM band is used by several other wireless technologies, such as microwave ovens, portable phones, 802.11b, and 802.11g. The interference caused by these additional waves degrades the data sent along the piconet.

Bluetooth designers have a goal to bring devices to under $10 per unit, and can operate on much less power than 802.11 technologies. On the other side, Bluetooth has a limited connection distance of about 30 ft–up to 300 ft if it uses an equivalent power of 802.11. In addition, Bluetooth currently has very low connection speeds; it supports 780 kbps, which may be allocated for 721 kbps unidirectional data transfer (57.6 kbps return direction) or up to 432.6 kbps for symmetric data transfers. Several standards committees (802.15.3 and 802.15.3a) have been working on developing Bluetooth devices with faster speeds, but it is likely that these solutions will sacrifice some of Bluetooth's advantages as well. Conversely, one committee (802.15.4) is developing a device that uses even less power, having even slower speed and smaller range [5]. As such, in the future Bluetooth will be able to handle an incredible range of applications in its various forms.

Bluetooth security

The first of Bluetooth's defenses is a natural one. Bluetooth connections use Frequency Hopping Spread Spectrum (FHSS), which means that the piconet changes operating frequencies around 1600 times per second. Any device wishing to listen in on the communication must first synchronize with the hopping pattern before it can begin to break the encryption scheme. Of course, Bluetooth does not rely on this natural protection.

As with the 802.11 standards, Bluetooth has several components it uses to enact security mechanisms. Every Bluetooth device has a unique 48 bit address that will identify it to other devices. Next, a 128 bit Personal Identification Number (PIN) must be manually entered or stored into the device, much like the WEP secret key. Every device also has a 128 bit randomly generated key used for authentication and an 8-128 bit key used for encryption. Finally, a Bluetooth device has the ability to randomly generate 128 bit values that are used for a variety of purposes in the security architecture. All of these components are used in the process of creating and securing links between Bluetooth devices.

Although Bluetooth security is fairly robust, a few flaws have been discovered. First, if unit keys are used, the device that supplies the unit key can be impersonated by the device that receives the unit key. Second, a short PIN number can be guessed and confirmed by an intruder, allowing it to obtain the link keys used by a piconet. Once this is done, the intruder can contact one of the devices and set up new link keys, thus hijacking the piconet. Although frequency hopping provides some defense for eavesdropping, the seed used for the pseudorandom frequency hopping can be determined by a intruder, allowing the intruder to synchronize itself with the piconet. Because encryption keys vary in size, a malicious device can declare a small encryption size and force minimal encryption on a piconet. Since Bluetooth addresses are considered unique, an intruder can also undermine security by spoofing the address of an existing device and impersonating it.

Fortunately, most of the flaws in Bluetooth security can be alleviated by careful configuration of the device. For instance, the security holes using unit keys can be avoided by specifying the use of combination keys instead. Problems with short PIN numbers can be eliminated by enforcing long passwords immune to dictionary attacks. Declaring a large minimum encryption size can prevent an intruder from undermining the encryption security. Avoiding low memory capacity devices will help eliminate some shortcuts Bluetooth takes in such cases that can be exploited by intruders. Finally, a Bluetooth device that will not reveal its frequency hopping seed can help prevent intruders from synchronizing with the piconet.

Advantages: Bluetooth is smaller, cheaper, and uses less power than the wireless LAN standards because of the modulation scheme used. Bluetooth also has a higher resistance to interference than the other solutions. A Bluetooth system is likely to have better security than WEP provides, although this can vary slightly between implementations.

Disadvantages: By using less power, Bluetooth sacrifices range–it has less range than the 802.11 standards. It also has a much lower bit rate than any of the LAN solutions. Bluetooth's main purpose is for a Personal Area Network (PAN) as opposed to a LAN; it may be possible to use it as a LAN, but such use is beyond the original intention of its design.

802.15.3a–Ultra Wideband (UWB)

Ultra Wideband (UWB) is an emerging interactive communications technology designed for short range, high data rate, low interference, and low power consumption [6]. All of the other wireless technologies work by sending a signal in a narrow band of frequency for a relatively long period. UWB, instead, uses a massive band of frequency for a very short period using little power. The low power and miniscule time requirements theoretically allow UWB to coexist with narrow band communication with little to no noticeable communications interference. UWB proponents have shown that under most circumstances, the interference caused by UWB is less than the natural noise in an environment [14].

UWB's development has been somewhat delayed by a deadlock in its standardization. UWB is slated to become IEEE standard 802.15.3a. Unfortunately, two factions, one led by Intel, the other by Motorola, have submitted competing proposals for the Physical (PHY) layer, neither of which garnering enough votes to be approved. Intel's group supports a proposal based on OFDM, while Motorola's group supports a plan based on Direct Sequence Code Division Multiple Access (DS-CDMA).

The properties of UWB suggest that the technology would work best as a high-rate PAN. At close range, the MBOA specification for UWB will support up to 480 Mbps data rate. Because of its low power consumption, however, the range of UWB is very small; the highest rate can only be supported up to about 7 meters away. After that distance, the data rate drops precipitously. Still, even at its maximum distance of about 30 meters, the minimum data rate supported by MBOA is still around 55 Mbps. This data rate is comparable than even the theoretical upper bounds of the best current 802.11 systems' data rates.

As this standard's additional properties could vary drastically depending on which proposal is eventually ratified, no further definite information can be given about the standard. The first implementations of UWB should be considered proprietary until either IEEE or the market chooses which PHY layer is superior.

Advantages: Ultra Wideband has the potential for remarkable data rates with low power cost. Its burst nature helps avoid interference and discourage intruders. Access to a wide frequency band also allows it to avoid interference from other wireless devices. This technology is a viable solution for wireless sensors where power consumption is not an issue but high bandwidth is required.

Disadvantages: The range of Ultra Wideband is less than the current LAN technologies. In addition, the difficulties in ratifying a standard for UWB will delay the growth of the industry greatly.

802.15.4–ZigBee Alliance

For some applications, the 802.15.1 (Bluetooth) standard did not go far enough. Out of the need for even lower battery consumption requirements came the IEEE 802.15.4 standard. The 802.15.4 standard provides lower power consumption and lower cost than Bluetooth, while not sacrificing data rates. The range of 802.15.4, on the other hand, actually increases as compared to 802.15.1. These specifications are geared towards wireless sensors and control systems, which need to last for many months or years on a single battery and do not require high bandwidth.

The ZigBee Alliance is a collection of companies that have teamed up to promote a wireless communication standard based on the IEEE 802.15.4 standard. The 802.15.4 specification covers the PHY and MAC hardware, while ZigBee starts at the MAC layer and adds a Data Link layer, a Network Layer, and an Application Interface. Thus, ZigBee encapsulates nearly the entire communication process from the end user's application.

Using a dual physical layer, ZigBee offers the ability to use the 2.4 GHz spectrum or the 868/915 MHz spectra. At 2.4 GHz, the data rate starts at 250 kbps; at 915 MHz, the data rate starts at 40 kbps; at 868 MHz, the data rate begins at 20 kbps. As usual, these rates will decrease as the distance between nodes increases. Its range is from 5 to 500m depending on the environment, but typical performance is around 50m. This compares favorably to Bluetooth while using a fraction of the power.

ZigBee systems are design with power consumption in mind. A ZigBee system is rarely active. Typical duty cycle for a system is about 0.01%. This means the system has an effective power consumption of 30μW in contrast to an active Bluetooth node, which consumes about 30 mW of continuous power.

ZigBee security

ZigBee offers security options for both the MAC layer and the NWK layer. MAC layer encryption, however, is only possible for single-hop communication; multi-hop messaging must only use NWK layer security. Both of these levels of security are based on the Advanced Encryption Standard (AES) cryptographic algorithm. With multiple options to choose from in both MAC and NWK layer security schemes, ZigBee has the best security of any current standard [7,15].

Advantages: ZigBee is smaller, cheaper, and uses less power than all of the other standards. ZigBee also has the best security of any current standard. ZigBee has very good range for using such little power.

Disadvantages: As it has a very low data rate (as little as 20 kbps) it can only handle small amounts of data.

HiperLAN/2

The typical architecture of a HiperLAN/2 network connects remote nodes, called Mobile Terminals, to a fixed network via one or more access points [8]. As with the 802.11 standards the Mobile Terminals (MT) connects wirelessly to an Access Point (AP). The APs support roaming; the network transfers the connection to the AP that provides the best performance as the MT moves around in the network range. The network is automatically configured, so manual frequency planning of the site is not necessary.

The general features of HiperLAN/2 are as follows:

- High data rate
- Connection-oriented
- Quality of Service (QoS) support
- Automatic frequency allocation
- Mobility support
- Power Save

HiperLAN/2 has a very high transmission rate, up to 54 Mbps at the PHY layer and up to 25 Mbps at the third layer. To achieve this data rate, HiperLAN/2 uses OFDM to transmit the analogue signals.

Because every MT must make a connection to an AP, HiperLAN/2 can support QoS very simply. Each connection can be given a level of QoS to control its amount of bandwidth, latency, etc. It is also possible to assign each connection a priority level relative to all the other connections. Because of its high data rate and easy QoS support, HiperLAN/2 is well equipped to handle time critical applications such as data streaming.

For wireless sensor networks that require energy management, the HiperLAN/2 standard is attractive. A HiperLAN/2 MT can request an AP to enter a low power state for a requested period to save power. When the MT wakes up, it checks to see if the AP has also returned; if not, the MT sleeps for another period. The amount of sleep time can vary based on the needs of the MT.

In Europe, a 455 MHz bandwidth is allocated for HiperLAN/2 systems in the 5 GHz range. To allow co-existence with other services, CEPT (Comite Europeen des Postes et Telecommunications) has set different operational limits (on power and features) for different sections of the band.

In the United States, a 300 MHz bandwidth is allocated to wireless LANs in the 5 GHz National Information Infrastructure (NII). In Japan, a 100 MHz band is allocated for Wireless LANs, and more spectrum allocation is under investigation. A cell of a HiperLAN/2 AP typically extends to approximately 30 (office indoor)–150 meters.

Table 1 shows a comparison of standard network parameters between HiperLAN/2 and the 802.11 family of technologies.

Table 1 Comparison of LAN technologies

Characteristic	**802.11**	**802.11b**	**802.11a**	**HiperLAN/2**
Spectrum	2.4 GHz	2.4 GHz	5 GHz	5 GHz
Max physical rate	2 Mb/s	11 Mb/s	54 Mb/s	54 Mb/s
Connectivity	Conn.-less	Conn.-less	Conn.-less	Conn.-oriented
QoS Support	(PCF)1	(PCF)1	(PCF)1	ATM/802.1p/RSVP/DiffServ
Frequency Selection	FH or DSSS	DSSS	Single Carrier	Single Carrier with DFS
Fixed Network Support	Ethernet	Ethernet	Ethernet	Ethernet, IP, ATM, UMTS, Fire Wire, PPP5

1. Point Control Function, a concept defined in 802.11 to allow certain time slots being allocated for real-time-critical traffic

HiperLAN/2 security

The HiperLAN/2 network has support for both authentication and encryption. With authentication both the AP and the MT can authenticate each other to ensure authorized access to the network (from the AP's point of view) or to ensure access to a valid network operator (from the MT's point of view). Authentication relies on the existence of a supporting function, such as a directory service, but which is outside the scope of HiperLAN/2.

The user traffic on established connections can be encrypted to protect against for instance eavesdropping and man-in-middle attacks.

Advantages: HiperLAN/2 has the same high data rate as 802.11a, only with a higher average throughput. HiperLAN/2 has built-in support for QoS, and is very good for time-sensitive applications. It can also change frequencies dynamically to avoid bands of interference.

Disadvantages: HiperLAN/2 was developed in Europe and has not found much popularity in the United States (or even Europe, for that matter). Using the 5 GHz frequency band naturally limits the range of communication.

Table 2 provides an overview of the wireless technologies discussed in this section.

Table 2 Comparison of Current Wireless Technologies

	802.11a	**802.11b**	**802.11ga**	**802.15.1 Bluetooth**	**802.15.3a UWBc**	**802.15.4 ZigBee**	**Hiper LAN/2**
Frequency	5 GHz	2.4 GHz	2.4 GHz	2.4 GHz	3.1-10.6 GHz	2.4 GHz 915 MHz	5 GHz
Raw Bit Rate	Up to 54 Mbps, 2x Turbo Mode	11 Mbps	54/11 Mbps for b compatibility	1-2 Mbps	~600 Mbps	250 kbps/40 kbps	54 Mbps
Effective Bit Rate	~24 Mbps	~4.5 Mbps	~7-16 Mbps	~500-700 kbps	~400 Mbps	N/A	~24 Mbps
Range	~60-300 ft indoor ~300-1200 ft out	~100-300 ft indoor ~500-1500 ft out	~100-300 ft indoor ~500-1500 ft out	~30 ft?	~15–60 ft	~15-1500 ft 150 ft typical	~90-450 ft
Frequency Modulation	OFDM	DSSS/CCK	OFDM/CCK	FHSS	OFDM or DS-CDMA	DSSS	OFDM
Power	~50 mW	~30 mW	~30 mW	~10 mW	~30 mW	.03 mW (typical)	~50 mW
Total Channels	12	11	11	79	N/A	65535	19
Concurrent Channels	8	3-6	3-6	N/A	N/A	65535b	dynamic
Users per Access Point	64	32	64	7	N/A	2^64	
Built-in Security	152 bit WEP	128 bit WEP	152/128 bit WEP	Security manager	N/A	AES	DES
Cost	High	Medium	Medium	Low	N/A	Very low	Medium

a. Because 802.15.3a is still in the process of ratification, all numbers are estimates, or otherwise listed as N/A
b. 802.11g is compatible with 802.11b, but its performance is limited to that of 802.11b's when used together.
c. Theoretical

Sensor network architecture

While choosing which standard and sensors to use, several details concerning the setup of the application must be carefully considered. The type of data communicated by a sensor has a major impact on the network design. In addition, there are several different ways for sensors to communicate with access points, each with its benefits and drawbacks.

Sensor intelligence

In recent years, the development of smart sensors has shed a new light on the role of sensors. In addition to gathering data, some smart sensors can extract statistical features such as RMS and kurtosis from the data in addition to performing advanced signal processing analysis such as FFTs and WTs. These features can then be sent to a central processing unit for monitoring and further health analysis and data trending. Although there may always be a need to gather raw sensor data for validation purposes, using smart sensors pushes the processing layer closer to the sensor and will ultimately reduce network traffic and simply network design.

An obvious dilemma arises in the use of smart sensor for wireless technology. Smart sensors require much more processing power and complexity, and will inevitably be more expensive. In addition, a change in the features gathered would require an update for every deployed sensor.

Overall, the level of processing performed by a sensor will have an effect on the wireless standard and network topology used for an application. This factor must be considered carefully while making a deployment decision.

Topology

Several different topologies have been developed for wireless technology, although nearly all are based on wired topologies. The star and mesh topologies are derived from wired networks. Though it is possible to make a wireless network based on the bus topology or the token ring topology, such a setup would be awkward and inefficient. Several architectures combining one or more of the standard topologies will also be examined.

Star networks

The star topology is the standard setup for wireless technology today. One or more Access Points (AP) connect the wireless nodes (in this case, a wireless sensor) to a wired network. A diagram of this kind of network can be seen in Figure 1. Although often a node can roam between APs, the node will communicate with only one AP at a time. The nodes are completely independent from one another, and cannot accept messages except via one of the APs. Repeaters can be part of the setup, but only to bridge the distance between a node and an AP. For the 802.11 standards, a node cannot act as a repeater.

The star topology allows nodes to be independent from one another. This setup is the natural formation for most of the standards, and will require little to no additional planning except to ensure each of the nodes are in range with the AP. A disadvantage of the star topology is that the network depends heavily on the APs, and if an AP is damaged a good portion of the network could be rendered inactive.

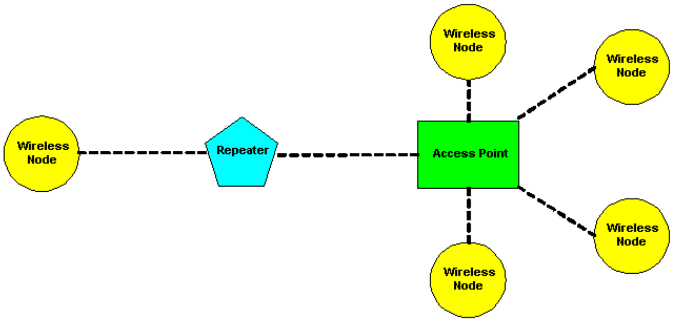

Figure 1 Star network

Mesh networks

A mesh topology consists of mobile nodes, repeaters, and access points. The nodes of a mesh network are network intelligent sensors that are able to also act as repeaters themselves. A diagram of a sample mesh network can be seen in Figure 2. A signal from a mobile node will take the best path available to an access point, regardless of how many times it is repeated. In fact, a mesh network often overpopulates a region with nodes and repeaters to provide multiple potential paths in case one node is overworked or malfunctioning. This extra redundancy also reduces the distance in which wireless communication is necessary. Minimizing distance increases signal strength, often resulting in much improved performance.

The mesh topology allows nodes to use one another to create a more reliable, more robust network. However, the necessity of sensors acting as repeaters adds an additional complexity and cost to sensor development. Further, overpopulating an area with sensors naturally increases the cost of a network.

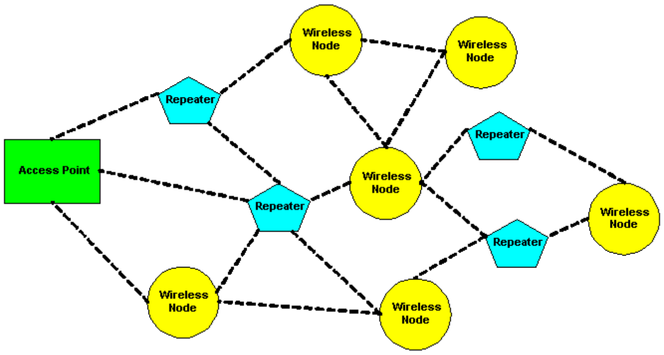

Figure 2 Mesh network

Hybrid networks

A hybrid network combines the functionality of both star and mesh networks. A hybrid topology contains nodes, repeaters, and access points. The nodes of a hybrid topology are simple wireless sensors that are each dedicated to a single repeater situated close to the sensors. However, the repeaters form a mesh network, taking any path to the nearest access point. A diagram of a hybrid network is shown in Figure 3.

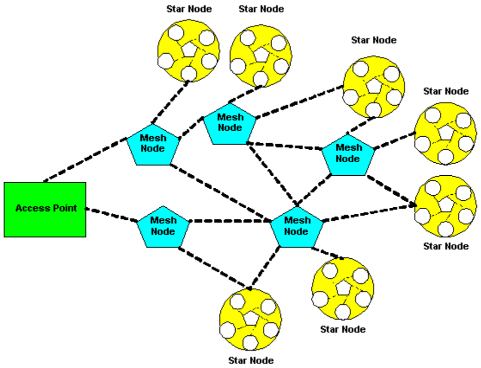

Figure 3 Hybrid network

As can be expected, the hybrid topology merges the advantages and disadvantages of the two different network types. The star portion allows the sensors to be simple wireless sensors, without the need to add repeater functionality. The mesh network of repeaters provides redundancy and robustness, up to a point. A hybrid network still has the weakness of a star network; if one of the key repeaters goes down, none of its associated sensors can reach the network any longer. The redundancy and complexity of the repeaters also adds to the cost of the network, although not as significantly as a pure mesh network.

Partially wired networks

For lack of a better name, a partially wired network allows traditional wired sensors to be used in a wireless network. In this topology, wired sensors all connect to a central box that transmits the information wirelessly into one of the previously mentioned topologies. The sensors and hub together can be considered a single node in a wireless star or wireless mesh topology. An example of a partially wired network can be seen in Figure 4

The main advantage a partially wired topology has over its completely wireless counterpart is that ordinary wired sensors can be used. Wired sensors are likely to be less expensive and more reliable. Such architectures use very little wiring compared to a fully wired network, as the sensor/hub combination must be very close to begin with. Thus, the vulnerability and weight of wires are minimized. Additionally, the hub can potentially do feature processing on the data provided by the sensors to minimize the network flow. One disadvantage of this setup is that the wires are heavier and can potentially fail but does allow a mechanism to slowly merge to an all wireless network.

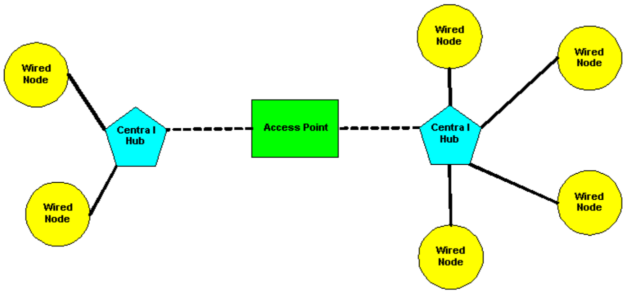

Figure 4 **Partially wired network**

Applicability of architectures for wireless networks

Each of these architectures has certain features that are preferable for a shipboard environment. The point-to-point star network is the simplest type and is supported by the most currently available sensors. Mesh networks provide a redundant, robust topology that can automatically adjust to the gain or loss of a sensor. Hybrid networks combine the advantages of both star and mesh networks. Wired star networks are able to use current sensor technology in a wireless environment.

The choice between using a star or mesh network has several other consequences of interest to control systems. In the case of damage recovery, the mesh network is best able to re-route network traffic to working access points. Sensors in a star network also have this ability, but only if the sensor is within range of a working access point. Mesh networks require more power to operate, especially when sensors act as repeaters. It is not possible to predict the battery drain of a given sensor in a mesh network, because the network configures itself to use the best path, which may change during operations. Star networks are more predictable and use less power, as each sensor only uses the power it needs to transmit data to the access point. Hybrid networks have all of these consequences to the degree that the two topologies are integrated.

Table 3 provides a summary of the relative strengths and weaknesses of the architectures.

Table 3 **Comparison of networking topologies**

Topology	Fully Wired	Star	Mesh	Hybrid	Wired Star
Robustness	Lowest	Medium	Highest	High	Medium
Flexibility	Lowest	High	Highest	Medium	Low
Speed	Highest	Medium	Lowest	Low	High
Vulnerability	Highest	Lowest	Low	Medium	High
Weight	Highest	Lowest	Medium	Low	High
Power Drain	Lowest	Medium	Highest	High	Low
Cost	High	Lowest	Highest	Low	Medium

Available Wireless Sensors and Nodes

This section provides a wide cross-section of the available wireless sensors currently available on the market. Systems components made by Emerson, Microstrain, and Techkor are included even though their communication technology is a proprietary format. Although proprietary technologies by their very closed nature make systems integration and future retrofitting difficult, they are still a viable solution for system development and will not excluded.

Table 4 provides a list of sensors and associated design parameters. The systems mentioned seem to encompass a level of survivability (battery backup and flexible network topology) and flexibility (protocol used and sensors types available) that could be applicable to an aerospace wireless sensor system.

Table 4 Comparison of current wireless sensors

Company	**3eti**	**CSI-Wireless**	**Crossbow**	**Emerson**	**MicroStrain**	**MicroStrain**	**Oceana**	**RLW**	**Techkor**
Product	NCAP 3e560i	Asset-Link Wireless IO Node	MTS 310 + MICA 2	RF MicroAnalyzer	EmbedSense	G-Link	ICHM 20/20 Wireless IO Node	S2NAP Wireless Node	Maintenance Watchdog
Device Type	Sensor Node, Unprocessed	Wireless Node	Sensor	Wireless Node w/Processing	Sensor	Sensor	Wireless Node, Unprocessed	Wireless Node, w/Processing	sensor/w Processing
Purpose	Any	Any	T,H,BP,A,M	T, A	T, S	A	Any	Any	A, T, Tach
Weight	2.5 kg	~0.4 kg	~0.25 kg	0.5 kg	12 g	7 g w/o battery	0.28 kg	~ 1 kg	2.8 oz w/battery
Dimensions	12.5 in. x 9 in. x 4.375 in.	6 in. x 3.5 in. x.75 in.	2.25 in. x 1.25 in. x.25 in.	Height: 4.0 in., Diameter: 2.5 in.	Height:.26 in. Diameter = 1.45 in.	1 in. x 1 in. x 0.5 in.	4.74 in. x 2 in. x 3.15 in.	4 in. x 6.375 in. x 2 in.	Height: 2.5 in. Diameter: 1.25 in.
Power Options	line power	line power	line power, battery backup	Battery Powered	External	Battery or Line	Line, optional external battery backup	line power	battery
Battery	N/A	optional external backup	1.1 AH (2 AA batteries)	3.6 VDC, 5.2 AH	N/A	2.4 AH	Lithium Ion	N/A	1 AH
Energy Use	2A peak, 110V AC	120 to 500 mA (7V)	33 mA, <16 uA sleep	~30 mA	0.5 W AC	<1.1 mA	2W peak	< 30 W	14W peak
Standard	802.11b	Cellular	Proprietary (TinyOS)	Proprietary	Proprietary	Proprietary	802.15.1	802.11a,b,g others available	Proprietary
Frequency Band	2.4 GHz	916 MHz	315, 433, 915 MHz	2.4 GHz	125 kHz (Inductive)	916 MHz	2.4 GHz	2.4 GHz	902 to 921 MHz
Architecture	Star Network	Star Network	Mesh Network	Star Network	RFID	Star Network	Star Network	Star Network	Star Network
Data Rate	11 Mbps	1200 baud	38.4 kbps	N/A	9600 bps	19.2 kbps	56 kbps	11 Mbps	11 Mbps
Range	300 ft +	N/A	500 to 1000 ft outdoors	>300 ft	in.	100 ft	300 ft	300 ft	300 ft
Cost	$2000 to 2500	$300 for a node	$90 - $500 per node	$1549	~ $3295	~ $2000 for a starter kit	~ $2200	~$2500	~ $3650

A	accelerometer (vibration)	T	temperature	Tach	tachometer
BP	barometric pressure	M	magnetometer		
H	humidity	S	strain		

Wireless study conclusion

From this study on current wireless technologies, it can be deduced that in the short term the 802.11a, b and g standards seem to have the greatest potential applicability to system integration of wireless sensors. With mobile computing driving these standards, it seems nature to leverage these standards for develop sensor networks. However, there are other factors, such as power requirements, that also play an important role in sensor development. The following explains how each wireless technology's characteristics and network design affects its applicability to the development of smart sensors.

Although Ultra Wideband shows great promise, it is a long way from full realization. Its high data rate and low power consumption make it ideal for most sensor applications, even ones requiring high data flow such as accelerometers. It also has security benefits of burst transmission. Until a clear standard for this technology emerges, however, a large-scale installation may be unable to upgrade to better equipment should another standard be widely accepted.

HiperLAN/2 has many desirable features but despite this has not found much acceptance in commercial circles. Limited acceptance of a technology will invariably lead to increased cost and limited COTS applications.

Bluetooth (802.15.1) is rich in features and has wide commercial acceptance. The drawback of Bluetooth is inherent in its original intended purpose. Bluetooth was originally designed for PAN (personal area network) structures. Scaling Bluetooth up to a level where it can support the needs of the large monitoring and control systems may be difficult. Bluetooth was never designed for high bandwidth devices, and incorporating them will bring with it compromises.

ZigBee Alliance (802.15.4) is a scaled down version of Bluetooth and as such brings with all of the disadvantages of Bluetooth but does offer a very good security options.

802.11a, b and g have the widest commercial acceptance (particularly so for the mutually compatible b and g standards). Significant resources are being applied to 802.11 research and development. Security of communications problems with these standards seem to have been successfully addressed. 802.11b and g, being compatible and widely available, put them at the forefront of the wireless technologies.

New developments are the process to deliver a higher throughput amendment to the 802.11 standard. This new standard, labeled "802.11n," will be backward compatible with 802.11a and 802.11b. The "n" designation calls for rates of at least 100 Mb/s, as measured at the interface between the 802.11 MAC and higher layers. This will give a four to five-time improvement over the 802.11a and 802.11b devices.

It is known that single-frequency communication systems suffer from multipath interference that can render them ineffective in confined spaces [16]. However, spread spectrum and frequency-hopping systems, currently used in wireless local area networks (WLANs), have been shown to operate effectively in confined environments. Nevertheless, the transfer characteristics of these signals relative to bulkheads, doors, ducts, mask cable transits, and compartment penetrations/obstructions were until recently not understood at any level [16-23].

Although the evidence for the effectiveness of using wireless within a NPP is compelling, more testing is needed to gain a better understanding of the propagation modes in this environment and their relative impact on other RF signals.

References

1. LAN MAN Standards Committee of the IEEE Computer Society, *Wireless LAN medium access control (MAC) and physical layer (PHY) specifications*, IEEE Standard 802.11, 1999 Edition, 1999.
2. LAN MAN Standards Committee of the IEEE Computer Society, *Wireless LAN medium access control (MAC) and physical layer (PHY) specifications*, Amendment 1: High-speed Physical Layer in the 5 GHz band, IEEE Standard 802.11a, 1999 Edition, 1999.

3. LAN MAN Standards Committee of the IEEE Computer Society, Supplement to 802.11-1999, *Wireless LAN MAC and PHY specifications: Higher speed Physical Layer (PHY) extension in the 2.4 GHz band*, IEEE Standard 802.11b, 1999 Edition, 1999.
4. LAN MAN Standards Committee of the IEEE Computer Society, *Wireless LAN medium access control (MAC) and physical layer (PHY) specifications*, Amendment 4: Further Higher-Speed Physical Layer Extension in the 2.4 GHz Band, IEEE Standard 802.11g, 2003 Edition, 2003.
5. LAN MAN Standards Committee of the IEEE Computer Society, *Wireless Medium Access Control (MAC) and Physical Layer (PHY) Specifications for Wireless Personal Area Networks (WPANs™)*, IEEE Standard 802.15.1, 2002 Edition, 2002.
6. LAN MAN Standards Committee of the IEEE Computer Society, *Wireless Medium Access Control (MAC) and Physical Layer (PHY) Specifications for High Rate Wireless Personal Area Networks (WPAN)*, IEEE Standard 802.15.3, 2003 Edition, 2003.
7. LAN MAN Standards Committee of the IEEE Computer Society, *Wireless Medium Access Control (MAC) and Physical Layer (PHY) Specifications for Low Rate Wireless Personal Area Networks (LR-WPANs)*, IEEE Standard 802.15.4, 2003 Edition, 2003.
8. Martin Johnsson, HiperLAN/2–The Broadband Radio Transmission Technology Operating in the 5 GHz Frequency Band, HiperLAN/2 Global Forum, 1999.
9. J. Williams, The IEEE 802.11b security problem. I, *IT Professional*, Volume: 3, Issue: 6, pp. 95-96, November-December 2001.
10. A. Engst, Fleishman, G., 802.11gs Extreme Emergence, The O'Reilly Open Source Convention, Portland, OR, Jan. 23, 2003.
11. Bluetooth SIG, Core Specification of the Bluetooth System, Version 1.2, Nov. 5, 2003.
12. K.V. Sairam, , N. Gunasekaran, and S.R. Redd, Bluetooth in wireless communication, Communications Magazine, IEEE, Volume: 40, Issue: 6, pp. 90-96, June 2002.
13. Wang Wei-Shin, Bluetooth: a new era of connectivity, Microwave Magazine, IEEE, Volume: 3, Issue: 3, pp. 38-42, Sept. 2002.
14. T. Naito, *Seamless Ultra-Wide-Band Transmission Technologies*, Fujitsu Labs., Kawasaki, Japan, March 2003.
15. Patrick Kinney, ZigBee Technology: Wireless Control that Simply Works, Communications Design Conference, Oct. 2, 2003.
16. J. Balboni, J. Tingley, R. Ford, K. Toomey, and J. Vytal, *An Empirical Study of Wireless Propagation Aboard Naval Vessels*, IEEE Publications, 2001.
17. E. L. Mokole, M. Parent, J. Valenzi, E. Tomas, B. T. Gold, T. T. Street, and S. N. Samadda, Initial Bistatic Measurements of Electromagnetic Propagation In An Enclosed Ship Environment, The Antenna Applications Symposium, September 15-17, 2004.
18. G Singh, The Cebrowski Institutes Center for the Study of Mobile Devices and Communications-Research Agenda, The Naval Postgraduate School, January 2003.
19. N. Borisov, I. Goldberg, and D. Wagner, Intercepting Mobile Communications: the Insecurity of 802.11, Proc. Of the 7th ACM International Conference on Mobile Computing and Networking. Rome, July 2001.
20. T. T. Street, *Wireless, Spread Spectrum, Low Level RF, DC Communications Network for Repair #2 and the Submarine Mockup Area on ex-USS SHADWELL*, Report 6180/0724.1, Naval Research Laboratory, 22 November 1995.
21. T. T. Street and R. A. Robinson, *Wireless Communications Network RF Emission Survey*, Report 6180/0198, Naval Research Laboratory, 20 June 1997.
22. E. L. Mokole, M. Parent, S. N. Samaddar, J. Valenzi, and E. Tomas, *Preliminary Report on Electromagnetic Propagation in an Enclosed Ship Environment*, Report 5340/193, Naval Research Laboratory, 30 October 1998.
23. R. J. McConnell, *Testing and Evaluation of Shipboard Wireless Components*, a thesis from The Naval Postgraduate School, March 2000.

Appendix C: Piping elbow test loop

I. Development of electrodes[1]

The Ag/AgCl (water) electrode was developed and tested before using in the FAC test. For verifying the developed sensor, the performance tests were carried out in both room temperature and high temperature conditions to obtain the calibration relation with changing conditions. First, room temperature test for this electrode was performed to measure and review the potential differences between this electrode and SCE (Saturated Calomel Electrode). Six different electrodes were measured and impedance values of each electrode were specified. No correlation between potential difference and impedance was found in this test. Maximum deviation between electrodes was 60 mV. Potential difference of this electrode, which is used in the high-temperature test, was 257 mV_{SCE} @16°C. This value shows a difference from theoretical potential value of about 12 mV. This corresponds to 1.5×10^{-5} M of Cl ion concentration. Potential change shows a drastic drop at the beginning, and then becomes stable after 100 hours operation. It means that at least 100-hours are needed to stabilize electrode signal. Reproducibility of this electrode cannot be guaranteed considering potential deviation between electrodes. To measure pH, the Gold-plated Ni electrode was used in the FAC test.

After the preliminary test, a test loop was developed to test electrodes up to 290ºC. Pressure and temperature were controlled to identify whether the developed sensor shows good applicability to the FAC test. In this work, reference and pH electrode are developed and tested in the high temperature and pressure environment. Ag/AgCl (water) and Ag/AgCl (Sat. CuCl) electrodes are applicable as reference electrodes, and for the short period, Ag/AgCl (0.01 M KCl) electrode is also feasible. AUEN, similar to hydrogen electrode, is suggested to measure pH. Test result shows that AUEN is feasible in this application.

Figure 1 shows autoclave with installed electrodes, including Ag/AgCl (Water), Ag/AgCl (Sat. CuCl), Ag/AgCl (0.01 M KCl), AUEN, Pt, and $Cu/Cu_2O/ZrO_2$ electrodes.

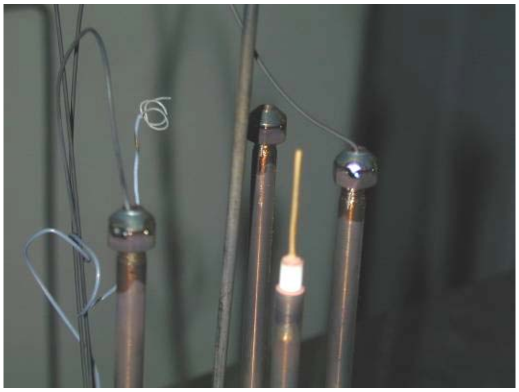

Figure 1 Electrodes installed in the autoclave

Intrinsic sensor. Intrinsic optic sensor is used to measure the environmental effect, which is converted to a light signal within the fiber. In this case, the four designations can be used. First of all, microbend sensors are used for measuring strain, pressure, and vibration. Others are blackbody sensors for measuring temperature, interferometric sensors, and distributed sensors. Distributed sensors are used by Rayleigh, Raman, mode coupling, and quasi-distributed method.

The interferometric sensors have been demonstrated to provide the highest-performance in the group of intrinsic sensors. Mode coupling, Sagnac, Mach-Zehnder, and Michelson types are the main methods of interferometric fiber-optic sensors. Figure 2 shows a diagram illustrating the types of interferometric fiber-optic sensors and their usages.

---

[1] This section includes details for electrode development, which is introduced in Section 4.2.2.1.

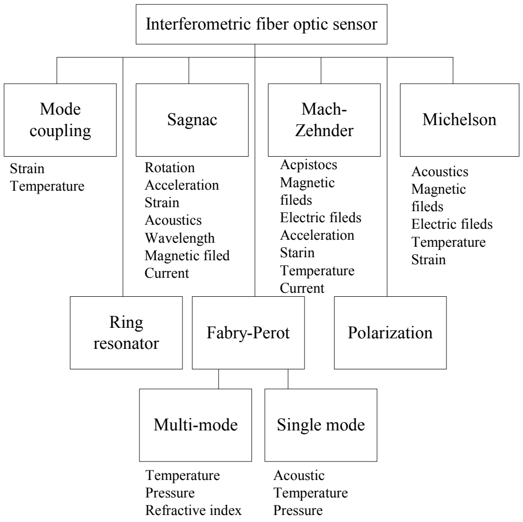

Figure 2 **Interferometric fiber sensors**

Optical fiber sensor applications

Temperature sensor by using long-period fiber grating

Figure 3 shows a diagram for the temperature sensor setup using long-period fiber grating (LPG) with gold coating. As shown in Figure 4, the LPG transmission spectrums are changed by the temperature variations, thus providing thermal coefficients due to calculating index variation per temperature changes.

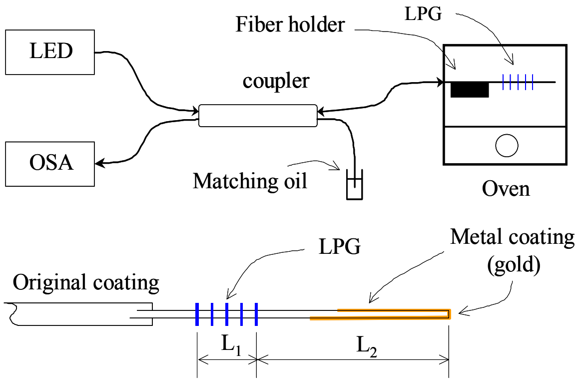

Figure 3 **Setup using an optical fiber temperature sensor with LPG**

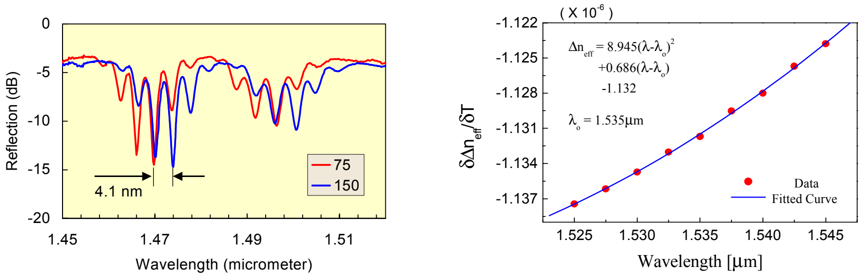

Figure 4 **Results of temperature sensor.** *Left: spectrum shift per temperature variations. Right: calculated thermal coefficient*

Strain sensor using 3 × 3 fiber-optic Michelson interferometric sensor

Figure 5 shows the 3 × 3 Michelson interferometric sensor for measuring the structural strain variation with the arctangent signal-processing method. This system can measure the increase and decrease variations or distinction methods for the loading and unloading directions. This 3 × 3 Michelson interferometric sensor especially shows real-time strain measurement.

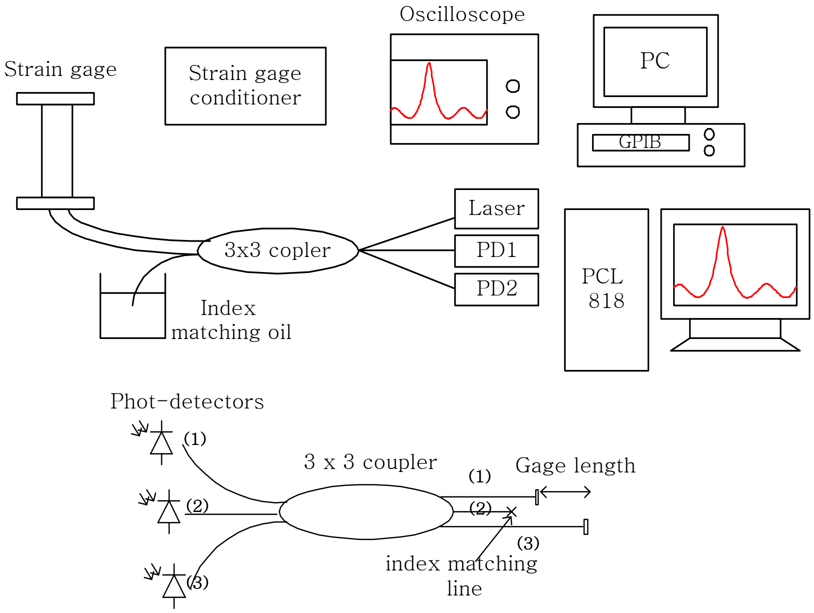

Figure 5 **Schematic diagram of the real-time strain measurement system**

Fiber optics vibration sensors

If the vibrating target can be incorporated into an interferometer, an optical technique may be used as a non-contacting and non-loading technique to monitor vibration. If the combination of lasers and fiber-optics is used, no direct line of sight is required for the monitored surface to be incorporated into an interferometer.

Vibration can be measured by sensing intensity or phase changes. The techniques that incorporate fibers to measure vibration are interferometric methods. These methods utilize intensity where the coupling efficiency between two fibers is modulated by the vibrating surface, polarization where the vibration modulates the fiber birefringence, frequency-modulated continuous wave, speckle interferometry, and electronic speckle pattern interferometry. Interferometric methods are applicable to velocity, acceleration, and flow sensing.

II. Analysis of wearing rate[1]

Description of Sanchez-Caldera's model

Sanchez-Caldera model [1, 2] is a theoretical model that can predict the rate of materials reduction induced by FAC.

$$\frac{dm}{dt} = k_g \frac{\theta\left(C_e - C_\infty\right)}{\frac{1}{k} + \left(1 - f\right)\left[\frac{1}{h_D} + \frac{\delta}{D}\right]} \qquad (1)$$

---

[1] This section includes details for analysis of wearing rate, which is introduced in Section 4.4.3.3.

where $\frac{dm}{dt}$ = wear rate [kg/m^{2}s]

k_g = geometrial factor

C_e = equilibrium concentration of iron species [kg/m^3]

C_∞ = iron species concentration in the bulk water [kg/m^3]

θ = porosity

$k = A\exp(-Q/RT)$, the reaction rate constant [m/s]

f = fraction of oxidized metal converted into magnetite at the metal-oxide interface (constant $f = 0.5$)

h_D = mass transfer coefficient [m/s]

δ = oxide thickness [m]

D = diffusion coefficient of the dissolved ferrous species [m^2/s]

The original Sanchez-Caldera model does not include the geometrical factor, k_g. This factor was introduced to allow this model to be applied to this work to consider a straight pipe condition to complex geometry, such as piping elbow,. From an empirical FAC model [3], the value of the geometrical factor for piping elbow is around 7.5 because the value for straight piping is unity.

To calculate the solubility of magnetite, Sanchez-Caldera introduced the work of Sweeton and Baes [4], which provides the experimental data on the solubility of magnetite as a function of temperature, hydrogen concentration, and pH. The commercially available computer code, HSC Chemistry®, was used to obtain the thermodynamic data for ferrous ions. The procedure to calculate the solubility of magnetite is as follows:

$$Fe_3O_4(s) + 6H^+ + H_2(g) = 3Fe^{2+} + 4H_2O;\quad K_1 \tag{2}$$

$$Fe^{2+} + H_2O = FeOH^+ + H^+;\quad K_2 \tag{3}$$

$$Fe_3O_4(s) + 3H^+ + H_2(g) = 3FeOH^+ + H_2O;\quad K_1K_2^3 \tag{4}$$

$$Fe^{2+} + H_2O = FeO(aq) + 2H^+;\quad K_3 \tag{5}$$

$$Fe_3O_4(s) + H_2(g) = 3FeO(aq) + H_2O;\quad K_1K_3^3 \tag{6}$$

$$Fe^{2+} + 2H_2O = HFeO_2^- + 3H^+;\quad K_4 \tag{7}$$

$$Fe_3O_4(s) - 3H^+ + H_2(g) = 3HFeO_2^- - 2H_2O;\quad K_1K_4^3 \tag{8}$$

Solubility of iron species:

$$\left[Fe^{2+}\right]=\left[K_1\left[H^+\right]^6 P_{H_2}\right]^{1/3}$$
$$\left[FeOH^+\right]=\left[K_1K_2^3\left[H^+\right]^3 P_{H_2}\right]^{1/3}$$
$$\left[FeO(aq)\right]=\left[K_1K_3^3 P_{H_2}\right]^{1/3} \tag{9}$$
$$\left[HFeO^-\right]=\left[K_1K_4^3\left[H^+\right]^{-3} P_{H_2}\right]^{1/3}$$
$$C_e=\left[Fe^{2+}\right]+\left[FeOH^+\right]+\left[FeO(aq)\right]+\left[HFeO^-\right]$$

$$P_{H_2}=K_{H_2}\cdot x_{H_2} \tag{10}$$

The equilibrium constants for each reaction are summarized in Table 1, which were fitted by using data from [5]. Equilibrium concentration of iron species C_e can be obtained from this.

Table 1 Summary of coefficients for each reaction's equilibrium constant

	A[1]	B	C	D	E
K_1	1.1522e+5	-1843.7	-0.27457	662.56	-5.6772e+6
K_2	-20620	320.27	0.047047	-115.75	1.0633e+6
K_3	-39380	618.99	0.092605	-224.67	1.8678e+6
K_4	745.05	-165.42	-0.031102	59.791	-4.4318e+5
K_{H_2}	-2573.6	56.071	2.2895e-4	-17.986	6908.3

[1] $$\log_{10} K=\frac{A}{T}+B+CT+D\log_{10}T+\frac{E}{T^2},\quad T(K)$$

Iron species concentration in the bulk water, C_∞, is negligible compared with the equilibrium concentration of iron species.

Porosity of magnetite, θ, changes with temperature as follows [2]:

$$\theta=0.03 \quad \left(T<150^oC\right)$$
$$\theta=-0.004\times T(^oC)+0.15 \quad \left(150^oC\le T\le 175^oC\right) \tag{11}$$
$$\theta=0.01 \quad \left(T>300^oC\right)$$

In the previous equations, the porosity has negative values within the range 150°C ≤T ≤ 175°C. Therefore, we modify the original equation such that the porosity linearly decreases from 0.03 to 0.01 within the range of 150°C ≤T ≤ 300°C:

$$\theta=-1.333\times10^{-4}\times T(^oC)+0.05 \quad \left(150^oC\le T\le 300^oC\right) \tag{12}$$

Reaction rate k is shown here [1]:

$$k=2.35\times10^{14}\exp\left(\frac{-17873}{T(K)}\right) \tag{13}$$

Diffusion coefficient, D, is calculated from Equation (14) [2]:

$$D = 1.04\times10^{-7}\,T(K)/\mu_f \qquad (14)$$
$$\text{where } \mu_f = \text{viscosity of water [kg/m - s]}$$

The self-diffusion coefficient of the ion D_i is related to the ionic radius R_i through the Stokes-Einstein equation [15]:

$$\begin{aligned} D_i &= k_B T/6\pi\mu R_i \quad \text{(stick boundary condition)} \\ &= k_B T/4\pi\mu R_i \quad \text{(slip boundary condition)} \end{aligned} \qquad (15)$$

Estimating the diffusivity by using Equation (15), there was discrepancy as much as several orders of magnitude. It seems that there may be a mistake in Equation (14), maybe in the order of constant. Therefore, we used available diffusivity data for Fe^{2+} ion [7]:

$$\begin{aligned} D_{Fe^{2+}} &= 3.3883\times10^{-10} + 1.3698\times10^{-11}t + 1.6824\times10^{-13}t^2 - 1.5445\times10^{-16}t^3, \\ &\left(0^oC \le t \le 300^oC\right) \end{aligned} \qquad (16)$$

The original data for the viscosity of saturated water from [8] were fitted as following equation.

$$\begin{aligned} \mu(T) &= 0.0023732 - 4.6688/T + 3465.6/T^2 - 1.1277\times10^6/T^3 + 1.4018\times10^8/T^4 \\ &295K < T < 630K \end{aligned} \qquad (17)$$

Scanning electron microscope observation by Keck of worn planting piping showed oxide thickness δ, around 10 µm, which is the value recommended for use.

Mass transfer coefficient, h_D [2]

$$\begin{aligned} \mathrm{Re} &= \frac{\bar{u}d}{\nu_f} \\ \text{where } \bar{u} &= \frac{4\dot{m}}{\pi\rho_f d^2}, \text{ average fluid velocity [m/s]} \\ d &= \text{pipe diameter [m]} \\ \nu_f &= \text{liquid kinematic viscosity [m}^2\text{/s]} \end{aligned} \qquad (18)$$

To get liquid kinematic viscosity, the specific volume of water as a function of temperature must be known. The original data for the specific volume of saturated water from [8] were fitted into the following equations:

$$\begin{aligned} v_f(T) = &-0.021088 + 0.00027808T - 1.3774\times10^{-6}T^2 + 3.353\times10^{-9}T^3 \\ &- 4.0106\times10^{-12}T^4 + 1.8929\times10^{-15}T^5, \qquad 273K < T < 640K \end{aligned} \qquad (19)$$

$$\mathrm{Sc} = \frac{\nu_f}{D} \qquad (20)$$

$$\begin{aligned} h_D &= \frac{D}{d}\left(2.0 + a\,\mathrm{Re}^b\,\mathrm{Sc}^{1/3}\right) \\ \text{where } a &= 0.86 - \frac{10.0}{(4.7+\mathrm{Sc})^3} \text{ and } b = 0.0165 - 0.011\mathrm{Sc}\exp(\text{-Sc}) \end{aligned} \qquad (21)$$

Keck [2] introduced Berger and Hau's expression to calculate the mass transfer coefficient. Reviewing other references [9], it was found that in Equation (21), the expressions for "a" and "b" were not correct. The correct Berger and Hau's expression is as follows:

$$h_D = \frac{D}{d}\left(2.0 + a\,\mathrm{Re}^b\,\mathrm{Sc}^{1/3}\right)$$

$$\text{where } a = 0.0165 - 0.011\mathrm{Sc}\exp(\text{-}\mathrm{Sc}) \text{ and } b = 0.86 - \frac{10.0}{(4.7+\mathrm{Sc})^3} \qquad (22)$$

The normal water chemistry of the secondary coolant system is deaerated with hydrazine and rendered slightly alkaline with ammonia. In a laboratory-scaled experiment, due to time limitations, an acceleration test was not conducted but should be performed. Therefore, we considered a slightly reducing environment with 150 ppb hydrogen and acidic solution. The pH of the test solution is one of the key parameters in the acceleration test.

Figure 6 shows the predicted wall thickness results reduced by FAC as a function of time and pH. From this figure, considering that the wall thickness of the test specimen is 3.6 mm and the reasonable test duration for single test condition is about two weeks, the reasonable pH is around 4.0.

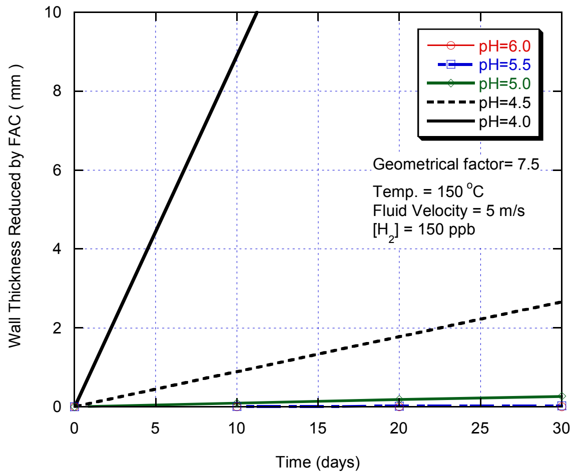

Figure 6 **Predicted wall thickness results reduced by FAC as a function of time**

Figure 7 shows the wall thickness reduced by FAC after 15 days as a function of temperature at pH 4.0 and 4.5. As shown in this figure, there was a maximum FAC rate at around 160°C (it has been reported that usually the FAC rate has a maximum value at around 150°C). The temperature dependency of the predicted results seems to be reasonably acceptable. Figure 8 shows the reduced wall thickness after 15 days as a function of flow velocity. It shows that there is no significant difference between the results of 5 m/s and 10 m/s. In the case of 5 m/s, the empirical model [3] shows that the FAC rate is about two times higher than in the case of 10 m/s, which may result from the uncertainty of mass transfer coefficient h_D used in Sanchez-Caldera model.

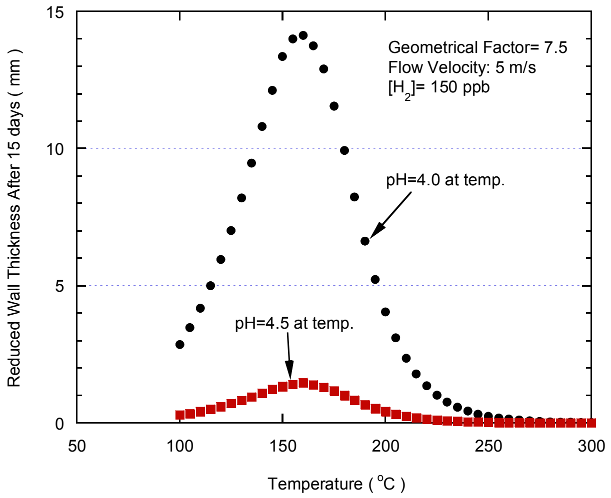

Figure 7 **Reduced wall thickness after 15 days as a function of temperature**

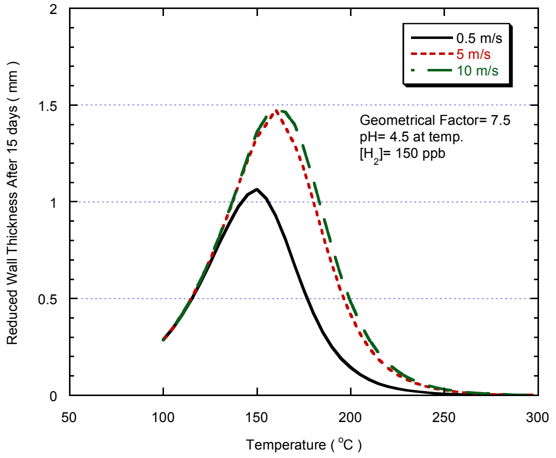

Figure 8 **Reduced wall thickness after 15 days as a function of flow velocity and temperature**

Figure 9 shows the experimental results for the influence of hydrazine on FAC rate without oxygen [10]. The pH of the test solution was adjusted to 9.0 at 25°C with ammonia and hydrazine was added to scavenge oxygen. If the needed ammonia content to make the solution with pH = 9.0 at 25°C is known, we can calculate high-temperature pH by using MULTEQ-REDOX®, a thermodynamic code [11].

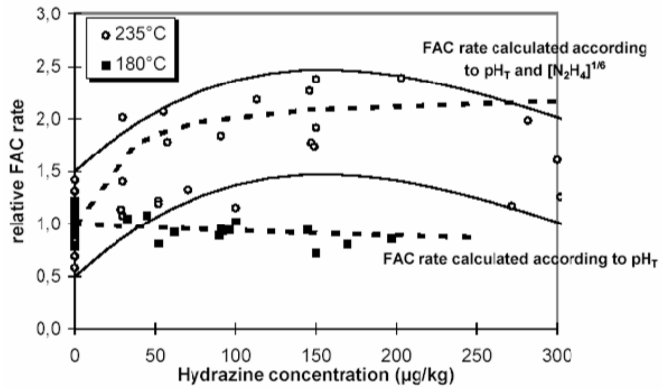

Figure 9 **Relative FAC rate versus hydrazine concentration for tubular carbon steel specimens exposed to a single-phase flow at 180°C and 235°C using ammonia (pH_{25C} = 9.0) [10]**

Using the pH data of feedwater or normal blow-down water in PWR [12], we extrapolated Equation (23) to the lower pH regions as shown in Figure 10.

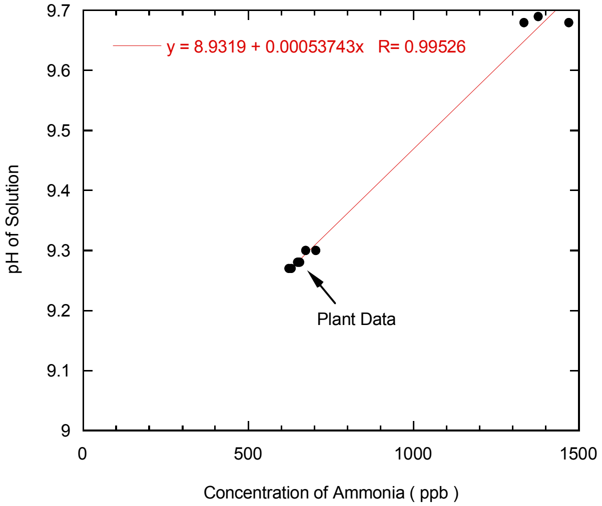

Figure 10 Feedwater and normal blow-down water pH as a function of ammonia concentration [12]

$$pH = 0.00053743 \times C_{NH_3}(ppb) + 8.9319 \quad @25\ ^{o}C \tag{23}$$

From Equation (23), the needed ammonia content for pH = 9.0 is about 130 ppb. Table 2 shows the temperature coefficients for the pH of 130 ppb ammonia solution as a function of hydrazine concentration. The high-temperature pH values were calculated by using MULTEQ-REDOX code and the pH data were fitted as polynomial formula. The current Sanchez-Caldera model cannot consider the effect of hydrazine on FAC directly; therefore, by using this code, the hydrogen concentration equivalent to the reducing power of hydrazine could be estimated as described in Table 3.

Figure 2 shows the predicted relative FAC rate results compared to experimental data. the model predicts that the FAC rate increases sharply at the transition from no hydrazine to 50 ppb hydrazine. Experimental results show that at 180°C, there is no significant influence of hydrazine on FAC rate; however, at 235°C, the hydrazine addition increases the FAC rate by a factor of two compared to the no-hydrazine condition. In the model results, FAC rate slightly increases with hydrazine addition at both 180°C and 235°C, but the FAC rate at 180°C is lower than that at 235°C. The discrepancy between predicted and experimental results may come from indirect simulation of hydrazine effect that the equivalent hydrogen concentration is estimated and used as the input value instead of hydrazine. The experimental data of hydrogen water chemistry, such as CANDU feeders, are more appropriate to use to verify the current model than that of PWR secondary water chemistry. The model also predicted the wall thickness reduction after 15 days for the case of an ammonia and hydrazine mixture, as shown in Figure 12. The FAC rate has a maximum at around 180°C. The reduced wall thickness is estimated to be 10 to 100 nm (less than 1 μm). Considering that the test duration was less than 100 hours [10] and the oxide thickness is assumed to be 10 μm, the predicted FAC rate is too low and unreasonable.

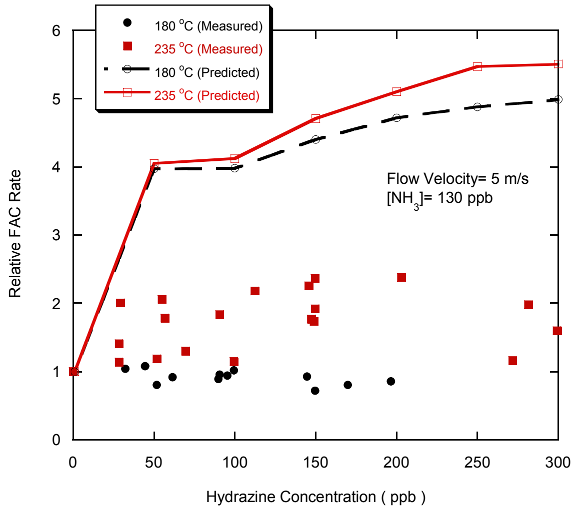

Figure 11 **Predicted FAC rate results compared to experimental data**

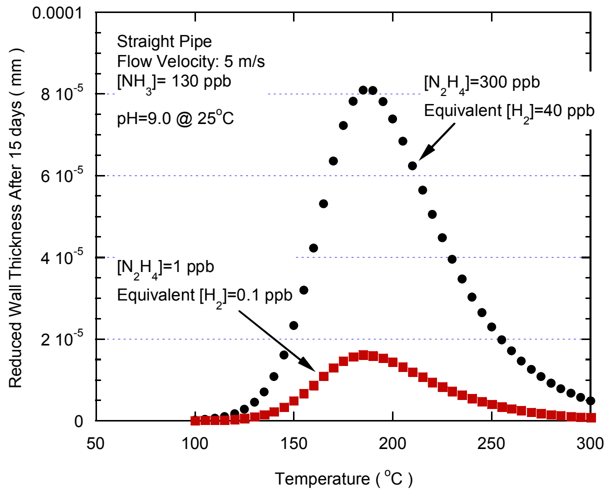

Figure 12 **Reduced wall thickness after 15 days for the case of ammonia and hydrazine mixture solution**

Table 2 **Lifetime averaged CANDU-6 operating conditions [13]**

Operating Conditions	Wolsong-1	Gentilly 2	Point Lepreau
Temperature (°C)	307	307[1]	307[1]
Flow Velocity (m/s)	11.95	12.79	14.50
pH @ 25°C	10.5	10.61	10.63
[Li Conc. (ppm)]	[2.19]	[2.83]	[2.96]
$[H_2]$ (ppb)[2]	540	540	540
Tube ID (cm)	5.9	5.9	5.9
Oxide Thickness (μm)[3]	1	1	1
Geometrical Factor, k_c[4]	5	5	5

1 The same as Wolsong-1 because not reported.
2 Arbitrary value, 6 cc/kg
3 Referenced from [14]
4 Arbitrary value considering that the geometrical factor of 90° elbow is 7.5.

CANDU feeders' wall-thinning data is also used to verify this FAC model. Table 3 shows the lifetime averaged CANDU-6 operating conditions. LiOH concentration is estimated from the pH value at room temperature. The estimated Li concentration is used as an input value for calculating the high-temperature pH with MULTEQ-REDOX code. Table 3 shows the summary of coefficients for the pH of each CANDU NPP's primary solution.

Table 3 Summary of coefficients for the pH of each CANDU NPP's primary solution

Coefficients	Wolsong-1	Gentilly 2	Point Lepreau
A[1]	11.755	12.558	13.723
B	-0.048273	-0.061137	-0.080646
C	0.00024046	0.00032728	0.00044729
D	-6.6544e-7	-9.1792e-7	-1.2366e-6
E	8.5316e-10	1.1198e-9	1.4298e-9

$$pH(t) = A + Bt + Ct^2 + Dt^3 + Et^4 ,\ t\left({}^{o}C\right), \left(150^{o}C \le t \le 325^{o}C\right)$$

The predicted wall-thinning rate is compared with the measured data, as shown in Table 4 and Figure 13. The current model underestimates the wall-thinning rate of CANDU feeders by as much as a factor of 15. The underestimation of the FAC model developed for mainly PWR secondary side was also reported at other plants [14]. The modeling results under the CANDU condition have an unusual temperature dependency, as shown in Figure 14. The FAC rate has a maximum value around 230°C and decreases at 300°C; however, over 300°C, the FAC rate starts to increase again. From these predicted results, the wall-thinning rate at 265°C (the inlet feeder's temperature) is higher than that of outlet feeders. The inlet feeders did not suffer from significant FAC phenomena [13]. However, these results can be interpreted that at inlet feeders, the bulk coolants are in saturated states and at outlet feeders (with higher coolant temperature conditions) are in under saturated states because the primary circuit is a closed loop.

Table 4 Average feeder wall-thinning rate

Plant Name	Wolsong-1	Gentilly 2	Point Lepreau
Measured Data	93 μm/yr	94 μm/yr	110 μm/yr
Predicted Data	5.7 μm/yr	6.9 μm/yr	7.7μm/yr

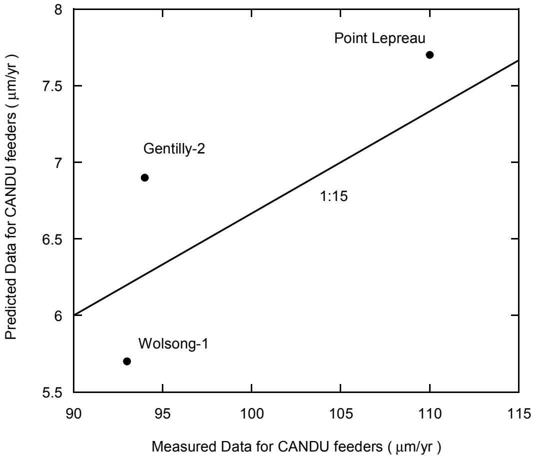

Figure 13 Predicted wall-thinning rate for CANDU outlet feeders compared to measured NPP data

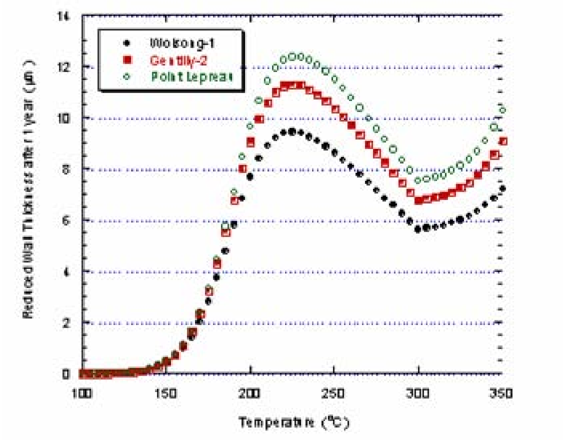

Figure 14 **Reduced wall thickness after one year as a function of temperature**

Figure 15 shows the experimental results by Sanchez-Caldera at the flow velocity of 0.57 m/s and 3.13 m/s [1]. The wall- thinning rate is predicted in the case of Sanchez-Caldera's experiment. The pH of test solution is 5.5 at room temperature and adjusted with hydrochloric acid. The dissolved oxygen concentration is less than 200 ppb. It appears as an oxidizing condition, but in this model, the deaerated condition is assumed, which means that the dissolved hydrogen concentration is 0.1 ppb. Figure 16 shows the predicted wall-thinning rate for Sanchez-Caldera's experiment compared to the measured data. The current model predicts the thinning rate to an order of magnitude below the measured data.

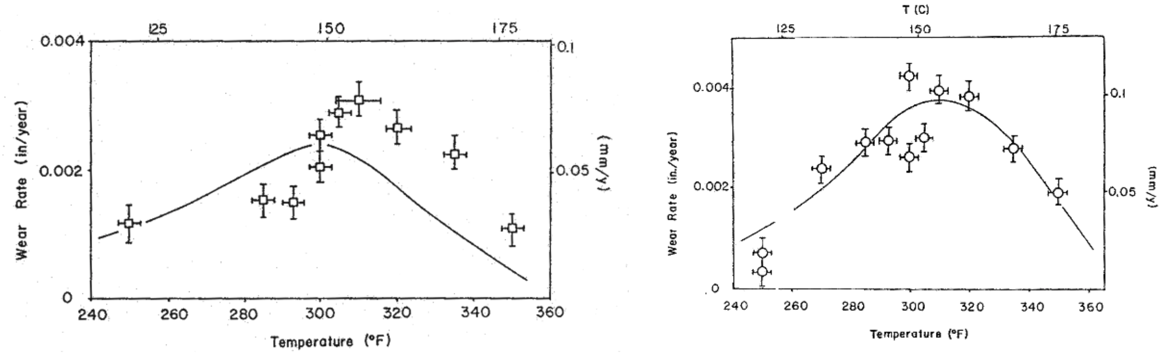

(a) 0.57 m/s (b) 3.13 m/s

Figure 15 **Experimental results by Sanchez-Caldera at two flow velocities [1]**

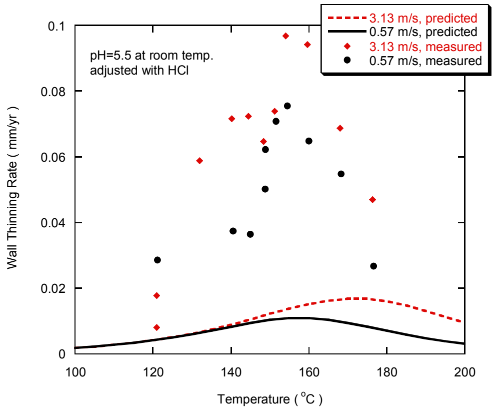

Figure 16 **Predicted wall- thinning rate for Sanchez-Caldera's experiment compared to the measured data**

The bulk concentration of ferrous ions C_∞ is assumed negligible in this prediction. However, if a slightly acidic test solution with the pH of 4.5 is used, the bulk concentration can become significant. The increase in bulk concentration will decrease the FAC rate. Equation (1) is the FAC rate in a steady-state condition. However, as shown in Figure 17, it may take some time to achieve a steady-state FAC rate and even weight gain is possible at an initial stage. It is expected to take more time in a real experiment to reach an expected wall thickness than the predicted case due to the initial weight gain. If the acidic environment is used in FAC tests, the thickness profile along the flow path at piping elbow specimen can be different from that under NPP conditions. This problem needs to be further studied. The current model cannot include the effect of chemical compositions of steel, especially Cr and Mo contents. The material parameter should be also investigated when modeling FAC.

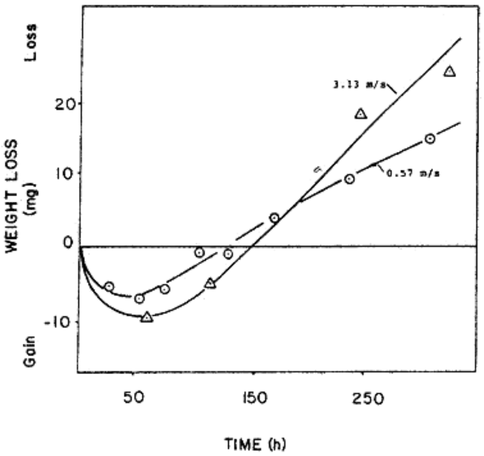

Figure 17 **Weight change of test specimen as a function of time [1]**

Lister's model

Lister and Lang [14] have developed a mechanistic model for predicting flow-assisted and general corrosion of carbon steel in CANDU primary coolants. They account for electrochemical considerations in their model and assume that the main processes of FAC include the diffusion of dissolved iron species and the magnetite dissolution and mass transfer. The solubility at metal-to-oxide interface and oxide-to-coolant interface and the dissolution rate constant are dependent on the ECP at each interface. The corrosion rate for CANDU outlet feeders is given by Equation (24):

$$\frac{dm}{dt} = \frac{S \cdot C^{e}_{M-O} - \dfrac{k_d F^* C^{e}_{O-C} + kC_b}{k_d F^* + k}}{0.476(1.101 + \phi_i)\left[\dfrac{\delta_i \zeta}{\rho_{ox}(1-\phi_i)\phi_i D_{Fe}} + \dfrac{1}{k_d F^* + k}\right]} \tag{24}$$

where : S = supersaturation factor to account for small crystallite size (assumed 1.1);

C^e_{M-O} = solubility at M - O interface;

C^e_{O-C} = solubility at O - C interface;

k_d = magnetite dissolution rate constant;

k = mass transfer coefficient;

F^* = surface area factor (assumed $\sqrt{3}$);

C_b = bulk coolant concentration of dissolved iron;

ϕ_i = porosity of oxide layer;

ζ = tortuosity (assumed 1.2 for oxide layer);

δ_i = oxide thickness;

ρ_{ox} = density of magnetite;

D_{Fe} = diffusivity of dissolved iron.

A computer program solves for corrosion rate and film thickness iteratively at each time step, using the iron balance equation for the dissolved layer:

$$0.723\frac{d\delta_i}{dt} = 0.476\frac{dm}{dt}(1-\phi_i) - k_d F^*\left(C^e_{O-C} - C_b\right) \tag{25}$$

and the electrochemical quantities C^e_{M-O}, C^e_{O-C}, and k_d are adjusted for the computed potential at each time step. For the electrochemical processes involved, the rate as an equivalent current, i, is described in terms of Butler-Volmer kinetics.

To correlate FAC rate and the measured data from electrochemical sensors, such as ECP sensor and pH sensor, a FAC model that can include the effect of ECP and pH is needed. Lister's model can be one of them if the parameters and assumptions tuned for CANDU feeders are adjusted for PWR primary environments.

Conclusions

- To predict the consumed time for a FAC test and construct a test matrix, available FAC models were reviewed and some of them were applied to predict the time.
- Sanchez-Caldera's model was slightly modified and the solubility of iron was calculated from the HSC Chemistry code.
- Sanchez-Caldera's model overestimated the effect of hydrazine on FAC rate and predicted the FAC rate in CANDU feeders and in a slightly acidic environment at a factor of 15 to 10 lower.
- Based on the predicted results from available models, pH = 4.5 and dissolved hydrogen concentration = 150 ppb were selected as the conditions of the test solution.

Water chemistry control. The developed test loop is designed to validate both electrochemical and mechanical sensors. Electrochemical sensors need well-controlled water chemistry. First, we calculate the amount of chemicals required to induce a satisfactory wearing rate as discussed in the previous chapter. We decided to use HBO_3 and HNO_3 to make the acidic environment (pH =~4 to 4.5). By using the MULTEQ-REDOX code, we decided to use 400 ppm of HBO_3 and 10 ppm of HNO_3. This is calculated from iteration steps and the pH will be about 3.71 at 150°C. This is slightly lower than the design criteria. As a test solution, demineralized water is used and after mixed it with the chemicals, we perform bubbling with 5% hydrogen and 95% nitrogen gas (it takes ~3 hours). Next to the backpressure regulator, we install a conductivity meter and DO meter to measure the water environment. It indicates that the dissolved oxygen is below 1 ppb and conductivity is ~30 to 40 μs.

References

1. R. G. Keck and P. Griffith, prediction of Erosive-Corrosive Wear in Low-Carbon Steel Piping Conveying Water or Wet Steam, *ASME Journal of Engineering for Gas Turbines and Power*, Vol. 112, p.555-560, 1990
2. L. E. Sanchez-Caldera, The Mechanism of Corrosion-Erosion in Steam Extraction Lines of Power Stations, *ASME Journal of Engineering for Gas Turbines and Power*, Vol. 110, p.180-1841988
3. Von W. Kastner and K Riedle, Empirisches Modell zur Berechnung von Materialbtrgen durch Erosionskorrosion, *VGB KRAFTWERKSTECHNIK 66*, Heft 12, p.1171-1178, 1986
4. F. Sweeton and C. Baes, The Solubility of Magnetite and Hydrolysis of Ferrous Ion in Aqueous Solutions at Elevated Temperatures, *J. Chem. Thermodynamics*, Vol. 2, p. 479-500, 1970
5. Antti Roine, Outokumpu HSC Chemistry® for Windows: Chemical Reaction and Equilibrium Software with Extensive Thermochemical Database, User's Guide, Version 4.0, 1999.
6. J. N. Agar, C. Y. Mou, and Jeong-long Lin, Single-Ion Heat of Transport in Electrolyte Solutions. A Hydrodynamic Theory, *J. Phys. Chem.*, Vol. 93, No. 5, p. 2079-2082, 1989
7. R. Mills and V. M. M. Lobo, Self-Diffusion in Electrolyte Solutions: a Critical Examination of Data Compiled from the Literature, *ELSEVIER*, p. 320, 1989
8. F. P. Incropera and D. P. DeWitt, *Fundamentals of Heat and Mass Transfer*, 3rd Ed., John Wiley & Sons, 1990.
9. Cragnolino, A Review of Erosion-Corrosion of Steels in High Temperature Water, *Proc. 3rd Environmental Degradation of Materials in Nuclear Power Systems-Water Reactors*, Ed. G. J. Theus and J. R. Weeks, The Metallurgical Society, Traverse City, Michigan, p. 397-406, 1987
10. De Bouvier, M. Bouchacourt, and K. Fruzzetti, Redox Conditions Effect on Flow Accelerated Corrosion: Influence of Hydrazine and Oxygen, *Proc. Int. Conf. Water Chemistry in Nuclear Reactors Systems*, Avignon, France, April 22-26, 2002
11. MULTEQ: Equilibrium of an Electrolytic Solution With Vapor-Liquid Partitioning Volume 3: Theory Manual, EPRI NP-5561-CCML Volume 3, Palo Alto, CA: Electric Power Research Institute, 1992
12. Report of Diagnostics in Steam Generator (II)–1997, KEPCO and SNU, 1998
13. Development of Diagnostics in Feed Piping and Fuel in CANDU Reactor, KAERI/RR-2226/2001, KAERI, 2002
14. H. Lister and L. C. Lang, A Mechanistic Model for Predicting Flow-Assisted and General Corrosion of Carbon Steel in Reactor Primary Coolants, *Proc. Int. Conf. Water Chemistry in Nuclear Reactors Systems*, Avignon, France, April 22-26, 2002.

Report References

1. M. Leybold and J. Bracken, *I-NERI-Check Valve Data Review of September 2003 Test Session and Specification of ARL Check Valve Test Bed*, February, 2004
2. V. Luk, *Condition Monitoring through Advanced Sensor and Computational Technology–Year 2 Report (January–December) 2003*
3. H. Cramer, *Stationary and Related Stochastic Processes: Sample Function Properties and Their Applications*, John Wiley and Sons, New York, 1967. See also B. S. Everitt, *The Cambridge Dictionary of Statistics*, Cambridge University Press, London, p. 319, 2002
4. H. E. Hurst, Long-Term Storage Capacity of Reservoirs, *Trans. Amer Soc Civil Engineers*, Vol. 116, p. 770, 1951
5. S. Kotz, *Encyclopedia of Statistical Science–Volume 3,* John Wiley and Sons, New York, 1999 p. 689. See also B. Mandelbrot and J. W. Van Ness, Fractional Brownian Motion, Fractional Noises and Applications, *SIAM Review*, Vol. 10, p. 422, (1968)
6. M. Gilmore, et al, Investigation of rescaled range analysis, the Hurst exponent, and long-time correlations in plasma turbulence, *Phys Plasmas*, 9, p. 1312, 2002
7. T. G. Leyton, *The Acoustic Bubble*, Academic Press, San Diego, 1997. See also publications of Ulrich Parlitz and Detlef Lohse

8. S. J. Orfanidis, *Optimal Signal Processing: An Introduction,* Macmillan, New York, 1988
9. Wax, M., Kailath, T., Detection of Signals by Information Theoretic Criteria, *IEEE Trans Acoustics, Speech, and Signal Processing*, Vol. ASSP-33, p. 387, 1985, and included references
10. S. L. Marple, *Digital Spectral Analysis with Applications,* Prentice-Hall, Englewood Cliffs, 1987.
11. O. De Bouvier, M. Bouchacourt, and K. Fruzzetti, Redox Conditions Effect on Flow Accelerated Corrosion Influence of Hydrazine and Oxygen, *Proc Int Conf Water Chemistry in Nuclear Reactors Systems*, SFEN, Avignon, France, April 2002.
12. Benjamin L. Dow Jr., et al., Update: Repair and Replacement Trends, *Nucl. Eng. Int.*, Vol. 43, No. 523, pp. 38-40, 1998
13. Fluent, Inc., Release Notes for FLUENT 6.2.9–Beta Version, November 16, 2004.
14. S-E. Kim, Large Eddy Simulation Using Unstructured Meshes and Dynamic Subgrid-Scale Turbulence Models, AIAA Paper 2004-2548, 34th AIAA Fluid Dynamics Conference and Exhibit, Portland, OR,June 28-July 1, 2004
15. L. Ong, and J. Wallace, 1996, The velocity field of the turbulent very near wake of a circular cylinder, *Experiments in Fluids*, 20:441-453.
16. B. Cantwell and D. Coles, 1983, An experimental study of entrainment and transport in the turbulent near wake of a circular cylinder, *J Fluid Mech,* 136:321-374.
17. R. D. Blevins, , *Flow-Induced Vibration*, Second Edition, Krieger Publishing Company, Malabar, FL, 2001
18. M. Breuer, Numerical and modeling influences on large eddy simulations for the flow past a circular cylinder, *Int J Heat Fluid Flow*, 19:512-521, 1998
19. M. Breuer, Large Eddy Simulation of the Subcritical Flow Past a Circular Cylinder: Numerical and Modeling Aspects, *Int J for Numerical Methods in Fluids*, 28:1281-1302, 1998
20. M. Breuer, A challenging test case for large eddy simulation: high Reynolds number circular cylinder flow, *Int J Heat Fluid Flow*, 21:648-654, 2000
21. Fluent, Inc., *Modeling Turbulence*, Chapter 10 of FLUENT 6.2 User's Guide, Draft, October 22, 2004.
22. W. M. Kays, *Convective Heat and Mass Transfer*, McGraw-Hill Book Company, New York, 1966.
23. L. M. Lourenco and C. Shih, Characteristics of the plane turbulent near wake of a circular cylinder, a particle image velocimetry study, 1993; data provided by M. Breuer, November 9, 2004
24. C. Norberg, Fluctuating lift on a circular cylinder: review and new measurements, *J Fluids and Structures*, 17:57-96, 2003
25. O. Simonin and M. Barcouda, Measurement of fully developed turbulent flow across tube bundle, 3rd Intl Symp of Applications of Laser Anemometry to Fluid Mechanics, Lisbon, Portugal, 1986
26. O. Simonin and M. Barcouda, Measurements and prediction of turbulent flow entering a staggered tube bundle, 4th Intl Symp of Applications of Laser Anemometry to Fluid Mechanics, Lisbon, Portugal, 1988.

DISTRIBUTION:

1 Suibel Schuppner
Manager I-NERI Program
NE-20/ Germantown Building
U.S. Department of Energy
1000 Independence Avenue S.W.
Washington, DC 20585-1290

1 Ken Osborne
DOE Project Manager
1955 Fremont Avenue
Idaho Falls, ID 83401-1235

1 Dennis Kreid
Executive Agent
Pacific Northwest National Laboratory
NSB Building
3230 Q Street
PO Box 999, MS K7-68
Richland, WA 99352

2 Gye Seok Lee
Div. of Nuclear R&D Program
Korea Science and Engineering Foundation (KOSEF)
180-1. Gajeong-Dong
Yousung-Gu, Daejon-Ity, 305-350
KOREA

1 Mitchell S. Lebold
Applied Research Laboratory
The Pennsylvania State University
P.O. Box 30 (North Atherton Street)
State College, PA 16804-0030

1 Jeff Bracken
Applied Research Laboratory
The Pennsylvania State University
P.O. Box 30 (North Atherton Street)
State College, PA 16804-0030

1	MS 0370	Laura Swiler
1	0380	Benjamin Spencer
1	0719	Stephen Webb
1	0736	Marianne Walck
1	0744	Michael Hessheimer
1	0744	Jason Petti
1	0771	John Kelly
1	0836	Greg Homicz
1	1078	Stephen Martin
1	1081	Jonathan Weiss

10	MS 1160	Vincent Luk
1	1161	David Craft
1	9018	Central Technical Files, 8945-1
2	0899	Technical Library, 9616
2	0612	Review & Approval Desk, 9612 For DOE/OSTI